Doping ns^2-Ions and Lanthanide Ions in Metal-Halide Perovskites: Visible to Short-Wave Infrared Emission

विद्या वाचस्पति की उपाधि की अपेक्षाओं की आंशिक पूर्ति में प्रस्तुत शोध प्रबंध

A thesis submitted in partial fulfilment of the requirements of the degree of Doctor of Philosophy

द्वारा / By
हबीबुल आरफ़ीन/
Habibul Arfin

पंजीकरण सं. / Registration No.: 20183604

शोध प्रबंध पर्यवेक्षक / Thesis Supervisor:
डॉ. अंगशुमन नाग / Dr. Angshuman Nag

IISER PUNE

भारतीय विज्ञान शिक्षा एवं अनुसंधान संस्थान पुणे
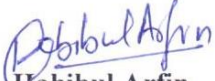INDIAN INSTITUTE OF SCIENCE EDUCATION AND RESEARCH PUNE
2023

This thesis is dedicated to

My parents, Teachers and Friends

without whom none of my success would be possible.

Declaration

I declare that this written submission represents my ideas in my own words and wherever other's ideas have been included, I have adequately cited and referenced the original sources. I also declare that I have adhered to all principles of academic honesty and integrity and have not misrepresented, fabricated or falsified any idea/ data/ fact/ source in my submission. I understand that violation of the above will be cause for disciplinary action by the Institute and can also evoke penal action from the sources which have thus not been properly cited or from whom proper permission has not been taken when needed.

Date: 31-08-2023

Habibul Arfin
(ID: 20183604)

Certificate

I certify that the work incorporated in the thesis entitles "**Doping ns^2-Ions and Lanthanide Ions in Metal-Halide Perovskites: Visible to Short-Wave Infrared Emission**" submitted by **Mr. Habibul Arfin** was carried out by the candidate, under my supervision. The work presented here or any part of it has not been included in any other thesis submitted previously. For the award of any degree or diploma from any other university or institution. For the completion of the thesis, a few results are taken from collaborators after their permission and are clearly mentioned in the thesis.

Date: 31-08-2023

Dr. Angshuman Nag
(Research Supervisor)

Acknowledgements

direction. Your mentorship continues to guide me. To my current lab mates – Parikshit, Sajid, Barnali, Taniya, Urmila, Srijita, Animesh, Manmayuri, Pavithra, Ajinkya – I wish you all the best in your future endeavors.

I extend my appreciation to all my friends and family members for their unwavering support during times of need. To my friends at IISER Pune – Sanchayita, Pragalbh, Ardhra, Himan, Abhishek, Kirti, Muskan, Souvik, Tumpa, Pooja – you have become an integral part of my life over these years. Our shared memories of monsoons in Pune, cooking sessions, and celebrations are constant source of joy. Your warm friendship brought out the best in me both professionally and personally. To my family, words fall short in expressing the depth of my emotions and gratitude. Your unwavering strength and support made my journey seamless.

Lastly, I extend my acknowledgment to the University Grants Commission (UGC), India, for providing the fellowship that made it possible for me to embark on and complete this research journey. Without this support, navigating the complexities of life as a researcher would have been significantly more challenging.

List of Abbreviations

0D: Zero dimensional

3D: Three dimensional

CBM: Conduction band maximum

CIE: International commission on illumination

EDS: Energy dispersive X-ray spectroscopy

FA: Formamidinium

FESEM: Field emission scanning electron microscopy

FRET: Förster resonance energy transfer

FWHM: Full width at half maximum

EXAFS: Extended X-ray absorption fine structure

HOMO: Highest occupied molecular orbital

ICP-AES: Inductively coupled plasma atomic emission spectroscopy

ICP-MS: Inductively coupled plasma mass spectroscopy

IRF: Instrument response function

LED: Light-emitting diode

LUMO: Lowest unoccupied molecular orbital

MA: Methylammonium

NP: Nanoparticles

Pc-LED: Phosphor converted LED

PL: Photoluminescence

PLE: Photoluminescence excitation

PLQY: Photoluminescence quantum yield

PMT: Photomultiplier tube

PMMA: poly (methyl methacrylate)

PXRD: Powder X-ray diffraction

List of Abbreviations

RES: Relaxed excited state

STE: Self-trapped exciton

SWIR: Short-wave infrared

TCSPC: Time-correlated single-photon counting

TGA: Thermogravimetric analysis

VBM: Valance band maximum

UV: Ultraviolet

RES: Relaxed excited state

Synopsis

Lead halide perovskites are being extensively explored in recent times for their promising optoelectronic properties. However, lead toxicity and structural stability impose some limitations for their wide spread commercial applications. Lead free halide double perovskites are proposed as alternatives to lead halide perovskites. But the lead free halide double perovskites lack the interesting semiconducting and optical properties of lead based perovskites. Interestingly, the halide double perovskites have intriguing structural properties such as octahedral sites and compositional tunability, that can make double perovskites a promising class of host materials for doping luminescent centers. Lanthanide ions with narrow emission feature are promising emitters, especially for short-wave infrared emission (900-1700 nm). We realized that In^{3+} ions in $Cs_2AgInCl_6$ double perovskite have similar ionic radii and oxidation state compared to lanthanide ions, and therefore, Er^{3+}- and Yb^{3+}-doped $Cs_2AgInCl_6$ are prepared emitting 1540 and 990 nm radiation, respectively. However, the samples required to be excited at wavelength below 350 nm. The large energy difference between excitation and emission causes a large energy loss, even for an ideal luminescence efficiency. This thesis explores the potential of halide double perovskites to host lanthanide luminescent centers and reduces the energy difference between the excitation and emission by codoping ns^2-ions like Bi^{3+}, Sb^{3+}, Te^{4+}.

Another related lead free system is Cs_2SnCl_6 vacancy ordered perovskite, that has electronically isolated $[SnCl_6]^{2-}$ octahedral. Doping Bi^{3+} and Sb^{3+} in Cs_2SnCl_6 provides opportunity to study the optical properties of luminescent centers in isolated octahedrons unlike the corner shared octahedrons in double perovskites. With the help of temperature dependent photoluminescence spectroscopy, we find the mechanistic origin of excitation and emission processes in Bi^{3+}- and Sb^{3+}-doped Cs_2SnCl_6.

The thesis has five chapters. A brief discussion about all the chapters are given below.

Chapter 1: Introduction

This chapter introduces the fundamental ideas used in the research and the motivation behind the work presented in this thesis. It starts by briefly explaining the perovskite structure. It then discusses the promise of lead halide perovskites for optoelectronic applications. Due to concerns about lead toxicity, the focus shifts to lead-free halide perovskites. The potential of lead-free halide double perovskite structure is highlighted as a suitable host for doping various types of luminescent centers. Luminescent centers such as lanthanide ions (Er^{3+}, Yb^{3+}) and ns^2-ions (Bi^{3+}, Sb^{3+}, Te^{4+}) are doped. The nature of electron transitions of these luminescent

centers, are explained. The chapter concludes by outlining the scope of the thesis. This involves addressing challenges related to lanthanide doping into halide perovskites, and the propose solution involving the codoping of ns^2-ions to mitigate these challenges.

Chapter 2: Bi^{3+}-Er^{3+} and Bi^{3+}-Yb^{3+} Codoped $Cs_2AgInCl_6$ Double Perovskite: Visible to Short-Wave Infrared Emitters

Lanthanide ions (Ln^{3+} = Er^{3+}, Yb^{3+}) doped in $Cs_2AgInCl_6$ require high energy excitation (>3.45 eV) which causes large energy gap between excitation and emission, leading to an energy loss. To address the issue, this chapter introduces the idea of codoping Bi^{3+} and Ln^{3+} in halide perovskites. A synthesis methodology is developed to codoped Bi^{3+} and Ln^{3+} ions into $Cs_2AgInCl_6$ double perovskite. The resulting products are rigorously examined using powder X-ray diffraction, energy dispersive spectroscopy and inductively coupled plasma mass spectrometry to ensure their composition and phase purity. The optical absorption and emission properties of the Bi^{3+}-Ln^{3+} codoped $Cs_2AgInCl_6$ are systematically investigated to elucidate the distinct contributions of the various ions. Bi^{3+} doping notably decreases the excitation energy, enabling the material to excite with 370 nm light. Bi^{3+}-Er^{3+} codoped $Cs_2AgInCl_6$ emits 1540 nm radiation due to f-electrons of Er^{3+}, which is useful for efficient optical communication with minimal losses. We extended this strategy for another lanthanide, Yb^{3+}, forming Bi^{3+}-Yb^{3+} codoped samples, emitting at 994 nm.

Chapter 3: Short Wave Infrared Emissions from Te^{4+}-Ln^{3+} (Ln: Er, Yb) Codoped $Cs_2NaInCl_6$ Double Perovskites

Bi^{3+}-Ln^{3+} codoped $Cs_2AgInCl_6$ sample that we discussed in the previous chapter, photodegrade on ultraviolet (UV) light excitation. Ag^+ present in the host might be the possible reason because Ag^+ is known to get reduce under UV light. This issue is addressed by replacing Ag^+ with Na^+. $Cs_2NaInCl_6$ double perovskite is environmentally benign and its wide band gap (~5.1 eV) makes it photo-inactive and photo-stable in the UV, visible, and short-wave infrared (SWIR) region. Ln^{3+} (Er^{3+} and Yb^{3+}) doping in $Cs_2NaInCl_6$ is achieved to obtain SWIR radiation at 1540 nm (0.81 eV) and 994 nm (1.247 eV). But the host has large band gap (~ 5.1 eV) so the required excitation energy is high (> 5.1 eV). The large Stokes shift for the excitation and SWIR emission reduces the power conversion efficiency. In this chapter we introduce the Te^{4+}-Ln^{3+} codoping in $Cs_2NaInCl_6$. The synthesis procedure is developed and the samples are thoroughly characterized. Te^{4+}-Er^{3+} codoped sample absorbs at the sub-band gap level around 3.1 eV (400 nm), because of $5s^2 \rightarrow 5s^1 5p^1$ electronic transitions. In the codoped samples, Er^{3+}

emissions are obtained by 400 nm excitation of Te^{4+}. Temperature (8 – 300 K) dependent photoluminescence excitation, emission, and lifetime measurements are carried out to reveal the mechanism of these energy transfer processes. The codoping is also demonstrated for Te^{4+}-Yb^{3+} codoped $Cs_2NaInCl_6$. Finally, we fabricated a simple phosphor converted light emitting diode (pc-LED) emitting SWIR radiation.

Chapter 4A: Origin of Luminescence in Sb^{3+}- and Bi^{3+}-Doped Cs_2SnCl_6 0D Perovskites: Excited State Relaxation and Spin-Orbit Coupling

Vacancy ordered perovskites (Cs_2SnCl_6) with isolated octahedrons provide opportunity to study the optical properties of luminescent centers (Bi^{3+}, Sb^{3+}) in isolated octahedrons. Cs_2SnCl_6 host is non-luminescent and have absorption below 350 nm. So, the host optical properties do not interfere with that of luminescent centers (Bi^{3+}, Sb^{3+}). In Bi^{3+}-doped and Sb^{3+}-doped Cs_2SnCl_6, the outermost s-electrons (ns^2) of respective ions are responsible for both light absorption (ns^2 to ns^1np^1) and emission (ns^1np^1 to ns^2). We observed that at cryogenic temperatures, Sb^{3+}-doped Cs_2SnCl_6 shows two emission peaks, but Bi^{3+}-doped Cs_2SnCl_6 shows only one emission peak. Why so? In this chapter we address the question. Temperature dependent photoluminescence emission and excitation spectra are utilized to reveal the origin of luminescence in both Sb^{3+}- and Bi^{3+}-doped Cs_2SnCl_6. For Sb^{3+} dopant, the combination of Jahn-Teller distortion and spin-orbit coupling gives rise to two minima in the relaxed excited state $^3T_{1u}^*$, resulting into two emission peaks. Whereas for Bi^{3+} dopant, the spin-orbit coupling significantly dominates over the Jahn-Teller splitting yielding a single minimum in relax excited state $^3T_{1u}^*$, and therefore, a single emission peak.

Chapter 4B: Optical Properties of Bi^{3+}-Sb^{3+} codoped Cs_2SnCl_6 Vacancy Ordered 0D Perovskites

Bi^{3+} and Sb^{3+} codoping in Cs_2SnCl_6, and their effect on optical properties of each other, have not been studied well. In this chapter, we compare the optical properties Bi^{3+}-Sb^{3+} codoped system, with that of Bi^{3+}-doped and Sb^{3+}-doped Cs_2SnCl_6. The codoped samples show dual emission feature, a combination of 450 nm blue light emission because of Bi^{3+} doping and 650 nm red light emission because of Sb^{3+} doping. Overall, we find that the optical emission and excitation properties of the codoped samples largely the addition of those optical properties in Bi^{3+}-doped and Sb^{3+}-doped Cs_2SnCl_6.

Chapter 5: Thesis Summary and Future Outlook

In this section, we summarized the work presented in this thesis and highlight the major findings. Based on our findings and current literature a future research outlook is also provided.

Table of Contents

Chapter 1: Introduction

Chapter 2: Bi^{3+}-Er^{3+} and Bi^{3+}-Yb^{3+} Codoped $Cs_2AgInCl_6$ Double Perovskite: Visible to Short-Wave Infrared Emitters

Chapter 3: Short Wave Infrared Emissions from Te^{4+}-Ln^{3+} (Ln: Er, Yb) Codoped $Cs_2NaInCl_6$ Double Perovskites

Table of Contents

Chapter 4A: Origin of Luminescence in Sb^{3+}- and Bi^{3+}-Doped Cs_2SnCl_6 0D Perovskites: Excited State Relaxation and Spin-Orbit Coupling

Chapter 4B: Optical Properties of Bi^{3+}-Sb^{3+} Codoped Cs_2SnCl_6 0D Perovskite

Chapter 5: Thesis Summary and Future Outlook

Chapter 1

Introduction

1.1 Perovskite

The term "perovskite" is given to mineral $CaTiO_3$, after the Russian mineralogist Lev Perovski.[1] After the invention of X-ray crystallography, it is found that the crystal structure of $CsTiO_3$ is quite common and formed by a large number of compounds with variety of cation and anions.[2-6] Nowadays, "perovskite" generally refers to the crystal structure of $CaTiO_3$ with the chemical formula ABX_3, where A and B represent cations and X denotes an anion. For instance, in $CaTiO_3$, there are two cations: Ca^{2+} and Ti^{4+}, along with the anion O^{2-}. In the perovskite structure, the smaller cation (Ti^{4+} or B) forms octahedra with the anions (O^{2-} or X). These octahedrons are corner-shared with the neighboring octahedra in all three dimensions, creating cuboctahedra voids which are occupied by larger cations (Ca^{2+} or A), as shown in Figure 1.1. For a crystal system to be called perovskite, it should have close structural resemblance with $CaTiO_3$ and also composition similar to the generic formula of ABX_3.
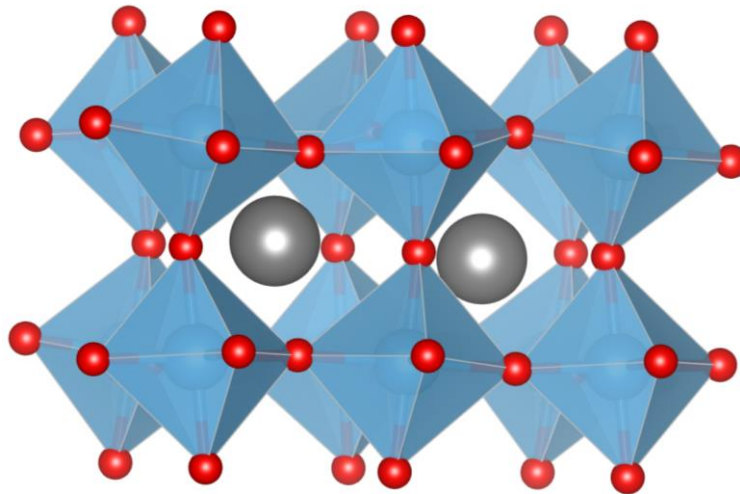
Figure 1.1: Crystal structure of $CaTiO_3$ (ICSD 16688), or general perovskite structure with ABX_3 unit cell formula. The gray color sphere represents the A-site cation Ca^{2+}, sky blue sphere represents B-site cation Ti^{4+}, which form octahedron with six anions X (O^{2-} , red spheres).

Victor Moritz Goldschmidt studied number of perovskite system and found that the formation of perovskite structure is dependent on the ionic radius of the ions.[2, 7] The ability of a set of ions A, B, and X to form the ABX_3 perovskite structure can be predicted by using the Goldschmidt tolerance factor (t). The relation between (t) and ionic radii is:

$$\text{Goldschmidt tolerance factor (t)} = \frac{r_A + r_X}{\sqrt{2}\,(r_B + r_X)} \qquad (1)$$

were, r_A represents the ionic radius of the larger cation, r_B is the ionic radius of the smaller cation, and r_X is the ionic radius of the anion. For a stable cubic perovskite structure, the value of "t" should fall within the range of 0.81 to 1.11.[8] Any changes in the values of A, B, or X will influence the distortion of the crystal structure, its stability, and all other properties.

Perovskite crystal structures are found in numerous oxide and halide compounds. These can be broadly categorized into two groups: oxide perovskites and halide perovskites. Oxide perovskites have been extensively studied for various applications since the last century. They exhibit characteristics like high-temperature superconductivity, ferroic properties, magnetoresistance, and are also used in fuel cell and battery electrode materials[9], heterogeneous catalysis[10], and more.[11]

Halide perovskites, although known since the late 18th century, weren't explored significantly until the late 19th century. The electronic and optical potential of halide perovskites began to capture the interest of materials researchers in the early 20th century. Since then, the exploration of halide perovskites has grown exponentially, especially in terms of their optoelectronic properties.[12]

1.2 Lead Halide Perovskites

Lead halide perovskites are one of the most studied halide perovskites.[12] Lead halide perovskites are represented by the formula $APbX_3$, where A stands for certain positively charged particles like Cs^+, Rb^+, MA^+ (MA: methylammonium), FA^+ (FA: formamidinium) and X represents negatively charged particles known as halides, such as Cl^-, Br^-, or I^-. In the structure of perovskites, the lead and halide components come together to form octahedra, while the "A" anion fit into the space created by the octahedron corner sharing, similar to how it's shown in Figure 1.1.

Halide perovskites are easier to synthesize, modify and have promising semiconductor properties compare to oxide perovskites. The easy synthesis has greatly contributed to the rapid advancement of this field.[13-14] Lead halide perovskites have some impressive characteristics, for example, large absorption coefficient (order of 10^5 cm^{-1}) which allow a small amount of material to absorb the visible light efficiently.[15-16]. Lead halide perovskites have reasonable charge carrier good charge mobility which allow efficient photovoltaic devices.[17] Facile halide exchange allow tunable optical absorption and emission properties.[14, 17]

These favorable properties have enabled to fabricate highly efficient solar cells that have power conversion efficiency close to 25.73%.[18] Achieving this level of efficiency in such a short time is remarkable compared to the decades it took for traditional silicon-based solar cells to reach the same level.[19] These lead halide perovskites also demonstrate high photoluminescence (PL) quantum yield with narrow emission feature, which is desirable for creating high-quality displays. Significant efforts are now being made to make these materials suitable for commercial applications. The synthesis of nanocrystals was a major advancement for these materials.[20-22] Nanocrystals show tunable, narrow emission properties as shown in Figure 1.2. These materials possess defect tolerant nature, enabling good optical properties to be achieved with relatively little effort. Nanocrystals have enabled the stabilization of $CsPbI_3$ cubic phase that is not naturally stable in bulk crystals.[23-25]
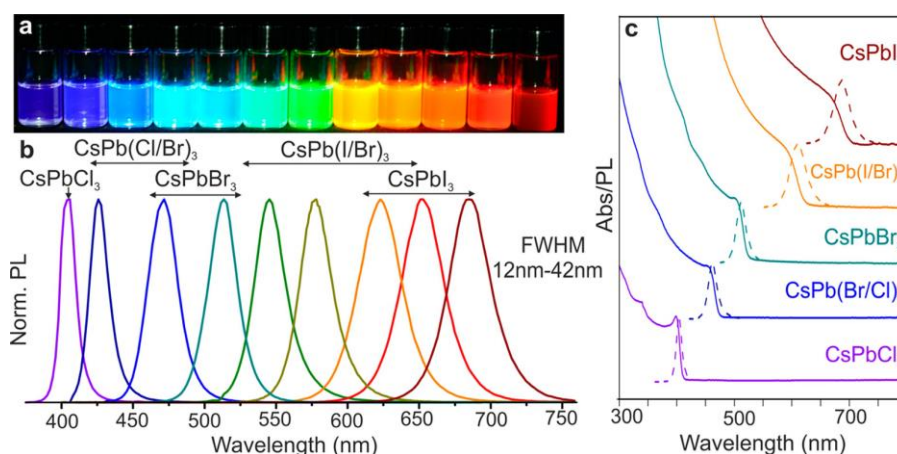
Figure 1.2: (a) Digital image of colloidal $CsPbX_3$ NCs (X = Cl, Br, I), under 365 nm UV light excitation. (b) The emissions are size- and composition-tunable covering the entire visible spectral region with narrow and bright emission as shown. (c) Halide dependent absorption and emission spectra. Adapted from reference[21] with permission. Copyright © 2015, American Chemical Society.

Lead halide perovskites have shown promising optical and photovoltaic properties but these have two major issues.[26] Firstly, the toxic nature of lead poses a problem, and secondly, these materials are vulnerable to moisture and have high solubility in water. This solubility is a concern for the environment because these materials can dissolve in water and harm living organisms. The main reason for their toxicity lies in the presence of Pb^{2+} ions, which can mimic essential ions like Ca^{2+}, Fe^{2+}, and Zn^{2+} in biological systems. Lead toxicity can lead to various health issues such as neurological disorders, high blood pressure, kidney damage, and anemia.[27] Researchers are exploring different chemical and physical methods to tackle these challenges. One approach involves the enclosing the material within a protective layer to prevent lead exposure to the environment. This is done by creating core-shell type structure on

individual particle or encapsulating the complete device structure in insulating, stable protective layer.[27] Another approach is to substitute the lead component with less toxic elements, while still maintaining the perovskite structure and properties.

1.3 Lead Free Halide Perovskites
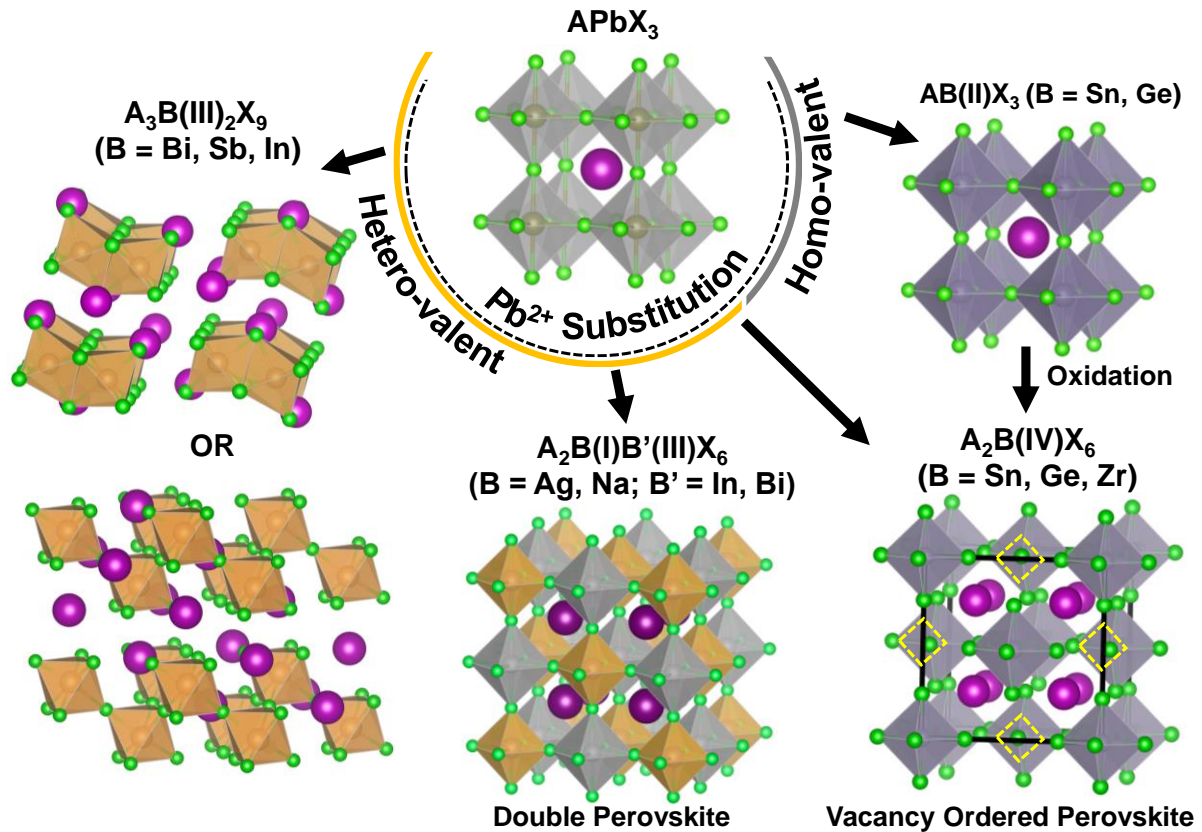
Figure 1.3: Schematics show the lead halide perovskite crystal structure and few possible derivative structures which are obtained on Pb^{2+} substitution with homo-valent and hetero-valent ions. In the chemical formula, A represents the monovalent cation such as Cs^+, Rb^+ (dark magenta color spheres in the structures); B represents the ions which replaces the Pb^{2+} ion and form octahedron with six halides (X = Cl, Br, I; green spheres). The substitutions give rise to perovskite, non-perovskite, double perovskite and vacancy ordered perovskite structure. The yellow squares in the vacancy ordered perovskite structure highlight the vacant octahedral sites.

There are efforts being made to make lead halide perovskite stable by compositional tunability like impurity ion doping, but the expected wide spread application still can cause huge problem. To address the toxicity problem caused by Pb^{2+}, researchers are looking for alternative materials that are environmentally friendly and don't contain lead (Figure 1.3). To find such material, one strategy is to replace Pb^{2+} with ions that have similar properties, such promising candidates can be found in the periodic table. We have learnt that the elements within the same group in the periodic table share similar chemical characteristics. Pb, Sn and Ge are in the

same group so, potential candidates to replace Pb^{2+}. Sn^{2+} and Ge^{2+} can form perovskite structures and exhibit properties similar to lead perovskites, such as a direct band gap, good absorption coefficient, and tunable emission.[28] However, the stability of Sn^{2+}- or Ge^{2+}-based perovskites is compromised by the ease of oxidation to corresponding tetra-valent cations.[29-30] This oxidation process dissociates the perovskite structure, leading to deterioration of optical properties and charge transport.

Another approach is to replace Pb^{2+} by hetero-valent substitution. There are many possibilities in this substitution such as, substitution by mono-valent, tri-valent, tetra-valent ion or a pair of two ions. Many of these substituted structures do not form perovskite structure or perovskite similar structure. Here, we will discuss the Pb-free system with vacancy ordered and double perovskite structure. If we replace two Pb^{2+} cations by a tetra-valent cation (Sn^{4+}, Zr^{4+}, Ti^{4+}), then the alternative metal octahedron sites will be vacant as shown in the bottom right panel in Figure 1.3. Each octahedron will be isolated. This type of structures is often termed as vacancy ordered perovskite structure (Figure 1.3). The case of double perovskite structure will be discussed in the following sub-section.

1.4 Lead Free Halide Double Perovskites

Halide double perovskites are being explored as a more environmentally friendly substitute for lead perovskites.[31-33] These double perovskites are formed by replacing two lead ions with a combination of monovalent and trivalent ions, see Figure 1.3.[33] These ions occupy alternate octahedral positions within the crystal lattice, maintaining the 3D perovskite structure. The term "double perovskite" is used because of the involvement of two types of cations in creating the octahedral network. A similar chemical composition, K_2NaAlF_6 was known as far back as the 19th century and is called "Elpasolite".[34-35] The crystal structure of K_2NaAlF_6 was first solved in 1932,[36] and similar compositions with the same structure were subsequently called elpasolites. Because of popularity of perovskite and crystal similarity, elapsolites are rebranded as double perovskite.

In recent years, both theoretical and experimental studies have been conducted to investigate the potential of halide double perovskites as lead-free photovoltaic materials and light emitter.[37-40] Double perovskites consist of monovalent and trivalent metal centers, allowing for a wide range of compositions. Theoretical predictions have identified hundreds of possible compositions based on thermodynamic stability and structural parameters.[37, 39] While many

compositions have been achieved experimentally, there are still numerous compositions that remained unexplored. Figure 1.4 show the elements highlighted in light blue color from which at least one double perovskite is experimentally reported. The colored triangles at the corners of each square indicates the role of ion in a double perovskite composition as indicated on top the of periodic table.
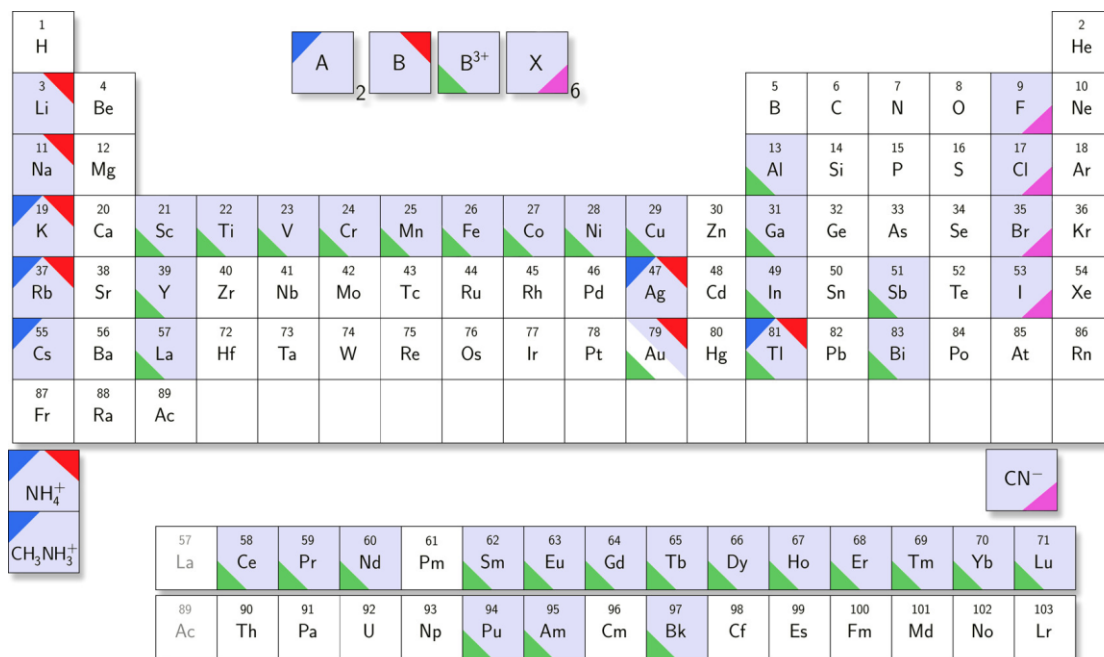
Figure 1.4: The stoichiometric chemical composition of a double perovskite is shown on top with color coding. The blue highlighted elements have at least one experimentally reported double perovskite composition. The triangle at the corner of the highlighted elements identifies the contribution to double perovskite composition. Adapted from reference[41] with permission. Copyright © 2016, American Chemical Society.

A double perovskite composition, represented as $A_2B^IB^{III}X_6$, comprises two types of octahedral metal centers, $[BX_6]^{5-}$ and $[BX_6]^{3-}$. These two metal centers can be arranged in six different ways within a 2x2x2 supercell, as depicted in Figure 1.5. Theoretical calculations for the $Cs_2AgBiCl_6$ composition suggest that the alternative arrangement of monovalent and trivalent metal halide octahedra yields the lowest total energy, primarily due to minimized electrostatic energy in this configuration. This arrangement of alternating monovalent and trivalent metal octahedra is also observed experimentally, resulting in the standard double perovskite structure. Similarly, the formation of other compositions, such as $Cs_2AgInCl_6$, is observed experimentally. The energy differences between different octahedral arrangements are small, as shown in Figure 1.5, suggesting that other arrangements could also be obtained in certain synthesis conditions with distinct optical properties. This area remains unexplored and could potentially reveal interesting properties.
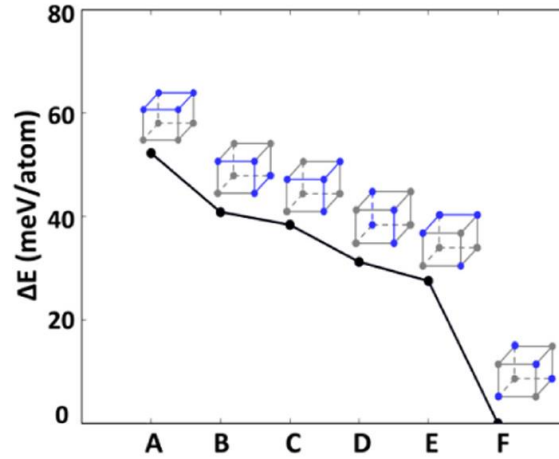
Figure 1.5: Cubes show possible arrangements of $[AgCl_6]^{5-}$ (gray dot) and $[BiCl_6]^{3-}$ (blue dot) motif in $Cs_2AgBiCl_6$. These arrangements have different total energy. The difference in total energy (ΔE) of various arrangements (A, B, C, D, E and F) with the most stable arrangement (F) is plotted. Adapted from reference[42] with permission. Copyright © 2017, American Chemical Society.

The structural stability of a double perovskite composition can be predicted by using the following (2) and (3) empirical relations. These relations were stablished for perovskites[8] but later extended to double perovskite as well.

$$\text{Goldschmidt tolerance factor (t)} = \frac{r_A + r_X}{\sqrt{2} \ (\frac{r_B + r_{B\prime}}{2} + r_X)} \quad (2)$$

And
$$\text{Octahedral factor } (\mu) = \frac{r_B + r_{B\prime}}{2r_X} \quad (3)$$

Where, r_A, r_B, $r_{B\prime}$, and r_X are the ionic radii of A^+, B^+, B^{3+} and X^- ions, respectively. From the existing halide perovskite statistics, it is found that the perovskite structure is possible if $0.44 < \mu < 0.90$ and $0.81 < t < 1.11$ are satisfied.[42]

1.5 Valence and Conduction Band Edges of Halide Double Perovskites

We first discuss the valence band maxima (VBM) and conduction band minima (CBM) of lead halide perovskite like $CsPbI_3$. The VBM has contribution of $6s^2$ of Pb^{2+} and halide np^5 ($6p^5$ for I) orbital, and the CBM has contribution of 6p orbital of Pb^{2+} (Figure 1.6).[43] Both VBM and CBM are antibonding in nature. This antibonding nature of band edges play important role in defect tolerant nature of lead halide perovskites.

Energy levels of CsPbI$_3$
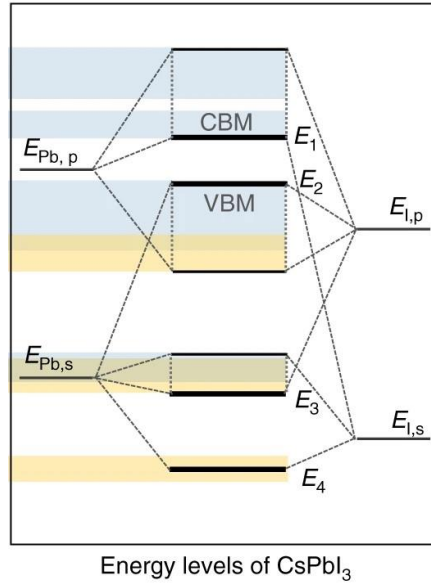
Figure 1.6: Energy level diagram of CsPbI$_3$. Adapted from reference[43] with permission. Copyright © 2019, The Author(s).

Table 1.1: Possible combination of B$^+$ and B^{3+} metal centers to form a double perovskite structure. Adapted from reference[44] with permission. Copyright © 2017, American Chemical Society.

B$^+$ \ B^{3+}		Group 3 Sc, Y	Group 13 Al, Ga, In(3+), Tl(3+)	Group 15 Sb(3+), Bi (3+)
Group 1	Na, K, Rb, Cs	Direct *(All forbidden)*	Direct *(All forbidden)*	Mostly Direct *(Weak transition)*
Group 11	Cu, Ag, Au	Indirect	Direct *(partial forbidden)*	Indirect
Group 13	In(1+), Tl(1+)	Direct *(Weak transition)*	Indirect	Direct *(Strong transition)*

When we replace Pb^{2+} by a pair of monovalent and trivalent cations, the cations could be of various nature like they may have s^2 electron in the valence shell (e.g., In$^+$, Tl$^+$, Sb^{3+}, Bi^{3+}) similar to Pb^{2+}. Or, have empty valence s and p orbital like (Na$^+$, K$^+$, Rb$^+$, In^{3+}). Or have s and d electrons (Ag$^+$). Depending on the nature of cations, the possible halide double perovskites could be divided broadly into nine categories (as shown in Table 1), which affect their band structure and electronic properties. Yan and coworkers calculated band structure of these compositions at Perdew-Burke-Ernzerhof (PBE) level.[44] For group 1 and group 3 or 13 composition the band gap is found to be direct with even parity. So, the electronic transitions

between the band edge are forbidden at all k points. The set of group 11 and group 13 cation for example $Cs_2AgInCl_6$, the VBM derived from Ag 4d and Cl3p orbital and CBM is derived from In 5s orbital. It has a direct band gap at Γ point but the parity of VBM and CBM is same at this point. Leading to parity forbidden transition from valence band to conduction band at the Γ point. The conduction band parity changes with k, at different k, the transition is allowed. For group 1 and group 13, for example Cs_2KBiCl_6, the band gap is direct but the transition dipole is small. Similar is the case for the group 13 and group 3 composition. For the composition of group 13 and group 15, the band gap found to be direct and have good transition dipole. But experimentally synthesizing this composition are difficult because of the possible oxidation of In^+ to In^{3+} and Tl^+ is toxic.

From the above discussion it is clear that group 11 and group 13 containing compositions are stable have direct band gap. So, in Chapter 2 we have taken $Cs_2AgInCl_6$ as our host material. All the halide double perovskites which are experimentally reported show poor emission property because of forbidden or indirect band gap nature.[31-33, 37, 45] At the same time these have good structural properties such as octahedral site which is preferred by a number of luminescent centers and compositional flexibility which allow to incorporate luminescent centers in these positions. When I started working there were few reports on the doping in halide double perovskites.[38, 46-48] Seeing the potential of halide perovskites to host different luminescent centers, the exploration and understanding of luminescent center doping in halide double perovskite to improve/impart desired optical functionalities became a major goal of this thesis work.

1.6 Luminescent Centers

As the name suggest, the centers or site, such as ions, atoms, group of atoms, defect or charge which show luminescence property is known as luminescent centers.[49-50] When the luminescence centers are incorporated in an inert host lattice, the luminescence property of the crystal or material is mainly governed by the luminescence center. Phosphors containing the luminescent centers dominate the current lighting industry. For example, many of the currently used white light emitting diodes (LEDs) have a InGaN chips (which emit blue light around 450 nm) coated with Eu^{2+} doped $SrSi_2O_2N_2$[51-52] (green emitter) and Eu^{2+} doped $Sr_2Si_5N_8$[53] (red emitter) phosphors. Such applications make luminescent centers an important class of material for research and development.

The luminescent centers are of various kinds and can be classified on different basis.[50] On the basis of physical state of luminescent center, one can divide them in F-center (defect and charge), ion, cluster and molecular luminescent center. F-center (F stand for farbe which means color) are formed when the anion vacancy in the crystal is occupied by one or more unpaired electrons. For example, when alkali halides are expose to high energy X-rays, this gives rise to halide vacancy occupied by electron and as a result these alkali halides show new absorption and emission property.[54-55] In a crystal multiple atoms can interact to each other, often form cluster and show luminescent property.[56] π-conjugated organic molecules also show luminescence properties and can be regarded as luminescent centers.[57] These luminescent centers are not further discussed in this thesis. The other set of luminescent centers such as ions or atoms can be incorporated intentionally with control and hugely utilized in light emitting phosphors that are currently being used in LEDs.

Ion luminescent centers can be classified in the following categories (Table 1.2) based on the nature of the electronic transitions they undergo. These are briefly mentioned below.

(1) Ions with s^2-s^1p^1 electronic transition: Ions possessing an s^2 electron in their valence shell orbital show optical properties arising from electronic transitions between s^2 and s^1p^1 states. A more detailed discussion of this category is presented in the subsequent section.

(2) Ions with d-d electronic transition: Transition metal ions with partially filled d-orbitals show optical properties originating from electronic transitions within the d-orbitals various energy configuration (states). Examples are Mn^{2+}, Cr^{3+} and other transition metal ions.

(3) Ions with $3d^{10}$-$3d^9 4s^1$ type electronic transition: Transition metal ions with fully filled d-orbitals, such as Cu^+, Ag^+, and Au^+, show optical properties due to $3d^{10}$ to $3d^9 4s^1$ type electronic transitions. The s-orbitals and d-orbitals lies at the valence shell, which results in a pronounced sensitivity to the crystal field, leading to broad optical absorption and emission features.

(4) Ions with f-f electronic transition: Lanthanide ions bearing unpaired f-electrons undergo f to f electronic transitions. These f-orbitals are situated under the valence shell and are less influenced by the crystal field. Consequently, these transitions yield well-defined, narrow emission features. This category will be discussed in greater detail in subsequent section.

(5) Ions with $4f^n$-$4f^{(n-1)}5d^1$ electronic transition: Certain lanthanide ions exhibit $4f^n$ to $4f^{(n-1)}5d^1$ transitions, involving both f- and d-orbitals. These transitions show broader emission features attributed to the engagement of d-orbitals.

The subsequent sections will discuss the optical characteristics of two categories (1 and 4) of luminescent centers used in this thesis.

Table 1.2: Category of ion luminescent centers based on the type of electronic transitions they undergo.

S. No.	Transitions	Luminescent centers
1	ns^2 - ns^1np^1	Ga^+, In^+, Tl^+, Ge^{2+}, Sn^{2+}, Pb^{2+}, Sb^{3+}, Bi^{3+}, Te^{4+}, Cu^-, Ag^-, Au^-
2	d - d	Transition metal ions (e.g., $Mn+$, Cr^{3+}, Mn^{4+})
3	$3d^{10}$ - $3d^9\,4s^1$	Cu^+, Ag^+, Au^+
4	f - f	Lanthanides and actinides ions
5	$4f^n$ - $4f^{(n-1)}\,5d^1$	Ce^{3+}, Pr^{3+}, Sm^{2+}, Eu^{2+}, Tm^{2+}, Yb^{2+}

In ion luminescent centers the charge carriers are mostly localized on the luminescent centers and their optical properties can be explained by a localized model, often by configuration coordinate model. Simple diatomic model is the basis of configuration coordinate model. In the diatomic model, the total energy of the system varies with internuclear distance. And, for polyatomic molecules, huge number of coordinates are needed for similar presentation. These coordinates are approximated by a single configuration coordinate in one dimensional configuration coordinate model as shown in Figure 1.7.[50] In configuration coordinate model only the luminescent ion and the nearest neighbors are considered for simplicity. By considering so, the set of ions can be treated as molecule and the large number of lattice vibration can be approximated by a set of normal coordinates, known as configuration coordinate. This model can qualitatively explain a number of observations such as Stokes shift, absorption or emission bandwidth and temperature dependance. As shown in Figure 1.7, absorption happens following the Frank-Condon principle. After excitation, the charge carrier

undergoes in non-radiative relaxation followed by emission from the lowest excited state to ground state.
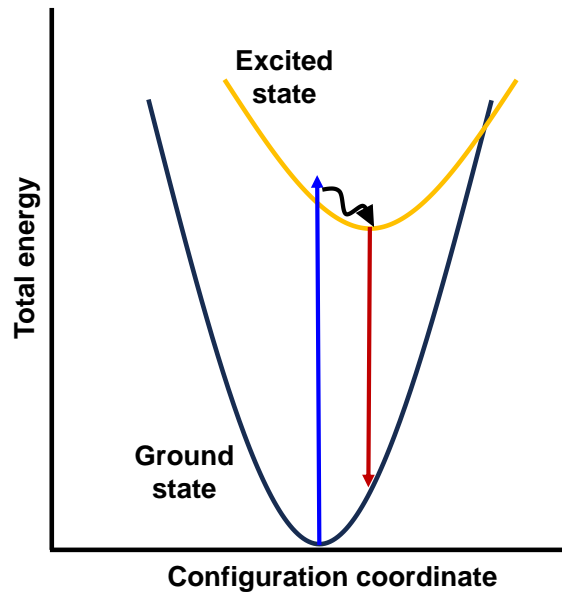
Figure 1.7: A schematic representation of configuration coordinate model. The blue solid line represents the absorption followed by the non-radiative relaxation (curvy line) and the red line represent the emission.

1.6.1   Luminescent Centers with ns^2 - ns^{1}np^1 Transitions (ns^2-ions)

ns^2 $\leftrightarrow$ ns^{1}np^1 transitions are shown by the ions such as Tl$^+$, Pb^{2+}, Sb^{3+}, Bi^{3+}, Te^{4+}, Ag$^-$, Au$^-$, Ga$^+$, In$^+$, Ge^{2+}, Sn^{2+}, Cu$^-$ which have ns^{2}np^0 valence shell electronic configuration.[50, 58] These ions are generally known as ns^2 ions. To understand the optical absorption and emission properties of such ions we first need to understand energy level diagram of these ions. These energy levels almost completely explain the observed optical properties. So, let's start from a free isolated ns^2-ion in the ground state with ns^{2}np^0 valence shell electronic configuration. When sufficient energy photon falls on these ions, one of the ns^2 electron gets promoted to np orbital and form ns^{1}np^1 state as shown in the left side of Figure 1.8. For ns^{2}np^0 ground state, total orbital angular momentum (L) = 0 and total spin angular momentum (S) = 0 so the corresponding term is ^{1}S$_0$. For ns^{1}np^1 configuration, L = 1, S = 0 and 1 so the corresponding terms are ^{1}P and ^{3}P. Spin-orbit coupling (Russel-Saunders coupling) split the degenerate ^{3}P$_{0,1,2}$ states. The most of the ns^2-ions are heavier elements and have stronger spin-orbit coupling because spin orbit coupling is proportional to Z^4, where Z is effective nuclear charge. So, in ns^2-ions spin-orbit coupling (j-j coupling) becomes significant and leads to mixing of ^{1}P$_1$ and ^{3}P$_1$ states, as a result the ^{3}P$_1$ gets stabilize in energy and represented by ^{3}P$_1^*$ whereas ^{1}P$_1$

increase in energy and represented by $^1P_1^*$. Because of this mixing the spin forbidden $^1S_0 \to$ $^3P_1$ transition becomes nearly allowed.

In ns^2-ion, $^1S_0 \to {}^3P_0$ transition is spin forbidden as well as ΔJ $(0 \leftrightarrow 0)$ forbidden, where J is total angular momentum of electron. $^1S_0 \to {}^3P_1^*$ transition becomes nearly allowed because of $^1P_1$ and $^3P_1$ mixing. $^1S_0 \to {}^3P_2$ transition becomes partially allowed on coupling with lattice vibrations. $^1S_0 \to {}^1P_1$ transition is allowed. In the order of increasing energy, the possible transitions are $^1S_0 \to {}^3P_1^*$, $^1S_0 \to {}^3P_2$ and $^1S_0 \to {}^1P_1$, which are also known as A- band, B-band and C-band transitions, respectively, as shown in Figure 1.8.
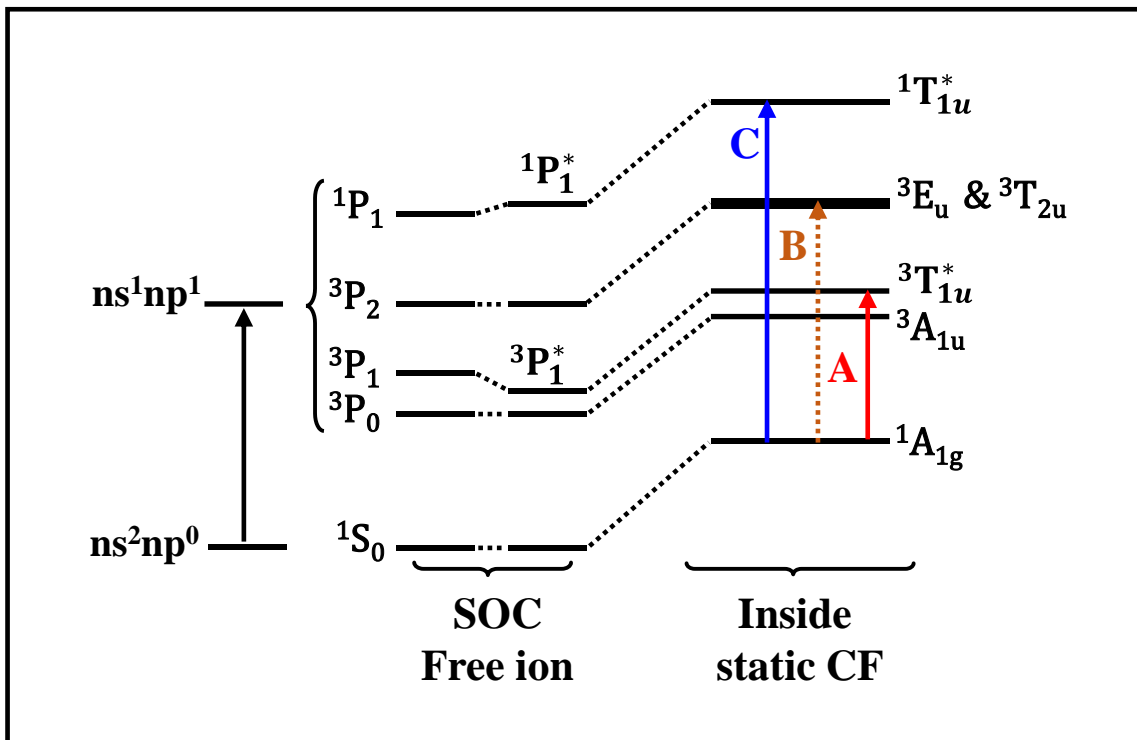
Figure 1.8: Schematic presentation of energy state and transitions in a ns^2-ion. The energy states are represented by the term symbols. At the right side, when the ion present in the crystal field, the energy states are represented in Mulliken symbols. SOC represent the spin-orbit coupling and CF represent the crystal field.

When the ns^2-ions are present in the crystal field, the energy of ground as well as excited state increases. In a cubic crystal field, the energy states are represented by Mulliken symbols. $^1A_{1g}$, $^3A_{1u}$, $^3T_{1u}^*$, $(^3E_u + {}^3T_{2u})$ and $^1T_{1u}^*$ Mulliken notations are used corresponding to $^1S_0$, $^3P_0$, $^3P_1^*$, $^3P_2$ and $^1P_1^*$ states, respectively.[58] Due to electron lattice interaction in the crystal, the absorption or emission bands gets broaden. In ns^2-ions, nucleus causes major splitting, so the effect of crystal field is minimum. So, when these ions are present in octahedral crystal field the trend of energy levels remains almost similar.

1.6.2 Luminescent Centers with f-f Electronic Transitions

f-f electronic transitions are shown by the lanthanide series ions which have unpaired 4f electrons such as Pr^{3+}, Nd^{3+}, Pm^{3+}, Sm^{3+}, Eu^{3+}, Gd^{3+}, Tb^{3+}, Dy^{3+}, Ho^{3+}, Er^{3+}, Tm^{3+}, Yb^{3+}. Lanthanide series elements generally possess +3 oxidation state. The general electronic configuration can be written as $[Kr]\,4d^{10}4f^{n}5s^{2}5p^{6}6s^{0}$. From electronic configuration, it is clear that the f-electrons lie inside the valence shell and does not participate in bonding. As a result, the f electronic levels are not much affected by host crystal field and show narrow emissions at fixed positions. For example, Figure 1.9a shows the emission spectra of lanthanide ions doped in $CsPbCl_3$ nanocrystals.[59] The emission features are narrow. And, appear at similar energy if we doped the same lanthanide ion in different host material (Figure 19a, b, c). These emissions originate from the f-f electronic transition of a particular lanthanide ion.
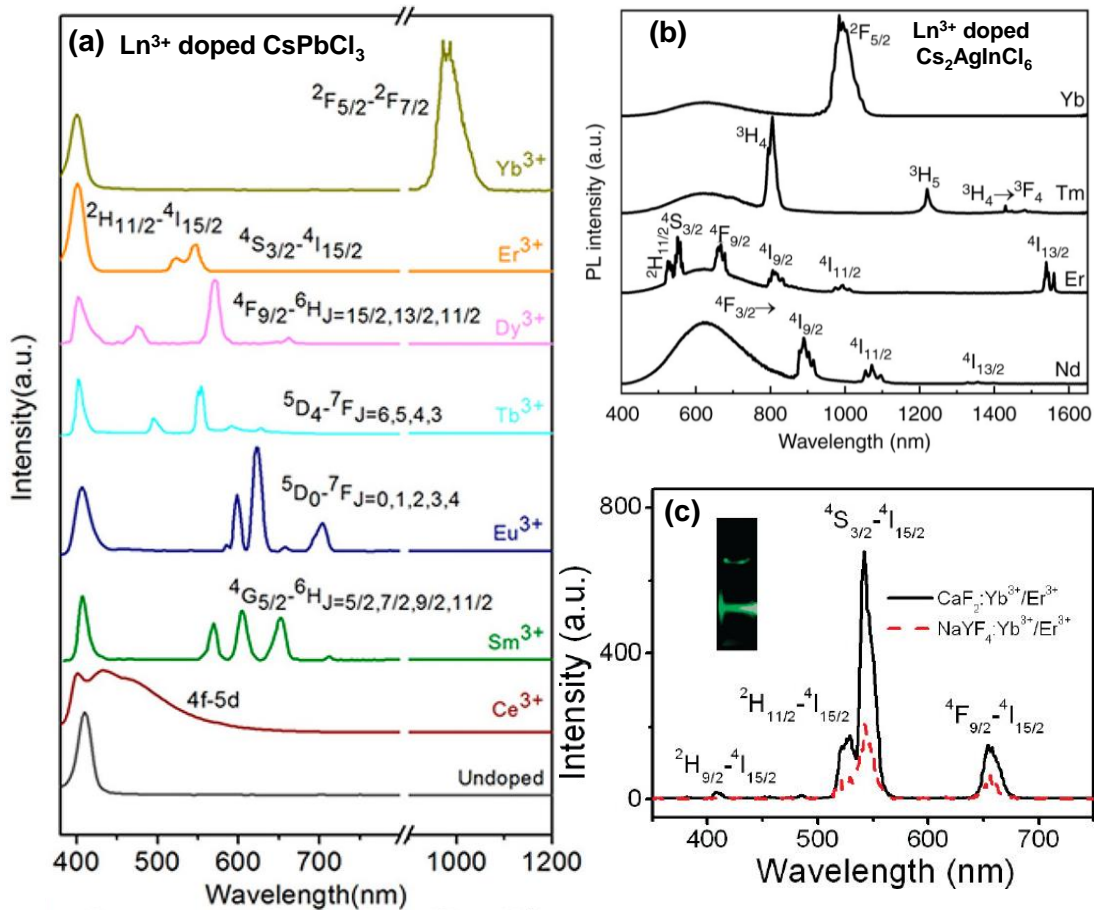
Figure 1.9: (a) Emission spectra of Ln^{3+} doped $CsPbCl_3$ nanocrystals. (b) Emission spectra of Ln^{3+} doped $Cs_2AgInCl_6$. (c) Up-conversion emission spectrum of Yb^{3+}/Er^{3+} codoped CaF_2. The f-f electronic transitions correspond to emissions are shown in the Figures. Figure (a) is adapted from reference[59] with permission. Copyright © 2017, American Chemical Society. Figure (b) is adapted from reference[60] with permission. Copyright © 2022, The Author(a). Figure (c) is adapted from reference[61] with permission. Copyright © 2009, American Chemical Society.

Lanthanide ions emit sharp narrow emission from blue visible to infrared region. Which make these lanthanides an important luminescent center. But lanthanides have poor absorption cross section because of parity forbidden f-f electronic transitions and most of the times these require a sensitizers or high intensity lasers for excitation.[62] A sensitizer is an ion or molecule which is capable of absorbing light and transferring the excitation energy to a nearby activator (emitter), and the activator emits its characteristic emission.[50, 63] The process of *activator* excitation by *sensitizer* is known as sensitization. For lanthanide sensitization the widely accepted energy transfer mechanism is Foster resonance energy transfer (FRET). For this to happen, the sensitizer and activator should be nearby and the absorption of activator should overlap with emission of sensitizer. The efficiency of this is proportional to r^{-6}. Where r is distance between sensitizer and activator.[64]

1.7 Strategies to Sensitize Lanthanide Luminescent Center

Lanthanides have poor absorption cross section (10^{-21} -10^{-22} cm^2). Therefore, lanthanide sensitization is important to achieve intense lanthanide emission with normal excitation sources such as xenon lamp or LED chips. Different strategies are utilized to sensitize lanthanide ions as shown in Figure 1.10. Figure 1.10a shows that a good absorbing ion such as Bi^{3+}, Mn^{4+}, Cr^{3+}, Ce^{3+} with absorption cross-section of 10^{-20} -10^{-18} cm^2 are codoped with lanthanide.[62, 65-70] These ions absorb the excitation light and transfer energy non-radiatively to lanthanide, and lanthanide exhibit characteristic emissions. In this strategy the hosts are usually inert and do not show optical properties. This strategy is very versatile because multiple sensitizers and emitters can be simultaneously incorporated in the host, with desired optical absorption and emission properties. Because the two centers, sensitizer and emitter are present in the same crystal, the two centers are expected to be located nearby, and hence, the maximum energy transfer is expected. This strategy could be use in bulk as well as in nanocrystals.

Plasmonic nanoparticles (NPs) with absorption cross-section of 10^{-13} -10^{-11} cm^2 are utilized to sensitize lanthanide doped or lanthanide-based nanocrystals (Figure 1.10b).[62, 71-73] In this case the energy transfer takes place from one material to Ln^{3+} in another material. Energy transfer to be efficient, maximum surface overlap should be there. Therefore, this method can be used effectively only in nanocrystals. Dyes with absorption cross-section 10^{-17} -10^{-16} cm^2 have been demonstrated to sensitized lanthanide doped nanoparticles.[62, 74-75] In this case the organic dyes are attached to crystal surface (Figure 1.10c). So, this method is useful for nanocrystals. Conjugated organic molecules could be directly coordinate to lanthanide ions, and form

complexes. The system formed by this method has stability issue because of organic part. Also, lanthanide emission in the short-wave infrared region is quenched by these organic components. This issue will be discussed in detail in the next section. Semiconductors with good absorption cross section of 10^{-13} -10^{-11} cm^2 are utilized to sensitize Ln^{3+} ions. Semiconductor NC could be attached to lanthanide doped NC for this purpose, similar to the case of plasmonic NP as shown in Figure 1.10b. Another approach is to dope the semiconductors with lanthanide ions. The semiconductor will absorb the excitation light and non-radiative transfer its energy to lanthanide ion as shown in the Figure 1.10d.
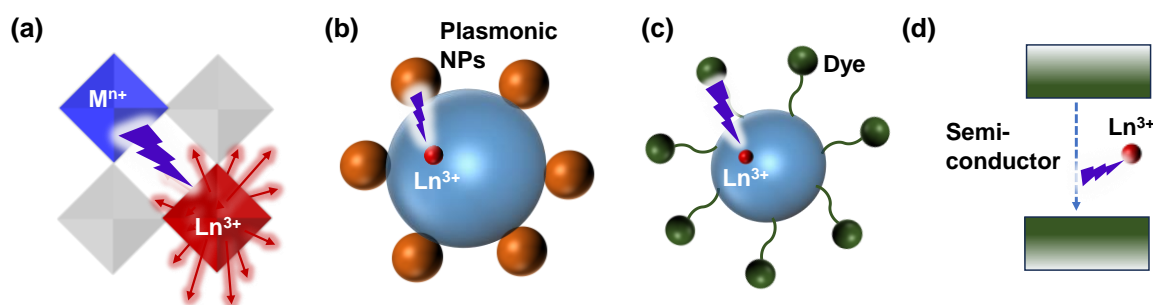
Figure 1.10: Schematic presentation of various lanthanide sensitization methods. (a) Good absorbing ions M^{n+} (Bi^{3+}, Cr^{3+}, Ce^{3+}, Mn^{4+}) are codoped with lanthanide ions (Ln^{3+}). (b) Plasmonic nanoparticles (NPs) are attached to the surface of Ln^{3+} doped nanocrystals. (c) Dye molecules are attached to Ln^{3+} doped nanocrystals. (d) Ln^{3+} are doped in semiconductor nanocrystals.

Traditional semiconductors like CdSe, GaAs, Si, InP have tetrahedral coordination, whereas the large lanthanide ions prefer octahedral or higher coordination sites; This mismatch makes lanthanide ion doping difficult in semiconductors.[76-77] Lead halide perovskite with octahedral site have been doped with lanthanide ions but lead toxicity is a major concern for their application.[59, 78-79] Lead free double perovskites with octahedral sites are promising host for lanthanides. But, unlike lead perovskite, these are insulators with higher band gaps. Chapter 2 and 3 of this thesis explore the possibility of lanthanide doping in lead-free halide double perovskite and the modulation of excitation energy.

1.8 Applications of Lanthanide Ion Emission

Lanthanides have been utilized in commercial light emitting materials and lasers.[80] For example, YVO$_4$:Eu^{3+} is the first lanthanide-based phosphor introduced in 1965.[81] Since then the lanthanide doped phosphor have been hugely explored. Currently, various lanthanide doped

phosphor is commercially used. Tb^{3+} doped $Y_3Al_5O_{12}$ (YAG) is used as green phosphor in cathode ray tube display. $CaAlSiN_3:Eu^{2+}$ and $Sr[Mg_3SiN_4]:Eu^{2+}$ are used as red phosphor In LEDs.[82] Lanthanide also found widespread application in lasers. Nd doped YAG laser one of the most commonly used laser.[80] Few of the lanthanide emits in the shortwave infrared region. For example, Er^{3+} emit strongly 1540 nm radiation, which fall in the biological transparent window and found application in biological deep tissue imaging, it also falls in the fused silica transparency window and used in optical telecommunication.

1.9 Short-wave Infrared Emissions are Difficult to Obtain; Why?

Electromagnetic waves 0f 900-1700 nm wavelength are known as short-wave infrared (SWIR) waves. SWIR emissions fall in the overlapping region of both the lower energy end electronic transition and the vibrational overtone transition. The SWIR emissions, which falls in the energy range 1.38-0.73 eV, are generated by electronic transition between ground state and excited state. So, the required energy gap between ground state and excited state is small. But moving from visible emission to SWIR emission, as the energy gap between ground state and excited state decreases, the emission efficiency decreases. This could be understood by following explanations.

In organic emitters, dye molecules, the emission originate due to electronic transition from lowest unoccupied molecular orbital (LUMO) to highest occupied molecular orbital (HOMO). As the energy gap between LUMO and HOMO decreases, the overlap between ground state and excited state increases[83], and the charge carrier in the excited state (LUMO) with the help of vibrational state may non-radiatively relax to ground state (HOMO) as shown in Figure 1.11a.

In the case of inorganic semiconductors, the emission originates due to electronic transition from conduction band minima (CBM) to valence band maxima (VBM). The Fermi-Dirac distribution gives the distribution of electron between valence band and conduction band. As the band gap narrow down, the CBM and VBM move closer to E_F. In such case, at any temperature the electron population in the conduction band becomes significant as shown in Figure 1.11b. This leads to decrease in the emission intensity or lower photoluminescent quantum yield in small band gap semiconductors. So, organic dye and inorganic semiconductor both show decreased emission efficiency for SWIR emission because of the respective reasons mentioned here.
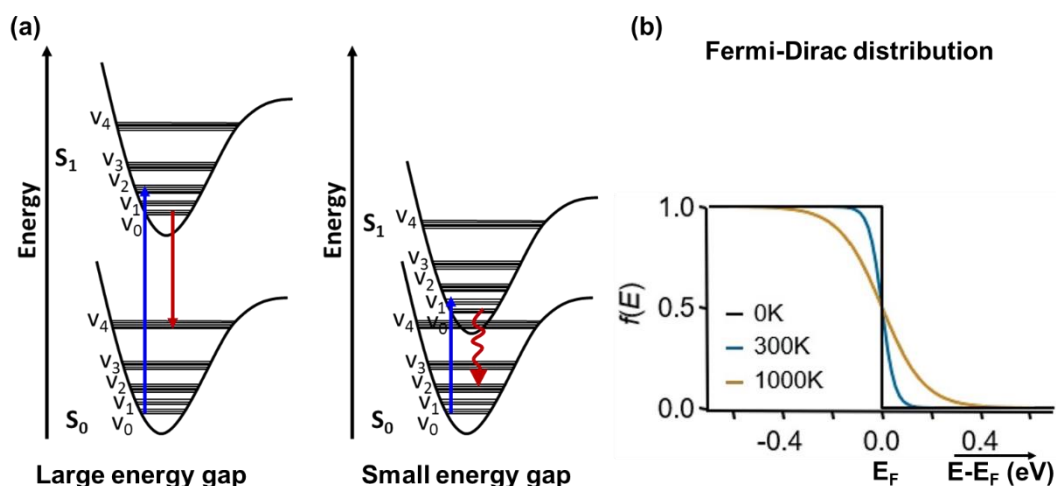
Figure 1.11: (a) Schematic presentation of ground (S_0) and first excited state (S_1) of a dye molecule with vibrational levels. The absorption is shown by the blue straight line and emission by red straight line. In the small energy gap case, the relaxation is non radiative and shown by red curvy arrow. (b) Fermi-Dirac distribution of electrons at different temperature for a semiconductor. $f(E)$ is the probability that the electron will have energy E, E_F is Fermi energy and T is temperature. Figure (b) is adapted from reference[84] with permission. Copyright © 2023, The Author(s).

If the emitting material contains hetero-atom bond such as C-X, H-X (X = N, H, O, S, Cl, Br, I), in such case the anharmonicity in the vibration will be large and the vibrational overtone will be significant. These vibrational overtone falls in the range SWIR. For example, the fundamental vibrational frequency of v(O-H) is 3600 cm^{-1} (2777 nm) and the vibrational overtone has the 7199 cm^{-1} (1389 nm) energy, which falls in SWIR range. So, the surrounding elements containing C-X or H-X bonds have ability to absorb the SWIR emission. The organic molecules contain plenty of such bond and because of this, organic semiconductors or organic-lanthanide complex are not that successful SWIR emitter. Inorganic semiconductors are free from this external factor and may play a major role. But semiconductors need to have small band gap in SWIR range with minimum defects. Currently, PbS, PbSe, HgTe nanocrystal based materials are being used to get SWIR emission. Also InAs nanocrystals being explored for SWIR emission but still the synthesis requires harsh condition and high-quality nanocrystal synthesis is a challenge. On the other hand, the lanthanide Er^{3+} and Yb^{3+} emit SWIR emission from f-f electronic transition. If we could incorporate lanthanide in a host, we obtain the SWIR emission. This make Er^{3+} and Yb^{3+} doping important to obtain SWIR emission.

1.10 Scope of this Thesis

Lead-free halide perovskites contain octahedral sites, which are preferred by various luminescent centers. This intrinsic characteristic presents an opportunity to incorporate

luminescent centers, such as lanthanide ions and ns^2-ions. These dopants hold the potential to tune the optical functionalities of lead-free perovskite materials. This thesis explores the potential of doping lanthanide ions (Er^{3+}, Yb^{3+}) and ns^2-ions (Bi^{3+}, Sb^{3+}, Te^{4+}) in lead free halide perovskites. Through this study, we aim to understand and impart novel luminescent properties of doped lead-free halide perovskites. This comprehensive study includes material design, thorough characterization, and an in-depth exploration of the photophysical properties.

First of all, an appropriate halide perovskite host lattice is chosen for the incorporation of luminescent lanthanide dopants in the lattice. Lanthanides prefer coordination number ≥ 6 and usually exists in +3 oxidation state. Halide double perovskites, such as $Cs_2AgInCl_6$, has In^{3+} in octahedral environment, and therefore, can be a suitable host for lanthanide doping (Figure 1.13a).[85-87] When, we started this work, there were only two reports of lanthanide ion doping in the halide double perovskites.[88-89] The potential of halide perovskites to host lanthanide ions, and the scientific curiosity on how the optical properties will manifest after the doping, lead us to study lanthanide doping in halide perovskites.
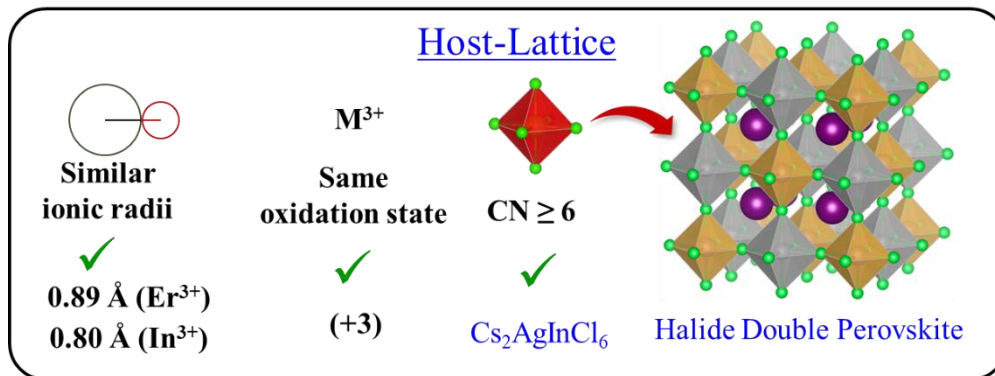
Figure 1.13: Structural and compositional parameters of halide double perovskites suitable for lanthanide doping.

Lanthanide ion doped in halide double perovskite ($Cs_2AgInCl_6$) require higher energy excitation (> 3.54 eV) and have large energy difference between excitation and emission which causes huge energy loss. Also, the available efficient excitation sources, UV LED chips, like GaN emit at 365 nm (3.40 eV) or at higher wavelength. So, there is need to reduce the excitation energy.
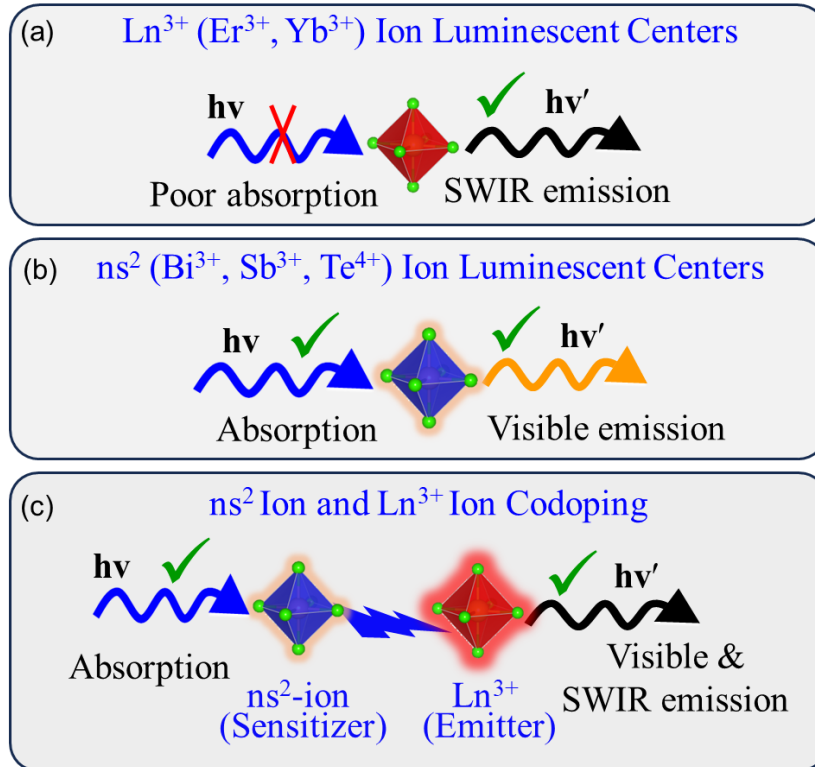
Figure 1.14: Schematic presentation of absorption and emission in (a) lanthanide ion (Ln^{3+}), (b) ns^2 ion, and (c) ns^2 ion-Ln^{3+} codoped double perovskites. Octahedrons represent the dopant sites, where each dopant is bonded to six halide ions (green spheres).

Lanthanide ion emits distinct narrow emissions from f-f electronic transitions, which are parity forbidden in nature. One can observe emission from lanthanide but with long lifetime. Because f-f transitions are forbidden, lanthanide show poor optical absorption (Figure 1.14a), and lanthanides does not introduce any absorption feature to host material. To address this issue, we introduce the concept of Bi^{3+} (ns^2-ion) and lanthanide ion (Er^{3+}, Yb^{3+}) codoping in $Cs_2AgInCl_6$ in the Chapter 2 of this thesis. The ns^2-ion with nearly allowed $^1S_0 \rightarrow {}^3P_1^*$ transition could effectively absorb light and introduce new lower-energy sub-bandgap absorption feature. The absorption is followed by $^3P_1^* \rightarrow {}^1S_0$ transition related emission as shown in Figure 1.14b. When we codope ns^2-ion with lanthanide ion, the ns^2-ion absorbs the light, and then non-radiatively transfer its energy to lanthanide ion. Subsequently, the lanthanide ion emits the characteristic narrow emission (Figure 1.14c). Different choices of double perovskite hosts, and doping with ns^2-ions and lanthanide ions have been explored in Chapter 2-3. Temperature (7 K - 300 K) dependent PL, PL excitation and PL lifetime measurements are carried out to elucidate the photo-excitation and emission processes. Phosphor converted LEDs are assembled to demonstrate the applicability of the codoping.

Doping ns^2-ions not only act as a sensitizer for lanthanides. The ns^2-ion dopants themselves show interesting emission properties. PL of ns^2-ion doped in alkali halides have been studied extensively in the early 19th century.[58, 90-91] There has been correlation stablished in different ns^2-ions, their emissions and the host materials. We found that the Sb^{3+} and Bi^{3+} doped Cs_2SnCl_6 0D perovskites emit orange and blue color emission and these emissions are expected to originate from the $^3P_1^* \rightarrow {}^1S_0$ transition of respective ions. But at low temperature the Sb^{3+} doped sample show dual emission feature where the Bi^{3+} doped sample show single emission feature at all temperature. Chapter 4 of this thesis discusses the origin of this contrasting emission features.

1.11 References

1. Breternitz, J.; Schorr, S. What Defines a Perovskite? *Adv. Energy Mater.* **2018,** *8*, 1802366.

2. Goldschmidt, V. M. Die Gesetze der Krystallochemie. *Sci. Nat.* **1926,** *14*, 477-485.

3. Peña, M. A.; Fierro, J. L. G. Chemical Structures and Performance of Perovskite Oxides. *Chem. Rev.* **2001,** *101*, 1981-2018.

4. Kubicek, M.; Bork, A. H.; Rupp, J. L. M. Perovskite Oxides – A Review on a Versatile Material Class for Solar-to-Fuel Conversion Processes. *J. Mater. Chem. A* **2017,** *5*, 11983-12000.

5. He, H.; Yang, Z.; Xu, Y.; Smith, A. T.; Yang, G.; Sun, L. Perovskite Oxides as Transparent Semiconductors: a Review. *Nano Converge.* **2020,** *7*, 32.

6. Wang, T.; Chen, H.; Yang, Z.; Liang, J.; Dai, S. High-Entropy Perovskite Fluorides: A New Platform for Oxygen Evolution Catalysis. *J. Am. Chem. Soc.* **2020,** *142*, 4550-4554.

7. Bartel, C. J.; Sutton, C.; Goldsmith, B. R.; Ouyang, R.; Musgrave, C. B.; Ghiringhelli, L. M.; Scheffler, M. New Tolerance Factor to Predict the Stability of Perovskite Oxides and Halides. *Sci. Adv.* **2022,** *5*, eaav0693.

8. Li, C.; Lu, X.; Ding, W.; Feng, L.; Gao, Y.; Guo, Z. Formability of ABX_3 (X = F, Cl, Br, I) Halide Perovskites. *Acta Crystallogr. B: Struct. Sci. Cryst. Eng. Mater.* **2008,** *64*, 702-707.

9. Sunarso, J.; Hashim, S. S.; Zhu, N.; Zhou, W. Perovskite Oxides Applications in High Temperature Oxygen Separation, Solid Oxide Fuel Cell and Membrane Reactor: A Review. *Prog. Energy Combust. Sci.* **2017,** *61*, 57-77.

10. Zhu, J.; Li, H.; Zhong, L.; Xiao, P.; Xu, X.; Yang, X.; Zhao, Z.; Li, J. Perovskite Oxides: Preparation, Characterizations, and Applications in Heterogeneous Catalysis. *ACS Catalysis* **2014,** *4*, 2917-2940.

11. Rao, C. N. R. Perovskites. In *Encyclopedia of Physical Science and Technology (Third Edition)*, Meyers, R. A., Ed. Academic Press: New York, **2003**, 707-714.

12. Dey, A.; Ye, J.; De, A.; Debroye, E.; Ha, S. K.; Bladt, E.; Kshirsagar, A. S.; Wang, Z.; Yin, J.; Wang, Y.; Quan, L. N.; Yan, F.; Gao, M.; Li, X.; Shamsi, J.; Debnath, T.; Cao, M.; Scheel, M. A.; Kumar, S.; Steele, J. A.; Gerhard, M.; Chouhan, L.; Xu, K.; Wu, X. G.; Li, Y.; Zhang, Y.; Dutta, A.; Han, C.; Vincon, I.; Rogach, A. L.; Nag, A.; Samanta, A.; Korgel, B. A.; Shih, C. J.; Gamelin, D. R.; Son, D. H.; Zeng, H.; Zhong, H.; Sun, H.; Demir, H. V.; Scheblykin, I. G.; Mora-Sero, I.; Stolarczyk, J. K.; Zhang, J. Z.; Feldmann, J.; Hofkens, J.; Luther, J. M.; Perez-Prieto, J.; Li, L.; Manna, L.; Bodnarchuk, M. I.; Kovalenko, M. V.; Roeffaers, M. B. J.; Pradhan, N.; Mohammed, O. F.; Bakr, O. M.; Yang, P.; Muller-Buschbaum, P.; Kamat, P. V.; Bao, Q.; Zhang, Q.; Krahne, R.; Galian, R. E.; Stranks, S. D.; Bals, S.; Biju, V.; Tisdale, W. A.; Yan, Y.; Hoye, R. L. Z.; Polavarapu, L. State of the Art and Prospects for Halide Perovskite Nanocrystals. *ACS Nano* **2021,** *15*, 10775-10981.

13. Dunlap-Shohl, W. A.; Zhou, Y.; Padture, N. P.; Mitzi, D. B. Synthetic Approaches for Halide Perovskite Thin Films. *Chem. Rev.* **2019,** *119*, 3193-3295.

14. Shamsi, J.; Urban, A. S.; Imran, M.; De Trizio, L.; Manna, L. Metal Halide Perovskite Nanocrystals: Synthesis, Post-Synthesis Modifications, and Their Optical Properties. *Chem. Rev.* **2019,** *119*, 3296-3348.

15. De Roo, J.; Ibáñez, M.; Geiregat, P.; Nedelcu, G.; Walravens, W.; Maes, J.; Martins, J. C.; Van Driessche, I.; Kovalenko, M. V.; Hens, Z. Highly Dynamic Ligand Binding and Light Absorption Coefficient of Cesium Lead Bromide Perovskite Nanocrystals. *ACS Nano* **2016,** *10*, 2071-2081.

16. Maes, J.; Balcaen, L.; Drijvers, E.; Zhao, Q.; De Roo, J.; Vantomme, A.; Vanhaecke, F.; Geiregat, P.; Hens, Z. Light Absorption Coefficient of $CsPbBr_3$ Perovskite Nanocrystals. *J. Phys. Chem. Lett.* **2018,** *9*, 3093-3097.

17. Jena, A. K.; Kulkarni, A.; Miyasaka, T. Halide Perovskite Photovoltaics: Background, Status, and Future Prospects. *Chem. Rev.* **2019,** *119*, 3036-3103.

18. Park, J.; Kim, J.; Yun, H.-S.; Paik, M. J.; Noh, E.; Mun, H. J.; Kim, M. G.; Shin, T. J.; Seok, S. I. Controlled Growth of Perovskite Layers with Volatile Alkylammonium Chlorides. *Nature* **2023,** *616*, 724-730.

19. Goetzberger, A.; Luther, J.; Willeke, G. Solar cells: Past, Present, Future. *Sol. Energy Mater.Sol.* **2002,** *74*, 1-11.

20. Schmidt, L. C.; Pertegás, A.; González-Carrero, S.; Malinkiewicz, O.; Agouram, S.; Mínguez Espallargas, G.; Bolink, H. J.; Galian, R. E.; Pérez-Prieto, J. Nontemplate Synthesis of $CH_3NH_3PbBr_3$ Perovskite Nanoparticles. *J. Am. Chem. Soc.* **2014,** *136*, 850-853.

21. Protesescu, L.; Yakunin, S.; Bodnarchuk, M. I.; Krieg, F.; Caputo, R.; Hendon, C. H.; Yang, R. X.; Walsh, A.; Kovalenko, M. V. Nanocrystals of Cesium Lead Halide Perovskites ($CsPbX_3$, X = Cl, Br, and I): Novel Optoelectronic Materials Showing Bright Emission with Wide Color Gamut. *Nano Lett.* **2015,** *15*, 3692-3696.

22. Zhang, F.; Zhong, H.; Chen, C.; Wu, X.-g.; Hu, X.; Huang, H.; Han, J.; Zou, B.; Dong, Y. Brightly Luminescent and Color-Tunable Colloidal $CH_3NH_3PbX_3$ (X = Br, I, Cl) Quantum Dots: Potential Alternatives for Display Technology. *ACS Nano* **2015,** *9*, 4533-4542.

23. Swarnkar, A.; Marshall, A. R.; Sanehira, E. M.; Chernomordik, B. D.; Moore, D. T.; Christians, J. A.; Chakrabarti, T.; Luther, J. M. Quantum Dot–Induced Phase Stabilization of α-CsPbI3 Perovskite for High-Efficiency Photovoltaics. *Science* **2016,** *354*, 92-95.

24. Mir, W. J.; Swarnkar, A.; Nag, A. Postsynthesis Mn-doping in $CsPbI_3$ Nanocrystals to Stabilize the Black Perovskite Phase. *Nanoscale* **2019,** *11*, 4278-4286.

25. Masi, S.; Gualdrón-Reyes, A. F.; Mora-Seró, I. Stabilization of Black Perovskite Phase in $FAPbI_3$ and $CsPbI_3$. *ACS Energy Lett.* **2020,** *5*, 1974-1985.

26. Boyd, C. C.; Cheacharoen, R.; Leijtens, T.; McGehee, M. D. Understanding Degradation Mechanisms and Improving Stability of Perovskite Photovoltaics. *Chem. Rev.* **2019,** *119*, 3418-3451.

27. Ravi, V. K.; Mondal, B.; Nawale, V. V.; Nag, A. Don't Let the Lead Out: New Material Chemistry Approaches for Sustainable Lead Halide Perovskite Solar Cells. *ACS Omega* **2020,** *5*, 29631-29641.

28. Konstantakou, M.; Stergiopoulos, T. A Critical Review on Tin Halide Perovskite Solar Cells. *J. Mater. Chem. A* **2017,** *5*, 11518-11549.

29. Qiu, X.; Cao, B.; Yuan, S.; Chen, X.; Qiu, Z.; Jiang, Y.; Ye, Q.; Wang, H.; Zeng, H.; Liu, J.; Kanatzidis, M. G. From Unstable $CsSnI_3$ to Air-Stable Cs_2SnI_6: A Lead-Free Perovskite Solar Cell Light Absorber with Bandgap of 1.48 eV and High Absorption Coefficient. *Sol. Energy Mater. Sol. Cells* **2017,** *159*, 227-234.

30. Yang, W.-F.; Igbari, F.; Lou, Y.-H.; Wang, Z.-K.; Liao, L.-S. Tin Halide Perovskites: Progress and Challenges. *Adv. Energy Mater.* **2020,** *10*, 1902584.

31. McClure, E. T.; Ball, M. R.; Windl, W.; Woodward, P. M. Cs_2AgBiX_6 (X = Br, Cl): New Visible Light Absorbing, Lead-Free Halide Perovskite Semiconductors. *Chem. Mater.* **2016,** *28*, 1348-1354.

32. Slavney, A. H.; Hu, T.; Lindenberg, A. M.; Karunadasa, H. I. A Bismuth-Halide Double Perovskite with Long Carrier Recombination Lifetime for Photovoltaic Applications. *J. Am. Chem. Soc.* **2016,** *138*, 2138-2141.

33. Volonakis, G.; Filip, M. R.; Haghighirad, A. A.; Sakai, N.; Wenger, B.; Snaith, H. J.; Giustino, F. Lead-Free Halide Double Perovskites via Heterovalent Substitution of Noble Metals. *J. Phys. Chem. Lett.* **2016,** *7*, 1254-1259.

34. Cross, C. W. a. H., W. F. On Minerals of the Cryolite Group Recently Found in Colorado. *Am. J. Sci.* **1883,** *s3-26*, 271-294.

35. Wolf, N. R.; Connor, B. A.; Slavney, A. H.; Karunadasa, H. I. Doubling the Stakes: The Promise of Halide Double Perovskites. *Angew. Chem. Int. Ed.* **2021,** *60*, 16264-16278.

36. Menzer, G. Über die Kristallstrukturen der Kryolithgruppe. *Fortschr. Mineral.* **1932,** *17*, 61.

37. Zhou, J.; Xia, Z.; Molokeev, M. S.; Zhang, X.; Peng, D.; Liu, Q. Composition Design, Optical Gap and Stability Investigations of Lead-Free Halide Double Perovskite $Cs_2AgInCl_6$. *J. Mater. Chem. A* **2017,** *5*, 15031-15037.

38. Luo, J.; Wang, X.; Li, S.; Liu, J.; Guo, Y.; Niu, G.; Yao, L.; Fu, Y.; Gao, L.; Dong, Q.; Zhao, C.; Leng, M.; Ma, F.; Liang, W.; Wang, L.; Jin, S.; Han, J.; Zhang, L.; Etheridge, J.; Wang, J.; Yan, Y.; Sargent, E. H.; Tang, J. Efficient and Stable Emission of Warm-White Light from Lead-Free Halide Double Perovskites. *Nature* **2018,** *563*, 541-545.

39. Bartel, C. J.; Clary, J. M.; Sutton, C.; Vigil-Fowler, D.; Goldsmith, B. R.; Holder, A. M.; Musgrave, C. B. Inorganic Halide Double Perovskites with Optoelectronic Properties Modulated by Sublattice Mixing. *J. Am. Chem. Soc.* **2020,** *142*, 5135-5145.

40. Muscarella, L. A.; Hutter, E. M. Halide Double-Perovskite Semiconductors Beyond Photovoltaics. *ACS Energy Lett.* **2022,** *7*, 2128-2135.

41. Giustino, F.; Snaith, H. J. Toward Lead-Free Perovskite Solar Cells. *ACS Energy Lett.* **2016,** *1*, 1233-1240.

42. Zhao, X.-G.; Yang, J.-H.; Fu, Y.; Yang, D.; Xu, Q.; Yu, L.; Wei, S.-H.; Zhang, L. Design of Lead-Free Inorganic Halide Perovskites for Solar Cells via Cation-Transmutation. *J. Am. Chem. Soc.* **2017,** *139*, 2630-2638.

43. Tao, S.; Schmidt, I.; Brocks, G.; Jiang, J.; Tranca, I.; Meerholz, K.; Olthof, S. Absolute Energy Level Positions in Tin- and Lead-Based Halide Perovskites. *Nat. Commun.* **2019,** *10*, 2560.

44. Meng, W.; Wang, X.; Xiao, Z.; Wang, J.; Mitzi, D. B.; Yan, Y. Parity-Forbidden Transitions and Their Impact on the Optical Absorption Properties of Lead-Free Metal Halide Perovskites and Double Perovskites. *J. Phys. Chem. Lett.* **2017,** *8*, 2999-3007.

45. Li, Y.-J.; Wu, T.; Sun, L.; Yang, R.-X.; Jiang, L.; Cheng, P.-F.; Hao, Q.-Q.; Wang, T.-J.; Lu, R.-F.; Deng, W.-Q. Lead-Free and Stable Antimony–Silver-Halide Double Perovskite $(CH_3NH_3)_2AgSbI_6$. *RSC Adv.* **2017,** *7*, 35175-35180.

46. Xiao, Z.; Du, K.-Z.; Meng, W.; Mitzi, D. B.; Yan, Y. Chemical Origin of the Stability Difference between Copper(I)- and Silver(I)-Based Halide Double Perovskites. *Angew. Chem. Int. Ed.* **2017,** *56*, 12107-12111.

47. K, N. N.; Nag, A. Synthesis and Luminescence of Mn-doped $Cs_2AgInCl_6$ Double Perovskites. *Chem. Commun.* **2018,** *54*, 5205-5208.

48. Locardi, F.; Cirignano, M.; Baranov, D.; Dang, Z.; Prato, M.; Drago, F.; Ferretti, M.; Pinchetti, V.; Fanciulli, M.; Brovelli, S.; De Trizio, L.; Manna, L. Colloidal Synthesis of Double Perovskite $Cs_2AgInCl_6$ and Mn-Doped $Cs_2AgInCl_6$ Nanocrystals. *J. Am. Chem. Soc.* **2018,** *140*, 12989-12995.

49. G. Blasse, B. C. G. Luminescent Materials. *Springer Berlin, Heidelberg* **1994**.

50. Ru-Shi Liu, X. W. Phosphor Handbook Fundamentals of Luminescence. *CRC Press* **2022**.

51. Bachmann, V.; Jüstel, T.; Meijerink, A.; Ronda, C.; Schmidt, P. J. Luminescence Properties of $SrSi_2O_2N_2$ Doped with Divalent Rare Earth Ions. *J. Lumin.* **2006,** *121*, 441-449.

52. Barzowska, J.; Majewska, N.; Jankowski, D.; Grzegorczyk, M.; Mahlik, S.; Michalik, D.; Sopicka-Lizer, M.; Aleshkevych, P.; Zhydachevskyy, Y.; Suchocki, A. Mechanism of the Luminescence Enhancement of $SrSi_2N_2O_2{:}Eu^{2+}$ Phosphor via Manganese Addition. *J. Phys. Chem. C* **2022,** *126*, 5292-5301.

53. Piao, X.; Horikawa, T.; Hanzawa, H.; Machida, K.-i. Characterization and Luminescence Properties of $Sr_2Si_5N_8{:}Eu^{2+}$ Phosphor for White Light-Emitting-Diode Illumination. *Appl. Phys. Lett.* **2006,** *88*, 161908.

54. Howard, C. L. H.; Kerr, P. F. Blue Halite. *Science* **1960,** *132*, 1886-1887.

55. Zielasek, V.; Hildebrandt, T.; Henzler, M. Surface Color Centers on Epitaxial NaCl Films. *Phys. Rev. B* **2000,** *62*, 2912-2919.

56. Wang, J.-J.; Chen, C.; Chen, W.-G.; Yao, J.-S.; Yang, J.-N.; Wang, K.-H.; Yin, Y.-C.; Yao, M.-M.; Feng, L.-Z.; Ma, C.; Fan, F.-J.; Yao, H.-B. Highly Luminescent Copper Iodide Cluster Based Inks with Photoluminescence Quantum Efficiency Exceeding 98%. *J. Am. Chem. Soc.* **2020,** *142*, 3686-3690.

57. Ha, J. M.; Hur, S. H.; Pathak, A.; Jeong, J.-E.; Woo, H. Y. Recent Advances in Organic Luminescent Materials with Narrowband Emission. *NPG Asia Mater.* **2021,** *13*, 53.

58. Jacobs, P. W. M. Alkali Halide Crystals Containing Impurity Ions with the ns^2 Ground-State Electronic Configuration†. *J. Phys. Chem. Solids* **1991,** *52*, 35-67.

59. Pan, G.; Bai, X.; Yang, D.; Chen, X.; Jing, P.; Qu, S.; Zhang, L.; Zhou, D.; Zhu, J.; Xu, W.; Dong, B.; Song, H. Doping Lanthanide into Perovskite Nanocrystals: Highly Improved and Expanded Optical Properties. *Nano Lett.* **2017,** *17*, 8005-8011.

60. Jin, S.; Li, R.; Huang, H.; Jiang, N.; Lin, J.; Wang, S.; Zheng, Y.; Chen, X.; Chen, D. Compact Ultrabroadband Light-Emitting Diodes Based on Lanthanide-Doped Lead-Free Double Perovskites. *Light. Sci. Appl.* **2022,** *11*, 52.

61. Wang, G.; Peng, Q.; Li, Y. Upconversion Luminescence of Monodisperse CaF_2:Yb^{3+}/Er^{3+} Nanocrystals. *J. Am. Chem. Soc.* **2009,** *131*, 14200-14201.

62. Marin, R.; Jaque, D. Doping Lanthanide Ions in Colloidal Semiconductor Nanocrystals for Brighter Photoluminescence. *Chem. Rev.* **2021,** *121*, 1425-1462.

63. DeLuca, J. A. An Introduction to Luminescence in Inorganic Solids. *J. Chem. Educ.* **1980,** *57*, 541.

64. Uh, H.; Petoud, S. Novel Antennae for the Sensitization of Near Infrared Luminescent Lanthanide Cations. *C. R. Chim.* **2010,** *13*, 668-680.

65. Buissette, V.; Moreau, M.; Gacoin, T.; Boilot, J.-P.; Chane-Ching, J.-Y.; Le Mercier, T. Colloidal Synthesis of Luminescent Rhabdophane $LaPO_4$:Ln^{3+}·xH_2O (Ln = Ce, Tb, Eu; x ≈ 0.7) Nanocrystals. *Chem. Mater.* **2004,** *16*, 3767-3773.

66. Zheng, W.; Zhou, S.; Chen, Z.; Hu, P.; Liu, Y.; Tu, D.; Zhu, H.; Li, R.; Huang, M.; Chen, X. Sub-10 nm Lanthanide-Doped CaF_2 Nanoprobes for Time-Resolved Luminescent Biodetection. *Angew. Chem. Int. Ed.* **2013,** *52*, 6671-6676.

67. Marciniak, L.; Bednarkiewicz, A.; Drabik, J.; Trejgis, K.; Strek, W. Optimization of Highly Sensitive YAG:Cr^{3+},Nd^{3+} Nanocrystal-Based Luminescent Thermometer Operating in an Optical Window of Biological Tissues. *Phys. Chem. Chem. Phys.* **2017,** *19*, 7343-7351.

68. Marciniak, L.; Bednarkiewicz, A. Nanocrystalline NIR-to-NIR Luminescent Thermometer Based on Cr^{3+},Yb^{3+} Emission. *Sens. Actuators B: Chem.* **2017,** *243*, 388-393.

69. Trejgis, K.; Marciniak, L. The Influence of Manganese Concentration on the Sensitivity of Bandshape and Lifetime Luminescent Thermometers Based on $Y_3Al_5O_{12}$:Mn^{3+},Mn^{4+},Nd^{3+} Nanocrystals. *Phys. Chem. Chem. Phys.* **2018,** *20*, 9574-9581.

70. R Bajgiran, K.; Darapaneni, P.; Melvin, A. T.; Dorman, J. A. Effects of Weak Electric Field on the Photoluminescence Behavior of Bi^{3+}-Doped YVO_4:Eu^{3+} Core–Shell Nanoparticles. *J. Phys. Chem. C* **2019**, *123*, 13027-13035.

71. Park, W.; Lu, D.; Ahn, S. Plasmon Enhancement of Luminescence Upconversion. *Chem. Soc. Rev.* **2015**, *44*, 2940-2962.

72. Das, A.; Mao, C.; Cho, S.; Kim, K.; Park, W. Over 1000-Fold Enhancement of Upconversion Luminescence Using Water-Dispersible Metal-Insulator-Metal Nanostructures. *Nat. Commun.* **2018**, *9*, 4828.

73. Dong, J.; Gao, W.; Han, Q.; Wang, Y.; Qi, J.; Yan, X.; Sun, M. Plasmon-Enhanced Upconversion Photoluminescence: Mechanism and Application. *Rev. Phys.* **2019**, *4*, 100026.

74. Wang, X.; Valiev, R. R.; Ohulchanskyy, T. Y.; Ågren, H.; Yang, C.; Chen, G. Dye-Sensitized Lanthanide-Doped Upconversion Nanoparticles. *Chem. Soc. Rev.* **2017**, *46*, 4150-4167.

75. Wang, J.; Deng, R. Energy Transfer in Dye-Coupled Lanthanide-Doped Nanoparticles: From Design to Application. *Chem. Asian J.* **2018**, *13*, 614-625.

76. Martín-Rodríguez, R.; Geitenbeek, R.; Meijerink, A. Incorporation and Luminescence of Yb^{3+} in CdSe Nanocrystals. *J. Am. Chem. Soc.* **2013**, *135*, 13668-13671.

77. Creutz, S. E.; Fainblat, R.; Kim, Y.; De Siena, M. C.; Gamelin, D. R. A Selective Cation Exchange Strategy for the Synthesis of Colloidal Yb^{3+}-Doped Chalcogenide Nanocrystals with Strong Broadband Visible Absorption and Long-Lived Near-Infrared Emission. *J. Am. Chem. Soc.* **2017**, *139*, 11814-11824.

78. Mir, W. J.; Mahor, Y.; Lohar, A.; Jagadeeswararao, M.; Das, S.; Mahamuni, S.; Nag, A. Postsynthesis Doping of Mn and Yb into $CsPbX_3$ (X = Cl, Br, or I) Perovskite Nanocrystals for Downconversion Emission. *Chem. Mater.* **2018**, *30*, 8170-8178.

79. Mir, W. J.; Sheikh, T.; Arfin, H.; Xia, Z. G.; Nag, A. Lanthanide Doping in Metal Halide Perovskite Nanocrystals: Spectral Shifting, Quantum Cutting and Optoelectronic Applications. *NPG Asia Mater.* **2020**, *12*, 9.

80. Tessitore, G.; Mandl, G. A.; Maurizio, S. L.; Kaur, M.; Capobianco, J. A. The Role of Lanthanide Luminescence in Advancing Technology. *RSC Adv.* **2023**, *13*, 17787-17811.

81. Levine, A. K.; Palilla, F. C. A New, Highly Efficient Red-Emitting Cathodoluminescent Luminescent Phosphor (YVO_4:Eu) for Color Television. *Appl. Phys. Lett.* **2004**, *5*, 118-120.

82. Xia, Z.; Liu, Q. Progress in Discovery and Structural Design of Color Conversion Phosphors for LEDs. *Prog. Mater. Sci.* **2016**, *84*, 59-117.

83. Thimsen, E.; Sadtler, B.; Berezin, M. Y. Shortwave-Infrared (SWIR) Emitters for Biological Imaging: A Review of Challenges and Opportunities. *Nanophotonics* **2017,** *6*, 1043-1054.

84. Klein, A.; Albe, K.; Bein, N.; Clemens, O.; Creutz, K. A.; Erhart, P.; Frericks, M.; Ghorbani, E.; Hofmann, J. P.; Huang, B.; Kaiser, B.; Kolb, U.; Koruza, J.; Kübel, C.; Lohaus, K. N. S.; Rödel, J.; Rohrer, J.; Rheinheimer, W.; Souza, R. A.; Streibel, V.; Weidenkaff, A.; Widenmeyer, M.; Xu, B.-X.; Zhang, H. The Fermi Energy as Common Parameter to Describe Charge Compensation Mechanisms: A Path to Fermi Level Engineering of Oxide Electroceramics. *J. Electroceramics* **2023**.

85. Volonakis, G.; Haghighirad, A. A.; Milot, R. L.; Sio, W. H.; Filip, M. R.; Wenger, B.; Johnston, M. B.; Herz, L. M.; Snaith, H. J.; Giustino, F. $Cs_2InAgCl_6$: A New Lead-Free Halide Double Perovskite with Direct Band Gap. *J. Phys. Chem. Lett.* **2017,** *8*, 772-778.

86. Luo, J.; Li, S.; Wu, H.; Zhou, Y.; Li, Y.; Liu, J.; Li, J.; Li, K.; Yi, F.; Niu, G.; Tang, J. $Cs_2AgInCl_6$ Double Perovskite Single Crystals: Parity Forbidden Transitions and Their Application For Sensitive and Fast UV Photodetectors. *ACS Photonics* **2018,** *5*, 398-405.

87. Yang, B.; Mao, X.; Hong, F.; Meng, W.; Tang, Y.; Xia, X.; Yang, S.; Deng, W.; Han, K. Lead-Free Direct Band Gap Double-Perovskite Nanocrystals with Bright Dual-Color Emission. *J. Am. Chem. Soc.* **2018,** *140*, 17001-17006.

88. Lee, W.; Hong, S.; Kim, S. Colloidal Synthesis of Lead-Free Silver–Indium Double-Perovskite $Cs_2AgInCl_6$ Nanocrystals and Their Doping with Lanthanide Ions. *J. Phys. Chem. C* **2019,** *123*, 2665-2672.

89. Mahor, Y.; Mir, W. J.; Nag, A. Synthesis and Near-Infrared Emission of Yb-Doped $Cs_2AgInCl_6$ Double Perovskite Microcrystals and Nanocrystals. *J. Phys. Chem. C* **2019,** *123*, 15787-15793.

90. Ranfagni, A.; Mugnai, D.; Bacci, M.; Viliani, G.; Fontana, M. P. The Optical Properties of Thallium-like Impurities in Alkali-Halide Crystals. *Adv. Phys.* **1983,** *32*, 823-905.

91. Choi, K. O.; Lee, S. W.; Bae, H. K.; Jung, S. H.; Chang, C. K.; Kang, J. G. Spectroscopic Studies of Sb^{3+} Color Centers in Alkali Halide Single Crystals. *J. Chem. Phys.* **1991,** *94*, 6420-6428.

Chapter 2

Bi³⁺-Er³⁺ and Bi³⁺-Yb³⁺ Codoped Cs₂AgInCl₆ Double Perovskite: Visible to Short-Wave Infrared Emitters

Bi^{3+}-Er^{3+} and Bi^{3+}-Yb^{3+} Codoped $Cs_2AgInCl_6$ Double Perovskite: Visible to Short-Wave Infrared Emitters

Abstract

Bi^{3+} and lanthanide ions have been codoped in metal oxides as optical sensitizers and emitters. But such codoping is not known in typical semiconductors such as Si, GaAs, and CdSe. Metal halide perovskite with coordination number 6 provides an opportunity to codope Bi^{3+} and lanthanide ions. Codoping of Bi^{3+} and Ln^{3+} (Ln = Er and Yb) in $Cs_2AgInCl_6$ double perovskite is presented here. Bi^{3+}-Er^{3+} codoped $Cs_2AgInCl_6$ shows Er^{3+} f-electron emission at 1540 nm (suitable for low-loss optical communication). Bi^{3+} codoping decreases the excitation (absorption) energy, such that the samples can be excited with ca. 370 nm light. At that excitation, Bi^{3+}-Er^{3+} codoped $Cs_2AgInCl_6$ shows ca. 45 times higher emission intensity compared to the Er^{3+} doped $Cs_2AgInCl_6$. Similar results are also observed in Bi^{3+}-Yb^{3+} codoped sample emitting at 994 nm. Temperature-dependent (5.7 K to 423 K) photoluminescence is used to understand the optical sensitization and emission processes.

Graphical Abstract

Bi³⁺-Er³⁺ and Bi³⁺-Yb³⁺ Codoped Cs₂AgInCl₆ Double Perovskite: Visible to Short-Wave Infrared Emitters
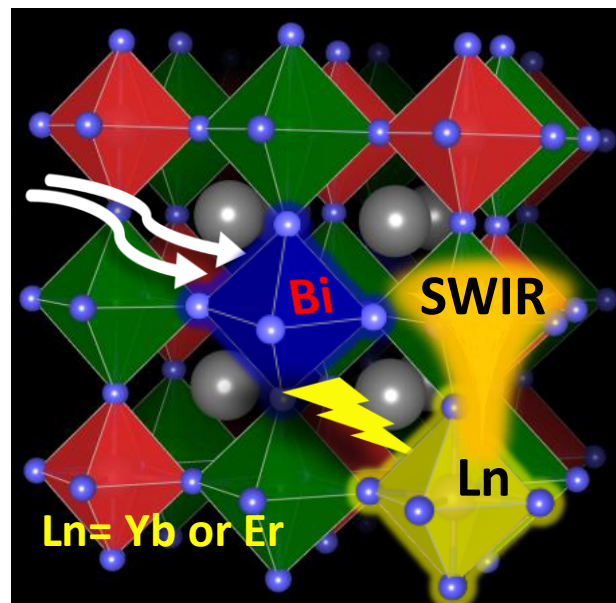
2.1 Introduction

Lead halide perovskites have emerged as an important class of semiconductor.[1-9] In these perovskites, the Pb site has a coordination number of 6, unlike traditional semiconductors including Si, GaAs, CdSe, CuZnSnS₄, which possess coordination number = 4 for metal sites. This octahedral site in perovskites is suitable for incorporation of lanthanide dopants, since lanthanides prefer coordination number $\geq$ 6.[10-14] Such lanthanide doping resulted into interesting optical properties in the visible and infrared region, including efficient quantum cutting phenomenon achieving photoluminescence (PL) quantum yield close to 200% for Yb *f*-electron emission.[15]

Despite several advantages, major issues with these lead halide perovskites remain their poor stability and toxicity. There are various attempts being made to discover Pb-free metal halide perovskites with efficient optical and optoelectronic properties.[16-20] In this category, double perovskites , such as Cs₂AgInCl₆ are emerging, because double perovskites retain the 3D perovskite structure similar to Pb-halide perovskites.[21-29] But the problem with metal halide double perovskites is wide or indirect band gap, limiting their optical and optoelectronic properties in the visible and infrared region. To address this issue, new light emission channel in double perovskites were first introduced with Mn^{2+} doping, and then by doping lanthanides like Yb^{3+} and Er^{3+}.[30-34] But the excitation energy is too high (< 350 nm) and is not suitable for excitation with commercial UV light-emitting diodes (LEDs) that typically produce light $\geq$365 nm. Another interesting development is doping Bi^{3+} in $Cs_2Ag_{1-x}Na_xInCl_6$, tailoring both absorption and broad-band visible-light emission.[35-37]
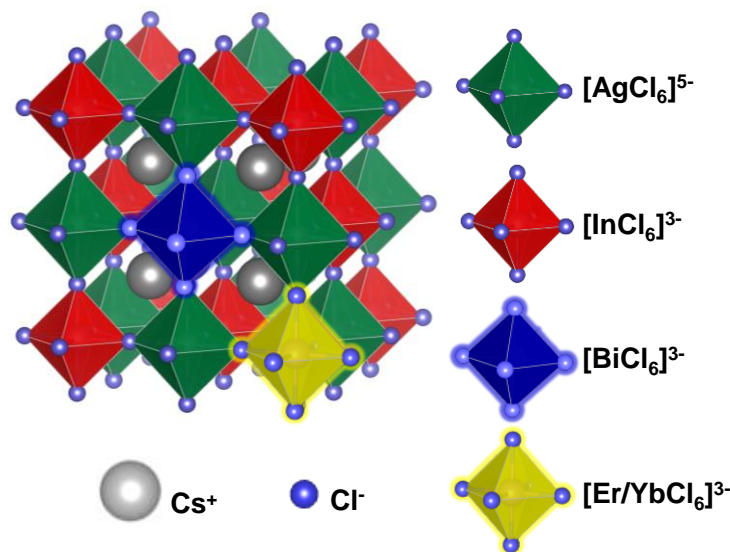
Figure 2.1: Schematics of Bi^{3+}-Er^{3+}/ Yb^{3+} codoping in Cs₂AgInCl₆ lattice.

Bi^{3+}-Er^{3+} and Bi^{3+}-Yb^{3+} Codoped $Cs_2AgInCl_6$ Double Perovskite: Visible to Short-Wave Infrared Emitters

To date, near infrared emission from Ln^{3+} (Ln = Er or Yb) doped double perovskites remains weak in intensity, along with having very high excitation energy (< 350 nm).[32-33] To overcome these problems, we introduce herein the idea of codoping Bi^{3+} and Ln^{3+} into the lattice of $Cs_2AgInCl_6$ (see Figure 2.1). Bi^{3+} codoping introduces new energy states giving rise to new optical absorption channel at a lower energy compared to band gap of undoped sample. This absorbed energy is then efficiently transferred to Er^{3+} or Yb^{3+} f-electrons promoting the short-wave infrared (SWIR) dopant emissions. Note that the Er^{3+} emission at 1540 nm is suitable for low-loss optical telecommunication.

2.2 Experimental Section

2.2.1 Chemicals

Cesium chloride (CsCl, 99.9%), indium (III) chloride ($InCl_3$, anhydrous powder, ≥99.999%), silver chloride (AgCl, 99.999%), erbium chloride hexahydrate ($ErCl_3.6H_2O$, 99.995%), ytterbium chloride hexahydrate ($YbCl_3.6H_2O$, 99.9%), hydrochloric acid (HCl, 37 wt %, 99.99%) are purchased from Sigma Aldrich Chemicals. All the chemicals are used without any further purification.

2.2.2 Synthesis of Er^{3+} Doped $Cs_2AgInCl_6$

Er^{3+} doped microcrystals are synthesized by modifying the synthesis method for undoped $Cs_2AgInCl_6$ microcrystals, reported by Volonakis *et. al.*[23] In a typical synthesis of 0.5% Er^{3+} (with respect to concentration of In^{3+}) doped $Cs_2AgInCl_6$, 0.25 mmol of $InCl_3$, 0.25 mmol of $AgCl_3$ and a very high (0.75 mmol) precursor concentration of $ErCl_3.6H_2O$ are taken in a vial with 2 mL HCl. The reaction mixture is then kept at 80 °C in an oil bath with vigorous stirring until all the precursors get dissolved. Then 0.5 mmol of CsCl is added to the reaction mixture, which immediately leads to precipitation of microcrystals. The reaction is continued for another 20 minute to make sure that it is complete. The obtained precipitates are filtered out, washed three times with ethanol, dried in an oven at 100 °C and then stored in a glass vial under ambient conditions for further characterization.

2.2.3 Synthesis of Yb^{3+} Doped $Cs_2AgInCl_6$

The synthesis procedure is very much similar to that for Er^{3+} doped $Cs_2AgInCl_6$ discussed above. The only difference is the use of $YbCl_3.6H_2O$ precursor instead of $ErCl_3.6H_2O$. For

Chapter 2

Bi^{3+}-Er^{3+} and Bi^{3+}-Yb^{3+} Codoped Cs$_2$AgInCl$_6$ Double Perovskite: Visible to Short-Wave Infrared Emitters

1.2% Yb^{3+} doping (with respect to concentration of In^{3+}) in the product, 0.25 mmol of YbCl$_3$.6H$_2$O precursor is added.

2.2.4 Synthesis of Bi^{3+} Doped Cs$_2$AgInCl$_6$

The synthesis procedure is very much similar to that for Er^{3+} doped Cs$_2$AgInCl$_6$ discussed above. The only difference is the use of BiCl$_3$ (0.0012 mmol) precursor instead of ErCl$_3$.6H$_2$O.

2.2.5 Synthesis of Bi^{3+} -Er^{3+} Codoped Cs$_2$AgInCl$_6$

The synthesis procedure is very much similar to that for Er^{3+} doped Cs$_2$AgInCl$_6$ discussed above. The only difference is the use of BiCl$_3$ (0.0012 mmol) precursor in addition to different amounts of ErCl$_3$.6H$_2$O. See Table 2.1 and 2.2 for the details of precursor concentrations and Er^{3+} percentages in the product.

2.2.6 Synthesis of Bi^{3+} -Yb^{3+} Codoped Cs$_2$AgInCl$_6$

The synthesis procedure is very much similar to that for Bi^{3+}-Er^{3+} codoped Cs$_2$AgInCl$_6$ discussed above. The only difference is the use of YbCl$_3$.6H$_2$O precursor instead of ErCl$_3$.6H$_2$O. See Table 2.1 and 2.2 for the details of precursor concentrations and Yb^{3+} percentages in the product.

2.2.7 Coating Commercial UV LED with Bi^{3+}-Er^{3+} codoped Cs$_2$AgInCl$_6$

We have made down conversion light emitting diodes (LEDs) by coating our Bi^{3+}-Er^{3+} codoped Cs$_2$AgInCl$_6$ on a commercial UV LED. The UV LED emits 360 to 385 nm light, which is suitable for excitation of our sample. To make the coating on UV LED, Bi^{3+}-Er^{3+} codoped Cs$_2$AgInCl$_6$ sample is mixed with 10 weight % of poly (methyl methacrylate) (PMMA) in toluene. Then the mixture is drop casted on top of the UV LEDs. The LEDs are powered by 3.2 V, 30 mA source.

2.2.8 Characterization

Powder X-ray diffraction (PXRD) patterns are recorded using a Bruker D8 Advance X-ray diffraction machine equipped with Cu Kα (1.54 Å) radiation. A Zeiss Ultra Plus instrument is used for field emission scanning electron microscopy (FESEM) imaging and energy dispersive X-ray spectroscopy (EDS). The obtained results from EDS elemental analysis support the stoichiometric ratio of Cs, Ag, In and Cl with Cs$_2$AgInCl$_6$ composition. For all sample the dopant (Er^{3+}, Yb^{3+} and Bi^{3+}) concentrations determined by EDS analysis is not consistent

Chapter 2

Bi^{3+}-Er^{3+} and Bi^{3+}-Yb^{3+} Codoped Cs$_2$AgInCl$_6$ Double Perovskite: Visible to Short-Wave Infrared Emitters

because of the low (~1%) concentration of dopants. For elemental analysis of the Er^{3+}, Yb^{3+}, Bi^{3+} and In^{3+}, inductively coupled plasma mass spectroscopy (ICP−MS) is carried out by using a quadrupole-ICP−MS (Thermo iCAP-Q) spectrometer. The dopant percentages are presented with respect to concentration of In in the sample. Thermogravimetric analysis (TGA) data are recorded using a Perkin-Elmer STA 6000 instrument. The samples are heated in the range 30–800 °C at the heating rate of 10 °C per minute, under N$_2$ atmosphere.

Diffused reflectance spectra of microcrystalline powders in the UV−visible−NIR region are recorded using a Shimadzu UV-3600 plus UV−vis−NIR spectrophotometer. Then Kubelka-Munk transformation[38-39] is used for the analysis of diffuse reflectance spectra. It relates the reflectance data with absorption coefficient as in equation (1):

$$F(R) = \alpha/s = (1-R)^2/2R \qquad (1)$$

where F(R) is the Kubelka-Munk function, R is reflectance, α is absorption coefficient and s is the scattering factor. For photoluminescence (PL) measurements, powder samples are hold between two quartz sample holders. Steady-state PL, PL Excitation (PLE), and PL decay dynamics (time-correlated single photon counting) are measured using Edinburgh FLS980 Instrument. The samples are excited at 360 nm wavelength using xenon lamp for steady state PL and PLE measurements. A microsecond flash lamp is used to excite samples with 360 nm radiation to monitor the PL decay dynamics in the SWIR region. PL decay are fitted by mono- and bi- exponential decay functions as mentioned wherever used. Temperature dependent PL, PLE and PL decay dynamics are studied in the same Edinburgh FLS980 Instrument coupled with a cryostat. The powder samples are placed between two sapphire substrates and fix in a gold coated copper sample holder. The sample holder is fixed in a closed cycle He cryostat (Advanced Research Systems) attached with Lake Shore 335 temperature controller to achieve the desired temperatures in the range of 8 - 300 K.

2.2.9 Methodology to Compare the PL Intensity

For comparison of PL intensity, 5 wt% of the powder sample was thoroughly mixed with BaSO$_4$ powder. BaSO$_4$ does not interfere with excitation and near infrared emission of the sample. So, the role of BaSO$_4$ is to dilute the sample, similar to a solvent in a colloidal dispersion. For every measurement, equal amount mixed (sample + BaSO$_4$) powder is taken in a quartz sample holder which has a definite size groove in it and PL spectra are recorded at multiple spots of the mixed powder. Then the average out spectra are used for comparison.

2.3 Results and Discussion

2.3.1 Synthesis and Characterization of Undoped/ Doped/ Codoped Cs₂AgInCl₆

The synthesis methodology for codoping is developed by modifying the synthesis of undoped $Cs_2AgInCl_6$ reported by Volonakis et al.[23] (see the experimental section for detail). Schematic in Figure 2.2 shows the synthesis protocol.
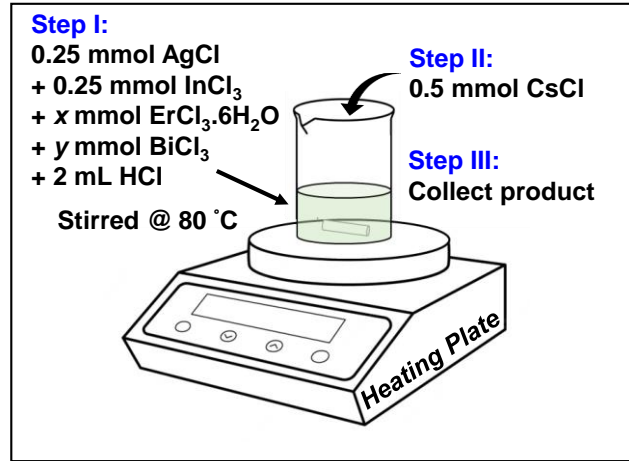
Figure 2.2: Schematic of synthesis Bi^{3+}-Er^{3+} codoped $Cs_2AgInCl_6$.

Elemental analysis by EDS is presented in Table 2.1. The dopant concentrations are too small to get a reliable value by EDS. Therefore, EDS data mainly verify the composition of $Cs_2AgInCl_6$ host. Dopant percentages are determined by ICP-MS and presented in Table 2.2. Together, EDS and ICP-MS data provide the complete elemental analysis. In spite of using

Table 2.1: EDS data of Er^{3+}-doped, Yb^{3+}-doped, Bi^{3+}-doped, Bi^{3+}-Er^{3+} codoped and Bi^{3+}-Yb^{3+} codoped $Cs_2AgInCl_6$ products.

Sample Code	Cs : Ag : In : Cl (molar ratio)
0.9% Bi^{3+}-doped $Cs_2AgInCl_6$	2.1 : 1.0 : 1.0 : 6.3
0.5% Er^{3+}-doped $Cs_2AgInCl_6$	2.4 : 1.0 : 1.1 : 6.7
0.8% Bi^{3+}-0.1% Er^{3+} codoped $Cs_2AgInCl_6$	2.0 : 1.0 : 1.1 : 6.2
0.6% Bi^{3+} - 0.3% Er^{3+} codoped $Cs_2AgInCl_6$	2.2 : 1.0 : 1.1 : 6.5
1.1% Bi^{3+} - 0.5% Er^{3+} codoped $Cs_2AgInCl_6$	2.1 : 1.0 : 1.1 : 6.4
1.2% Yb^{3+}-doped $Cs_2AgInCl_6$	1.9 : 1.0 : 1.0 : 6.3
0.6% Bi^{3+}- 1.1% Yb^{3+} codoped $Cs_2AgInCl_6$	2.0 : 1.0 : 1.0 : 6.3

Bi^{3+}-Er^{3+} and Bi^{3+}-Yb^{3+} Codoped $Cs_2AgInCl_6$ Double Perovskite: Visible to Short-Wave Infrared Emitters

high amounts of Ln^{3+} precursors, only a small fraction of Ln^{3+} ions are present in the product. Better understanding of doping mechanism might increase the efficiency of Ln^{3+} doping. In difference, doping/codoping of Bi^{3+} is efficient. EDS elemental mapping data in Figure 2.3 suggest homogenous distribution of elements throughout the sample.

Table 2.2: Comparisons of dopant concentrations obtained from ICP-MS analysis of the Er^{3+}-doped, Yb^{3+}-doped, Bi^{3+}-doped, Bi^{3+}-Er^{3+} codoped and Bi^{3+}-Yb^{3+} codoped $Cs_2AgInCl_6$ products. The molar concentration of Er^{3+} ([Er]), Bi^{3+} ([Bi]) and Yb^{3+} ([Yb]) dopants are calculated with respect to that of In^{3+} ([In]). For example, Er^{3+} % = 100 × [Er]/[In]; Yb^{3+} % = 100 × [Yb]/[In]; and Bi^{3+} % = 100 × [Bi]/[In].

Sample Code	Precursor		Product (ICP-MS)	
	Er^{3+} %	Bi^{3+}%	Er^{3+} %	Bi^{3+} %
0.9% Bi^{3+}-doped $Cs_2AgInCl_6$	0.0	0.5	0.0	0.9
0.5% Er^{3+}-doped $Cs_2AgInCl_6$	150.0	0.0	0.5	0.0
0.8% Bi^{3+}-0.1% Er^{3+} codoped $Cs_2AgInCl_6$	35.0	0.5	0.1	0.8
0.6% Bi^{3+} - 0.3% Er^{3+} codoped $Cs_2AgInCl_6$	100.0	0.5	0.3	0.6
1.1% Bi^{3+} - 0.5% Er^{3+} codoped $Cs_2AgInCl_6$	150.0	0.5	0.5	1.1
Yb^{3+}/ Bi^{3+}-Yb^{3+} codoped $Cs_2AgInCl_6$				
Sample Code	Precursor		Product (ICP-MS)	
	Yb^{3+} %	Bi^{3+}%	Yb^{3+} %	Bi^{3+} %
1.2% Yb^{3+}-doped $Cs_2AgInCl_6$	100.0	0.0	1.2	0.0
0.6% Bi^{3+}- 1.1% Yb^{3+} codoped $Cs_2AgInCl_6$	100.0	0.5	1.1	0.6

FESEM images in Figure 2.4 shows micrometer sized crystals. Comparison of PXRD patterns, shown in Figure 2.5, confirms that no impurity peak is observed in the codoped samples. All the samples show the PXRD peaks corresponding to $Cs_2AgInCl_6$ in cubic phase.[40] No clear shift in the PXRD peak positions is observed after doping Bi^{3+} and Yb^{3+}/ Er^{3+}, probably because of the small amount of dopant ion incorporation and similar ionic radii of In^{3+} (0.80 Å) with the dopants Yb^{3+} (0.87 Å) , Er^{3+} (0.89 Å) and Bi^{3+} (1.03 Å).

Bi³⁺-Er³⁺ and Bi³⁺-Yb³⁺ Codoped Cs₂AgInCl₆ Double Perovskite: Visible to Short-Wave Infrared Emitters
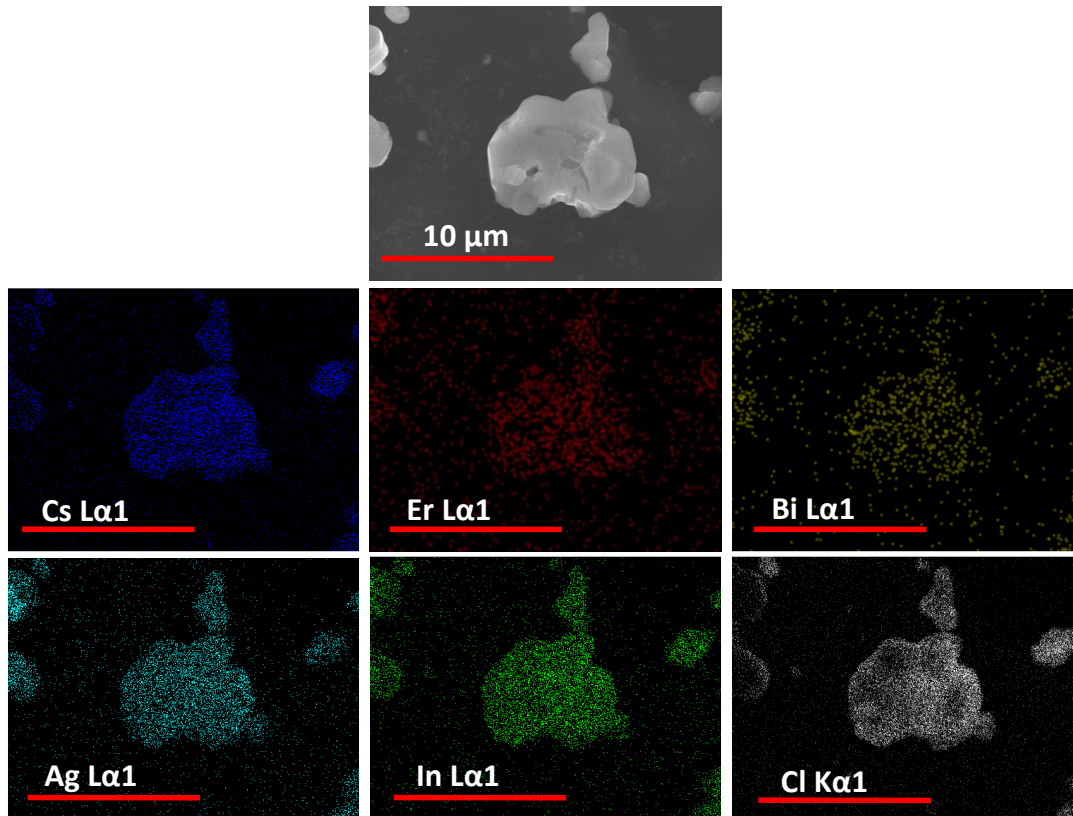
Figure 2.3: EDS elemental mapping data of 1.1% Bi^{3+}-0.5% Er^{3+} codoped $Cs_2AgInCl_6$. Scale bar is 10 µm.
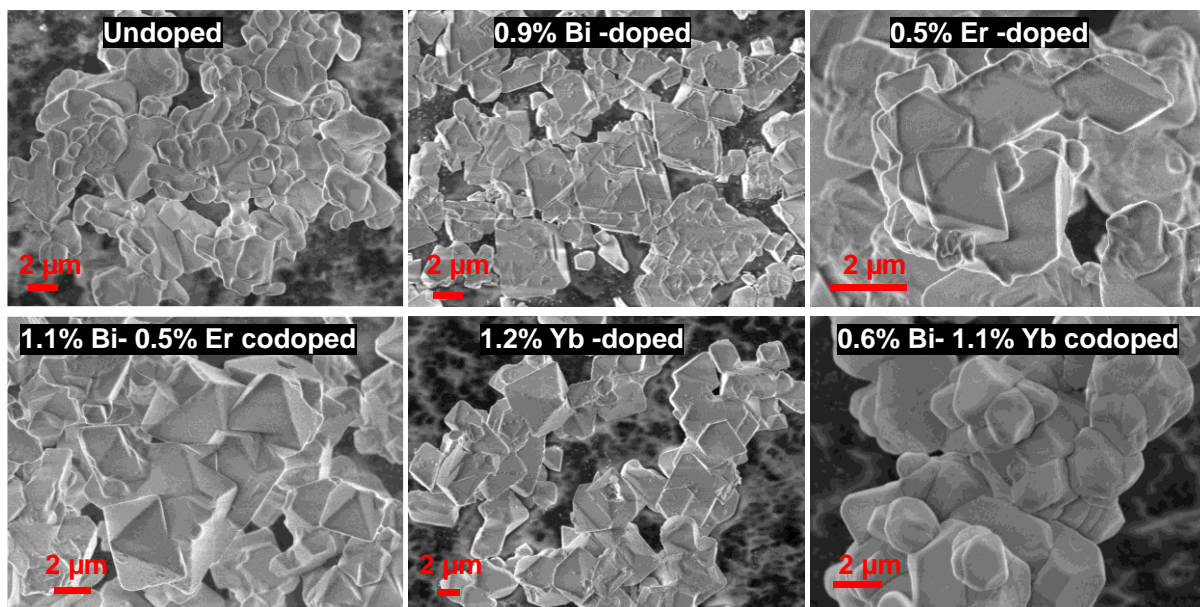
Figure 2.4: FESEM images of undoped, 0.9% Bi^{3+}-doped, 0.5% Er^{3+}-doped, 1.1% Bi^{3+}-0.5% Er^{3+} codoped, 1.2% Yb^{3+}-doped and 0.6% Bi^{3+}-1. 1% Yb^{3+} codoped $Cs_2AgInCl_6$ microcrystals.

Bi^{3+}-Er^{3+} and Bi^{3+}-Yb^{3+} Codoped $Cs_2AgInCl_6$ Double Perovskite: Visible to Short-Wave Infrared Emitters
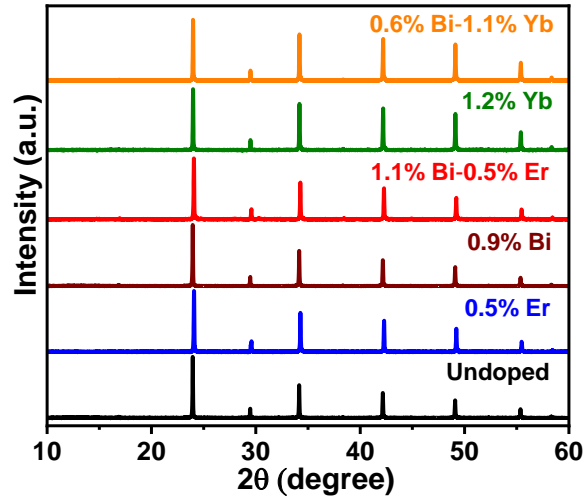
Figure 2.5: PXRD of undoped, 0.9% Bi^{3+}-doped, 0.5% Er^{3+}-doped, 1.1% Bi^{3+}-0.5% Er^{3+} codoped, 1.2% Yb^{3+}-doped and 0.6% Bi^{3+}-1.1% Yb^{3+} codoped $Cs_2AgInCl_6$.

2.3.2 Optical Properties of Undoped, 0.9% Bi^{3+}-doped, 0.5% Er^{3+}-doped, 1.1% Bi^{3+}-0.5% Er^{3+} codoped $Cs_2AgInCl_6$
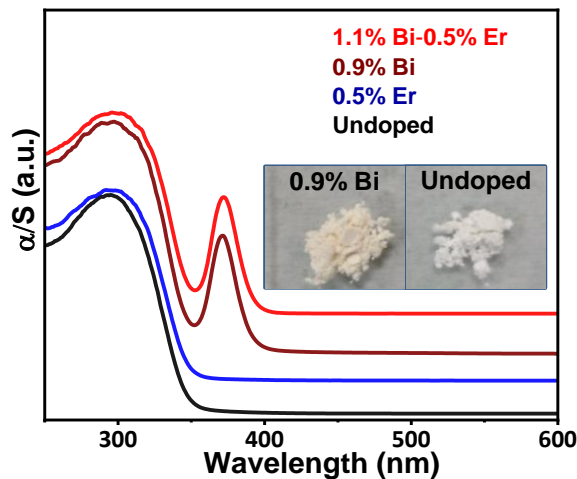
Figure 2.6: UV-visible absorption spectra of undoped, 0.9% Bi^{3+}-doped, 0.5% Er^{3+}-doped and 1.1% Bi^{3+}-0.5% Er^{3+} codoped $Cs_2AgInCl_6$. The absorption spectra are obtained through Kubelka−Munk transformation from the measured diffused reflectance spectra of powder samples, where α is the absorption coefficient and S is the scattering coefficient. Absorption spectra are shifted along Y-axis for clear presentation. Insets are photographs of Bi^{3+}-doped and undoped $Cs_2AgInCl_6$ under visible light.

UV-visible absorption spectra (Figure 2.6) of undoped and Er^{3+} doped $Cs_2AgInCl_6$ are similar, with intense absorption below 350 nm. Interestingly, Bi^{3+} doping gives rise to an intense new absorption with peak at 372 nm. This new absorption might arise due to $^1S_0 \rightarrow {}^3P_1^*$ transition of Bi^{3+}.[36, 41] This new absorption modifies the hue of the sample, making the Bi^{3+}-doped samples little yellowish white, compared to pure white color of samples without having Bi^{3+} (see the

Chapter 2

Bi^{3+}-Er^{3+} and Bi^{3+}-Yb^{3+} Codoped $Cs_2AgInCl_6$ Double Perovskite: Visible to Short-Wave Infrared Emitters

photographs in the inset of Figure 2.6). This modification of absorption spectrum with Bi^{3+} doping/codoping is qualitatively different from prior reports of Mn^{2+} and Ln^{3+} doping, where only the emission spectra get modified.
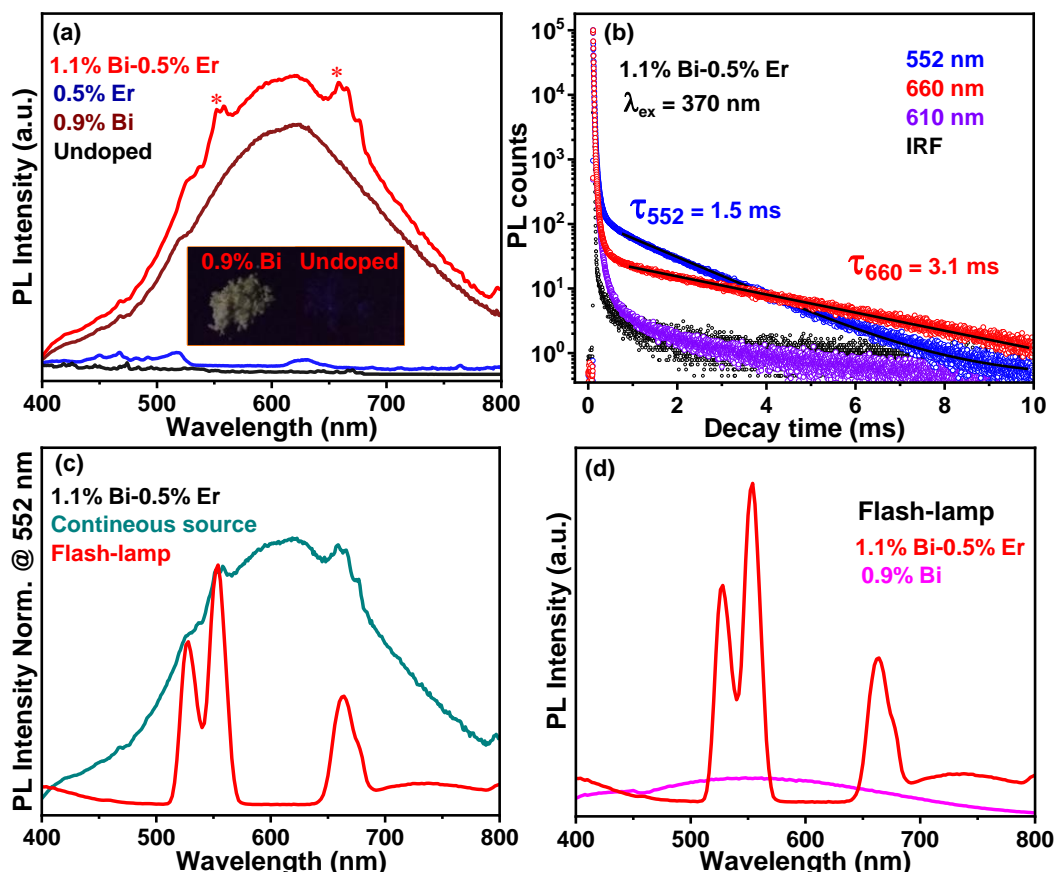
Figure 2.7: (a) PL spectra of undoped, 0.9% Bi^{3+}-doped, 0.5% Er^{3+}-doped and 1.1% Bi^{3+}-0.5% Er^{3+} codoped $Cs_2AgInCl_6$ in the visible region. (b) PL decay dynamics of 552 nm, 610 nm and 660 nm emission arising from 1.1% Bi^{3+}-0.5% Er^{3+} doped $Cs_2AgInCl_6$. (c) PL spectra of 1.1% Bi^{3+}-0.5% Er^{3+} codoped $Cs_2AgInCl_6$ excited with (excitation wavelength 360 nm) two different types of light sources, one continuous Xe-lamp and another flash-lamp (1.5-2.5 µs band-width, and 100 µs time delay). (d) PL spectra of 1.1% Bi^{3+}-0.5% Er^{3+} codoped $Cs_2AgInCl_6$ and 0.9% Bi^{3+}-doped $Cs_2AgInCl_6$ samples excited at 360 nm using a microsecond flash-lamp (1.5-2.5 µs band-width, and 100 µs time delay).

Figure 2.7a shows PL spectra of undoped, 0.9% Bi^{3+}-doped, 0.5% Er^{3+}-doped and 1.1% Bi^{3+}-0.5% Er^{3+} codoped $Cs_2AgInCl_6$ in visible. Bi^{3+} doping/codoping gives rise to visible light emission (Figure 2.7a). 1.1% Bi^{3+}-0.5% Er^{3+} codoped sample show sharp additional spectral features at 552 and 660 nm, indicated by * marks in Figure 2.7a. Figure 2.7b show the PL decay of 1.1% Bi^{3+}-0.5% Er^{3+} sample at 552 nm, 610 nm and 660 nm. PL decay show sharp initial decay due to instrument response function. 552 nm and 660 nm emissions have long decay component. The long components are fitted with singe exponential decay equation. 552 nm and 660 nm fitting results long PL lifetimes of 1.5 ms and 3.1 ms respectively. Whereas, the

Bi³⁺-Er³⁺ and Bi³⁺-Yb³⁺ Codoped Cs₂AgInCl₆ Double Perovskite: Visible to Short-Wave Infrared Emitters

PL decay at other positions of the broad spectrum, for example 610 nm, decay faster and falls in instrument response limit as shown in Figure 2.7b. PL spectra of 1.1% Bi^{3+}-0.5% Er^{3+} codoped Cs₂AgInCl₆ excited with two different types of light sources, one continuous Xe-lamp and another flash-lamp (1.5-2.5 µs band-width, and 100 µs time delay) are shown in Figure 2.7c. Since 552 nm and 660 nm peak originate from Er^{3+} emission with long (ms) lifetimes, these peaks show higher relative intensity compared to the broad PL envelop, when measured using the microsecond flash-lamp compared to that measured using continuous Xe-lamp excitation. PL spectra of 1.1% Bi^{3+}-0.5% Er^{3+} codoped Cs₂AgInCl₆ and 0.9% Bi^{3+}-doped Cs₂AgInCl₆ samples excited using a microsecond flash-lamp are shown in Figure 2.7d. The 552 nm and 660 nm peak arise only in those samples that are doped with Er^{3+}. Results shown in Figure 2.7b-d confirm that the 552 nm and 660 nm PL peak arise from *f-f* electronic transition of Er^{3+} dopants. The features at 552 nm and 660 nm are attribute to ${}^4S_{3/2} \rightarrow {}^4I_{15/2}$ and ${}^4F_{9/2} \rightarrow {}^4I_{15/2}$ transitions of Er^{3+} *f*-electrons.[42]
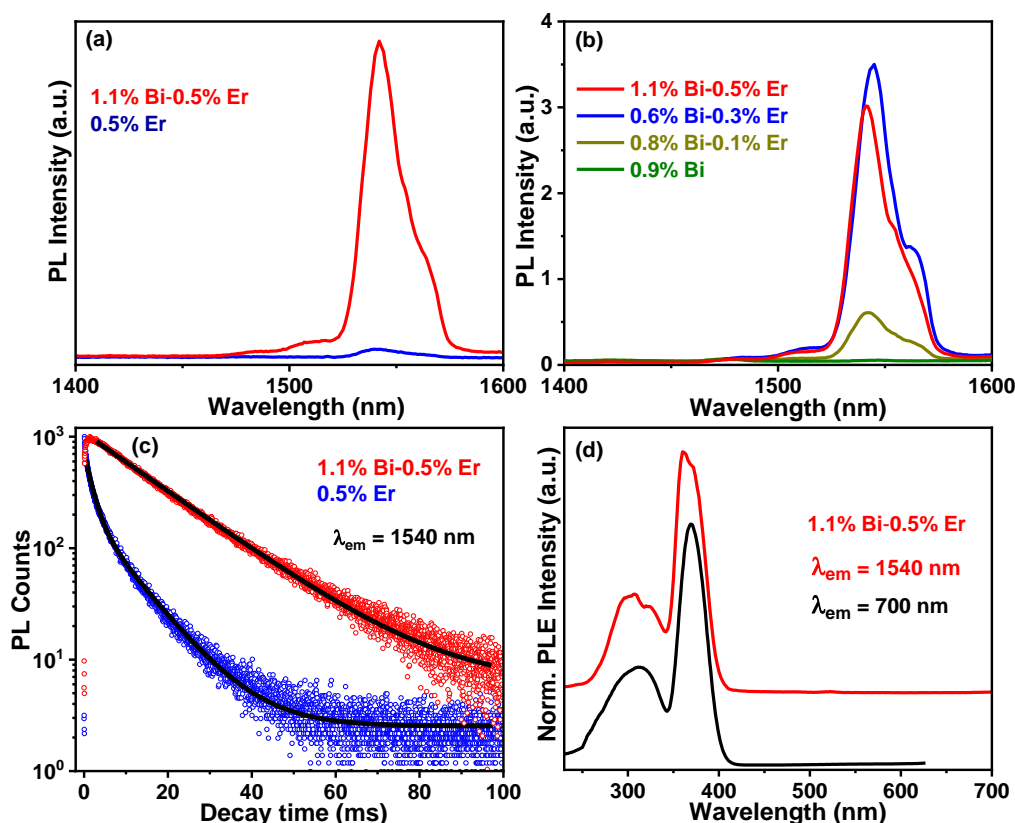
Figure 2.8: (a) SWIR PL spectra of 0.5% Er^{3+}-doped and 1.1% Bi^{3+}-0.5% Er^{3+} codoped Cs₂AgInCl₆ at 370 nm excitation. (b) PL spectra of Bi^{3+}-doped and Bi^{3+}-Er^{3+} codoped Cs₂AgInCl₆ microcrystals. (c) PL decay dynamics at 300 K for emission at 1540 nm arising from both Er^{3+} doped and Bi^{3+}-Er^{3+} codoped Cs₂AgInCl₆. Excitation was at 360 nm. (d) PL excitation (PLE) spectra of Bi^{3+}-Er^{3+} codoped Cs₂AgInCl₆ with emission wavelengths at visible (700 nm) and near infrared (1540) region. PLE spectra in (d) are shifted vertically for clarity in presentation.

More importantly, Figure 2.8a-b show the emission in SWIR region. Figure 2.8a shows SWIR emission at 1540 nm, owing to $^4I_{13/2} \rightarrow {}^4I_{15/2}$ transitions of Er^{3+} f-electron. The integrated intensity of this SWIR emission increases by ~45 times for Bi^{3+}-Er^{3+} codoped sample compared to only Er^{3+}-doped sample, after excitation with 370 nm light. Detailed methodologies to compare the PL intensity of these two samples are given in experimental section. Figure 2.8b shows that the intensity of the 1540 nm SWIR emission increases systematically with increasing the concentration of Er^{3+} in the Bi^{3+}-Er^{3+} codoped samples.

PL decay dynamics (Figure 2.8c) of Er^{3+} emission at 1540 nm for Er^{3+}-doped Cs₂AgInCl₆ show bi-exponential decay with two long lifetime components of 1.1 ms and 7.5 ms with 64% and 36% contributions respectively. Bi^{3+}-Er^{3+} codoped sample shows a single exponential decay with lifetime 16.4 ms. The long ms-scale lifetime is because of Laporte forbidden $^4I_{13/2} \rightarrow {}^4I_{15/2}$ transitions. It has been seen in prior literature that if lanthanide ions are well incorporated inside the crystals, then their f-electron emissions have longer ms scale lifetime.[43-44] Whereas, if lanthanides ions experience a non-crystalline surrounding, then the PL lifetimes decreases to microseconds. Therefore, the single exponential decay with lifetime of 16.4 ms for our Bi^{3+}-Er^{3+} codoped sample, is an indication of Er^{3+} doping into the host lattice. Compared to Er^{3+}-doped sample, Bi^{3+}-Er^{3+} codoped sample exhibit a longer PL decay along with enhanced PL intensity. These preliminary results suggest, Bi^{3+} probably improve the crystalline surrounding around the Er^{3+} ions reducing the trap states.[35] To the best our knowledge, this is the first report of ms scale PL lifetime from any Er^{3+} doped metal halide double perovskite systems. Note that the ms scale long lifetimes are desired for optical amplification. PL excitation (PLE) spectra (Figure 2.8d) corresponding to both broad visible light emission at 700 nm and the SWIR emission at 1540 nm for Bi^{3+}-Er^{3+} codoped Cs₂AgInCl₆ agree with absorption spectrum (Figure 2.6) of the sample. Particularly, the new absorption at 372 nm, obtained after Bi^{3+} codoping, efficiently results into the Er^{3+} emission at 1540 nm.

2.3.3 Temperature Dependent PL of 1.1% Bi³⁺-0.5% Er³⁺ Codoped Cs₂AgInCl₆

To understand the Er^{3+} SWIR emission better, we carried out PL measurements of Bi^{3+}-Er^{3+} codoped Cs₂AgInCl₆ at variable temperatures in the range 5.7 K to 300 K. Representative PL spectra in Figure 2.9 shows that at 300 K the PL spectrum shows multiple features with peaks at 1540 and 1555 nm along with a shoulder at around 1510 nm. Such multiple PL features arise due to crystal-field-split manifold of $^4I_{13/2}$ and $^4I_{15/2}$ states.[45-46] At lower temperatures, the PL

Bi³⁺-Er³⁺ and Bi³⁺-Yb³⁺ Codoped Cs₂AgInCl₆ Double Perovskite: Visible to Short-Wave Infrared Emitters
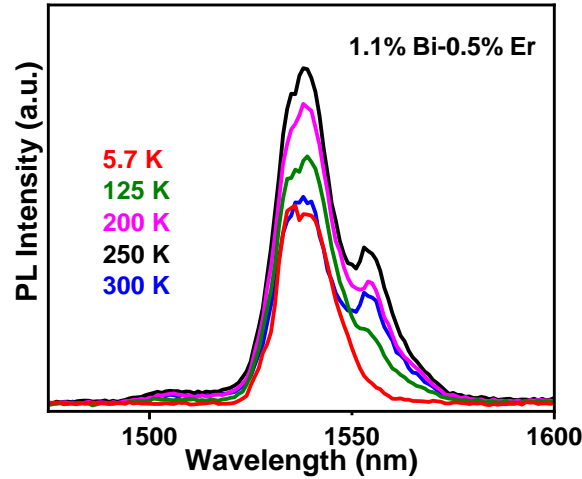
Figure 2.9: PL spectra of 1.1% Bi^{3+}-0.5% Er^{3+} codoped $Cs_2AgInCl_6$ measured at variable temperatures between 5.7 K to 300 K.

become more symmetric around 1538 nm peak. Intensity ratio of 1540 nm to 1555 nm (I_{1540}/I_{1555}) increases monotonically with decreasing temperature (Figure 2.10a). Similar temperature-dependent Er^{3+} emission was reported earlier from different Er^{3+}-doped hosts, [46] and was attributed to population redistribution among crystal-field-split manifolds at different temperatures.
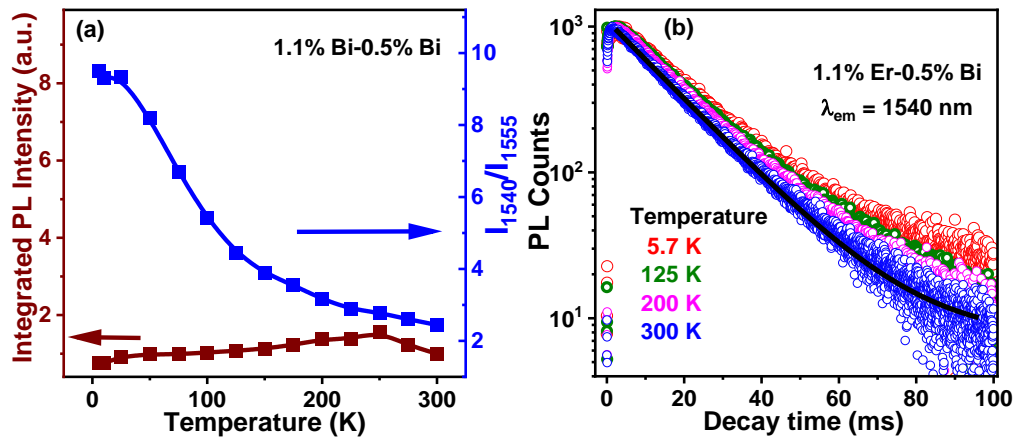
Figure 2.10: (a) Integrated PL intensity variation of 1.1% Bi^{3+}-0.5% Er^{3+} codoped $Cs_2AgInCl_6$ measured at variable temperatures between 5.7 K to 300 K. I_{1540} and I_{1555} in (a) are the peak intensities at 1540 nm and 1555 nm.

Interestingly, Figure 2.9 and 2.10a show that the integrated PL intensity does not change much throughout the temperature range of 5.7 K to 300 K, with maximum intensity at 250 K. Furthermore, Figure 2.10b shows that the PL lifetime of 1540 nm peak remains largely unchanged in the entire temperature range. This temperature-stable emission suggests that the 4*f* electrons of the Er^{3+} ions are well screened from surrounding defect sites, via the closed

$5s^2 5p^6$ outer shell electrons of Er^{3+}. Such temperature stability is again desired for practical applications.

2.3.4 Absorption and Emission Processes in Bi³⁺-Er³⁺ Codoped Cs₂AgInCl₆

Schematics in Figure 2.11 describe the process of optical absorption and emission in Bi^{3+}-Er^{3+} codoped $Cs_2AgInCl_6$. Bi^{3+}-codoping decreases the excitation energy to 350-400 nm range, which is suitable for excitation with commercial UV LED. The excitation energy is then transferred to states responsible for broad visible emission and Er^{3+} *f*-electrons. Er^{3+} *f*–electrons then de-excite via multiple transitions emitting light. Among them, the $^4I_{13/2} \rightarrow {}^4I_{15/2}$ transitions emitting 1540 nm light is technologically very relevant for low-loss optical fiber communication. Codoping of Bi^{3+} drastically enhances the intensity of this 1540 nm Er^{3+} emission. Bi^{3+} ions act as sensitizer for both the Er^{3+} SWIR emission and broad visible emission.
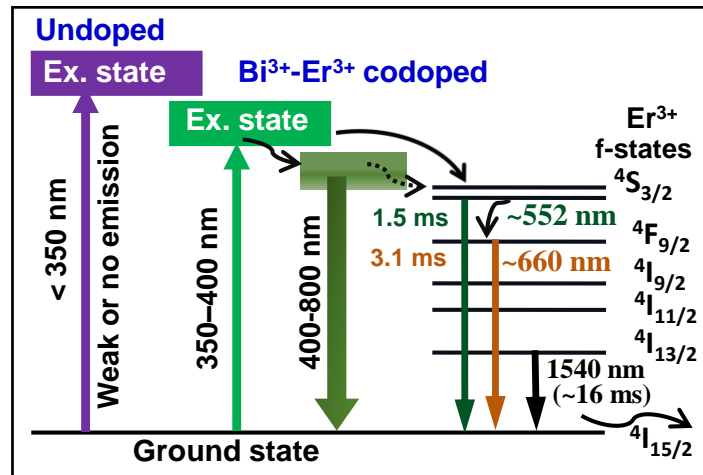
Figure 2.11: Schematics comparing optical absorption and emission processes in Bi^{3+}-Er^{3+} codoped $Cs_2AgInCl_6$ with that of undoped sample. Very weak or no emission is observed for undoped $Cs_2AgInCl_6$.

2.3.5 Phosphor Converted LED of 1.1% Bi³⁺-0.5% Er³⁺ Codoped Cs₂AgInCl₆

We have assembled a phosphor-converted LED of 1.1% Bi^{3+}-0.5% Er^{3+} codoped $Cs_2AgInCl_6$ by coating on commercial 370 nm LED chip (detail procedure is described in experimental section). UV LED chip strongly emit 370 nm UV light and has weak tail blue emission as shown in Figure 2.12a. On coating 1.1% Bi^{3+}-0.5% Er^{3+} codoped $Cs_2AgInCl_6$ on LED, LED emits bright warm white light which is visible in digital image (Figure 2.12b). To show that This LED also emit SWIR emission, SWIR emission spectra is recorded in fluorescence

spectrometer. Figure 2.12c show the emission spectrum in SWIR region with characteristic 1540 nm Er^{3+} emission.
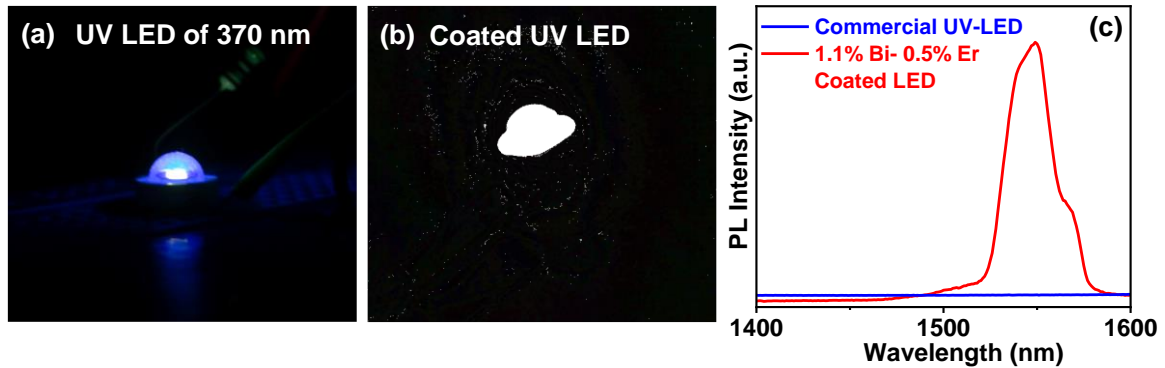
Figure 2.12: (a) Digital image of glowing 370 nm UV LED chip (b) Digital image of warm white light emitting 1.1% Bi^{3+}-0.5% Er^{3+} codoped $Cs_2AgInCl_6$ coated on 370 nm UV LED chip (c) SWIR Emission spectra of UV LED chip without coating and with 1.1% Bi^{3+}-0.5% Er^{3+} codoped $Cs_2AgInCl_6$ coating.

The combination of Bi^{3+}-Er^{3+} have been codoped earlier in metal oxide hosts like Gd_2O_3.[47] To the best of our knowledge, in metal halide perovskite, this is the first report of codoping Bi^{3+} and Ln^{3+} ions. Compared to oxides, metal halides are expected to provide better semiconducting properties. Furthermore, the synthesis of our Bi^{3+}-Ln^{3+} codoped $Cs_2AgInCl_6$ is very simple. These are moderate temperature (~80 °C) synthesis taking ~30 minute, unlike the typical high temperature (~1000 °C) solid state synthesis of oxides. To explore our codoping approach further, we have prepared Bi^{3+}-Yb^{3+} codoped $Cs_2AgInCl_6$. Details of synthesis and characterization are given in experimental section. Results suggest formation of phase-pure Bi^{3+}-Yb^{3+} codoped $Cs_2AgInCl_6$.

2.3.6 Optical Properties of Yb³⁺ Doped and Bi³⁺-Yb³⁺ Codoped Cs₂AgInCl₆

UV-visible absorption spectra of Bi^{3+}-Yb^{3+} codoped $Cs_2AgInCl_6$ in Figure 2.13a shows Bi^{3+} codoping gives rise to a new absorption peak at 372 nm, similar to the Bi^{3+}-Er^{3+} codoped samples. Bi^{3+}-Yb^{3+} codoped sample emit warm white light (Figure 2.13b) similar to Bi^{3+}-doped $Cs_2AgInCl_6$. The main difference between both series of samples arises in their SWIR emission. Figure 2.13c shows that both Yb^{3+}-doped and Bi^{3+}-Yb^{3+} codoped $Cs_2AgInCl_6$ exhibiting SWIR emission at 994 nm. The intensity of Yb^{3+} emission increases by ~27 times for the Bi^{3+}-Yb^{3+} codoped sample compared to the Yb^{3+} doped sample at 370 nm excitation wavelength. PL excitation spectrum for 990 nm emission is presented in Figure 2.13d. PL excitation spectrum matches with the absorption spectrum in Figure 2.13a, as well as with the

Bi³⁺-Er³⁺ and Bi³⁺-Yb³⁺ Codoped Cs₂AgInCl₆ Double Perovskite: Visible to Short-Wave Infrared Emitters
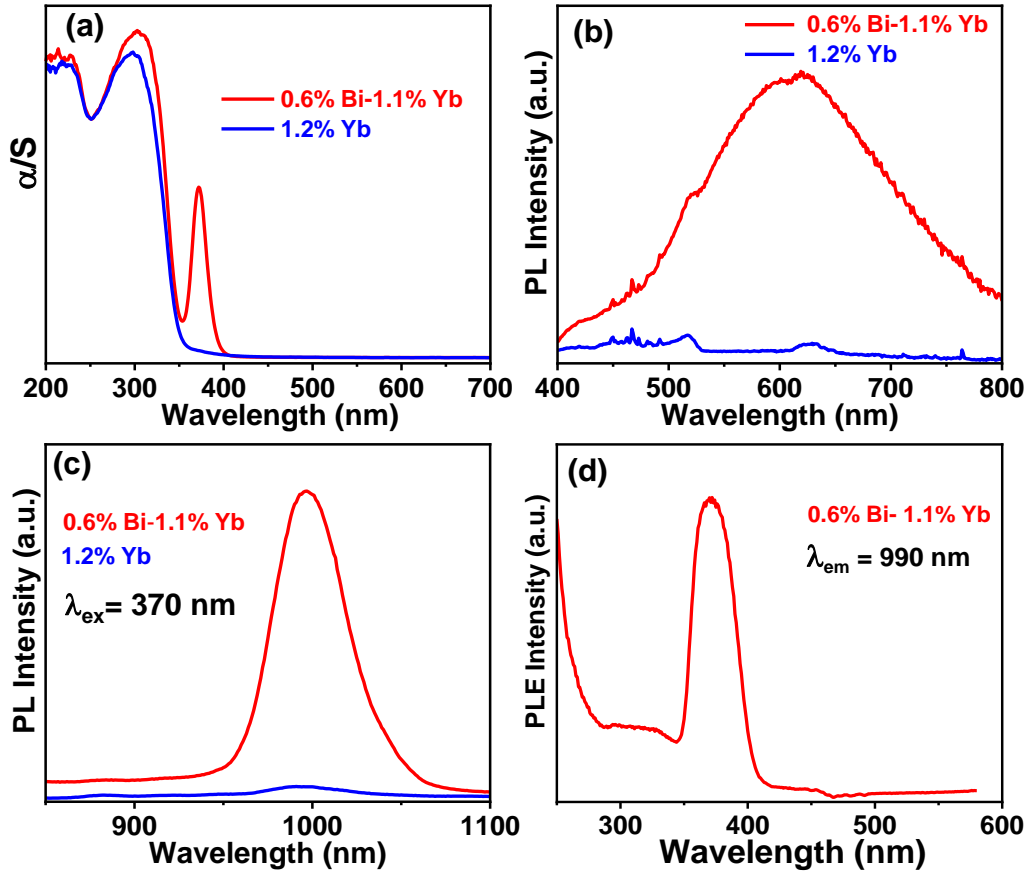
Figure 2.13: (a) UV-visible-near infrared absorption spectra of Yb^{3+}-doped and Bi^{3+}-Yb^{3+}codoped Cs₂AgInCl₆, obtained from the corresponding diffused reflectance spectra, by Kubelka-Munk transformation.[39] (b) PL spectra (c) SWIR spectra of Yb^{3+}-doped or Bi^{3+}-Yb^{3+} codoped Cs₂AgInCl₆ (d) PL excitation spectrum at 990 nm emission wavelength.

PL excitation spectrum of Bi^{3+}-Er^{3+} codoped Cs₂AgInCl₆ (Figure 2.8d). Therefore, Bi^{3+} codoping acts as sensitizers for both Er^{3+} and Yb^{3+} SWIR emission.
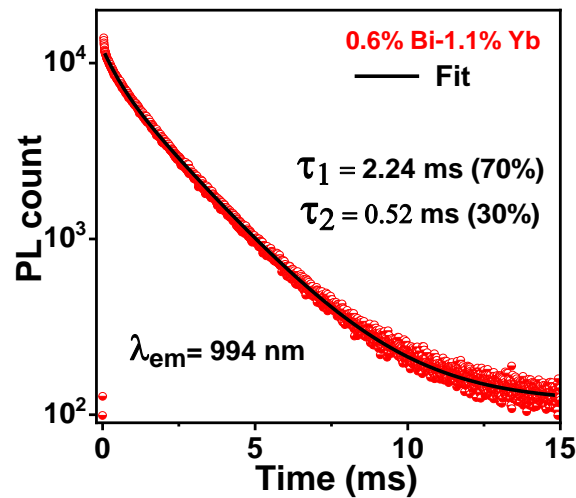
Figure 2.14: PL decay dynamics of Bi^{3+}-Yb^{3+} codoped Cs₂AgInCl₆ at 994 nm. The PL decay is fitted with bi-exponential function.

Bi³⁺-Er³⁺ and Bi³⁺-Yb³⁺ Codoped Cs₂AgInCl₆ Double Perovskite: Visible to Short-Wave Infrared Emitters

PL decay dynamics of the 994 nm emission is shown in Figure 2.14. PL decay is fitted with bi-exponential decay function. For 994 nm emission ms long PL lifetime is obtained, arising from Laporte forbidden $^2F_{5/2} \rightarrow {}^2F_{7/2}$ transitions of Yb^{3+} f-electrons.

2.3.7 Structural Stability and Emission Stability
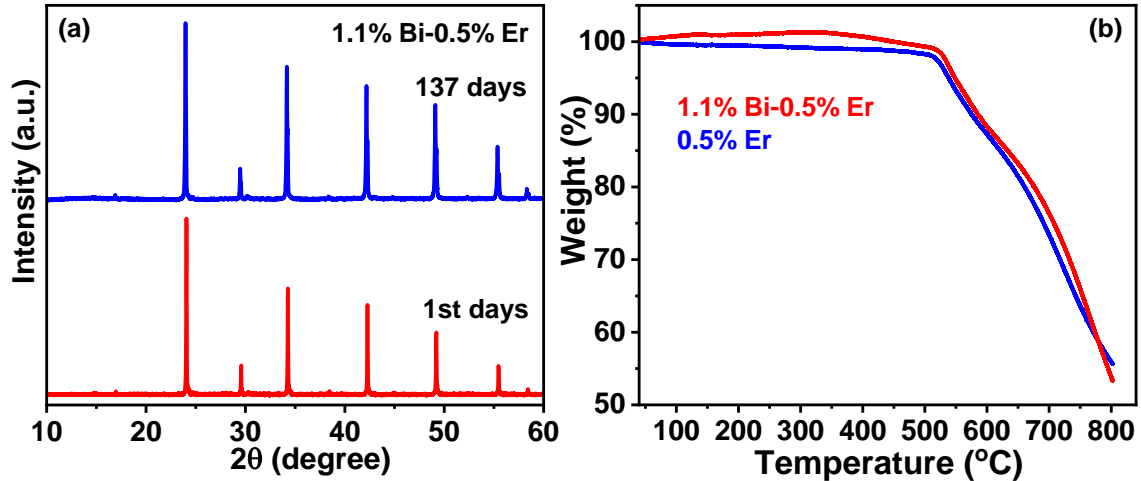
Figure 2.15: PXRD patterns of Bi^{3+}-Er^{3+} codoped $Cs_2AgInCl_6$ after storing it in ambient conditions. (b) Thermogravimetric analysis (TGA) data of Bi^{3+}-Er^{3+} codoped $Cs_2AgInCl_6$ and Er^{3+}-doped $Cs_2AgInCl_6$, measured under inert atmosphere.
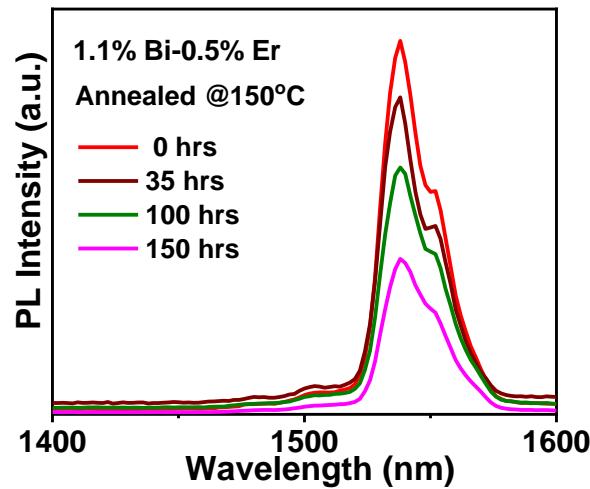
Figure 2.16: PL spectra of Bi^{3+}-Er^{3+} codoped $Cs_2AgInCl_6$ heated after drop casting the sample on a glass slide. The sample was heated using hot plate in ambient conditions for many hours. The sample retains its PL to good extent. But after a prolonged heating, black spots start to appear.

We have also studied he sample stability. In ambient conditions the powder sample is stable over many months (Figure 2.15a). Thermogravimetric analysis (TGA) data (Figure 2.15b) does not show any weight loss of Bi^{3+}-Er^{3+} codoped $Cs_2AgInCl_6$ up to 509 °C. The sample also

Chapter 2

Bi^{3+}-Er^{3+} and Bi^{3+}-Yb^{3+} Codoped Cs$_2$AgInCl$_6$ Double Perovskite: Visible to Short-Wave Infrared Emitters

retains a reasonably high fraction of its PL intensity after heating at 150 °C for about 150 h (Figure 2.16). After a prolonged heating at 150 °C or with continuous irradiation of UV light, some parts of the sample start to appear black.

2.4 Conclusion

In conclusion, we have prepared Bi^{3+}-Ln^{3+} (Ln = Er and Yb) codoped Cs$_2$AgInCl$_6$. The design of codoping system was based on our intention to modify both the optical absorption and emission spectra of the host. Bi^{3+} codoping gives rise to new absorption channel at 372 nm, which is suitable for excitation with commercial UV LEDs. The energy is then transferred to Er^{3+} and Yb^{3+} *f*-electrons, which de-excite by emitting light at 1540 and 994 nm respectively. Bi^{3+}-Er^{3+} and Bi^{3+}-Yb^{3+} codoped samples show ~45 and ~27 times more intense SWIR emission after excitation at 370 nm, compared to Er^{3+} doped and Yb^{3+} doped Cs$_2$AgInCl$_6$ samples, respectively. Such strategies imparting optical functionalities into metal halide double perovskites might lead future applications such as optical fiber communication, SWIR LEDs, and SWIR sensors.

2.5 References

1. Akkerman, Q. A.; Rainò, G.; Kovalenko, M. V.; Manna, L. Genesis, Challenges and Opportunities for Colloidal Lead Halide Perovskite Nanocrystals. *Nat. Mater.* **2018,** *17*, 394-405.

2. Chen, J.; Dong, C.; Idriss, H.; Mohammed, O. F.; Bakr, O. M. Metal Halide Perovskites for Solar-to-Chemical Fuel Conversion. *Adv. Energy Mater.* **2020**, *10*, 1902433.

3. Dutta, A.; Behera, R. K.; Pal, P.; Baitalik, S.; Pradhan, N. Near-Unity Photoluminescence Quantum Efficiency for All CsPbX^3 (X=Cl, Br, and I) Perovskite Nanocrystals: A Generic Synthesis Approach. *Angew. Chem. Int. Ed.* **2019,** *58*, 5552-5556.

4. Etgar, L.; Gao, P.; Xue, Z.; Peng, Q.; Chandiran, A. K.; Liu, B.; Nazeeruddin, M. K.; Grätzel, M. Mesoscopic CH$_3$NH$_3$PbI$_3$/TiO$_2$ Heterojunction Solar Cells. *J. Am. Chem. Soc.* **2012,** *134*, 17396-17399.

5. Kojima, A.; Teshima, K.; Shirai, Y.; Miyasaka, T. Organometal Halide Perovskites as Visible-Light Sensitizers for Photovoltaic Cells. *J. Am. Chem. Soc.* **2009,** *131*, 6050-6051.

6. Lee, M. M.; Teuscher, J.; Miyasaka, T.; Murakami, T. N.; Snaith, H. J. Efficient Hybrid Solar Cells Based on Meso-Superstructured Organometal Halide Perovskites. *Science* **2012,** *338*, 643-647.

Chapter 2

Bi^{3+}-Er^{3+} and Bi^{3+}-Yb^{3+} Codoped $Cs_2AgInCl_6$ Double Perovskite: Visible to Short-Wave Infrared Emitters

7. Manser, J. S.; Christians, J. A.; Kamat, P. V. Intriguing Optoelectronic Properties of Metal Halide Perovskites. *Chem. Rev.* **2016,** *116*, 12956-13008.

8. Swarnkar, A.; Chulliyil, R.; Ravi, V. K.; Irfanullah, M.; Chowdhury, A.; Nag, A. Colloidal $CsPbBr^3$ Perovskite Nanocrystals: Luminescence Beyond Traditional Quantum Dots. *Angew. Chem. Int. Ed.* **2015,** *54*, 15424-15428.

9. Tong, Y.; Fu, M.; Bladt, E.; Huang, H.; Richter, A. F.; Wang, K.; Müller-Buschbaum, P.; Bals, S.; Tamarat, P.; Lounis, B.; Feldmann, J.; Polavarapu, L. Chemical Cutting of Perovskite Nanowires into Single-Photon Emissive Low-Aspect-Ratio $CsPbX_3$ (X=Cl, Br, I) Nanorods. *Angew. Chem. Int. Ed.* **2018,** *57*, 16094-16098.

10. Pan, G.; Bai, X.; Yang, D.; Chen, X.; Jing, P.; Qu, S.; Zhang, L.; Zhou, D.; Zhu, J.; Xu, W.; Dong, B.; Song, H. Doping Lanthanide into Perovskite Nanocrystals: Highly Improved and Expanded Optical Properties. *Nano Lett.* **2017,** *17*, 8005-8011.

11. Zhou, D.; Liu, D.; Pan, G.; Chen, X.; Li, D.; Xu, W.; Bai, X.; Song, H. Cerium and Ytterbium Codoped Halide Perovskite Quantum Dots: A Novel and Efficient Downconverter for Improving the Performance of Silicon Solar Cells. *Adv. Mater.* **2017,** *29*, 1704149.

12. Milstein, T. J.; Kroupa, D. M.; Gamelin, D. R. Picosecond Quantum Cutting Generates Photoluminescence Quantum Yields Over 100% in Ytterbium-Doped $CsPbCl_3$ Nanocrystals. *Nano Lett.* **2018,** *18*, 3792-3799.

13. Luo, X.; Ding, T.; Liu, X.; Liu, Y.; Wu, K. Quantum-Cutting Luminescent Solar Concentrators Using Ytterbium-Doped Perovskite Nanocrystals. *Nano Lett.* **2019,** *19*, 338-341.

14. Mir, W. J.; Mahor, Y.; Lohar, A.; Jagadeeswararao, M.; Das, S.; Mahamuni, S.; Nag, A. Postsynthesis Doping of Mn and Yb into $CsPbX_3$ (X = Cl, Br, or I) Perovskite Nanocrystals for Downconversion Emission. *Chem. Mater.* **2018,** *30*, 8170-8178.

15. Mir, W. J.; Sheikh, T.; Arfin, H.; Xia, Z. G.; Nag, A. Lanthanide Doping in Metal Halide Perovskite Nanocrystals: Spectral Shifting, Quantum Cutting and Optoelectronic Applications. *NPG Asia Mater.* **2020,** *12*, 9.

16. Stoumpos, C. C.; Frazer, L.; Clark, D. J.; Kim, Y. S.; Rhim, S. H.; Freeman, A. J.; Ketterson, J. B.; Jang, J. I.; Kanatzidis, M. G. Hybrid Germanium Iodide Perovskite Semiconductors: Active Lone Pairs, Structural Distortions, Direct and Indirect Energy Gaps, and Strong Nonlinear Optical Properties. *J. Am. Chem. Soc.* **2015,** *137*, 6804-6819.

17. Pal, J.; Manna, S.; Mondal, A.; Das, S.; Adarsh, K. V.; Nag, A. Colloidal Synthesis and Photophysics of $M_3Sb_2I_9$ (M=Cs and Rb) Nanocrystals: Lead-Free Perovskites. *Angew. Chem. Int. Ed.* **2017,** *56*, 14187-14191.

Chapter 2

Bi^{3+}-Er^{3+} and Bi^{3+}-Yb^{3+} Codoped $Cs_2AgInCl_6$ Double Perovskite: Visible to Short-Wave Infrared Emitters

18. Benin, B. M.; Dirin, D. N.; Morad, V.; Wörle, M.; Yakunin, S.; Rainò, G.; Nazarenko, O.; Fischer, M.; Infante, I.; Kovalenko, M. V. Highly Emissive Self-Trapped Excitons in Fully Inorganic Zero-Dimensional Tin Halides. *Angew. Chem. Int. Ed.* **2018,** *57*, 11329-11333.

19. Ning, W.; Gao, F. Structural and Functional Diversity in Lead-Free Halide Perovskite Materials. *Adv. Mater.* **2019,** *31*, 1900326.

20. Zhou, L.; Liao, J.-F.; Huang, Z.-G.; Wei, J.-H.; Wang, X.-D.; Li, W.-G.; Chen, H.-Y.; Kuang, D.-B.; Su, C.-Y. A Highly Red-Emissive Lead-Free Indium-Based Perovskite Single Crystal for Sensitive Water Detection. *Angew. Chem. Int. Ed.* **2019,** *58*, 5277-5281.

21. Slavney, A. H.; Hu, T.; Lindenberg, A. M.; Karunadasa, H. I. A Bismuth-Halide Double Perovskite with Long Carrier Recombination Lifetime for Photovoltaic Applications. *J. Am. Chem. Soc.* **2016,** *138*, 2138-41.

22. Meng, W.; Wang, X.; Xiao, Z.; Wang, J.; Mitzi, D. B.; Yan, Y. Parity-Forbidden Transitions and Their Impact on the Optical Absorption Properties of Lead-Free Metal Halide Perovskites and Double Perovskites. *J. Phys. Chem. Lett.* **2017,** *8* (13), 2999-3007.

23. Volonakis, G.; Haghighirad, A. A.; Milot, R. L.; Sio, W. H.; Filip, M. R.; Wenger, B.; Johnston, M. B.; Herz, L. M.; Snaith, H. J.; Giustino, F. $Cs_2InAgCl_6$: A New Lead-Free Halide Double Perovskite with Direct Band Gap. *J. Phys. Chem. Lett.* **2017,** *8*, 772-778.

24. Connor, B. A.; Leppert, L.; Smith, M. D.; Neaton, J. B.; Karunadasa, H. I. Layered Halide Double Perovskites: Dimensional Reduction of $Cs_2AgBiBr_6$. *J. Am. Chem. Soc.* **2018,** *140*, 5235-5240.

25. Luo, J.; Li, S.; Wu, H.; Zhou, Y.; Li, Y.; Liu, J.; Li, J.; Li, K.; Yi, F.; Niu, G.; Tang, J. $Cs_2AgInCl_6$ Double Perovskite Single Crystals: Parity Forbidden Transitions and Their Application For Sensitive and Fast UV Photodetectors. *ACS Photonics* **2018,** *5*, 398-405.

26. Yang, B.; Mao, X.; Hong, F.; Meng, W.; Tang, Y.; Xia, X.; Yang, S.; Deng, W.; Han, K. Lead-Free Direct Band Gap Double-Perovskite Nanocrystals with Bright Dual-Color Emission. *J. Am. Chem. Soc.* **2018,** *140*, 17001-17006.

27. Igbari, F.; Wang, Z.-K.; Liao, L.-S. Progress of Lead-Free Halide Double Perovskites. *Adv. Energy Mater.* **2019,** *9*, 1803150.

28. Zhou, J.; Rong, X.; Zhang, P.; Molokeev, M. S.; Wei, P.; Liu, Q.; Zhang, X.; Xia, Z. Manipulation of Bi^{3+}/In^{3+} Transmutation and Mn^{2+}-Doping Effect on the Structure and Optical Properties of Double Perovskite $Cs_2NaBi_{1-x}In_xCl_6$. *Adv Opt Mater* **2019,** *7*, 1801435.

29. Kshirsagar, A. S.; Nag, A. Synthesis and Optical Properties of Colloidal $Cs_2AgSb_{1-x}Bi_xCl_6$ Double Perovskite Nanocrystals. *J. Chem. Phys.* **2019,** *151*, 161101.

30. K, N. N.; Nag, A. Synthesis and Luminescence of Mn-doped $Cs_2AgInCl_6$ Double Perovskites. *Chem. Commun.* **2018,** *54*, 5205-5208.

31. Locardi, F.; Cirignano, M.; Baranov, D.; Dang, Z.; Prato, M.; Drago, F.; Ferretti, M.; Pinchetti, V.; Fanciulli, M.; Brovelli, S.; De Trizio, L.; Manna, L. Colloidal Synthesis of Double Perovskite $Cs_2AgInCl_6$ and Mn-Doped $Cs_2AgInCl_6$ Nanocrystals. *J. Am. Chem. Soc.* **2018,** *140*, 12989-12995.

32. Lee, W.; Hong, S.; Kim, S. Colloidal Synthesis of Lead-Free Silver–Indium Double-Perovskite $Cs_2AgInCl_6$ Nanocrystals and Their Doping with Lanthanide Ions. *J. Phys. Chem. C* **2019,** *123*, 2665-2672.

33. Mahor, Y.; Mir, W. J.; Nag, A. Synthesis and Near-Infrared Emission of Yb-Doped $Cs_2AgInCl_6$ Double Perovskite Microcrystals and Nanocrystals. *J. Phys. Chem. C* **2019,** *123*, 15787-15793.

34. Chen, N.; Cai, T.; Li, W.; Hills-Kimball, K.; Yang, H.; Que, M.; Nagaoka, Y.; Liu, Z.; Yang, D.; Dong, A.; Xu, C.-Y.; Zia, R.; Chen, O. Yb- and Mn-Doped Lead-Free Double Perovskite Cs_2AgBiX_6 (X = Cl^-, Br^-) Nanocrystals. *ACS Appl. Mater. Interfaces* **2019,** *11*, 16855-16863.

35. Luo, J.; Wang, X.; Li, S.; Liu, J.; Guo, Y.; Niu, G.; Yao, L.; Fu, Y.; Gao, L.; Dong, Q.; Zhao, C.; Leng, M.; Ma, F.; Liang, W.; Wang, L.; Jin, S.; Han, J.; Zhang, L.; Etheridge, J.; Wang, J.; Yan, Y.; Sargent, E. H.; Tang, J. Efficient and Stable Emission of Warm-White Light from Lead-Free Halide Double Perovskites. *Nature* **2018,** *563*, 541-545.

36. Liu, Y.; Jing, Y.; Zhao, J.; Liu, Q.; Xia, Z. Design Optimization of Lead-Free Perovskite $Cs_2AgInCl_6$:Bi Nanocrystals with 11.4% Photoluminescence Quantum Yield. *Chem. Mater.* **2019,** *31*, 3333-3339.

37. Locardi, F.; Sartori, E.; Buha, J.; Zito, J.; Prato, M.; Pinchetti, V.; Zaffalon, M. L.; Ferretti, M.; Brovelli, S.; Infante, I.; De Trizio, L.; Manna, L. Emissive Bi-Doped Double Perovskite $Cs_2Ag_{1-x}Na_xInCl_6$ Nanocrystals. *Acs Energy Lett.* **2019,** *4*, 1976-1982.

38. Eickhoff, T.; Grosse, P.; Theiss, W. Diffuse reflectance spectroscopy of powders. *Vibrational Spectroscopy* **1990,** *1* (2), 229-233.

39. Kortüm, G. *Reflectance Spectroscopy*. Springer: New York: **1969**.

40. Zhou, J.; Xia, Z.; Molokeev, M. S.; Zhang, X.; Peng, D.; Liu, Q. Composition Design, Optical Gap and Stability Investigations of Lead-Free Halide Double Perovskite $Cs_2AgInCl_6$. *J. Mater. Chem. A* **2017,** *5*, 15031-15037.

41. Tan, Z.; Li, J.; Zhang, C.; Li, Z.; Hu, Q.; Xiao, Z.; Kamiya, T.; Hosono, H.; Niu, G.; Lifshitz, E.; Cheng, Y.; Tang, J. Highly Efficient Blue-Emitting Bi-Doped Cs_2SnCl_6 Perovskite Variant: Photoluminescence Induced by Impurity Doping. *Adv. Funct. Mater.* **2018,** *28,* 1801131.

42. Venkatramu, V.; León-Luis, S. F.; Rodríguez-Mendoza, U. R.; Monteseguro, V.; Manjón, F. J.; Lozano-Gorrín, A. D.; Valiente, R.; Navarro-Urrios, D.; Jayasankar, C. K.; Muñoz, A.; Lavín, V., Synthesis, Structure and Luminescence of Er^{3+}-doped $Y_3Ga_5O_{12}$ Nano-Garnets. *J. Mater. Chem.* **2012,** *22* (27), 13788-13799.

43. Lin, H.; Jiang, S.; Wu, J.; Song, F.; Peyghambarian, N.; Pun, E. Y. B., Er3 doped Na2O Nb2O5 TeO2glasses for optical waveguide laser and amplifier. *Journal of Physics D: Applied Physics* **2003,** *36* (7), 812-817.

44. Martín-Rodríguez, R.; Geitenbeek, R.; Meijerink, A., Incorporation and Luminescence of Yb3+ in CdSe Nanocrystals. *J. Am. Chem. Soc.* **2013,** *135* (37), 13668-13671.

45. Przybylinska, H.; Jantsch, W.; Suprun-Belevitch, Y.; Stepikhova, M.; Palmetshofer, L.; Hendorfer, G.; Kozanecki, A.; Wilson, R. J.; Sealy, B. J. Optically Active Erbium Centers in Silicon. *Phys. Rev. B* **1996,** *54*, 2532-2547.

46. Ivanova, Z. G.; Aneva, Z.; Ganesan, R.; Tonchev, D.; Gopal, E. S. R.; Rao, K. S. R. K.; Allen, T. W.; DeCorby, R. G.; Kasap, S. O. Low-Temperature Er^{3+} Emission in Ge–S–Ga Glasses Excited by Host Absorption. *J. Non-Cryst.* **2007,** *353*, 1418-1421.

47. Xu, Q.; Lin, B.; Mao, Y. Photoluminescence Characteristics of Energy Transfer Between Er^{3+} and Bi^{3+} in Gd_2O_3: Er^{3+}, Bi^{3+}. *J. Lumin.* **2008,** *128*, 1965-1968.

Chapter 3

Short Wave Infrared Emissions from Te^{4+}-Ln^{3+} (Ln: Er, Yb) Codoped $Cs_2NaInCl_6$ Double Perovskites

Declaration:

Short Wave Infrared Emissions from Te^{4+}-Ln^{3+} (Ln: Er, Yb) Codoped Cs$_2$NaInCl$_6$ Double Perovskites

Abstract

Cs$_2$NaInCl$_6$ double perovskite is environmentally benign and its wide band gap (~5.1 eV) makes it photo-inactive and photo-stable in the ultraviolet, visible, and short-wave infrared (SWIR) region. Interestingly, the octahedrally coordinated In^{3+} lattice site is suitable for doping lanthanide ions like Er^{3+} and Yb^{3+}, that can emit SWIR radiation at 1540 nm (0.81 eV) and 994 nm (1.247 eV), respectively. But the optical excitation of lanthanides is Laporte forbidden, and the host require excitation energy > 5.1 eV. The large Stokes shift for the excitation and SWIR emission reduces the power conversion efficiency. Here, we codoped Te^{4+} with Er^{3+} or Yb^{3+} into Cs$_2$NaInCl$_6$. The Te^{4+} absorbs at the sub-band gap level around 3.1 eV (400 nm), because of $5s^2 \rightarrow 5s^15p^1$ electronic transitions. Then the excited Te^{4+} transfers its energy non-radiatively to Er^{3+} or Yb^{3+} codopant. The de-excitation of Er^{3+} or Yb^{3+} through *f-f* electronic transitions emit SWIR radiation at 1540 and 994 nm, respectively, along with weak visible light emissions. Temperature (8 – 300 K) dependent photoluminescence excitation, emission, and lifetime measurements reveal the mechanism of these energy transfer processes. Finally, we fabricated a simple phosphor converted light emitting diode (pc-LED) emitting SWIR radiation.

Graphical Abstract

*Short Wave Infrared Emissions from Te^{4+}-Ln^{3+} (Ln: Er, Yb) Codoped $Cs_2NaInCl_6$
Double Perovskites*
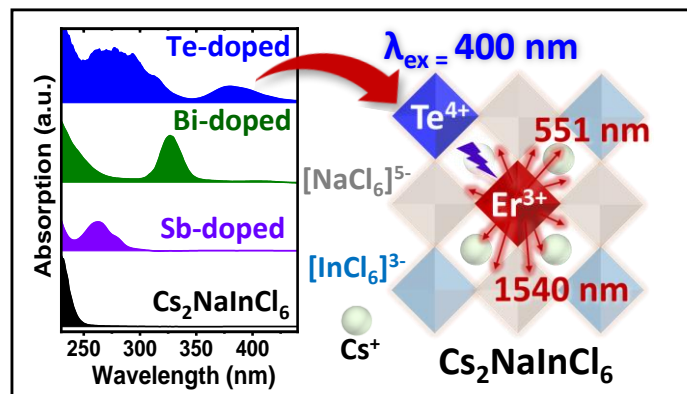
3.1 Introduction

Halide double perovskites like $Cs_2NaInCl_6$ is environmentally benign with a wide band gap of ~5.1 eV (243 nm).[1-2] Because of the wide band gap, $Cs_2NaInCl_6$ does not interact with most part of UV-visible radiation, making them photo-stable. Importantly, ions like In^{3+} has an octahedral coordination, and therefore, big lanthanide ions can be doped in $Cs_2NaInCl_6$.[3-5] Lanthanide ions like Er^{3+} and Yb^{3+} can emit short-wave infrared (SWIR) radiations,[6] that are important for optical fiber communication, security cameras, food processing and storing, bio-imaging and so on.[7-12] This SWIR radiations are due to *f-f* electronic transitions of the lanthanide ions. But the optical excitation of the same *f*-electrons is Laporte forbidden.[13] One solution to this problem is to codope lanthanides with another dopant that can absorb light. Here we codoped Te^{4+} and Ln^{3+} (Ln = Er, Yb) into $Cs_2NaInCl_6$.
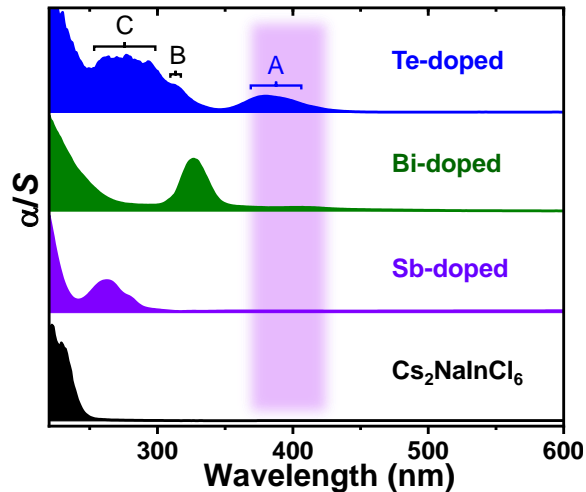
Figure 3.1: UV-visible absorbance spectra of undoped, Sb^{3+}-doped, Bi^{3+}-doped and Te^{4+}-doped $Cs_2NaInCl_6$. Absorption is recorded by diffuse reflectance spectroscopy and absorbance spectra are calculated using Kubelka-Munk transformation[14] of diffuse reflectance data. Where α is absorption coefficient and *S* is scattering factor. Lavender colored highlighted part shows the overlap of emission from commercially available 398 nm LED chip, with the absorption of different doped samples.

Similar strategies of Sb^{3+}-Ln^{3+} and Bi^{3+}-Ln^{3+} codoping in metal halide double perovskites have been reported earlier.[15-19] The Sb^{3+} and Bi^{3+} ions have two electrons in the outer most *s*-orbital (ns^2), and can absorb UV lights owing to $ns^2 \rightarrow ns^1np^1$ transitions.[20-28] As shown in Figure 3.1, Sb^{3+} and Bi^{3+} doping in $Cs_2NaInCl_6$ introduce new absorption peaks at 263 (weak absorption at 335 nm as well) and 327 nm respectively, below the band gap of the host.[29-31] This sub-band gap level absorptions reduces the input excitation energy of Sb^{3+} and Bi^{3+} doped $Cs_2NaInCl_6$ by 1.4 and 1.3 eV, respectively, compared to the host band gap. Also, the host does not get

excited in the optical excitation process, increasing its photo-stability. But still in a system like Sb^{3+}-Er^{3+} codoped Cs$_2$NaInCl$_6$, the energy difference between Sb^{3+} absorption and SWIR Er^{3+} emission is large (2.9 eV), causing huge non-radiative loss of the input energy. Therefore, it still remains an important material design challenge to reduce the Stokes shift between the excitation (in UV range) and the SWIR emission, in order to improve the power conversion efficiency of such SWIR emitters. This issue has motivated us to explore Te^{4+}-Ln^{3+}-codoped Cs$_2$NaInCl$_6$ double perovskites, since Te^{4+} are known to show $ns^2 \rightarrow ns^1np^1$ transitions, perhaps, at a lower energy compared to both Bi^{3+} and Sb^{3+}, as shown in Figure 3.1.

3.2 Experimental Section

3.2.1 Chemicals

Cesium chloride (CsCl, 99.9%), indium (III) chloride (InCl$_3$, anhydrous powder, ≥99.999%), sodium chloride (NaCl, 99.999%), erbium chloride hexahydrate (ErCl$_3$.6H$_2$O, 99.995%), ytterbium chloride hexahydrate (YbCl$_3$.6H$_2$O, 99.9%), tellurium chloride (TeCl$_4$, 99%) hydrochloric acid (HCl, 37 %) are purchased from Sigma Aldrich Chemicals. Isopropanol (≥ 99.80%) is purchased from Rankem. All the chemicals are used without any further purification.

3.2.2 Synthesis of Cs$_2$NaInCl$_6$

Cs$_2$NaInCl$_6$ microcrystals are synthesized by modifying the hydrothermal synthesis method reported by Zeng et al.[32] In a typical synthesis, 2 mmol CsCl, 1 mmol NaCl and 1 mmol InCl$_3$ are taken in a 25 mL teflon autoclave with 10 mL HCl. The hydrothermal autoclave is heated to 180 °C for 12 h. Then it is allowed to cool down to room temperature naturally. The obtained crystals are washed with isopropanol, dried in vacuum and stored in a glass vial under ambient conditions for further characterization.

3.2.3 Synthesis of Te^{4+} Doped Cs$_2$NaInCl$_6$

The synthesis methodology for Te^{4+}-doped Cs$_2$NaInCl$_6$ is very similar to that of the undoped Cs$_2$NaInCl$_6$. In addition to other precursors, 0.5% of TeCl$_4$ (mol %, with respect to InCl$_3$) is added.

3.2.4 Synthesis of Er^{3+} Doped and Te^{4+}-Er^{3+} Codoped Cs$_2$NaInCl$_6$

The Er^{3+} -doped and series of Te^{4+} -Er^{3+} codoped Cs$_2$NaInCl$_6$ are also prepared following the similar synthesis protocol that of undoped Cs$_2$NaInCl$_6$. In addition to other precursors, TeCl$_4$ and ErCl$_3$.6H$_2$O

precursors are added. The Te^{4+}-Er^{3+} codopants are optimized by using different amount of precursor concentrations, as tabulated in Table 3.1.

3.2.5 Synthesis Te^{4+}-Yb^{3+} Codoped Cs$_2$NaInCl$_6$

The Te^{4+}-Yb^{3+} codoped Cs$_2$NaInCl$_6$ are prepared by following the similar synthesis protocol that of undoped Cs$_2$NaInCl$_6$. In addition to other precursors, TeCl$_4$ and YbCl$_3$.6H$_2$O precursors are added as tabulated in Table 3.1.

3.2.6 Phosphor Converted LED (pc-LED) Fabrication: 10 mg of poly(methyl methacrylate) and 90 mg of 1.7% Te^{4+}- 5.9% Er^{3+} codoped compound are mixed with 100 μL toluene in a vial and stirred at 70 °C. After 20 min of stirring, a slurry is obtained. Which is then coated on a 398 nm LED chip. The coated LED is dried under IR lamp in vacuum. The pc-LED is placed inside the Edinburgh FLS980 spectrometer for the emission spectra measurement while the power is supplied by a Keithley 2450 source meter.

3.2.7 Characterization

Powder X-ray diffraction (PXRD) patterns are recorded using a Bruker D8 Advance X-ray diffraction machine equipped with Cu Kα (1.54 Å) radiation. A Zeiss Ultra Plus instrument is used for field emission scanning electron microscopy (FESEM) imaging and energy dispersive X-ray spectroscopy (EDS). The obtained results from EDS elemental analysis support the stoichiometric ratio of Cs, Na, In and Cl with Cs$_2$NaInCl$_6$ composition. Elemental analysis by employing inductively coupled plasma mass spectroscopy (ICP−MS) using a quadrupole-ICP−MS (Thermo iCAP-Q) spectrometer provided estimation of dopant concentrations.

3.2.8 Extended X-ray Absorption Fine Structure (EXAFS) Measurement

EXAFS measurements are performed at Deutsches Elektronen-Synchrotron (DESY), Petra III P64 beamline at Hamburg, Germany.[33] Measurements of In K edge, Te K edge and Er L$_3$ edge at ambient atmosphere are performed in fluorescence mode. Due to the small dopant percentage, the pellets are made of pure samples without adding boron nitride. The EXAFS data are processed using Athena software, which is a part of the Demeter 0.9.26 software suite[34], following the standard background subtraction procedure. We have carried out the fitting of the EXAFS data using Artemis software in the radial (R) space.

3.2.9 Optical Properties

Diffused reflectance spectra of microcrystalline powders in the UV−visible−NIR region are recorded using a Shimadzu UV-3600 plus UV−Vis−NIR spectrophotometer. Then Kubelka-Munk

transformation is used for the analysis of diffuse reflectance spectra. It relates the reflectance data with absorption coefficient as shown in equation (1):

$$F(R) = \alpha/S = (1-R)^2/2R \qquad (1)$$

where F(R) is the Kubelka-Munk function, R is reflectance, α is absorption coefficient and S is the scattering factor.[14] For photoluminescence (PL) measurements, powder samples are taken in a holder having a groove of fix dimension to insure that the sample amount remains similar in all measurements. Steady-state PL, PL Excitation (PLE), and PL decay dynamics (time-correlated single photon counting) are measured using Edinburgh FLS980 Instrument. The samples are excited by xenon lamp for steady state PL and PLE measurements, unless otherwise mentioned. A microsecond flash lamp is used for excitation to monitor the PL decay dynamics in millisecond (ms) range. Temperature dependent PL, PLE and PL decay dynamics are studied in the same Edinburgh FLS980 Instrument coupled with a cryostat. The powder samples are placed between two sapphire substrates and fix in a gold coated copper sample holder. The sample holder is fixed in a closed cycle He cryostat (Advanced Research Systems) attached with Lake Shore 335 temperature controller to achieve the desired temperatures in the range of 8 - 300 K. Experimental PL decay profiles are fitted with exponential decay functions shown in equations (2):

$$I_t = I_0 + \sum_{i=1}^{2} A_i e^{-\frac{t}{\tau_i}} \qquad (2)$$

Where, I_t is the PL counts at any time t, I_0 is the offset, and τ_i is the PL lifetime with contribution A_i.

3.3 Results and Discussion

3.3.1 Synthesis and Characterization

We have prepared undoped, Te^{4+}-doped, Er^{3+}-doped and Te^{4+}-Er^{3+} codoped Cs$_2$NaInCl$_6$ using hydrothermal reactions. FESEM images in Figure 3.2 show all four kinds of samples have octahedron morphology, similar to a prior report[18] of Cs$_2$NaInCl$_6$. The crystals are 100-300 µm in size. Figure 3.3 show EDS elemental mapping of 3.6% Te^{4+}-doped Cs$_2$NaInCl$_6$. Homogenous distribution of all the ions including Te^{4+} dopant is observed throughout the crystal. Figure 3.4 show EDS elemental mapping of 1.7% Te^{4+}- 5.9% Er^{3+} codoped Cs$_2$NaInCl$_6$ crystal. Homogenous distribution of all the ions throughout the crystals is observed, suggesting the desired Te^{4+}-doping or Te^{4+}-Er^{3+} codoping in the respective crystals.

Short Wave Infrared Emissions from Te^{4+}-Ln^{3+} (Ln: Er, Yb) Codoped $Cs_2NaInCl_6$ Double Perovskites
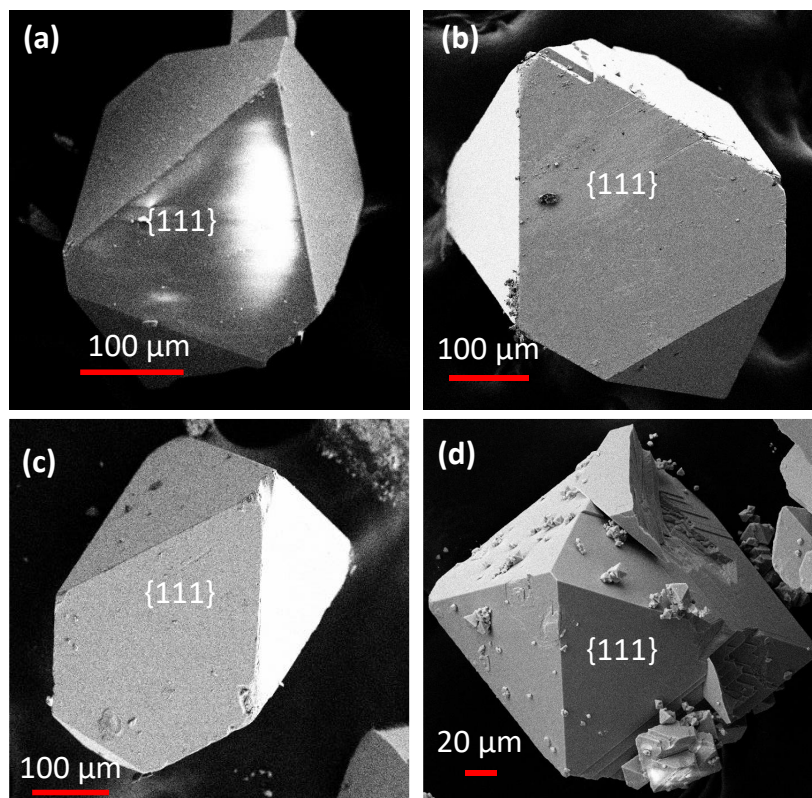
Figure 3.2: FESEM images of (a) undoped, (b) 3.6% Te^{4+}-doped, (c) 6.7% Er^{3+}-doped, and (d) 1.7% Te^{4+}-5.9% Er^{3+} codoped $Cs_2NaInCl_6$. Nearly octahedron morphology with dominant {111} facets is observed.
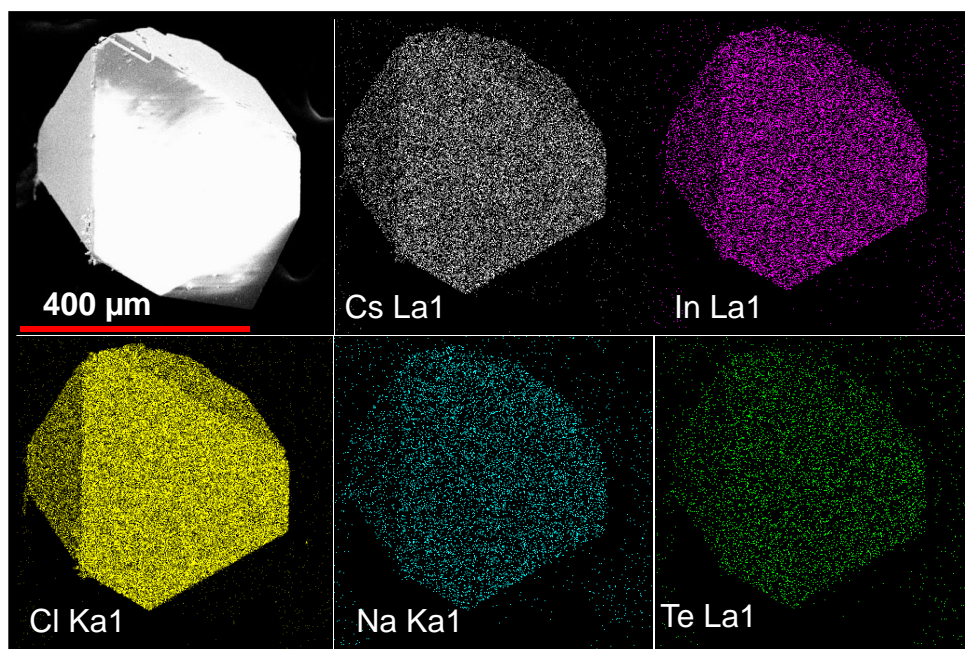
Figure 3.3: EDS elemental mapping of 3.6% Te^{4+}-doped $Cs_2NaInCl_6$.

Short Wave Infrared Emissions from Te^{4+}-Ln^{3+} (Ln: Er, Yb) Codoped Cs$_2$NaInCl$_6$ Double Perovskites
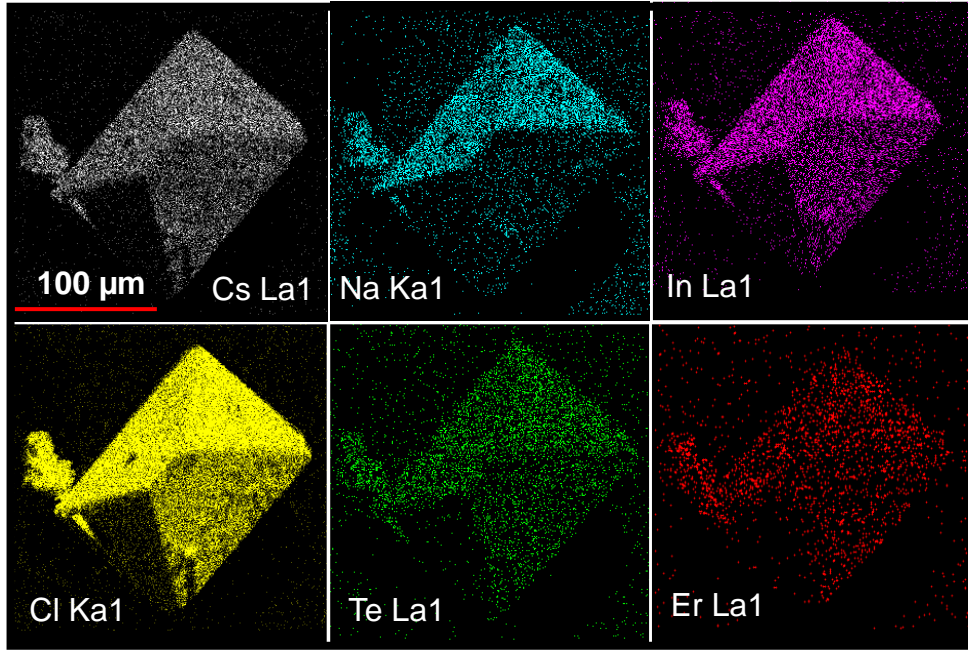
Figure 3.4: EDS elemental mapping of 1.7% Te^{4+}- 5.9% Er^{3+} codoped Cs$_2$NaInCl$_6$.

Table 3.1: EDS data of undoped, 3.6% Te^{4+}-doped, 6.7% Er^{3+}-doped and Te^{4+}-Er^{3+} codoped Cs$_2$NaInCl$_6$.

Sr. No.	Molar ratio of elements in the precursor Cs: Na: In: Cl: Te: Er	Atomic ratio of elements in the product (from EDS) [#] Cs: Na: In: Cl	Sample code
1.	2.00: 1.00: 1.00: x*: 0.00: 0.00	1.93: 0.98: 1.02: 6.13	undoped
2.	2.00: 1.00: 1.00: x*: 0.005: 0.00	1.88: 1.10: 0.96: 6.06	3.6% Te^{4+}-doped
3.	2.00: 1.00: 1.00: x*: 0.00: 1.00	1.86: 0.95: 1.01: 6.16	6.7% Er^{3+}-doped
Te^{4+}-Er^{3+} codoped			
4.	2.00: 1.00: 1.00: x*: 0.05: 1.00	1.92: 1.02: 0.93: 6.06	5.9% Te^{4+}-3.2% Er^{3+} codoped
5.	2.00: 1.00: 1.00: x*: 0.01: 1.00	1.84: 1.13: 0.93: 6.04	1.8% Te^{4+}-3.9% Er^{3+} codoped
6.	2.00: 1.00: 1.00: x*: 0.005: 1.00	1.89: 0.99: 0.93: 6.13	1.7% Te^{4+}-5.9% Er^{3+} codoped

x*: Shows that the Cl$^-$ ions are present in excess in the precursor because HCl is used as solvent.

#: The dopant concentrations are small to get a consistent EDS data for dopants. Therefore, EDS data mainly verify the composition of the Cs$_2$NaInCl$_6$ host. Together, EDS and ICP-MS data provide the complete elemental analysis. ICP-MS data is used to label the compounds.

Elemental ratio of Cs:Na:In:Cl, obtained from EDS (Table 3.1), agrees with the host compositions Cs$_2$NaInCl$_6$. But the dopant concentrations are small for a consistent quantitative

estimation using EDS. So, we mainly rely on ICP-MS method for estimating the dopant concentrations, as shown in Table 3.2. ICP-MS data show that the Te^{4+} doping is facile whereas the Er^{3+} doping is difficult. Similar poor efficacy of lanthanide doping in such halide perovskites has been observed in prior reports as well.[14,18] It is to be noted that all the dopant percentages mentioned here are the ones obtained from ICP-MS data, and the dopant % is calculated with respect to concentration of In^{3+} ions in the samples.

Table 3.2: ICP-MS data of 3.6% Te^{4+}-doped, 6.7% Er^{3+}-doped and Te^{4+}-Er^{3+} codoped Cs$_2$NaInCl$_6$ products. dopant % $= \frac{[dopant]}{[In]} \times 100$. Where, $[dopant]$ and $[In]$ are molar concentrations of dopant and indium.

Sr. No.	Molar % of elements in the precursor		Molar % of elements in the product		Sample code
	Te % = $\frac{[Te]}{[In]} \times 100$	Er % = $\frac{[Er]}{[In]} \times 100$	Te % = $\frac{[Te]}{[In]} \times 100$	Er % = $\frac{[Er]}{[In]} \times 100$	
1.	0.0	0.0	0.0	0.0	Undoped
2.	0.5	0.0	3.6	0.0	3.6% Te^{4+}-doped
3.	0.0	100.0	0.0	6.7	6.7% Er^{3+}-doped
Te^{4+}-Er^{3+} codoped					
4.	5.0	100	5.9	3.2	5.9% Te^{4+}-3.2% Er^{3+} codoped
5.	1.0	100	1.8	3.9	1.8% Te^{4+}-3.9% Er^{3+} codoped
6.	0.5	100	1.7	5.9	1.7% Te^{4+}-5.9% Er^{3+} codoped
Te^{4+}-Yb^{3+} codoped					
	Te % = $\frac{[Te]}{[In]} \times 100$	Yb % = $\frac{[Yb]}{[In]} \times 100$	Te % = $\frac{[Te]}{[In]} \times 100$	Yb % = $\frac{[Yb]}{[In]} \times 100$	Sample code
7.	0.5	100	0.4	9.0	Te^{4+}-Yb^{3+} codoped

Powder XRD patterns of the samples are shown in Figure 3.5a. The pattern for the undoped sample matches well with the reference data of cubic phase of Cs$_2$NaInCl$_6$ in $Fm\overline{3}m$ space group, similar to a prior report[35]. The 3.6% Te^{4+}-doped, 6.7% Er^{3+}-doped and 1.7% Te^{4+}- 5.9% Er^{3+} codoped samples also crystallizes in the same phase, without forming any crystalline impurity. The concentrations of Te^{4+} and Er^{3+} (Table 3.2) in the codoped samples have been varied, and in all the cases similar phase-pure XRD patterns are observed, as shown in Figure 3.5b. Table 3.3 shows that both the Te-Cl (2.54 Å) and Er-Cl (2.62 Å) bond lengths are

Short Wave Infrared Emissions from Te^{4+}-Ln^{3+} (Ln: Er, Yb) Codoped Cs$_2$NaInCl$_6$ Double Perovskites

relatively smaller compared to that of Cs-Cl (3.72 Å) and Na-Cl (2.75 Å), in similar perovskite systems. But Te-Cl and Er-Cl bond lengths are comparable to that of In-Cl (2.50 Å).[35-38] This similarity of bond lengths along the similar oxidation states of In^{3+} with Er^{3+} and Te^{4+}, suggest that dopants are expected to occupy the In^{3+} sites in the host lattice. It is to be noted that Te^{4+}-doping is an heterovalent one, so it might give rise to cation vacancies and/or interstitial anions to maintain the charge neutrality of the samples.
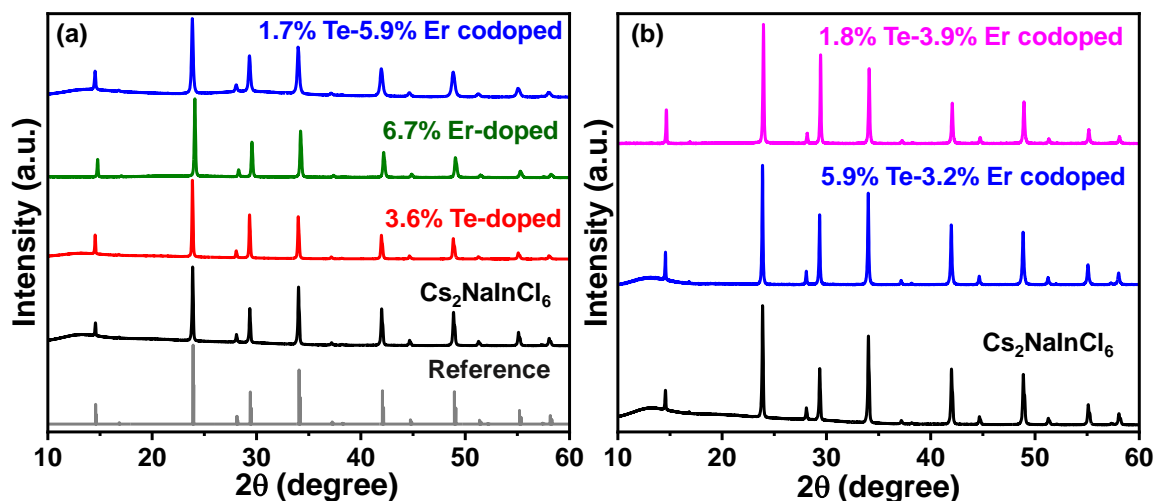
Figure 3.5: (a) EDS elemental mapping of 1.7% Te^{4+}- 5.9% Er^{3+} codoped Cs$_2$NaInCl$_6$. (b) Powder XRD patterns of undoped, 3.6% Te^{4+}-doped, 6.7% Er^{3+}-doped and 1.7% Te^{4+}- 5.9% Er^{3+} codoped Cs$_2$NaInCl$_6$. Reference pattern (ICSD: 132718) of Cs$_2$NaInCl$_6$ in cubic phase with space group Fm$\overline{3}$m is also plotted for a comparison.

Table 3.3: Metal Halide bond-length values in perovskite like structure. The values are obtained from reported single crystal data.

Bond	Bond Length (Å)	Compound
Te-Cl	2.5358	Cs$_2$TeCl$_6$ (0D, 293 K)[38-39]
In-Cl	2.500	Cs$_2$NaInCl$_6$ (3D, 305 K)[37]
Na-Cl	2.754	
Cs-Cl	3.718	
Er-Cl	2.62 ($\pm$ 0.2)	Cs$_2$NaErCl$_6$[36, 40] (ICSD 50361)

3.3.2 EXAFS Study to Find the Local Environment of Atoms

The local environment of host lattice atoms and dopants is investigated by EXAFS.[16, 41-42] The R-space data (Fourier transformed over a range of 3 to 12.5 Å) of the In K edges for the undoped and doped Cs$_2$NaInCl$_6$ are shown in Figure 3.6. There is hardly any change observed in the In K edge oscillations. Multi-shell fitting of In K edge of doped and undoped Cs$_2$NaInCl$_6$

Short Wave Infrared Emissions from Te^{4+}-Ln^{3+} (Ln: Er, Yb) Codoped Cs$_2$NaInCl$_6$ Double Perovskites

crystals are performed to derive the bond length and disorder in the lattice from the R-space data over a range of 1 to 8.0 Å considering six scattering paths, as shown in Figure 3.7a. We could consider the large range of R-space in fitting due to the good quality of the EXAFS signal as shown in Figure 3.7b. The fitting parameters derived from the analysis are shown in Table 3.4 and Figure 3.8a-e. Negligible variation in the disorder (Debye-Waller factor) of the local atomic structure of In suggests no change in the local atomic structure of the Cs$_2$NaInCl$_6$ lattice due to doping.
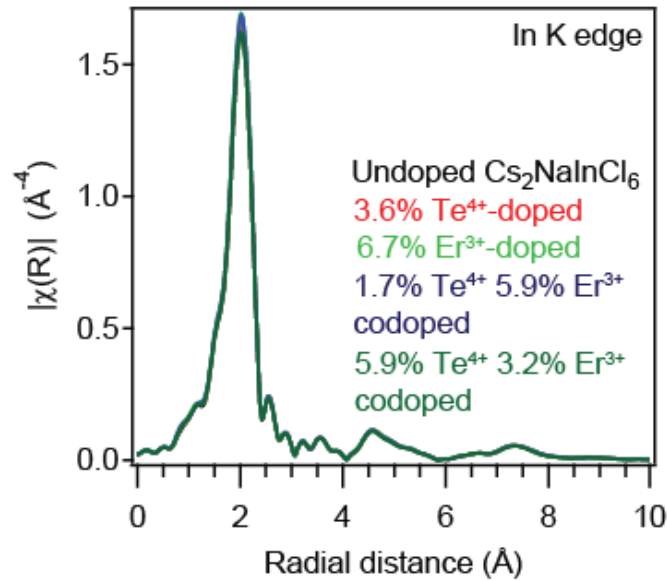
Figure 3.6: Comparison of In K edge EXAFS R-space plots for undoped Cs$_2$NaInCl$_6$, 3.6% Te^{4+}-doped, 6.7% Er^{3+}-doped, 1.7% Te^{4+}- 5.9% Er^{3+} codoped, and 5.9% Te^{4+}- 3.2% Er^{3+} codoped Cs$_2$NaInCl$_6$ crystals showing no significant change in local environment of In due to doping.
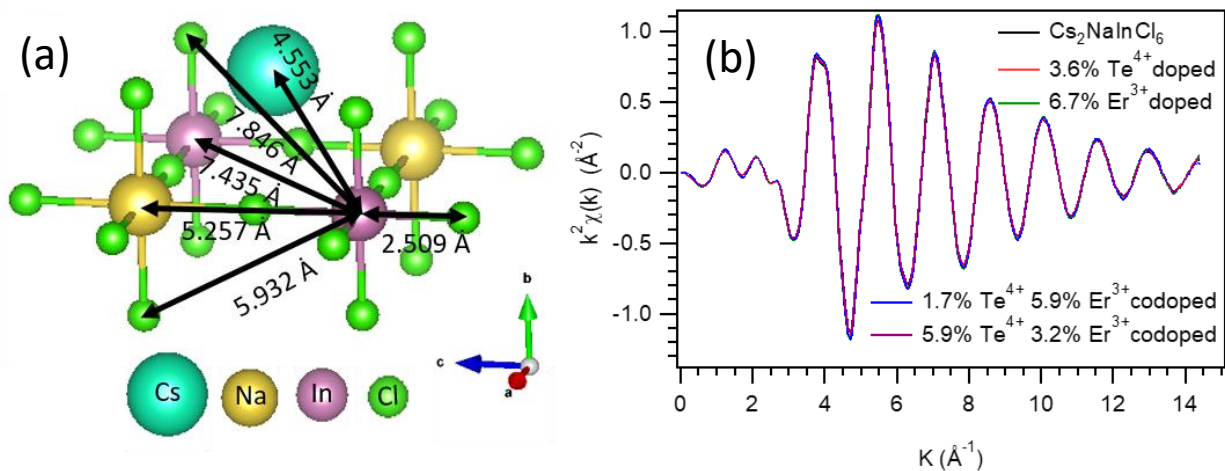
Figure 3.7: (a) Possible scattering paths from In atom in the crystal structure of Cs$_2$NaInCl$_6$ crystals considered in Feff calculations for modelling EXAFS data. (b) In K edge EXAFS data for doped and undoped Cs$_2$NaInCl$_6$ crystals in k-space.

Short Wave Infrared Emissions from Te⁴⁺-Ln³⁺ (Ln: Er, Yb) Codoped Cs₂NaInCl₆ Double Perovskites

Table 3.4. EXAFS multi-shell fitting of In K edge of undoped $Cs_2NaInCl_6$. $S_0^2 = 0.77$, R factor = 0.0061, Fourier transform range of 1 to 8.0 Å. The coordination number of each path is considered to be constant from the crystal structure file reported in reference [S35]. The initial fit is performed by guessing all the parameters (Δr, ΔE_0, σ^2). For the final fitting R (R= $R_{eff} \pm \Delta r$) and ΔE_0 are kept fixed to determine accurate values of disorder σ^2)

In K-edge Scattering paths	CN (fixed)	R (Å) (fixed)	σ^2 (Å²)	ΔE_0 (eV) (fixed)
In-Cl$_{3.1}$	6	2.508	0.005 ± 0.0001	4.226
In-Cs$_{2.1}$	8	4.383	0.035 ± 0.0070	4.226
In-Cl$_{3.1}$-Na-Cl$_{3.1}$-In	6	5.141	0.028 ± 0.0036	4.226
In-Cl$_{3.2}$	24	5.967	0.032 ± 0.0078	4.226
In-In$_{1.1}$	12	7.451	0.018 ± 0.0089	4.226
In-Cl$_{3.3}$	24	7.864	0.016 ± 0.0063	4.226
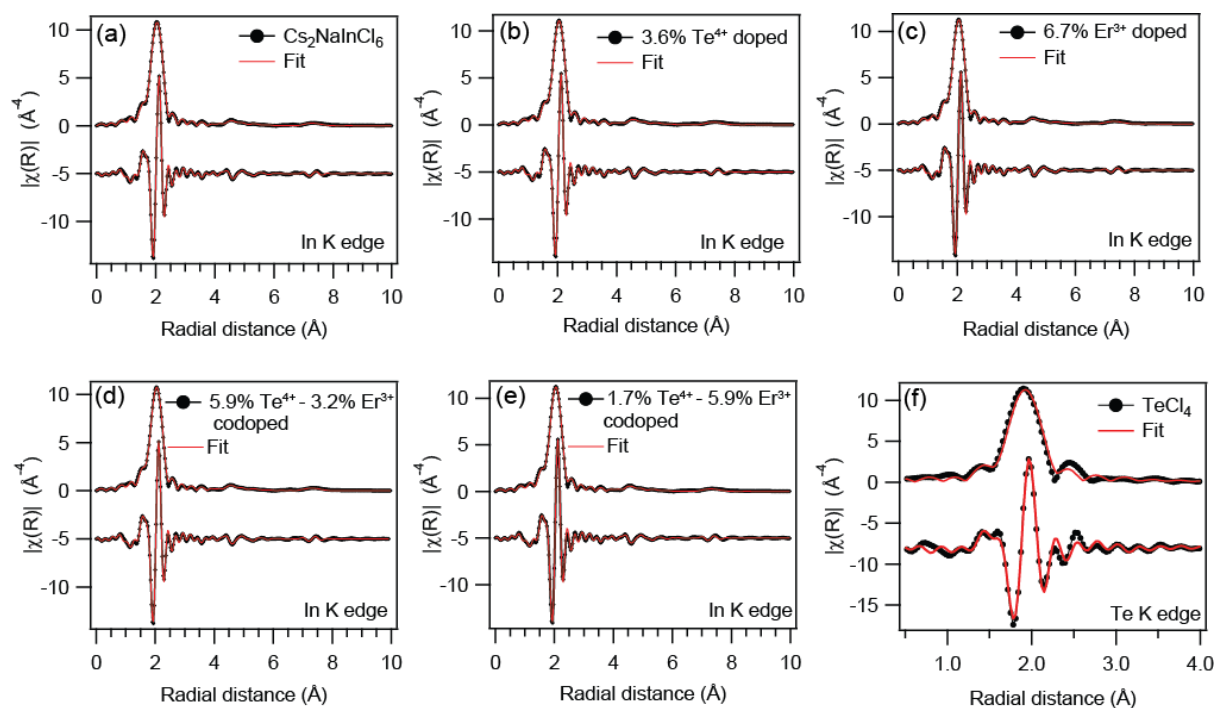
Figure 3.8: In K edge EXAFS data with fitting of magnitude of FT signal (top plot) and real part of (bottom plot) R space for (a) undoped, (b) 3.6% Te⁴⁺ -doped, (c) 6.7 % Er³⁺ -doped, (d) 5.9% Te⁴⁺- 3.2% Er³⁺ codoped, and (e) 1.7% Te⁴⁺-5.9% Er³⁺ codoped Cs₂NaInCl₆ crystals. (f) Te K edge EXAFS data with QFS fitting in R space for TeCl₄.

To check the local atomic structure around the dopants, we collected Te K edge EXAFS spectra of 5.9% Te⁴⁺- 3.2% Er³⁺ codoped Cs₂NaInCl₆ crystals and Er L₃ edge EXAFS spectra of 1.7% Te⁴⁺–5.9 % Er³⁺ codoped Cs₂NaInCl₆ crystals and analyzed using the quick first shell (QFS) fitting method as shown in Figure 3.9 (a, b). For samples with lower dopant concentrations, we

could not obtain good-quality EXAFS data from the dopant edges. We fitted four parameters, namely coordination number (CN), bond length (R), disorder/Debye-Waller factor (σ^2), and E_0 shift (ΔE_0), without any constraints or correlations. Our analysis revealed that the coordination numbers for the Te K edge and Er L_3 edge are 6.0 ± 0.5 and 6.0 ± 0.3, respectively, suggesting the formation of $TeCl_6$ and $ErCl_6$ octahedra, probably within the $Cs_2NaInCl_6$ lattice. Furthermore, the measured Te-Cl and Er-Cl bond lengths obtained from QFS were 2.513 ± 0.004 Å and 2.608 ± 0.003 Å, respectively. These values are found to be similar to the reported bond lengths of Te-Cl (2.536 Å) and Er-Cl (2.621 Å) for pure compositions of Cs_2TeCl_6 and $Cs_2NaErCl_6$.[16, 36, 38] We also collected and analyzed Te K edge EXAFS spectra of the $TeCl_4$ precursor (see Figure 3.8f). The fitting parameters show the coordination number of Te is 3.507 ± 0.630 and the Te-Cl bond length of 2.351 ± 0.0063 Å in $TeCl_4$ (see Table). These results again suggest the absence of $TeCl_4$ impurities in our codoped sample (Figure 3.5a).
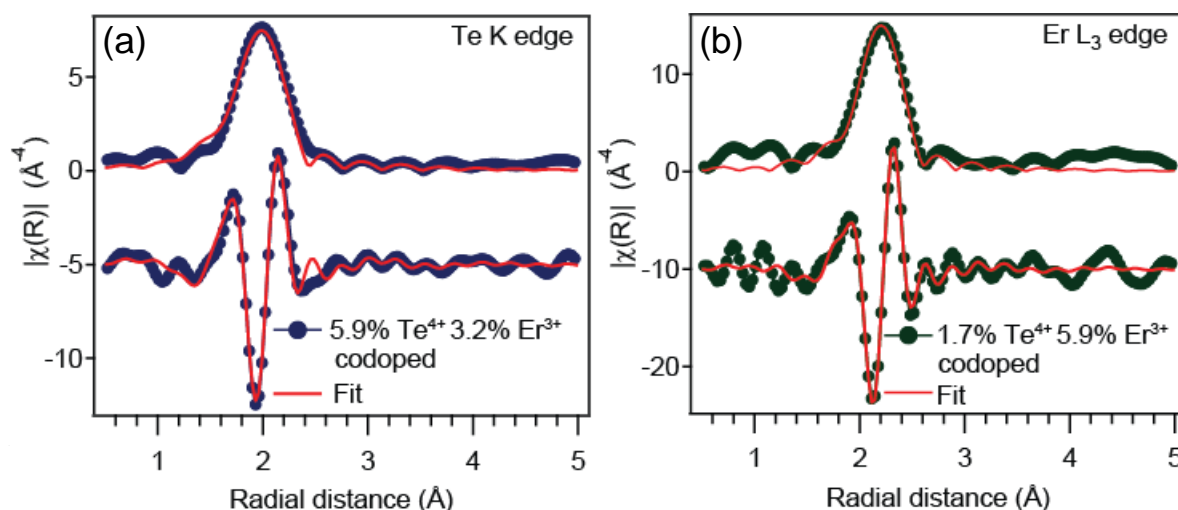
Figure 3.9: (a) Te K edge EXAFS data fitting in R-space for 5.9% Te⁴⁺- 3.2% Er³⁺ cooped Cs₂NaInCl₆ crystals. (b) Er L_3 edge EXAFS data fitting in R-space for 1.7% Te⁴⁺– 5.9% Er³⁺ codoped Cs₂NaInCl₆ crystals.

Table 3.5. Te K edge EXAFS quick first shell (QFS) fitting parameters for $TeCl_4$ reference sample ($S_0^2 = 0.99$, R factor = 0.020)

Scattering path	CN	R (Å)	σ^2 (Å²)	ΔE_0 (eV)
Te-Cl	3.507 ± 0.630	2.351 ± 0.0063	0.004 ± 0.0018	15.193 ± 2.0596

If Te⁴⁺ or Er³⁺ replaces Na⁺ site, then one would expect a significant change in the disorder of the In-Cl-Na-Cl-In bond length in In K edge EXAFS of Cs₂NaInCl₆ lattice after doping. We

have not observed any such change in the disorder of In-Cl-Na-Cl-In bond length in $Cs_2NaInCl_6$ after doping, as shown in Table 3.6. Overall, the EXAFS results suggest that Te^{4+} and Er^{3+} ions replace octahedral In^{3+} sites in the $Cs_2NaInCl_6$ crystals after doping.

Table 3.6: In k edge, EXAFS multi-shell fitting parameters of undoped and doped $Cs_2NaInCl_6$ crystals, showing the effect of doping on disorders of all bond distances ($S_0^2 = 0.77$)

Sample	Variation in disorder with doping in $Cs_2NaInCl_6$					
	In-Cl	**In-Cs**	**In-Cl-Na-Cl-In**	**In-Cl$_{3.2}$**	**In-In**	**In-Cl$_{03.3}$**
$Cs_2NaInCl_6$	0.0052 ± 0.0001	0.0347 ± 0.0082	0.0282 ± 0.0042	0.0327 ± 0.0083	0.0183 ± 0.0126	0.0166 ± 0.0083
3.6% **Te** doped	0.0050 ± 0.0001	0.0329 ± 0.0064	0.0278 ± 0.0036	0.0321 ± 0.0077	0.0183 ± 0.0091	0.0166 ± 0.0065
5.9% **Te**- 3.2% **Er** codoped	0.0052 ± 0.0001	0.0327 ± 0.0062	0.0286 ± 0.0037	0.0333 ± 0.0081	0.0197 ± 0.0110	0.0165 ± 0.0063
6.7% **Er**-doped	0.0049 ± 0.0001	0.0322 ± 0.0064	0.0271 ± 0.0036	0.0317 ± 0.0078	0.0191 ± 0.0107	0.0163 ± 0.0065
1.7% **Te** - 5.9% **Er** codoped	0.0049 ± 0.0001	0.0325 ± 0.0064	0.0278 ± 0.0037	0.0321 ± 0.0078	0.0187 ± 0.0100	0.0165 ± 0.0065

3.3.3 Optical Properties of Te⁴⁺ Doped Cs₂NaInCl₆

Figure 3.1 compares the UV-visible absorption spectra of the undoped and 3.6% Te^{4+}-doped $Cs_2NaInCl_6$. The undoped sample, has an absorption band edge at 243 nm, corresponding to the band gap of 5.1 eV, similar to prior reports.[1] After Te^{4+} doping, three new absorption bands appeared, which are indicated as A, B, and C bands, in Figure 3.1. In order to discuss the origin of these three bands, we need to consider the electronic configuration of Te^{4+}: $[Kr]4d^{10}5s^2$, where [Kr] indicates the electron configuration of Kr. Te^{4+} is known to absorb UV-visible light owing to the $5s^2 \rightarrow 5s^1 5p^1$ electronic transitions.[43] The ground state $5s^2$ has the term symbol $^1S_0$, and the excited state $5s^1 5p^1$ can have term symbols of $^3P_0$, $^3P_1^*$, $^3P_2$ and $^1P_1^*$ as shown in Figure 3.10. The symbol "*" represents the mixing of $^3P_1$ and $^1P_1$ states because of strong spin-orbit coupling. Consequently, transitions involving $^1S_0$ and $^3P_1^*$ becomes partially allowed. Three new absorption bands of 3.6% Te^{4+}-doped $Cs_2NaInCl_6$ at 380 nm, 313 nm, and 275 nm are assigned to $^1S_0 \rightarrow {}^3P_1^*$ (A-band), $^1S_0 \rightarrow {}^3P_2$ (B-band) and $^1S_0 \rightarrow {}^1P_1^*$ (C-band) transitions of Te^{4+}, respectively. It is noteworthy that the A-band absorption at 380 nm is significantly red-shifted compared to that of Sb^{3+}- or Bi^{3+}-doped $Cs_2NaInCl_6$ (Figure 3.1).

Short Wave Infrared Emissions from Te^{4+}-Ln^{3+} (Ln: Er, Yb) Codoped Cs$_2$NaInCl$_6$ Double Perovskites
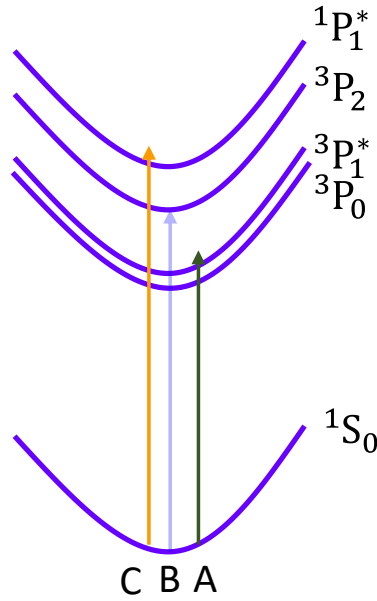
Figure 3.10: Schematic presentation of $5s^2 \rightarrow 5s^1 5p^1$ electronic transitions in Te^{4+} ion. A, B and C represent the electronic transitions named as A-band, B-band and C-band respectively.
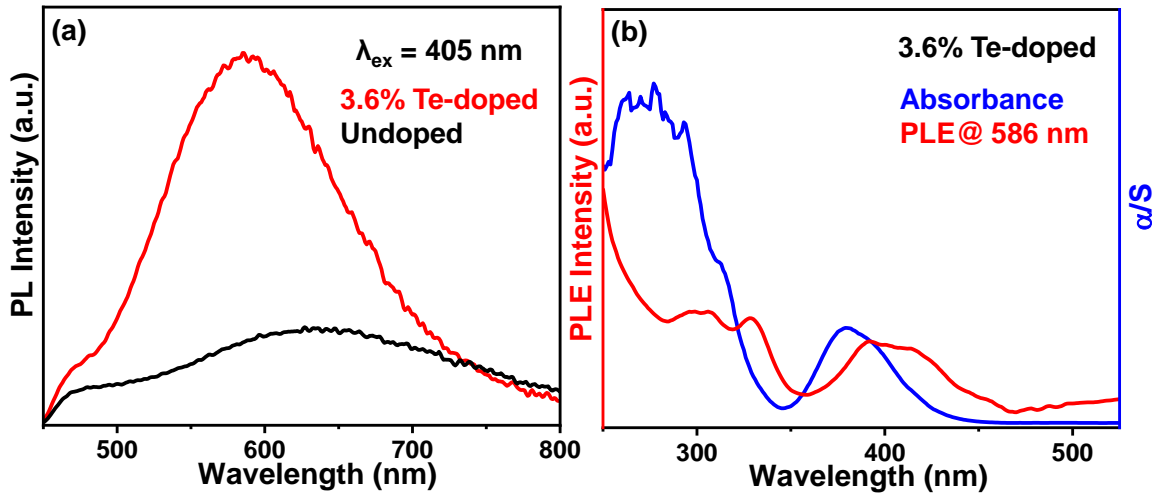
Figure 3.11: (a) PL spectra of undoped and 3.6% Te^{4+}-doped Cs$_2$NaInCl$_6$, excited with 405 nm pulse diode laser. (b) UV-visible absorption and PL excitation (PLE) spectra of 3.6% Te^{4+}-doped Cs$_2$NaInCl$_6$, measured at the emission wavelength 586 nm.

3.6% Te^{4+}-doped Cs$_2$NaInCl$_6$ has a weak emission with peak at 586 nm and this emission is different from the host emission, as shown in Figure 3.11a. PL excitation (PLE) spectrum measured at the 586 nm emission shows features at 400 nm, 328 nm and 299 nm (Figure 3.11b). The PLE features agree reasonably well with the A-, B-, C-absorption bands, suggesting that the emission originates via excitation of Te^{4+} dopants. We note that similar excitation and emission data were also reported in Te^{4+}-doped Cs$_2$ZrCl$_6$.[44-45] All these results suggest that the broad visible emission with peak at 586 nm appear because of de-excitation of Te^{4+} states, via $^3P_1^* \rightarrow {}^1S_0$ transition.

3.3.4 Temperature Dependent Photoluminescence of Te^{4+} Doped $Cs_2NaInCl_6$

To better understand the emission mechanism, temperature dependent PL are measured. The pseudo color contour map in Figure 3.12a and the corresponding spectra in Figure 3.12b show the Te^{4+} emission intensity increases systematically with decreasing the temperature, because of the suppression of non-radiative processes. The emission spectra narrow down with decrease in temperature. Also, there is a blue shift in PL peak position with decreasing temperature. The blue shift probably arises due to decrease in lattice parameters at lower temperature.
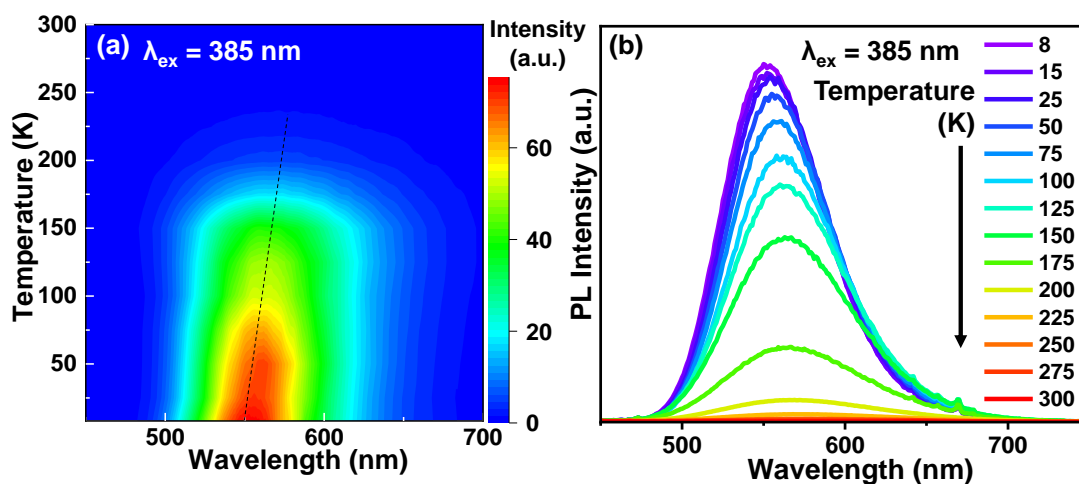
Figure 3.12: Temperature dependent (a) PL contour plot, and (b) PL spectra of 3.6% Te^{4+}-doped $Cs_2NaInCl_6$ at 385 nm excitation.
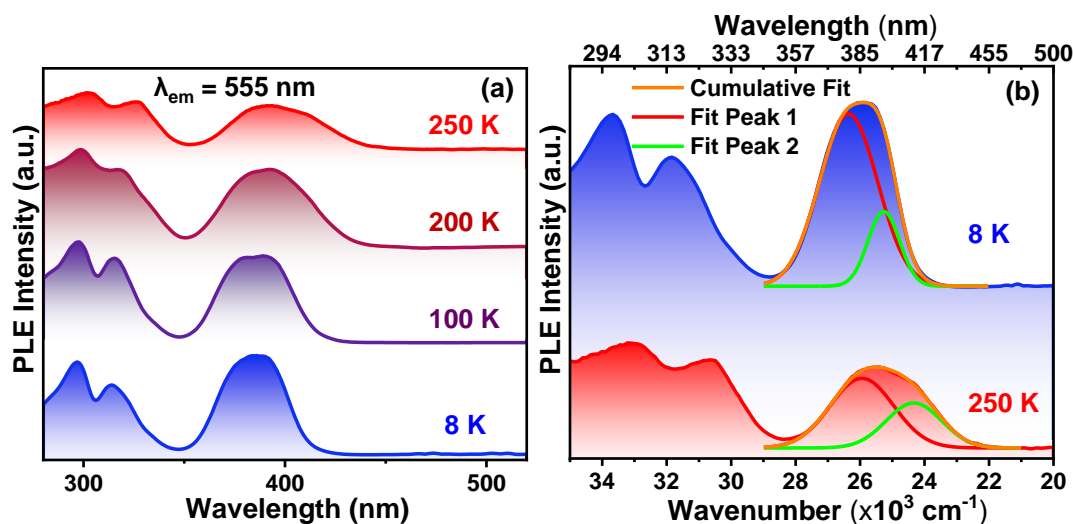
Figure 3.13: Temperature dependent (a) PL excitation (PLE) spectra of 3.6% Te^{4+}-doped $Cs_2NaInCl_6$. (b) PL excitation (PLE) spectra at 250 K and 8 K. 26000 cm⁻¹ excitation band (A-band) are fitted with two Gaussian peaks with the formula $y = y_0 + (A/(w\sqrt{\pi/2}))e^{(-2(\frac{x-x_c}{w})^2)}$. Where y is PL intensity, x is wavenumber in cm⁻¹, x_c is peak position, w is FWHM and A is integrated area under the peak. Fitting parameters are presented in Table 3.7.

Short Wave Infrared Emissions from Te^{4+}-Ln^{3+} (Ln: Er, Yb) Codoped Cs$_2$NaInCl$_6$ Double Perovskites

PL excitation spectrum is recorded to find the origin of the emission as shown in Figure 3.13a. PL excitation spectrum has three excitation bands similar to absorption spectrum in Figure 3.1. PL excitation band also slightly blue shifts and narrow down at low temperatures (Figure 3.13a). The excitation band around 400 nm appears to have two peaks, and can be deconvoluted in two Gaussian peaks, as shown in Figure 3.13b. The fitting parameters are presented in Table 3.7. The peak splitting decreases with decreasing temperature and possibly appear due to dynamical Jahn-Teller effect.[44, 46]

Table 3.7: Fitting parameters of around 400 nm excitation band.

Temperature		250 K	8 K
Peak 1	Peak center (cm^{-1})	25944	26357
	FWHM (cm^{-1})	1974	1806
Peak 2	Peak center (cm^{-1})	24331	25264
	FWHM (cm^{-1})	1716	983
Adj. R-Square		0.990	0.999

The PL decay profiles of the broad emission (~555 nm) of 3.6% Te^{4+}-doped Cs$_2$NaInCl$_6$ at different temperatures are shown in Figure 3.14. At temperatures 8 - 75 K, the decay profiles are fitted using a single-exponential decay equation. The decay systematically become faster at higher temperatures, and above 75 K, the decay becomes bi-exponential. The best fit parameters are presented in Table 3.8. Figure 3.15 summarizes the temperature dependent change in the PL lifetime of 555 nm emission. At 8 K, the PL lifetime is as high as 3.86 ms. The PL lifetime drastically decreases to 9.66 µs at 75 K. Such sudden change in PL lifetime can be explained by the separation of $^3P_0$ and $^3P_1^*$ states at low temperature (see Figure 3.10). $^3P_0$ and $^3P_1^*$ states are known to be thermally coupled at room temperature. But at very low temperatures, $^3P_0$ and $^3P_1^*$ energy separation increases and the population back transfer from $^3P_0 \rightarrow {}^3P_1^*$ state becomes in-efficient. This in-efficient back transfer results into spin-forbidden $^3P_0 \rightarrow {}^1S_0$ transition, with *J* remaining zero, which might drastically increase the PL lifetime at low temperature.[46-48] But the origin of such long lifetime needs further investigation. At temperatures above 200 K, PL lifetime and intensity, both decrease drastically because of the dominance of non-radiative decay channels.
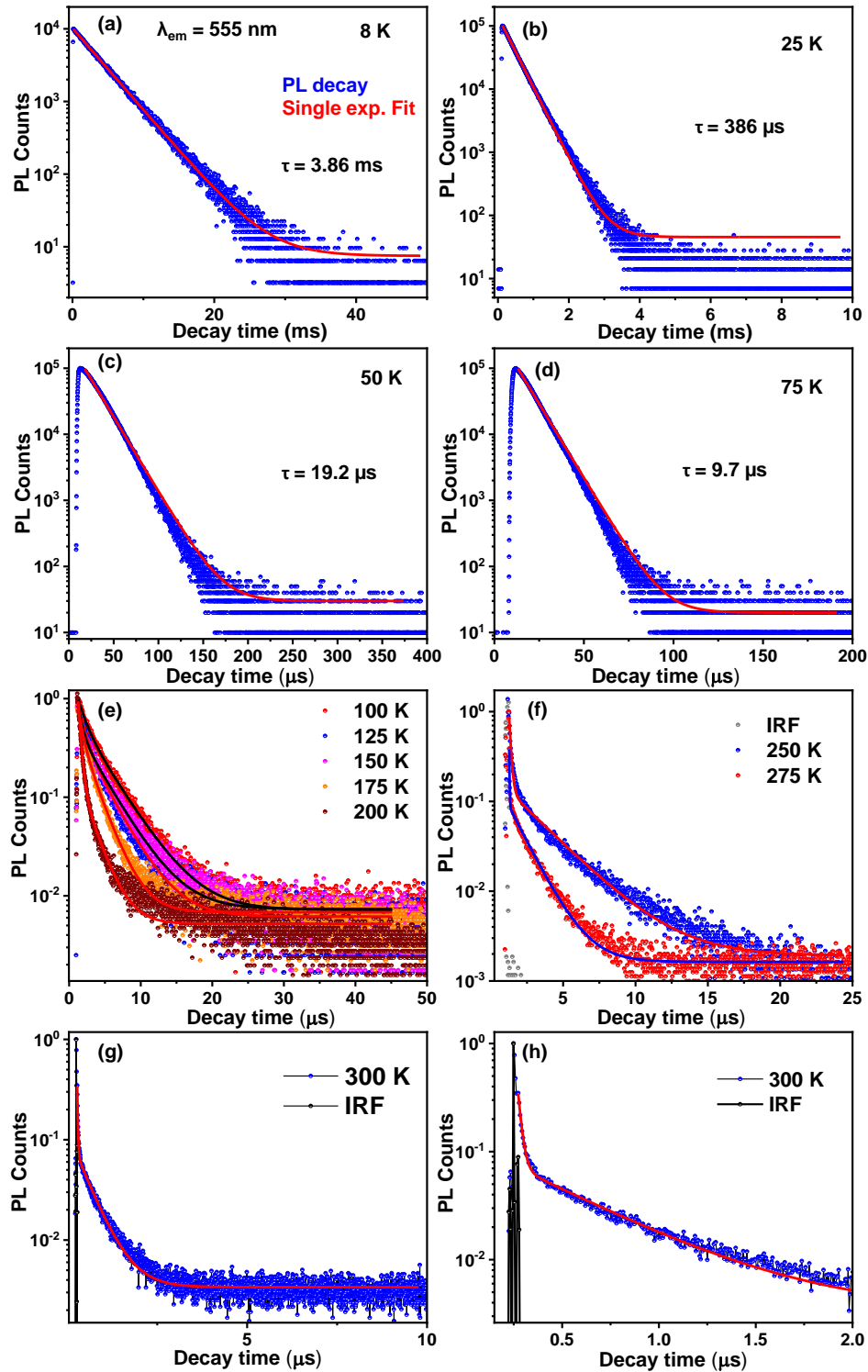
Figure 3.14: Temperature dependent PL decay profiles of 3.6% Te^{4+}-doped $Cs_2NaInCl_6$ for 555 nm emission. (a-d) PL decay in the temperature range of 8 - 75 K are fitted with single-exponential decay. These are recorded with 385 nm excitation with microsecond flash lamp. (e-g) PL decay profiles in the temperature range of 100 - 300 K, and are fitted with a bi-exponential decay equation. 100 - 300 K PL decay profiles are recorded with 405 nm pulse diode laser at different repetition rates. (h) Enlarge view shows that the PL decay at 300 K is not overlapping with the instrument response function (IRF) of the instrument. The fitting parameters are given in Table 3.8.

Short Wave Infrared Emissions from Te^{4+}-Ln^{3+} (Ln: Er, Yb) Codoped Cs$_2$NaInCl$_6$ Double Perovskites

**Table 3.8.** Fitting parameters of temperature dependent PL decay profiles (shown in Figure 3.12) of 555 nm emission of 3.6% Te^{4+}-doped Cs$_2$NaInCl$_6$.

Temperature	τ_1(µs)	A_1(%)	τ_2(µs)	A_2(%)	R-squared (COD)
8 K	-	-	3860	100	0.999
25 K	-	-	386	100	0.999
50 K	-	-	19.2	100	0.997
75 K	-	-	9.66	100	0.998
100K	1.01	61.49	3.70	38.51	0.997
125K	0.87	74.05	3.12	25.95	0.997
150K	0.46	88.88	3.13	11.12	0.996
175K	0.59	80.41	2.13	19.59	0.997
200 K	0.35	99.08	1.96	0.92	0.998
225 K	0.212	97.91	1.853	2.09	0.993
250 K	0.09	100.00	1.94	0.00	0.988
275 K	0.025	100.00	1.35	0.00	0.988
300 K	0.018	100.00	0.48	0.00	0.995
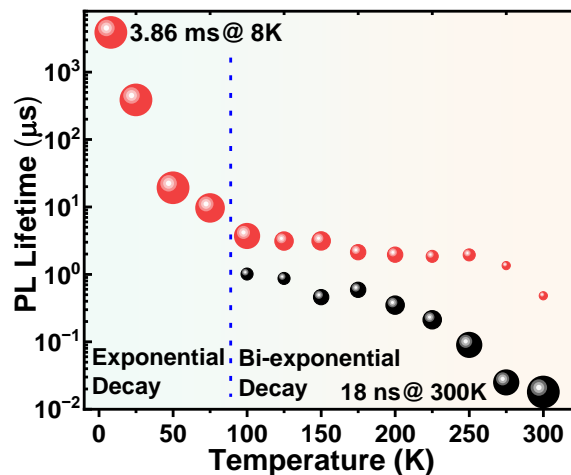
Figure 3.15: Temperature dependent PL lifetime of 3.6% Te^{4+}-doped Cs$_2$NaInCl$_6$. The lifetimes (in µs; λ_{em} = 555 nm) are plotted in log scale versus temperature. Above 75 K, red and black spheres represent two lifetimes obtained by biexponential fit and the sphere size represents the relative contribution (approx.) of two lifetimes.

*Short Wave Infrared Emissions from Te^{4+}-Ln^{3+} (Ln: Er, Yb) Codoped Cs$_2$NaInCl$_6$
Double Perovskites*

3.3.5 Optical Properties of Te^{4+}-Er^{3+} Codoped Cs$_2$NaInCl$_6$

The PL spectra of 1.7% Te^{4+}- 5.9% Er^{3+} codoped sample in the visible and SWIR range are shown in Figure 3.16a and b, respectively. Though the excitation at 420 nm implies excitation of Te^{4+} ion, the emission spectra are mainly dominated by Er^{3+} emission, at room temperature. In the visible range (Figure 3.16a), a broad Te^{4+} emission is also observed below the sharp Er^{3+} peaks. Inset in Figure 3.16a shows the digital image of 1.7% Te^{4+}- 5.9% Er^{3+} codoped sample under 400 nm xenon lamp excitation. The emission appears greenish in color because of the dominance of Er^{3+} emission around 515 nm to 570 nm range. Based on prior literature, the sharp emission peaks at 525 nm, 551 nm, 660 nm and 1540 nm, are assigned to $^2H_{11/2} \rightarrow {}^4I_{15/2}$, $^4S_{3/2} \rightarrow {}^4I_{15/2}$, $^4F_{9/2} \rightarrow {}^4I_{15/2}$ and $^4I_{13/2} \rightarrow {}^4I_{15/2}$ transitions of Er^{3+}, respectively.[13] The SWIR emission at 1540 nm remains in main focus because of its relevance for applications including optical fiber communication.
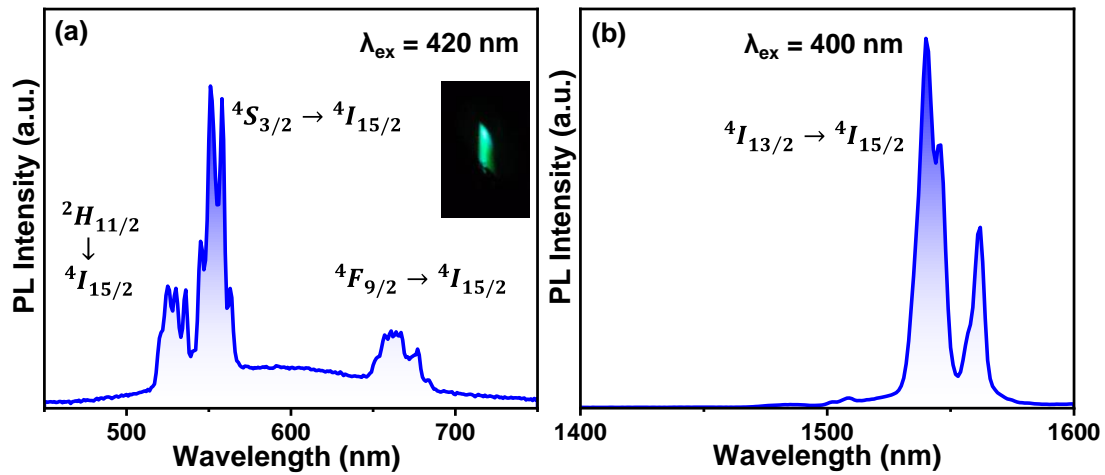
Figure 3.16: PL spectra of 1.7% Te^{4+}- 5.9% Er^{3+} codoped Cs$_2$NaInCl$_6$ in both (a) visible and (b) SWIR region. Inset of (a) shows the digital image of the sample under 400 nm excitation of xenon lamp.

The concentrations of both Te^{4+} and Er^{3+} in the codoped sample are also optimized to enhance the intensity of SWIR emission. Figure 3.17 shows that, 1.7% Te^{4+}- 5.9% Er^{3+} codoped sample is the optimum one to show intense SWIR emission. The broad visible emission (of Te^{4+}) increases on increasing the Te^{4+} precursor amount as shown in Figure 3.17a. We observed that the Er^{3+} doping percentage decreases on increasing the Te^{4+} precursor amount and vice versa as shown in Table 3.2.

Short Wave Infrared Emissions from Te^{4+}-Ln^{3+} (Ln: Er, Yb) Codoped Cs$_2$NaInCl$_6$ Double Perovskites
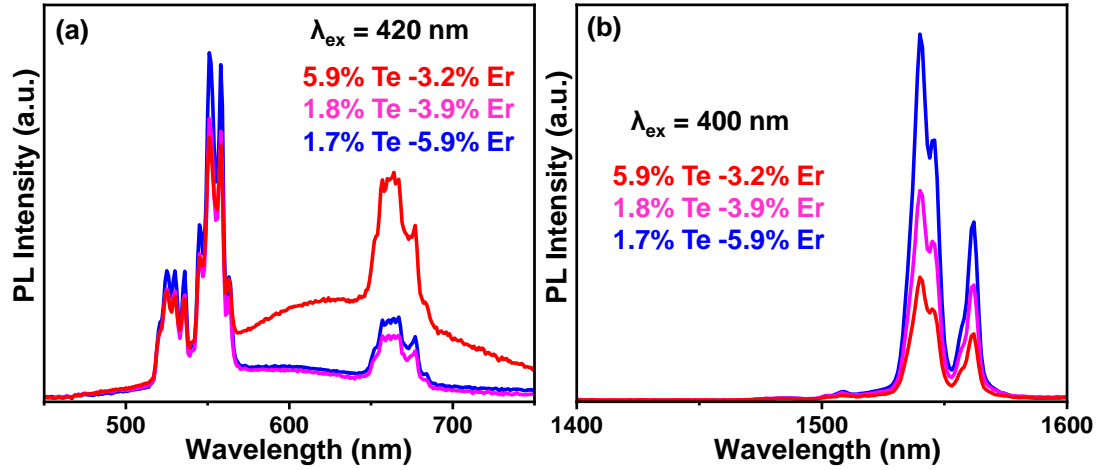
Figure 3.17: PL spectra in the (a) visible and (b) SWIR region with different concentrations of dopants in the Te^{4+}-Er^{3+} codoped Cs$_2$NaInCl$_6$.
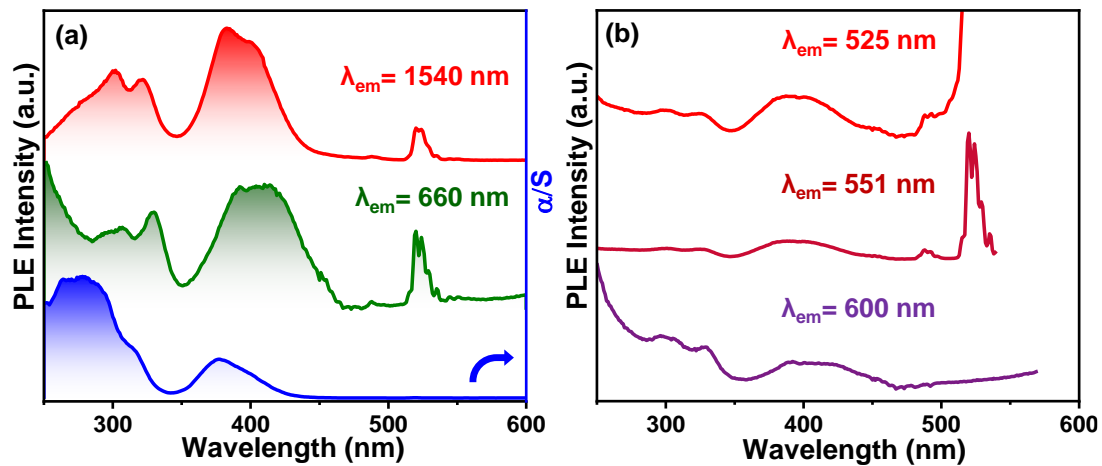
Figure 3.18: (a) and (b) Comparison of UV-visible absorption and PL excitation (PLE) spectra of 1.7% Te^{4+}- 5.9% Er^{3+} codoped Cs$_2$NaInCl$_6$.

UV-visible absorption spectrum of 1.7% Te- 5.9% Er^{3+} codoped Cs$_2$NaInCl$_6$ is shown in Figure 3.18a. The absorption features of the codoped sample are similar to that of Te^{4+}-doped sample, suggesting that the $5s^2 \rightarrow 5s^1 5p^1$ electronic transitions of Te^{4+} ions dominate the absorption spectrum. Expectedly, the Laporte forbidden Er^{3+} *f-f* transitions are not observed in absorption spectrum. PLE spectra for Er^{3+} emissions at 660 nm and 1540 nm are shown in Figure 3.18a. PLE spectra of both Er^{3+} emissions are similar, and are dominated by Te^{4+} absorption below 450 nm. This finding confirms that the sample gets mainly excited via $5s^2 \rightarrow 5s^1 5p^1$ transition of Te^{4+}, which non-radiatively transfers the excitation energy to Er^{3+}, and subsequent de-excitation of the Er^{3+} gives rise to the sharp emissions in the visible and SWIR range. Figure 3.18b shows that other Er^{3+} emissions at 525 nm and 551 nm, can also be excited via Te^{4+} ions. This interaction between Te^{4+} and Er^{3+} are possible only when the codopants are in close

proximity, providing indirect evidence of successful codoping in our microcrystals. In addition to the broad Te^{4+} contribution in PLE, Figure 3.18a shows sharp PLE features at 522 nm, because of the $^4I_{15/2} \rightarrow {}^2H_{11/2}$ transition of Er^{3+}. Optical absorption data in (Figure 3.19) shows a negligible absorption for the 522 nm excitation channel, compared to the broad Te^{4+} absorption below 450 nm. Therefore, the observation of significant PLE intensity at 522 nm in Figure 3.18a-b, suggests that the internal quantum efficiency of the Er^{3+} emissions at room temperature is higher when the Er^{3+} ions are directly excited at 522 nm, compared to excitation via Te^{4+} ions at <450 nm. The broad background emission of Te^{4+} at ~600 nm can be excited through Te^{4+} excitation, but the Er^{3+} excitation at 522 nm is insufficient to yield the broad emission (Figure 3.18b). Thus, in Te^{4+}-Er^{3+} codoped Cs$_2$NaInCl$_6$ samples, strong optical excitation happens through only Te^{4+} dopant, whereas emission happens through both Te^{4+} and Er^{3+} dopants.
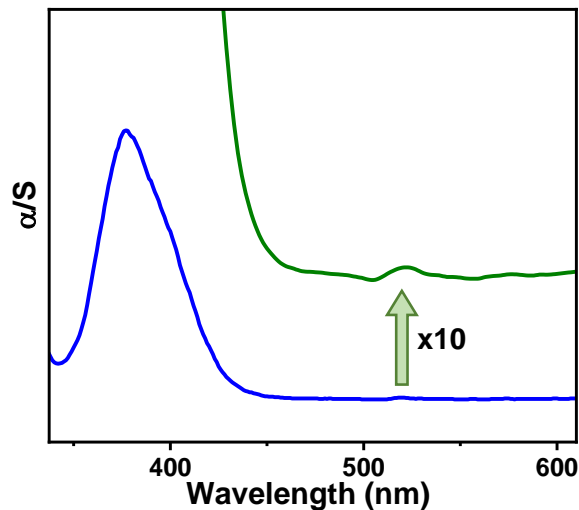
Figure 3.19: UV-visible absorption spectrum of 1.7% Te^{4+}- 5.9% Er^{3+} codoped Cs$_2$NaInCl$_6$. The absorption spectrum is obtained from diffuse reflectance spectrum by Kubelka-Munk transformation.

PL decay profiles of Er^{3+} emissions at 525, 551, 660, and 1540 nm, after excitation at 400 nm (Te^{4+} excitation), are shown in Figure 3.20a. The decay at 525 and 551 nm are almost on top of each other, and at longer wavelengths, the decay becomes slower. The decay profiles can be fitted with single exponential decay functions. The obtained PL lifetimes are 2.06, 2.11, 6.05, and 17.95 ms at emission wavelengths 525, 551, 660, and 1540 nm, respectively. The long lifetime of Er^{3+} emissions signify the Laporte forbidden *f-f* transitions. We further note that a long ms lifetime indicates that the lanthanide ion is located in a well-defined crystalline lattice,

whereas, a non-crystalline surrounding with plenty of non-radiative decay channels reduces the lifetime to µs range.[49-50] All the Te^{4+}-Er^{3+} codoped samples with different dopant concentrations have similar PL lifetime of 1540 nm Er^{3+} emission reflecting isolated nature of inner core *f-f* electronic transition (Figure 3.20b).
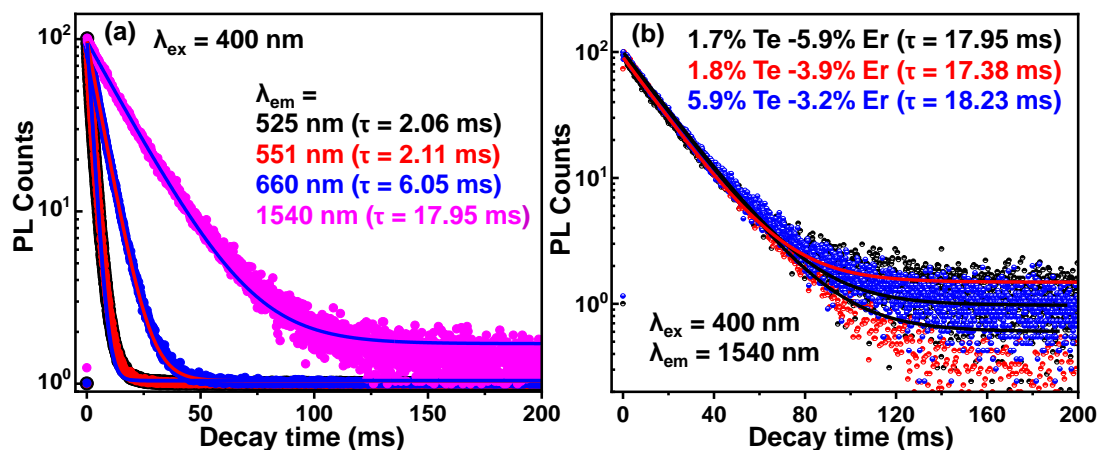
Figure 3.20: (a) PL decay of 1.7% Te^{4+}- 5.9% Er^{3+} codoped Cs$_2$NaInCl$_6$ at different emission wavelength. (b) PL decay of 1540 nm emission of Te^{4+}-Er^{3+} codoped Cs$_2$NaInCl$_6$ with different dopant concentrations. Experimental PL decay profiles at different emission wavelengths of Er^{3+} emissions are fitted with single exponential decay equation. The symbols represent experimental data and the solid lines represent the fitting data. The obtained PL lifetimes are shown in the figure.

3.3.6 Temperature Dependent Optical Properties of Te^{4+}-Er^{3+} Codoped Cs$_2$NaInCl$_6$

Figure 3.21 shows the temperature (8 - 300 K) dependent PL spectra of 1.7% Te^{4+} - 5.9% Er^{3+} codoped Cs$_2$NaInCl$_6$ in the visible region. The PL intensity increases with decreasing temperature because of the suppression of non-radiative processes. At lower temperatures, the broad visible emission becomes relatively more prominent. Figure 3.22a shows that the broad emission for the Te^{4+}-doped and Te^{4+}-Er^{3+} codoped samples at 8 K resembles each other. This broad emission in codoped and Te^{4+}-doped samples originates from the de-excitation of Te^{4+} state via $^3P_{0,1} \rightarrow {}^1S_0$ transition or related self-trap exciton (STE) emission. Interestingly, the Er^{3+} emission intensity at 525 nm diminishes, and 551 nm peak intensifies with decreasing temperature (Figure 3.22b). These peaks originate from $^2H_{11/2}$, $^2S_{3/2}$ states of Er^{3+} respectively, which are known to be thermally coupled states. The temperature dependent change in the relative intensity of these two peaks can be used for non-contact based temperature sensors as shown in Figure 3.22b.
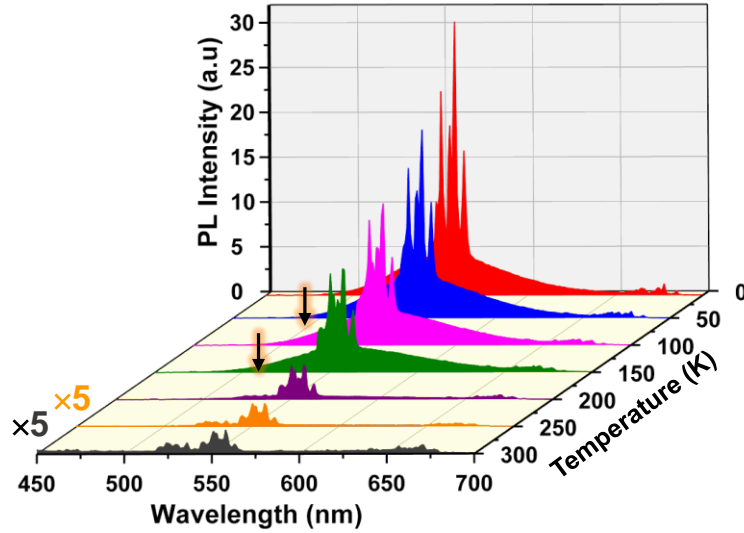
Figure 3.21: Temperature dependent (8 - 300 K) PL spectra of 1.7% Te^{4+}- 5.9% Er^{3+} codoped Cs$_2$NaInCl$_6$ in the (a) visible and (b) SWIR region. In (a), the intensity of 300 K and 250 K emission spectra are multiplied by 5, and the downward arrows indicate the decreasing intensity of 525 nm emission peak at lower temperatures.
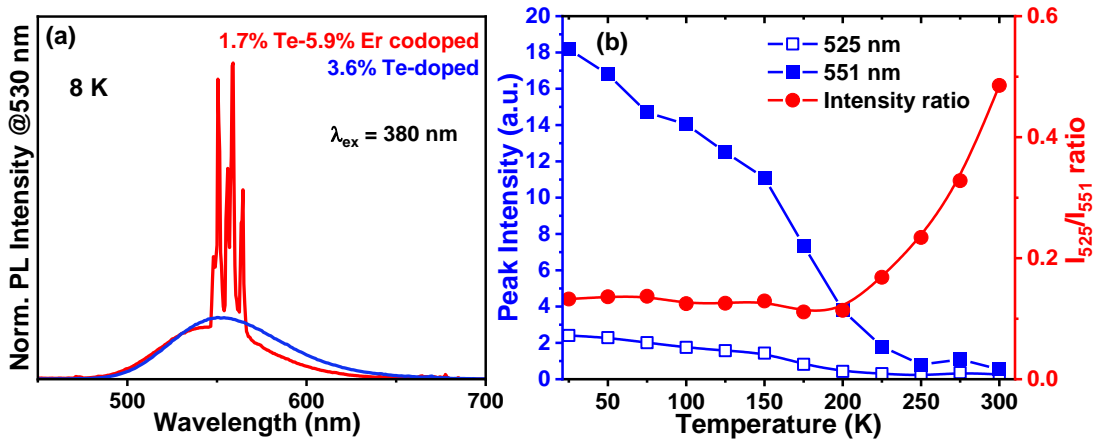
Figure 3.22: (a) PL spectra of 3.6% Te^{4+}-doped and 1.7% Te^{4+}- 5.9% Er^{3+} codoped Cs$_2$NaInCl$_6$ measured at 8 K. The PL intensity of both samples are normalized at 530 nm. (b) Change in PL peak intensity of 525 nm and 551 nm peaks, along with relative peak intensity ratio with temperature. The intensity ratio I$_{525}$/I$_{551}$ changes almost linearly in the 200-300 K range.

Figure 3.23 show that the 1540 nm SWIR emission intensity also increases with decreasing temperature. Similar to visible range Er^{3+} emissions, the relative intensity of multiple SWIR emission peaks at 1540 nm also varies with temperature. In the crystal field of the host, the *f*-electronic states $^4I_{13/2}$ and $^4I_{15/2}$ split, leading to multiple fine structures in the PL emission around 1540 nm. A change in temperature changes the population distribution in those split energy levels, changing the relative intensity of the PL fine structure peaks. At 8 K, these peaks count down almost to a single narrow peak at 1540 nm, with full width at half maxima (FWHM) as small as 1.32 meV. Figure 3.24 reflects the increased intensity of the PL excitation spectra

for 551 nm and 1540 nm emissions. Overall, the PL excitation features remain similar throughout the temperature range with slight blue shift at lower temperatures.
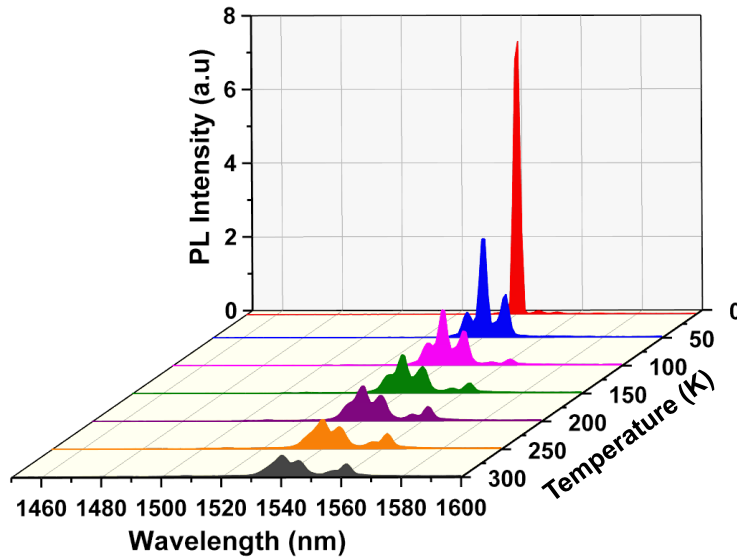
Figure 3.23: Temperature dependent (8 - 300 K) PL spectra of 1.7% Te^{4+}- 5.9% Er^{3+} codoped Cs$_2$NaInCl$_6$ in the SWIR region at 380 nm excitation.
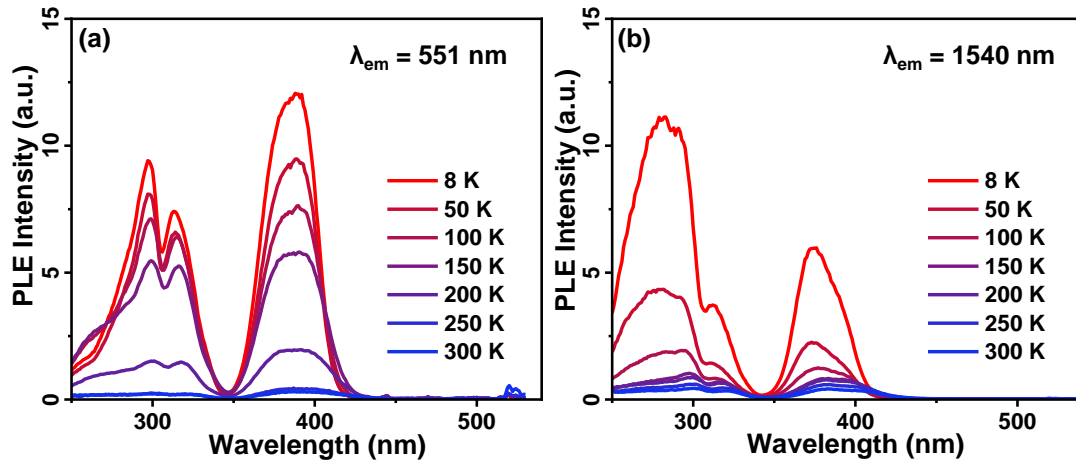
Figure 3.24: Temperature dependent PL excitation (PLE) spectra of 1.7% Te^{4+}- 5.9% Er^{3+} codoped Cs$_2$NaInCl$_6$ for (a) 551 nm and (b) 1540 nm emissions.

PL lifetimes of the 1.7% Te^{4+} - 5.9% Er^{3+} codoped sample for Er^{3+} emissions at both 551 and 1540 nm increases with decreasing temperature, as shown in Figure 3.25. 1540 nm emission lifetime increases to 28.26 ms at 8 K from 18.10 ms at 300 K as shown in Figure 3.25a. Similarly, Figure 3.25b show that 551 nm emission lifetime increases to 9.56 ms at 8 K from 2.33 ms at 300 K. Also, Figure 3.26 showss that the PL lifetime of the broad Te^{4+} emission (at 600 nm) of the codoped sample increases drastically from 20 μs at 50 K to 3.69 ms at 8 K, similar to that of the 3.6% Te^{4+}-doped Cs$_2$NaInCl$_6$ (Figure 3.15).

Short Wave Infrared Emissions from Te^{4+}-Ln^{3+} (Ln: Er, Yb) Codoped Cs$_2$NaInCl$_6$ Double Perovskites
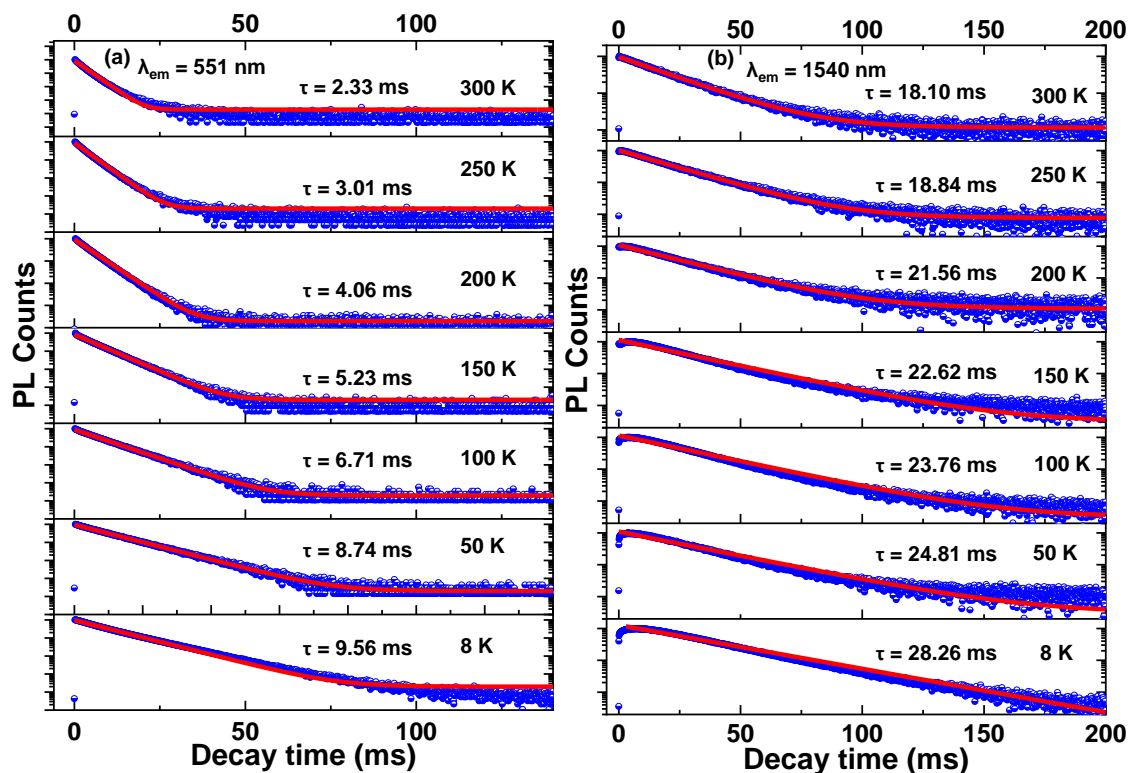
Figure 3.25: Temperature dependent PL decay of 1.7% Te^{4+}- 5.9% Er^{3+} codoped Cs$_2$NaInCl$_6$ for emission at (a) 551 nm, and (b) 1540 nm. λ_{ex} = 380 nm in both cases. The blue circles represent the PL decay and red solid lines are the mono-exponential decay fitting.
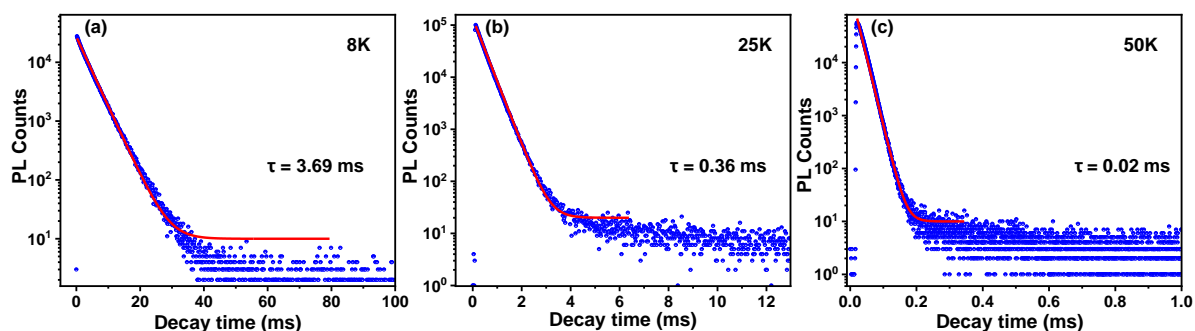
Figure 3.26: Temperature dependent PL decay of 1.7% Te^{4+}- 5.9% Er^{3+} codoped Cs$_2$NaInCl$_6$ for emission at 600 nm (broad Te^{4+} related emission) at λ_{ex} = 380 nm. The blue circles represent the PL decay and red solid line is the fitting. The data are fitted with single exponential decay equation.

3.3.7 Excitation and Emission Processes in Te^{4+}-Er^{3+} Codoped Cs$_2$NaInCl$_6$

Finally, the excitation and emission processes have been schematically summarized Figure 3.27. Cs$_2$NaInCl$_6$ required high energy for excitation (> 5.1 eV, < 243 nm), and does not lead to emission. Higher energy excitations generally activate more non-radiative paths, which is detrimental for PL emission. Introduction of Te^{4+} dopant reduces the excitation energy to 2.70 eV or 460 nm. Then the excited Te^{4+} themselves can lead to a weak broad visible light emission,

or can transfer its energy non-radiatively to excite the Er^{3+} codopant. After that the de-excitation of Er^{3+} via characteristic *f-f* transitions leads to sharp emissions at 525 nm, 551 nm, 660 nm and 1540 nm. The Er^{3+} ions can also be excited directly by absorption of 522 nm light because of $^4I_{15/2} \rightarrow {}^2H_{11/2}$ *f-f* transition. But the non-radiative excitation of Er^{3+} ion through the optically excited Te^{4+} ions is the significantly dominant pathway, compared to the direct optical excitation of Er^{3+}.
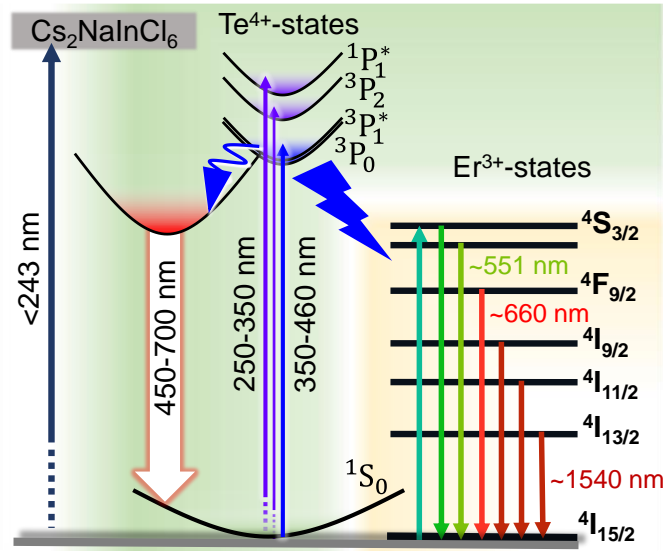
Figure 3.27: Schematic representation of the excitation and emission processes of Te^{4+}-Er^{3+} codoped Cs$_2$NaInCl$_6$.

3.3.8 Phosphor Converted LED of Te^{4+}-Er^{3+} Codoped Cs$_2$NaInCl$_6$
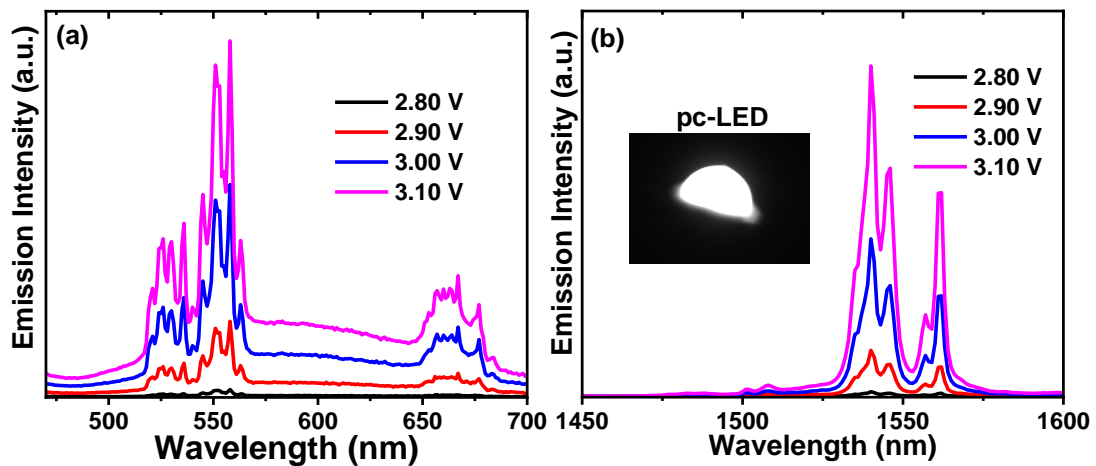
Figure 3.28: Emission spectra of 1.7% Te^{4+}- 5.9% Er^{3+} codoped Cs$_2$NaInCl$_6$ pc-LED in (a) visible and (b) SWIR region, for different operational voltages of the pc-LED. Inset in (b) shows the 1540 nm SWIR emission captured by using InGaAs camera working in the wavelength range of 950 – 1700 nm.

1.7% Te^{4+}- 5.9% Er^{3+} codoped Cs$_2$NaInCl$_6$ is mixed with poly (methyl methacrylate) and coated on commercial LED chip. We used a 398 nm LED chip which does not have visible or SWIR radiation. Figure 3.28a-b show that the pc-LED emit visible and SWIR radiations, similar to the PL spectra of 1.7% Te^{4+}- 5.9% Er^{3+} codoped Cs$_2$NaInCl$_6$ observed in Figure 3.16a-b. In the visible region, pc-LED emission contains both broad Te^{4+} emission and sharp Er^{3+} emissions at 525 nm, 551 nm and 660 nm. The SWIR emission of pc-LED shows the 1540 nm emission of Er^{3+}. Expectedly, the emission intensity increases with applied operational voltage of pc-LED because the 398 nm emission intensity of LED chip increases. The inset in Figure 3.28b shows the digital photograph of pc-LED with 3.1 V operational voltage, captured by InGaAs based NIR camera. The intensity captured here is because of the 1540 nm SWIR emission of the pc-LED.

3.3.9 Te^{4+}-Yb^{3+} Codoped Cs$_2$NaInCl$_6$

In order to generalize the Te^{4+} sensitization strategy for different lanthanides emitting SWIR radiations at different wavelengths, we also synthesized Te^{4+}-Yb^{3+} codoped Cs$_2$NaInCl$_6$. Powder XRD in Figure 3.29a confirms that the codoped system forms the same cubic crystal structure Cs$_2$NaInCl$_6$, without forming any crystalline impurity. Figure 3.29b shows the absorption spectrum of 0.4% Te^{4+} - 9.0% Yb^{3+} codoped Cs$_2$NaInCl$_6$ which is similar to 3.6% Te^{4+}-doped Cs$_2$NaInCl$_6$ (Figure 3.1).
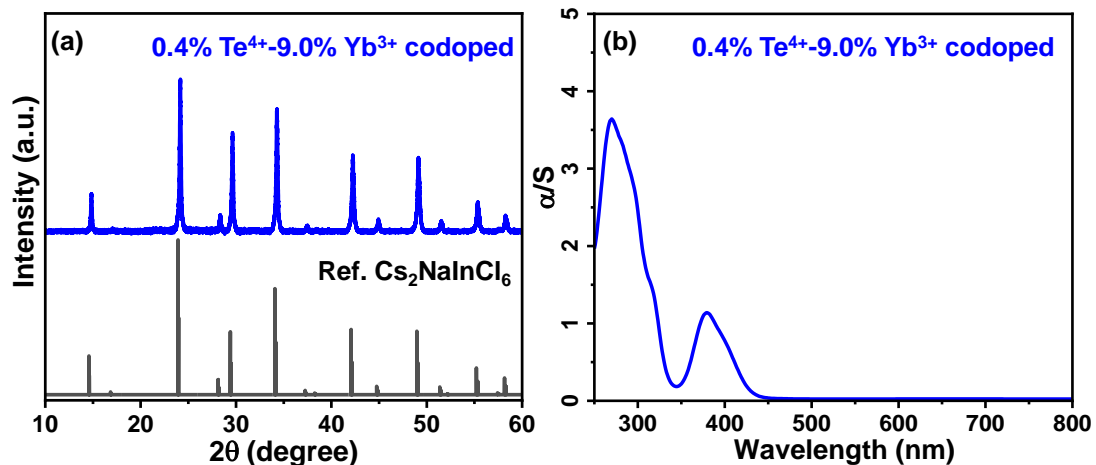
Figure 3.29: (a) Powder XRD pattern of 0.4% Te^{4+} - 9.0% Yb^{3+} codoped Cs$_2$NaInCl$_6$ compared with reference pattern of Cs$_2$NaInCl$_6$ (ICSD: 132718) in cubic phase with space group Fm$\overline{3}$m. (b) absorption spectrum of 0.4% Te^{4+} - 9.0% Yb^{3+} codoped Cs$_2$NaInCl$_6$.

Te^{4+}- Yb^{3+} codoped Cs$_2$NaInCl$_6$ emits SWIR radiation at 994 nm (Figure 3.30a) because of the $^2F_{5/2} \rightarrow {}^2F_{7/2}$ *f-f* electronic transition of Yb^{3+}. Weak visible Te^{4+} emission also observed in

this codoped system similar to 3.6% Te^{4+}-doped Cs$_2$NaInCl$_6$ (Figure 3.11a). The PL excitation spectrum in Figure 3.30a has an excitation band at 400 nm, which is assigned to Te^{4+} A-band transition (Figure 3.29b). So, the excitation spectrum confirms that the Yb^{3+} emission is getting sensitized by the codopant Te^{4+}. PL lifetime of the 994 nm emission has been found to be 3.7 ms (Figure 3.30b). This long lifetime is because of the parity forbidden *f-f* transition of Yb^{3+}. Overall, the mechanism of excitation and emission processes in Te^{4+}-Yb^{3+} codoped sample is very similar to that in the Te^{4+}-Er^{3+} codoped sample. This generic approach of doping and codoping halide double perovskites with different kinds of metal ions can yield the desired light emission properties in visible and SWIR region.[51-53]
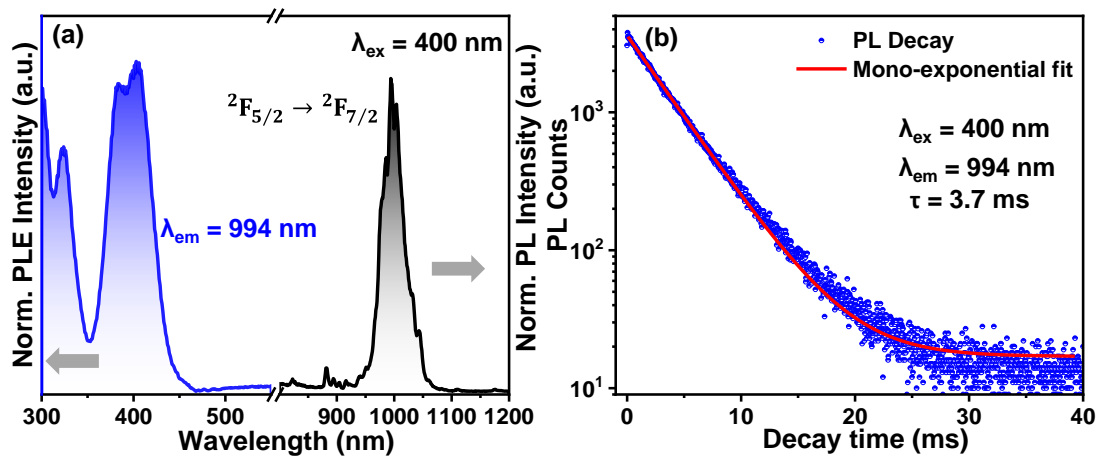
Figure 3.28: (a) PL (black) and PL excitation (blue) spectra of 0.4% Te^{4+}- 9.0% Yb^{3+} codoped Cs$_2$NaInCl$_6$. (b) PL decay profile of the sample fitted with a mono-exponential decay function.

3.4 Conclusion

We have prepared Te^{4+}-doped, Er^{3+}-doped, and Te^{4+}-Er^{3+} codoped Cs$_2$NaInCl$_6$ microcrystals using a hydrothermal synthesis method. Elemental analysis, extended structural analysis, and local atomic structure determined by EXAFS suggest a homogenous doping throughout the crystals, where both the Te^{4+} and Er^{3+} dopants occupy the octahedral In^{3+} sites of the host. The Te^{4+}-Er^{3+} codoping lead to optical excitation *via* Te^{4+} ions, and subsequent emission mainly through the Er^{3+} ions. $5s^2 \rightarrow 5s^15p^1$ electronic transitions of Te^{4+} gives three absorptions bands (A, B, and C) below the band gap energy of the host. Consequently, sub-band gap excitation around 380-450 nm is possible. Note that the obtained excitation energy of the Te^{4+} dopants is significantly lower than the Sb^{3+} or Bi^{3+} doped/codoped into similar halide perovskite systems. The excited Te^{4+} ions then can emit broad visible emission at 586 nm, or transfer its energy to the codopant Er^{3+}. Subsequently, Te^{4+}-Er^{3+} codoped Cs$_2$NaInCl$_6$ show characteristic Er^{3+} emissions at 525 nm, 551 nm, 660 nm and 1540. The SWIR emission at 1540 nm is suitable

for low-loss optical fiber communication. The PL lifetime of this emission is found to be 18.10 ms at room temperature and systematically increases to 28.26 ms at 8 K. The long lifetime is because of the Laporte forbidden *f-f* transition. Temperature dependent PL measurements in the range of 8-300 K provided detailed insights on the excitation and emission processes of Te^{4+}-doped, and Te^{4+}-Er^{3+} codoped Cs$_2$NaInCl$_6$. Also, we prepared a pc-LED by coating our 1.7% Te^{4+}- 5.9% Er^{3+} codoped Cs$_2$NaInCl$_6$ sample on commercial 398 nm LED chip. The pc-LED shows both the visible and SWIR emissions at a relatively low onset potential ~2.8 eV. Then we extended the design principle, *i.e.*, excitation by Te^{4+} and SWIR emission by Ln^{3+} to Te^{4+}-Yb^{3+} codoped Cs$_2$NaInCl$_6$ emitting at 994 nm. It appears that the design principle is a generic one for a series of Te^{4+}-Ln^{3+} codoped double perovskites, with choice of lanthanide ion deciding the emission wavelengths in both the visible and SWIR region.

2.5 References

1. Gray, M. B.; Hariyani, S.; Strom, T. A.; Majher, J. D.; Brgoch, J.; Woodward, P. M. High-Efficiency Blue Photoluminescence in the Cs$_2$NaInCl$_6$:Sb^{3+} Double Perovskite Phosphor. *J. Mater. Chem. C* **2020,** *8*, 6797-6803.

2. Dey, A.; Ye, J.; De, A.; Debroye, E.; Ha, S. K.; Bladt, E.; Kshirsagar, A. S.; Wang, Z.; Yin, J.; Wang, Y.; Quan, L. N.; Yan, F.; Gao, M.; Li, X.; Shamsi, J.; Debnath, T.; Cao, M.; Scheel, M. A.; Kumar, S.; Steele, J. A.; Gerhard, M.; Chouhan, L.; Xu, K.; Wu, X. G.; Li, Y.; Zhang, Y.; Dutta, A.; Han, C.; Vincon, I.; Rogach, A. L.; Nag, A.; Samanta, A.; Korgel, B. A.; Shih, C. J.; Gamelin, D. R.; Son, D. H.; Zeng, H.; Zhong, H.; Sun, H.; Demir, H. V.; Scheblykin, I. G.; Mora-Sero, I.; Stolarczyk, J. K.; Zhang, J. Z.; Feldmann, J.; Hofkens, J.; Luther, J. M.; Perez-Prieto, J.; Li, L.; Manna, L.; Bodnarchuk, M. I.; Kovalenko, M. V.; Roeffaers, M. B. J.; Pradhan, N.; Mohammed, O. F.; Bakr, O. M.; Yang, P.; Muller-Buschbaum, P.; Kamat, P. V.; Bao, Q.; Zhang, Q.; Krahne, R.; Galian, R. E.; Stranks, S. D.; Bals, S.; Biju, V.; Tisdale, W. A.; Yan, Y.; Hoye, R. L. Z.; Polavarapu, L. State of the Art and Prospects for Halide Perovskite Nanocrystals. *ACS Nano* **2021,** *15*, 10775-10981.

3. Li, S. R.; Hu, Q. S.; Luo, J. J.; Jin, T.; Liu, J.; Li, J. H.; Tan, Z. F.; Han, Y. B.; Zheng, Z.; Zhai, T. Y.; Song, H. S.; Gao, L.; Niu, G. D.; Tang, J. Self-Trapped Exciton to Dopant Energy Transfer in Rare Earth Doped Lead-Free Double Perovskite. *Adv. Opt. Mater.* **2019,** *7*, 1901098.

4. Mir, W. J.; Sheikh, T.; Arfin, H.; Xia, Z. G.; Nag, A. Lanthanide Doping in Metal Halide Perovskite Nanocrystals: Spectral Shifting, Quantum Cutting and Optoelectronic Applications. *NPG Asia Mater.* **2020,** *12*, 9.

5. Nie, J. H.; Zhou, B.; Fang, S. F.; Zhong, H. Z.; Li, H. A.; Shi, Y. M. Efficient Multicolor and White Photoluminescence in Erbium- and Holmium-Incorporated Cs$_2$NaInCl$_6$:Sb^{3+} Double Perovskites. *Chem. Mater.* **2022,** *34*, 6288-6295.

6. Pan, G.; Bai, X.; Yang, D.; Chen, X.; Jing, P.; Qu, S.; Zhang, L.; Zhou, D.; Zhu, J.; Xu, W.; Dong, B.; Song, H. Doping Lanthanide into Perovskite Nanocrystals: Highly Improved and Expanded Optical Properties. *Nano Lett.* **2017,** *17*, 8005-8011.

7. Ainslie, B. J. A Review of the Fabrication and Properties of Erbium-Doped Fibers for Optical Amplifiers. *J. Lightwave Technol.* **1991,** *9*, 220-227.

8. Wu, X.; Zhang, Y.; Takle, K.; Bilsel, O.; Li, Z.; Lee, H.; Zhang, Z.; Li, D.; Fan, W.; Duan, C.; Chan, E. M.; Lois, C.; Xiang, Y.; Han, G. Dye-Sensitized Core/Active Shell Upconversion Nanoparticles for Optogenetics and Bioimaging Applications. *ACS Nano* **2016,** *10*, 1060-6.

9. Buriak, J. M.; Kamat, P. V.; Schanze, K. S.; Alivisatos, A. P.; Murphy, C. J.; Schatz, G. C.; Scholes, G. D.; Stang, P. J.; Weiss, P. S. Virtual Issue on Metal-Halide Perovskite Nanocrystals—A Bright Future for Optoelectronics. *Chem. Mater.* **2017,** *29*, 8915-8917.

10. Gu, Y.; Guo, Z.; Yuan, W.; Kong, M.; Liu, Y.; Liu, Y.; Gao, Y.; Feng, W.; Wang, F.; Zhou, J.; Jin, D.; Li, F. High-Sensitivity Imaging of Time-Domain Near-Infrared Light Transducer. *Nat. Photonics* **2019,** *13*, 525-531.

11. Vasilopoulou, M.; Fakharuddin, A.; de Arquer, F. P. G.; Georgiadou, D. G.; Kim, H.; Yusoff, A. B.; Gao, F.; Nazeeruddin, M. K.; Bolink, H. J.; Sargent, E. H. Advances in Solution-Processed Near-Infrared Light-Emitting Diodes. *Nat. Photonics* **2021,** *15*, 656-669.

12. Liang, W.; Nie, C.; Du, J.; Han, Y.; Zhao, G.; Yang, F.; Liang, G.; Wu, K., Near-Infrared Photon Upconversion and Solar Synthesis Using Lead-Free Nanocrystals. *Nat. Photonics* **2023,** *17*, 346-353.

13. Reisfeld, R.; Jørgensen, C. K. Excited State Phenomena in Vitreous Materials. In *Handbook on the Physics and Chemistry of Rare Earths*, Elsevier: **1987**; Chapter 58, Vol. 9, pp 1-90.

14. Kortüm, G. *Reflectance Spectroscopy*. Springer: New York: **1969**.

15. Arfin, H.; Kaur, J.; Sheikh, T.; Chakraborty, S.; Nag, A. Bi^{3+}-Er^{3+} and Bi^{3+}-Yb^{3+} Codoped Cs$_2$AgInCl$_6$ Double Perovskite Near-Infrared Emitters. *Angew. Chem. Int. Ed.* **2020,** *59*, 11307-11311.

16. Liu, Y.; Rong, X.; Li, M.; Molokeev, M. S.; Zhao, J.; Xia, Z. Incorporating Rare-Earth Terbium(III) Ions into Cs$_2$AgInCl$_6$:Bi Nanocrystals Toward Tunable Photoluminescence. *Angew. Chem. Int. Ed.* **2020,** *59*, 11634-11640.

17. Jing, Y.; Liu, Y.; Jiang, X.; Molokeev, M. S.; Lin, Z.; Xia, Z. Sb^{3+} Dopant and Halogen Substitution Triggered Highly Efficient and Tunable Emission in Lead-Free Metal Halide Single Crystals. *Chem. Mater.* **2020,** *32*, 5327-5334.

18. Liu, Y.; Nag, A.; Manna, L.; Xia, Z. Lead-Free Double Perovskite Cs$_2$AgInCl$_6$. *Angew. Chem. Int. Ed.* **2021,** *60*, 11592-11603.

19. Saikia, S.; Joshi, A.; Arfin, H.; Badola, S.; Saha, S.; Nag, A. Sb^{3+}-Er^{3+}-Codoped Cs$_2$NaInCl$_6$ for Emitting Blue and Short-Wave Infrared Radiation. *Angew. Chem. Int. Ed.* **2022,** *61*, e202201628.

20. Harikesh, P. C.; Mulmudi, H. K.; Ghosh, B.; Goh, T. W.; Teng, Y. T.; Thirumal, K.; Lockrey, M.; Weber, K.; Koh, T. M.; Li, S.; Mhaisalkar, S.; Mathews, N. Rb as an Alternative Cation for Templating Inorganic Lead-Free Perovskites for Solution Processed Photovoltaics. *Chem. Mater.* **2016,** *28*, 7496-7504.

21. Guria, A. K.; Pradhan, N. Doped or Not Doped: Ionic Impurities for Influencing the Phase and Growth of Semiconductor Nanocrystals. *Chem. Mater.* **2016,** *28*, 5224-5237.

22. Perumal, S.; Bellare, P.; Shenoy, U. S.; Waghmare, U. V.; Biswas, K. Low Thermal Conductivity and High Thermoelectric Performance in Sb and Bi Codoped GeTe: Complementary Effect of Band Convergence and Nanostructuring. *Chem. Mater.* **2017,** *29*, 10426-10435.

23. Liu, Y.; Jing, Y.; Zhao, J.; Liu, Q.; Xia, Z. Design Optimization of Lead-Free Perovskite Cs$_2$AgInCl$_6$:Bi Nanocrystals with 11.4% Photoluminescence Quantum Yield. *Chem. Mater.* **2019,** *31*, 3333-3339.

24. Arfin, H.; Kshirsagar, A. S.; Kaur, J.; Mondal, B.; Xia, Z.; Chakraborty, S.; Nag, A. ns^2 Electron (Bi^{3+} and Sb^{3+}) Doping in Lead-Free Metal Halide Perovskite Derivatives. *Chem. Mater.* **2020,** *32*, 10255-10267.

25. Cho, J.; DuBose, J. T.; Kamat, P. V. Charge Injection from Excited Cs$_2$AgBiBr$_6$ Quantum Dots into Semiconductor Oxides. *Chem. Mater.* **2020,** *32*, 510-517.

26. Jin, S.; Li, R.; Huang, H.; Jiang, N.; Lin, J.; Wang, S.; Zheng, Y.; Chen, X.; Chen, D. Compact Ultrabroadband Light-Emitting Diodes Based on Lanthanide-Doped Lead-Free Double Perovskites. *Light. Sci. Appl.* **2022,** *11*, 52.

27. Wei, J.-H.; Liao, J.-F.; Zhou, L.; Luo, J.-B.; Wang, X.-D.; Kuang, D.-B. Indium-Antimony-Halide Single Crystals for High-Efficiency White-Light Emission and Anti-Counterfeiting. *Sci. Adv.* **2021,** *7*, eabg3989.

28. Jagadeeswararao, M.; Sim, K. M.; Lee, S.; Kang, M.; An, S.; Nam, G.-H.; Sim, H. R.; Oleiki, E.; Lee, G.; Chung, D. S. Stoichiometric Engineering of Cs$_2$AgBiBr$_6$ for Photomultiplication-Type Photodetectors. *Chem. Mater.* **2023,** *35*, 3095-3104.

29. Wang, C.-Y.; Liang, P.; Xie, R.-J.; Yao, Y.; Liu, P.; Yang, Y.; Hu, J.; Shao, L.; Sun, X. W.; Kang, F.; Wei, G. Highly Efficient Lead-Free (Bi,Ce)-Codoped Cs$_2$Ag$_{0.4}$Na$_{0.6}$InCl$_6$ Double Perovskites for White Light-Emitting Diodes. *Chem. Mater.* **2020,** *32*, 7814-7821.

30. Zhou, B.; Liu, Z. X.; Fang, S. F.; Zhong, H. Z.; Tian, B. B.; Wang, Y.; Li, H. N.; Hu, H. L.; Shi, Y. M. Efficient White Photoluminescence from Self-Trapped Excitons in Sb^{3+}/Bi^{3+}-Codoped Cs$_2$NaInCl$_6$ Double Perovskites with Tunable Dual-Emission. *ACS Energy Lett.* **2021,** *6*, 3343-3351.

31. Liu, Z.; Zhou, B.; Fang, S.; Nie, J.; Zhong, H.; Hu, H.; Li, H.; Shi, Y. Modulation of the Excitation States in All-Inorganic Halide Perovskites via Sb^{3+} and Bi^{3+} Codoping. *J. Phys. Chem. Lett.* **2023,** *14*, 1022-1028.

32. Zeng, R.; Zhang, L.; Xue, Y.; Ke, B.; Zhao, Z.; Huang, D.; Wei, Q.; Zhou, W.; Zou, B. Highly Efficient Blue Emission from Self-Trapped Excitons in Stable Sb^{3+}-Doped Cs$_2$NaInCl$_6$ Double Perovskites. *J. Phys. Chem. Lett.* **2020,** *11*, 2053-2061.

33. Caliebe, W. A.; Murzin, V.; Kalinko, A.; Görlitz, M. High-Flux XAFS-Beamline P64 at PETRA III. *AIP Conf Proc.* **2019,** *2054*, 060031.

34. Ravel, B.; Newville, M. ATHENA, ARTEMIS, HEPHAESTUS: Data Analysis for X-ray Absorption Spectroscopy Using IFEFFIT. *J. Synchrotron. Radiat.* **2005,** *12*, 537-41.

35. Noculak, A.; Morad, V.; McCall, K. M.; Yakunin, S.; Shynkarenko, Y.; Worle, M.; Kovalenko, M. V. Bright Blue and Green Luminescence of Sb(III) in Double Perovskite Cs$_2$MInCl$_6$ (M = Na, K) Matrices. *Chem. Mater.* **2020,** *32*, 5118-5124.

36. Poblete, V.; Acevedo, R.; Tanner, P. A. Spectroscopic Studies, Theoretical Models and Structural Characterization. I. -The Elpasolites Cs$_2$NaLnCl$_6$, where Ln^{3+}= Er^{3+},Yb^{3+}. *Rev. Mex. de Fis.* **1998,** *44*, 29-31.

37. Luo, J.; Wang, X.; Li, S.; Liu, J.; Guo, Y.; Niu, G.; Yao, L.; Fu, Y.; Gao, L.; Dong, Q.; Zhao, C.; Leng, M.; Ma, F.; Liang, W.; Wang, L.; Jin, S.; Han, J.; Zhang, L.; Etheridge, J.; Wang, J.; Yan, Y.; Sargent, E. H.; Tang, J. Efficient and Stable Emission of Warm-White Light from Lead-Free Halide Double Perovskites. *Nature* **2018,** *563*, 541-545.

38. Zi, L.; Xu, W.; Song, Z. J.; Sun, R.; Liu, S.; Xie, T. Y.; Zhu, J. Y.; Lu, S. Y.; Song, H. W. Highly Efficient and Stable Cs$_2$TeCl$_6$:Cr^{3+} Perovskite Microcrystals for White Light Emitting Diodes. *J. Mater. Chem. C* **2023,** *11*, 2695-2702.

39. Folgueras, M. C.; Jin, J.; Gao, M.; Quan, L. N.; Steele, J. A.; Srivastava, S.; Ross, M. B.; Zhang, R.; Seeler, F.; Schierle-Arndt, K.; Asta, M.; Yang, P. Lattice Dynamics and Optoelectronic Properties of Vacancy-Ordered Double Perovskite Cs$_2$TeX$_6$ (X = Cl$^-$, Br$^-$, I$^-$) Single Crystals. *J. Phys. Chem. C* **2021,** *125*, 25126-25139.

40. Project, T. M. Materials Data on Cs$_2$NaErCl$_6$ by Materials Project. *United States : N. p.* **2020,** DOI:10.17188/1276781.

41. Rao, M. J.; Shibata, T.; Chattopadhyay, S.; Nag, A. Origin of Photoluminescence and XAFS Study of (ZnS)$_{1-x}$(AgInS$_2$)$_x$ Nanocrystals. *J. Phys. Chem. Lett.* **2014,** *5*, 167-173.

42. Laguna-Marco, M. A.; Arias-Egido, E.; Piquer, C.; Cuartero, V.; Hernández-López, L.; Kayser, P.; Alonso, J. A.; Barker, J. A. T.; Fabbris, G.; Escanhoela, C. A.; Irifune, T. Magnetism of Ir^{5+}-Based Double Perovskites: Unraveling its Nature and the Influence of Structure. *Phys. Rev. B* **2020,** *101*, 014449.

43. Zeng, R.; Bai, K.; Wei, Q.; Chang, T.; Yan, J.; Ke, B.; Huang, J.; Wang, L.; Zhou, W.; Cao, S.; Zhao, J.; Zou, B. Boosting Triplet Self-Trapped Exciton Emission in Te(IV)-Doped Cs$_2$SnCl$_6$ Perovskite Variants. *Nano Res.* **2020,** *14*, 1551-1558.

44. Sun, J.; Zheng, W.; Huang, P.; Zhang, M.; Zhang, W.; Deng, Z.; Yu, S.; Jin, M.; Chen, X. Efficient Near-Infrared Luminescence in Lanthanide-Doped Vacancy-Ordered Double Perovskite Cs$_2$ZrCl$_6$ Phosphors via Te^{4+} Sensitization. *Angew. Chem. Int. Ed.* **2022,** *61*, e202201993.

45. Qing, X.; Wu, C.; Han, X. Efficient Near-Infrared Luminescence Based on Double Perovskite Cs$_2$SnCl$_6$ *Molecules,* **2023**, *28*, 3593.

46. Donker, H.; Smit, W. M. A.; Blasse, G. On the Luminescence of Te^{4+} in A$_2$ZrCl$_6$ (A = Cs, Rb) and A$_2$ZrCl$_6$ (A = Cs, Rb, K). *J. Phys. Chem. Solids* **1989,** *50*, 603-609.

47. Oomen, E. W. J. L.; Smit, W. M. A.; Blasse, G. On the Luminescence of Sb^{3+} in Cs$_2$NaMCl$_6$ (with M=Sc,Y,La): a Model System for the Study of Trivalent s^2 ions. *J. Phys. C: Solid State Phys.* **1986,** *19*, 3263.

48. Zhang, W.; Zheng, W.; Li, L.; Huang, P.; Gong, Z.; Zhou, Z.; Sun, J.; Yu, Y.; Chen, X. Dual-Band-Tunable White-Light Emission from Bi^{3+}/Te^{4+} Emitters in Perovskite-Derivative Cs$_2$SnCl$_6$ Microcrystals. *Angew. Chem. Int. Ed.* **2022,** *61*, e202116085.

49. Hai, L.; Shibin, J.; Jianfeng, W.; Feng, S.; Nasser, P.; Pun, E. Y. B. Er^{3+} doped Na$_2$O–Nb$_2$O$_5$–TeO$_2$ Glasses for Optical Waveguide Laser and Amplifier. *J. Phys. D: Appl. Phys.* **2003,** *36*, 812.

50. Martín-Rodríguez, R.; Geitenbeek, R.; Meijerink, A. Incorporation and Luminescence of Yb^{3+} in CdSe Nanocrystals. *J. Am. Chem. Soc.* **2013,** *135*, 13668-13671.

51. Liu, Y.; Molokeev, M. S.; Xia, Z. Lattice Doping of Lanthanide Ions in Cs$_2$AgInCl$_6$ Nanocrystals Enabling Tunable Photoluminescence. *Energy Mater. Adv.* **2021,** *2021*.

52. Zhang, A. R.; Liu, Y.; Liu, G. C.; Xia, Z. G. Dopant and Compositional Modulation Triggered Broadband and Tunable Near-Infrared Emission in Cs$_2$Ag$_{1-x}$Na$_x$InCl$_6$:Cr^{3+} Nanocrystals. *Chem. Mater.* **2022,** *34*, 3006-3012.

53. Saikia, S.; Ghosh, A.; Nag, A. Broad Dual Emission by Codoping Cr^{3+} and Bi^{3+} in Cs$_2$Ag$_{0.6}$Na$_{0.4}$InCl$_6$ Double Perovskite. *Angew. Chem. Int. Ed.* **2023,** e202307689.

Chapter 4A

Origin of Luminescence in Sb^{3+}- and Bi^{3+}-Doped Cs$_2$SnCl$_6$ 0D Perovskites: Excited State Relaxation and Spin-Orbit Coupling

Chapter 4A

Origin of Luminescence in Sb³⁺- and Bi³⁺-Doped Cs₂SnCl₆ 0D Perovskites: Excited State Relaxation and Spin-Orbit Coupling

Abstract

Sb^{3+}- and Bi^{3+}-doped Cs_2SnCl_6 zero-dimensional perovskites are emerging as stable and non-toxic phosphors for light emitting diodes. The outermost s-electrons (ns^2) of the dopants are responsible for both light absorption (ns^2 to ns^1np^1) and emission (ns^1np^1 to ns^2). At cryogenic temperatures, Sb^{3+} dopant shows two emission peaks, but Bi^{3+} shows only one emission peak. Why so? Here we address such questions, revealing the origin of luminescence in Sb^{3+}- and Bi^{3+}-doped Cs_2SnCl_6. We find that the emitting excited state ns^1np^1 is a triplet state $^3T_{1u}^*$. The notation "*" implies spin-orbit coupling between $^3T_{1u}$ and $^1T_{1u}$ states. After light absorption, $^3T_{1u}^*$ is occupied with one electron, which then undergoes Jahn-Teller distortion yielding relaxed excited state (RES). For Sb^{3+} dopant, the combination of Jahn-Teller distortion and spin-orbit coupling gives rise to two minima in RES $^3T_{1u}^*$, resulting into two emission peaks. Whereas for Bi^{3+} dopant, the spin-orbit coupling significantly dominates over the Jahn-Teller splitting yielding a single minimum in RES $^3T_{1u}^*$, and therefore, a single emission peak.

Graphical Abstract

Origin of Luminescence in Sb³⁺- and Bi³⁺-Doped Cs₂SnCl₆ 0D Perovskites: Excited State Relaxation and Spin-Orbit Coupling
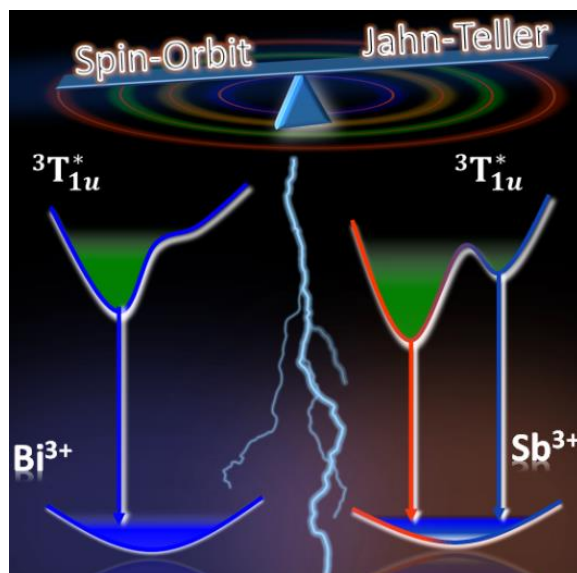
4A.1 Introduction

Zero dimensional perovskites like Cs_2SnCl_6 are more stable and environmentally benign, compared to lead-halide perovskites.[1-6] But Cs_2SnCl_6 does not show interesting optical or optoelectronic properties. To impart optical and optoelectronic functionality, ions like Sb^{3+} and Bi^{3+} with $5s^2$ and $6s^2$ outermost electronic configuration respectively, are doped into Cs_2SnCl_6.[7] Sb^{3+}-doped Cs_2SnCl_6 has been reported to emit orange light with photoluminescence (PL) quantum yield (QY) 37%, and Bi^{3+} doping resulted into blue light emission with QY 79%.[8-10] Such light emission from ns^2 electron doped perovskite systems might find potential applications as phosphor converted LED and X-ray scintillation.[11-14] But the mechanism of the light emission from Sb^{3+}- and Bi^{3+}-doped Cs_2SnCl_6 is not yet understood. Different parameters like spin-orbit coupling, Jahn-Teller distortion (electron-lattice coupling), and reduced symmetry of crystal field around the aliovalent dopants (Sb^{3+} or Bi^{3+} dopants replacing Sn^{4+}), makes optical transitions complex.[15] In this chapter, we provide insights on the optical transitions in Sb^{3+}- and Bi^{3+}-doped Cs_2SnCl_6.

Metal ions like In^+, Ga^+, Tl^+, Ge^{2+}, Sn^{2+}, Pb^{2+}, Sb^{3+} and Bi^{3+} have ns^2 electrons in the outermost orbitals, and often termed as ns^2-ions. Owing to interesting optical absorption and emission properties, ns^2-ions have been lattice-doped in a wide variety of hosts like alkali halides,[15-20] metal oxides[21-23] and zeolites[24]. The ground state of a ns^2-ion is $^1S_0$ and the excited states are $^1P_1$ and ^3P_n (n = 0, 1, 2), as shown in Figure 4A.1a. The diagonal matrix elements of spin-orbit coupling split ^3P into $^3P_0$, $^3P_1$ and $^3P_2$. For metals with high atomic number Z, off-diagonal matrix elements of spin-orbit coupling lead to mixing of $^3P_1$ and $^1P_1$ states, yielding $^3P_1^*$ and $^1P_1^*$. When the ns^2-ion is incorporated in a cubic crystal field, $^1A_{1g}$, $^3A_{1u}$, $^3T_{1u}^*$, ($^3E_u + ^3T_{2u}$) and $^1T_{1u}^*$ Mulliken notations are used corresponding to $^1S_0$, $^3P_0$, $^3P_1^*$, $^3P_2$ and $^1P_1^*$ states (Figure 4A.1a), respectively.[15] The optical transition $^1A_{1g} \rightarrow ^3A_{1u}$ is forbidden, $^1A_{1g} \rightarrow ^3T_{1u}^*$ (A-band) becomes partially allowed due to spin-orbit coupling, $^1A_{1g} \rightarrow (^3E_u + ^3T_{2u})$ (B-band) is forbidden but lattice vibrations can induce the transition, and $^1A_{1g} \rightarrow ^1T_{1u}^*$ (C-band) is allowed. For our Sb^{3+}- and Bi^{3+}-doped Cs_2SnCl_6, replacing Sn^{4+} with Sb^{3+} or Bi^{3+} is expected to give rise to a halide ion vacancy, distorting the crystal field around the dopant ions. Such distortion might fine-tune the energies of different states shown in Figure 4A.1a, but still, it serves as a good model to explain the optical properties. The A-band absorption is typically observed for Sb^{3+}- and Bi^{3+}-doped metal halide perovskites.[14] The higher energy C-

Origin of Luminescence in Sb^{3+}- and Bi^{3+}-Doped Cs$_2$SnCl$_6$ 0D Perovskites: Excited State Relaxation and Spin-Orbit Coupling

band absorption has not been clearly observed for ns^2-doped perovskites, probably because of its overlap with inter-band (valance band to conduction band) transition of the host.
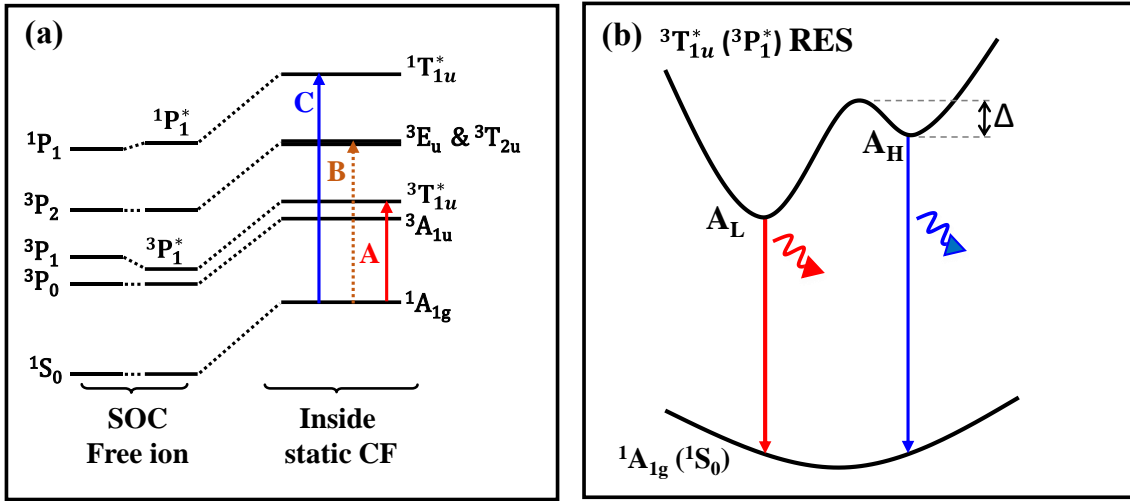
Figure 4A.1: (a) Schematic representation of ns^2-ion energy states as free ion and inside (host) static cubic field (CF). Spin-orbit coupling (SOC) splits the ^3P_n energy state and promotes mixing of $^3P_1$ and $^1P_1$ states. Mulliken notation is used to denote energy states inside static CF. A, B and C represent the optical absorption bands. (b) Schematic presentation of emission from $^3T_{1u}^*$ relaxed excited state (RES) to $^1A_{1g}$ ground state. A$_L$ and A$_H$ indicates the lower and higher energy minima of the RES. Δ represents the energy barrier for population transfer from A$_H$ to A$_L$.

We expect a stark difference between the A-band absorption ($^1A_{1g} \rightarrow {}^3T_{1u}^*$) and corresponding A-band emission ($^3T_{1u}^* \rightarrow {}^1A_{1g}$). The absorption (or excitation) occurs following the Frank-Condon approximation from ground state to an un-relaxed excited state $^3T_{1u}^*$. The lattice does not get a chance to reorganize during the fast absorption process. But after excitation, $^3T_{1u}^*$ state undergo lattice reorganization (relaxation), before the occurrence of $^3T_{1u}^* \rightarrow {}^1A_{1g}$ light emission. Therefore, we need to consider a relaxed excited state (RES) of $^3T_{1u}^*$ for A-band light emission. RES of $^3T_{1u}^*$ can have two minima on adiabatic potential energy surface (APES) (Figure 4A.1b), depending on the contributions from Jahn-Teller and spin-orbit coupling.[25-28]

Our temperature dependent (300 to 5 K) PL experiments show that the two emission peaks of Sb^{3+}-doped Cs$_2$SnCl$_6$ can be explained by the two minima of the same RES $^3T_{1u}^*$. This finding is different from prior report, where both singlet $^1T_{1u}^*$ and triplet $^3T_{1u}^*$ excited states were invoked to explain the two emission peaks in similar metal halide perovskite systems.[10, 13] For ns^2-doped alkyl halide systems, Fukuda suggested that the shape of $^3T_{1u}^*$ RES, particularly the relative depth of two minima depends on the parameter, $\frac{12\xi(1-\beta)}{b^2}$, where ξ represents spin-

Chapter 4A

Origin of Luminescence in Sb³⁺- and Bi³⁺-Doped Cs₂SnCl₆ 0D Perovskites: Excited State Relaxation and Spin-Orbit Coupling

orbit interaction, β represents difference in ground state and excited state APES curvature and b^2 represent electron-lattice interaction.[25-26] To verify such dependence in Cs_2SnCl_6 perovskite host, we compared the PL of Sb^{3+}- and Bi^{3+}-doped Cs_2SnCl_6. An increase in ξ for Bi^{3+} dopant, significantly decreases the relative depth of one of the minima of $^3T_{1u}^*$ RES, yielding a single emission peak.

4A.2 Experimental Section

4A.2.1 Chemicals

Cesium chloride (CsCl, 99.9 %), tin (II) chloride (SnCl₂, anhydrous powder, ≥99.99 %), bismuth chloride (BiCl₃, anhydrous powder, 99.998 %), antimony chloride (SbCl₃, 99.95%) and hydrochloric acid (HCl, 37 wt %, 99.99%) are purchased from Sigma Aldrich Chemicals. All the chemicals are used without any further purification.

4A.2.2 Synthesis of Doped and Undoped Cs₂SnCl₆

Cs_2SnCl_6 microcrystals are synthesized by following the method reported by Tan et al.[29] For undoped Cs_2SnCl_6 synthesis, 189.6 mg (1 mmol) $SnCl_2$, 336.72 mg (2 mmol) CsCl and 4 mL HCl are taken in a polytetrafluoroethylene (PTFE) hydrothermal autoclave. The hydrothermal autoclave is kept at 180 °C for 10 h, then cooled down to room temperature over a period of 20 h. White color crystals are formed. The crystals are filtered out, washed with ethanol and kept in vacuum for drying. The obtained sample powder is used for characterization and measurements.

For synthesis of Sb^{3+}- and Bi^{3+}-doped Cs_2SnCl_6, required dopant precursors are added while maintaining the other precursors and procedure exactly same as the undoped sample. For Sb^{3+}-doped Cs_2SnCl_6, 22.6 mg SbCl₃ (~ 0.1 mmol) is added. For Bi^{3+}-doped Cs_2SnCl_6, 31.18 mg (~ 0.1 mmol) BiCl₃ precursor is used. The used dopant percentage are close to optimized value reported in prior literature.[29-30] See Table 4A.2 for the details of dopant precursor concentrations and dopant percentages in the product.

4A.2.3 Characterization

Powder X-ray diffraction (PXRD) patterns are recorded using a Bruker D8 Advance X-ray diffraction machine equipped with Cu Kα (1.54 Å) radiation. A Zeiss Ultra Plus instrument is used for field emission scanning electron microscopy (FESEM) imaging and energy dispersive X-ray spectroscopy (EDS). For estimation of dopant (Sb and Bi) concentrations, inductively

Chapter 4A

Origin of Luminescence in Sb³⁺- and Bi³⁺-Doped Cs₂SnCl₆ 0D Perovskites: Excited State Relaxation and Spin-Orbit Coupling

coupled plasma atomic emission spectroscopy (ICP−AES) is carried out by using a ARCOS, simultaneous ICP spectrometer (SPECTRO Analytical Instruments GmbH, Germany). Diffused reflectance spectra of microcrystalline powders in the UV−visible region are recorded using a Shimadzu UV-3600 plus UV−vis−NIR spectrophotometer. Then KubelkaMunk transformation[31] is used for the analysis of diffuse reflectance spectra. It relates the reflectance data with absorption coefficient as in equation (1):

$$F(R) = \alpha/S = (1-R)^2 /2R \quad (1)$$

where F(R) is the Kubelka-Munk function, R is reflectance, α is absorption coefficient and S is the scattering factor. Steady-state photoluminescence (PL), PL Excitation (PLE), and PL decay dynamics (time-correlated single photon counting) are measured using Edinburgh FLS980 Instrument. Xenon lamp is used for steady state PL and PLE measurements. 340 nm pulsed LED (pulse width is 790 ps) and 405 nm pulsed diode laser (pulse width is 60 ps) excitation sources are used for PL decay measurement. For temperature dependent PL measurements, the sample is kept between two quartz substrate and mounted on a gold-plated sample holder. The sample holder is placed in a closed cycle He cryostat (Advanced Research Systems) attached with a temperature controller (Lake Shore Cryotronics) to achieve the desired lower temperatures.

4A.3 Results and Discussion

4A.3.1 Synthesis and Characterization of Undoped and Doped Cs₂SnCl₆
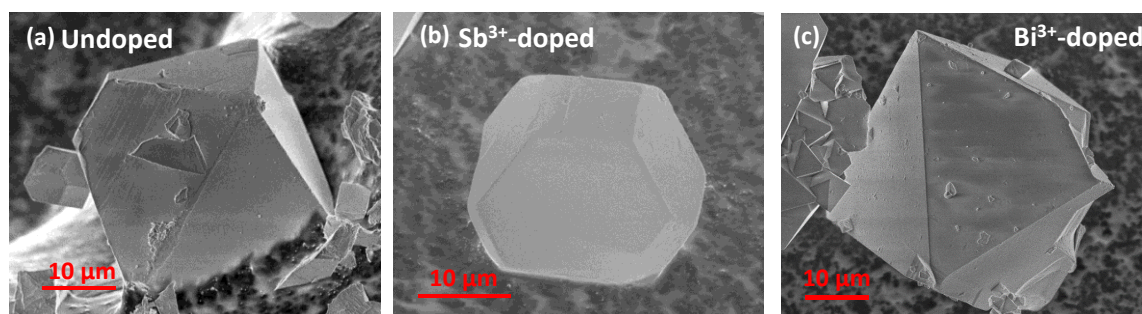
Figure 4A.2: FESEM images of (a) undoped (b) Sb³⁺-doped and (c) Bi³⁺-doped Cs₂SnCl₆.

We have synthesized undoped, Sb³⁺-doped, and Bi³⁺-doped Cs₂SnCl₆ by following a prior report.[8] (see the experimental section for details). Field emission scanning electron microscopy (FESEM) show micrometer size crystals for all the samples (Figure 4A.2). Energy dispersive X-ray spectroscopy (EDS) of all the samples show atomic ratio of Cs:Sn:Cl is close to 2:1:6

Origin of Luminescence in Sb³⁺- and Bi³⁺-Doped Cs₂SnCl₆ 0D Perovskites: Excited State Relaxation and Spin-Orbit Coupling

(see Table 4A.1), confirming the formation of Cs_2SnCl_6. The dopant concentration is determined by inductively coupled plasma atomic emission spectroscopy (ICP-AES). ICP-AES data in Table 4A.2 estimates a 1.8% Sb and 3.8% Bi (dopant % = 100×[dopant]/([dopant]+[Sn]) in the product for the dopant precursor concentration of 9.0 %.

Table 4A.1: Elemental analysis obtained from EDS data of undoped, Sb^{3+}-doped and Bi^{3+}-doped Cs_2SnCl_6. EDS data shows that presence of Sb and Bi in the corresponding doped samples. But the dopant concentration is very small for a reliable quantitative estimation using EDS.

Sample	Cs	Sn	Cl
Undoped	2.0	1.0	6.2
Sb^{3+}-doped	1.9	1.0	6.0
Bi^{3+}-doped	2.1	1.0	6.2

Table 4A.2: Dopant precursor feeding concentration and ICP-AES determined dopant concentration in the product. Dopant % = 100×[dopant]/ ([dopant] +[Sn]).

Sample	Dopant % used in precursor	Dopant % in product (from ICP-AES)
Sb^{3+}-doped Cs_2SnCl_6	9.0	1.8
Bi^{3+}-doped Cs_2SnCl_6	9.0	3.8
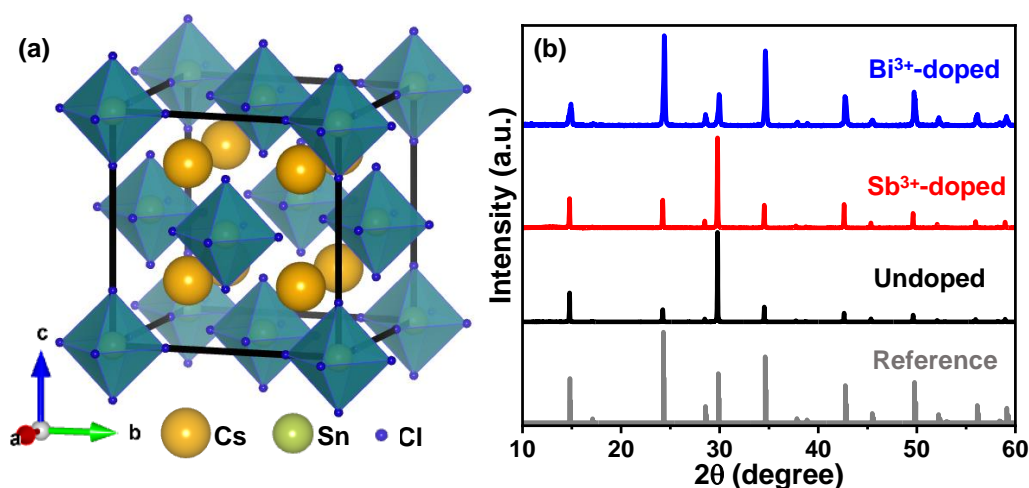
Figure 4A.3: (a) Schematics of crystal structure of Cs_2SnCl_6. The sizes of spheres representing the atoms are not according to relative size of atoms. (b) Powder XRD patterns of undoped, Sb^{3+}-doped and Bi^{3+}-doped Cs_2SnCl_6 along with reference data (ICSD#9023) for cubic phase of Cs_2SnCl_6.

Origin of Luminescence in Sb³⁺- and Bi³⁺-Doped Cs₂SnCl₆ 0D Perovskites: Excited State Relaxation and Spin-Orbit Coupling

Cs_2SnCl_6 is known to form cubic vacancy ordered 0D perovskite structure in which each $[SnCl_6]^{2-}$ octahedra are isolated, as shown by the schematic in Figure 4A.3a.[8] Powder X-ray diffraction (PXRD) patterns of undoped and Sb^{3+}-doped Cs_2SnCl_6 match with the reference data (ICSD# 9023) of Cs_2SnCl_6 with cubic space group Fm3m. The ionic radii of Sn^{4+} and Sb^{3+} in octahedral environment are 0.69 Å and 0.76 Å respectively.[32-33] Furthermore, the aliovalent substitution of Sn^{4+} with Sb^{3+} will lead to Cl^- vacancy, maintaining the charge neutrality of the system. So, one would expect some shift in XRD peak positions after Sb^{3+} doping. But the XRD data in Figure 3b do not show noticeable peak shift after Sb^{3+} doping, because of small amount (1.8%) of doping.

4A.3.2 Optical Properties of Sb^{3+} Doped Cs_2SnCl_6
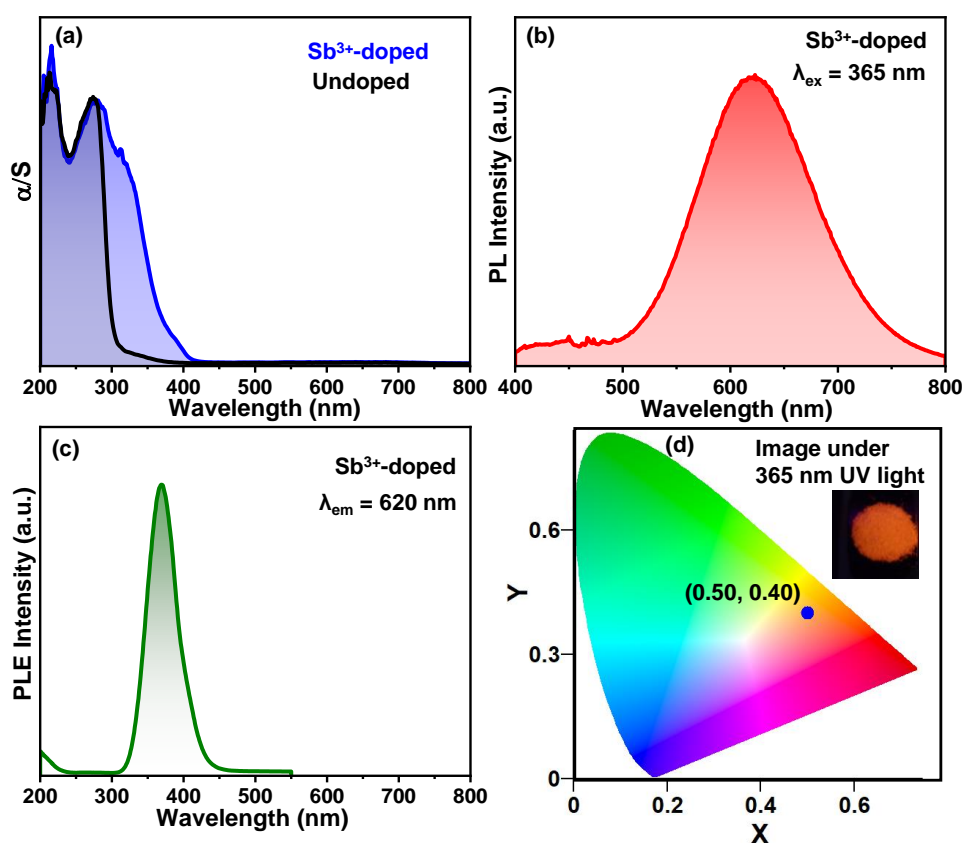
Figure 4A.4: (a) Optical absorption spectra of undoped and Sb^{3+}-doped Cs_2SnCl_6. Absorption spectra are obtained from Kubelka-Munk transformation of diffuse reflectance spectrum.[31] α is absorption coefficient and S is a scattering factor. (b) PL ($\lambda_{ex} = 365$ nm) spectrum and (c) PL Excitation ($\lambda_{em} = 620$ nm) spectrum of Sb^{3+}-doped Cs_2SnCl_6.

UV-visible absorption spectrum (Figure 4A.4a) of undoped Cs_2SnCl_6 shows a sharp absorption edge at ~314 nm, similar to a prior report.[34] Sb^{3+} doping introduces new absorption features at longer wavelengths that can be assign to A-band ($^1A_{1g} \rightarrow {}^3T_{1u}^*$) absorption of Sb^{3+}-ion.[10]

Chapter 4A

Origin of Luminescence in Sb³⁺- and Bi³⁺-Doped Cs₂SnCl₆ 0D Perovskites: Excited State Relaxation and Spin-Orbit Coupling

Undoped Cs_2SnCl_6 is non-luminescent. Interestingly, Sb^{3+}-doped Cs_2SnCl_6 shows a broad emission centered at 620 nm as shown in Figure 4A.4b. The full width at half maxima (FWHM) of the emission is 125 nm (0.40 eV). The PL excitation (PLE) spectrum for 620 nm emission is centered at 365 nm, and correspond to Sb^{3+} related A-band absorption (Figure 4A.4c). Photograph of the sample under 365 nm UV light shows orange color emission, as shown in inset of Figure 4A.4d. The Commission Internationale de l'Eclairage (CIE) diagram (Figure 4A.4d) obtained from the PL spectrum in Figure 4A.4b also agree with the neon orange emission with coordinate (0.50, 0.40).

4A.3.3 Temperature Dependent Optical Properties of Sb^{3+} Doped Cs_2SnCl_6
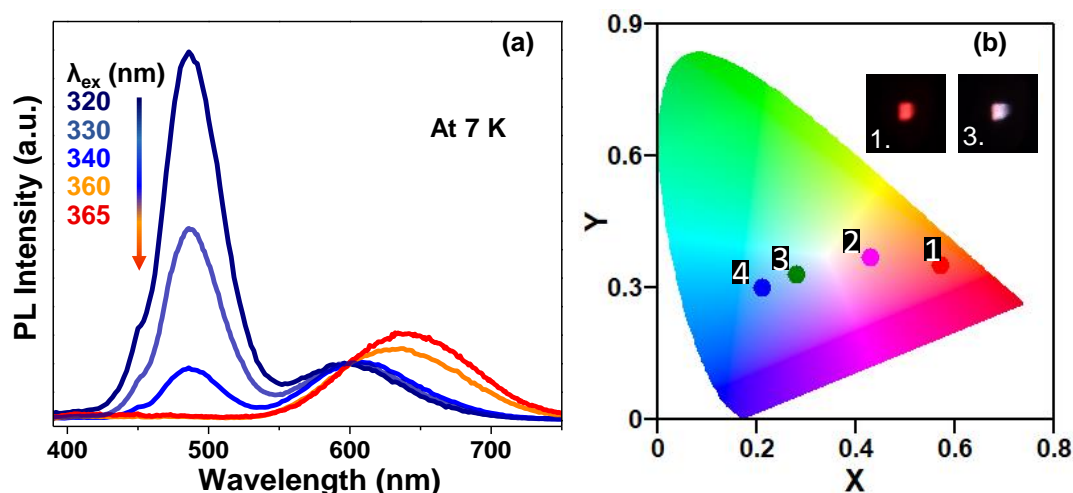
Figure 4A.5: (a) Excitation wavelength dependent emission spectra of Sb^{3+}-doped Cs_2SnCl_6 at 7 K. Corresponding CIE diagram in (b). The points represent the coordinates of emission color on excitation at (1) 365 nm (2) 340 nm, (3) 330 nm and (4) 320 nm. Digital photographs in inset (b) show the emission from sample at 7 K at (1) 365 nm and (3) 330 nm excitation.

To investigate the origin of emission, we compared PL at different temperatures. Figure 4A.5a shows the PL spectra of Sb^{3+}-doped Cs_2SnCl_6 measured at 7 K, after excitation at different wavelengths. The PL spectra changes rather unusually with excitation wavelength. At lower excitation wavelengths (320-340 nm), two emission peaks appear at 490 nm and 600 nm. Whereas at relatively longer excitation wavelengths (> 350 nm), a single emission peak around 620 nm is observed. The intensity of PL peak at 490 nm decreases, and that of longer wavelength emission increases systematically with increasing the excitation wavelength. Consequently, different emission color is obtained at different excitation wavelengths, as shown by the CIE diagram and photographs of PL colors in Figure 4A.5b. The inset of Figure 4A.5b show the digital image of the sample at 7 K on 365 nm (1) and 330 nm (3) excitation.

Origin of Luminescence in Sb³⁺- and Bi³⁺-Doped Cs₂SnCl₆ 0D Perovskites: Excited State Relaxation and Spin-Orbit Coupling

For comparison, Figure 4A.6 show the PL spectrum of undoped Cs_2SnCl_6 measured at 7.8 K. A very weak and broad emission with a peak at 640 nm is observed for the undoped sample after excitation at 330 nm. Therefore, the intense dual emission peaks at 490 nm and 600 nm observed for the Sb^{3+}-doped sample (Figure 4A.5a) is attributed to the Sb^{3+} dopants.
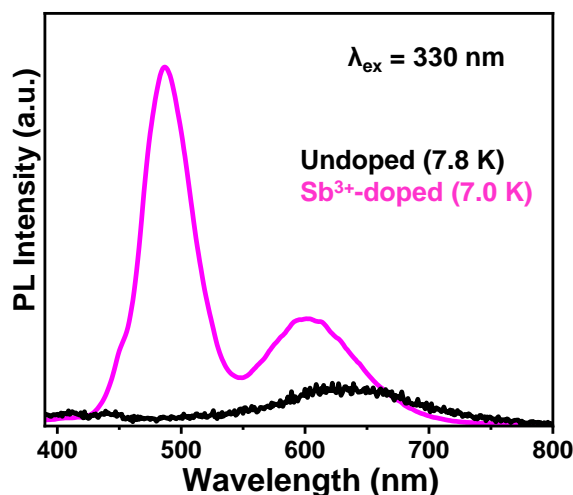
Figure 4A.6: Comparison of PL spectra of undoped and Sb^{3+}-doped Cs_2SnCl_6 around 7 K.

Two emission peaks indicate two different emissive excited states. Does it mean that the two excitations, A-band and C-band, gives rise to the two emission peaks at longer and shorter wavelengths, respectively? To answer this question, we recorded the PLE spectra for the emissions, at 7 K. Figure 4A.7 shows that PLE peaks are centered at 325 nm (3.82 eV) and 345 nm (3.59 eV) for 490 nm and 600 nm emissions, respectively. The energy difference between these two PLE peaks is only 0.23 eV. It has been shown in prior literature that the difference between A-band and C-band absorption energy for Sb^{3+}-doped KCl is ~1.6 eV.[35] Even the difference between A-band and weak B-band absorption energy for Sb^{3+}-doped KCl is ~ 1.3 eV, and the energy differences between these absorption bands remains similar for the entire measured temperature range (15-297 K). Not only Sb^{3+}-doped KCl, for a large number of combination of different ns^2 dopant ions and hosts, the energy difference between the A-band and its higher energy absorptions are found to be significantly larger than 1 eV.[35] Therefore, the observed two PLE peaks (Figure 4A.7), with a difference of only 0.23 eV, cannot be assigned to A-band and C-band (or B-band) excitations. Consequently, two emissions peaks (Figure 4A.5a) observed at 490 and ~600 nm cannot be assigned to singlet C-band emission ($^1T^*_{1u} \rightarrow {}^1A_{1g}$) and triplet A-band emission ($^3T^*_{1u} \rightarrow {}^1A_{1g}$). Instead, only the A-band excitation leading to the formation of RES $^3T^*_{1u}$ (Figure 4A.1b) giving two triplet emission minima, might explain the experimental results shown in Figure 4A.5a and 4A.7. Note that a similar RES

Chapter 4A

Origin of Luminescence in Sb³⁺- and Bi³⁺-Doped Cs₂SnCl₆ 0D Perovskites: Excited State Relaxation and Spin-Orbit Coupling

$^3T_{1u}^*$ was previously utilized to explain the emission properties of Sb³⁺-doped alkali halides single crystals.[27]
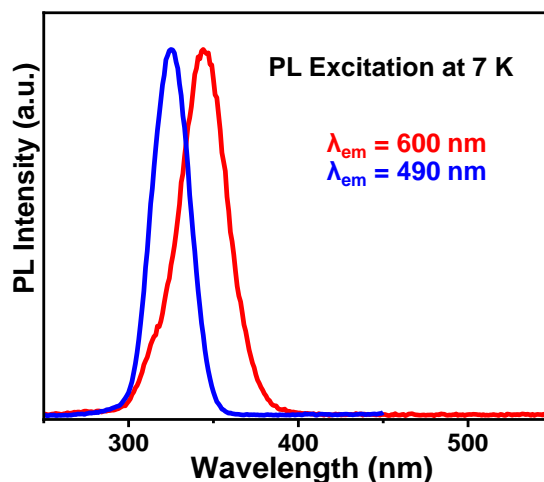
Figure 4A.7: Temperature dependent PL excitation spectra of Sb³⁺-doped Cs₂SnCl₆ for 490 nm and 600 nm emissions at 7 K.
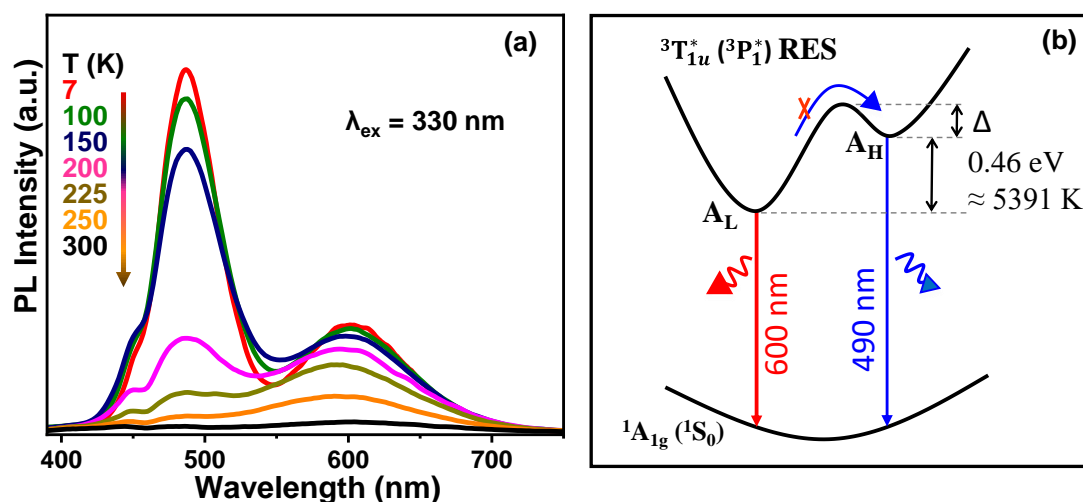
Figure 4A.8: Temperature dependent PL spectra of Sb³⁺-doped Cs₂SnCl₆ at 330 nm excitation. (b) Schematic representation of two energy minima A_H and A_L of $^3P_1^*$ RES of Sb³⁺-doped Cs₂SnCl₆. The difference between two emission energies is 0.46 eV. If we consider that both the emissions involve similar energies of $^1A_{1g}$ state, then we can assume that the energy difference between A_H and A_L is 0.46. So, the barrier for back transfer of charge carriers from A_L to A_H is very high, around 0.46 eV (≈ 5391 K) + Δ. So, A_L to A_H back transfer is negligible in the temperature range of 7 K to 400 K.

To have more insights on the PL properties, Figure 4A.8a shows how the dual emission features with excitation at 330 nm, depend on temperature. PL emission intensity of the of the 490 nm emission decreases with increasing temperature. The decrease in 490 nm emission intensity is accompanied by an increased intensity of 600 nm emission. This temperature dependent correlation between the intensity of both emissions can again be explained by the RES

Chapter 4A

Origin of Luminescence in Sb³⁺- and Bi³⁺-Doped Cs₂SnCl₆ 0D Perovskites: Excited State Relaxation and Spin-Orbit Coupling

$^3T^*_{1u}$ (Figure 4A.1b). There is an energy barrier "Δ" between the high-energy minimum (A_H) and low-energy minimum (A_L), as shown in Figure 4.1b. An increase in temperature provides thermal activation energy for electron transfer from A_H to A_L, overcoming the barrier Δ. The magnitude of the barrier is small since we observe the 490 nm emission just below 250 K. This transfer of excited state population from A_H to A_L explains the decrease in PL intensity of high-energy peak at 490 nm, at the expense of increase in intensity of low-energy peak at 600 nm. However, the barrier for the back transfer of electrons from A_L to A_H is too high (Figure 4A.8b) to be observed in the measured temperature dependent PL.
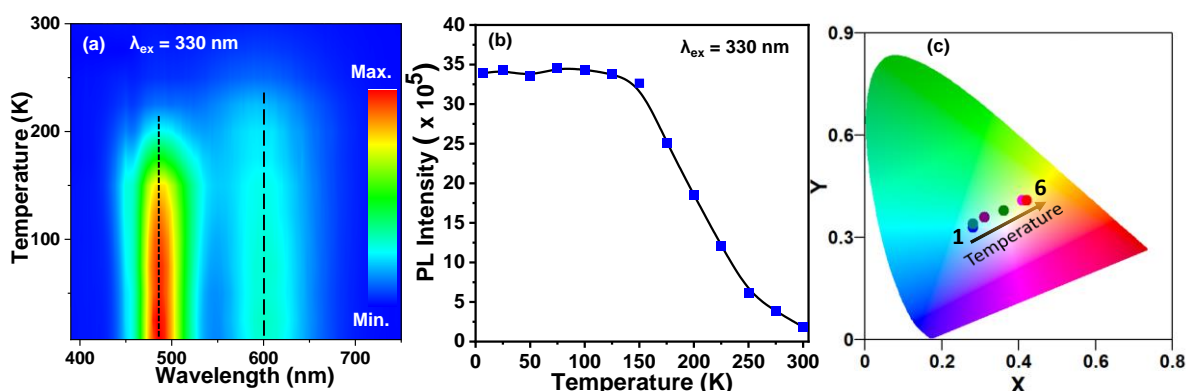
Figure 4A.9: (a) Temperature dependent Pseudo colormap of Sb³⁺-doped Cs₂SnCl₆ at 330 nm excitation. The black dash lines indicate the emission peak positions. (b) Temperature dependence of integrated emission intensity at 330 nm excitation. The blue squares are representing the experimental data and the black line is a guide to eye. (c) CIE diagram of temperature dependent emission at 330 nm wavelength excitation. The points (1 to 6) represent emission color at 7 K, 150 K, 175 K, 200 K, 225 K and 250 K respectively along the arrow.

Figure 4A.9a shows the pseudo colormap of the temperature dependent PL after excitation at 330 nm. The trends shown by the representative spectra in Figure 4A.8a, is maintained throughout all the temperatures as shown in the colormap. Overall, the peak positions of both emissions, and their FWHM, do not change much with measurement temperature. These are signatures of emissions from localized atom related states. The integrated intensity including both the emissions increases with decreasing temperature (see Figure 4A.9b) till ~150 K, because of the suppression of non-radiative decay channels. At further lower temperatures, the intensity remains largely unchanged. Interestingly, since the intensity ratio between the two peaks changes with temperature, the overall emission color also changes with temperature. CIE diagram in Figure 4A.9c shows the temperature dependent color changes. Such ratiometric change in PL intensity and color change, might find significance in remote sensing of temperature.[36]

Origin of Luminescence in Sb³⁺- and Bi³⁺-Doped Cs₂SnCl₆ 0D Perovskites: Excited State Relaxation and Spin-Orbit Coupling

Figure 4A.10a shows the pseudo colormap of temperature dependent PL of Sb^{3+}-doped Cs_2SnCl_6, after excitation at 365 nm. Some of the representative spectra are also shown in Figure 4A.10b. A single-peak emission is observed at all temperatures. The peak position remains largely unchanged from 300 K to 200 K region, but further decrease in temperature to 7 K shows a small red-shift. The origin of this small red-shift at lower temperatures is not yet understood, but might be related to possible modification in local structure at lower temperatures. The PL remains broad (FWHM = 103 nm = 0.32 eV) even at 7 K, indicating localized or trapped emission center. Figure 4A.10c shows that the PL intensity increases with decreasing temperatures from 300 K to 200 K because of the suppression in thermal quenching. Further decrease in temperature slightly decreases the PL intensity. It is noteworthy that PL excitation edge blue-shifts with decrease in temperature (Figure 4A.10d). This blue-shift in PLE decreases the excitation by 365 nm light, which in turn results into the decrease in PL intensity (Figure 4A.10b) below 200 K.
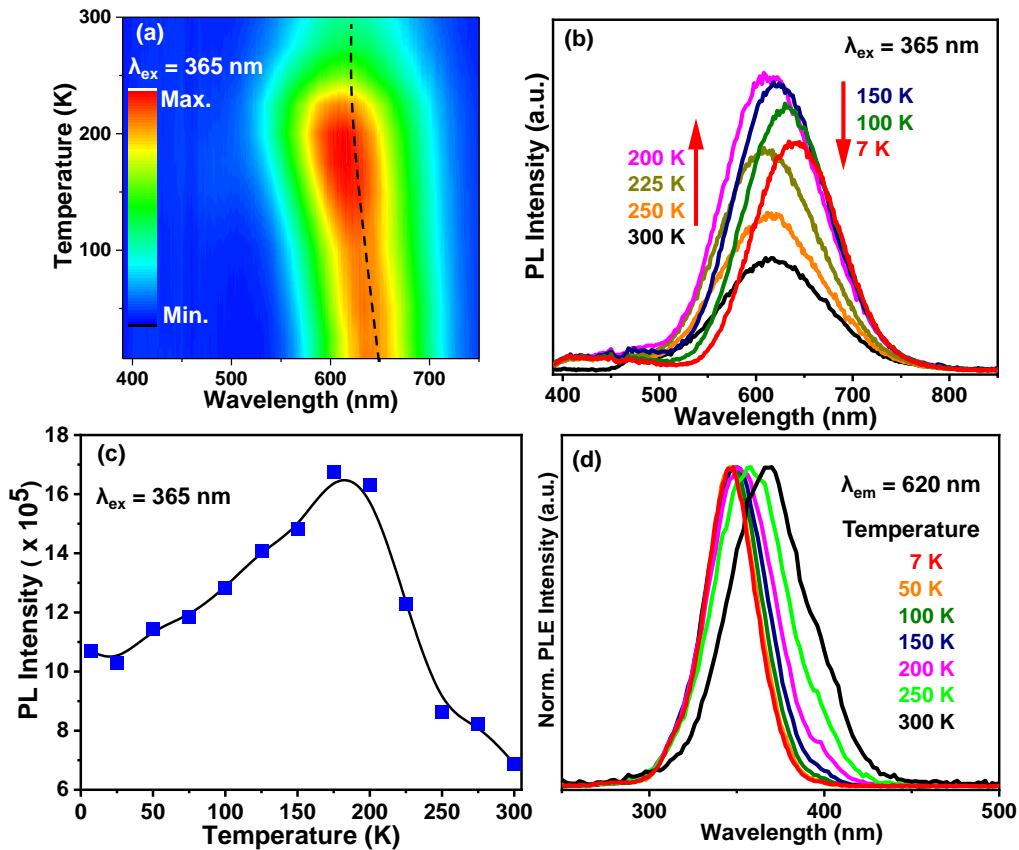
Figure 4A.10: Temperature dependent emission of Sb^{3+}-doped Cs_2SnCl_6 at 365 nm excitation (a) Pseudo colormap. The black dash line indicates the emission peak position. (b) emission spectrum (c) Temperature dependence of integrated emission intensity Sb^{3+}-doped Cs_2SnCl_6 after excitation at 365 nm. The blue squares are representing the experimental data and the black line is a guide to eye. (d) Temperature dependent PL excitation (PLE) spectra of Sb^{3+}-doped Cs_2SnCl_6 for 620 nm emission.

Origin of Luminescence in Sb³⁺- and Bi³⁺-Doped Cs₂SnCl₆ 0D Perovskites: Excited State Relaxation and Spin-Orbit Coupling
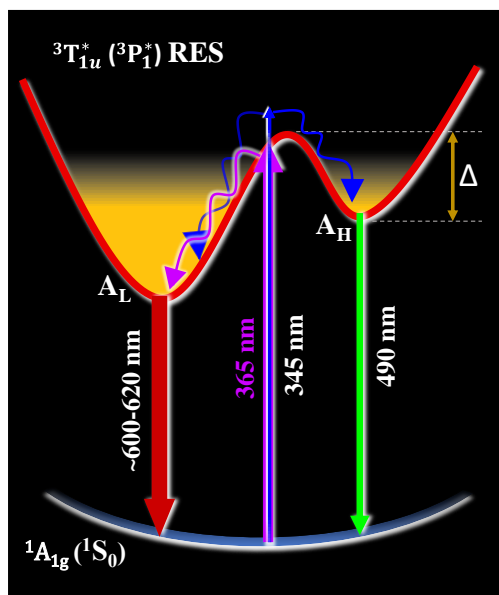
Figure 4A.11: Schematic representation of light emission mechanism of Sb^{3+}-doped Cs_2SnCl_6.

We summarize the excitation and emission process of Sb^{3+}-doped Cs_2SnCl_6 using the schematic shown in Figure 4A.11. Excitation takes place corresponding to $^1A_{1g} \rightarrow$ $^3T_{1u}^*$ transition (A-band). The singly occupied $^3T_{1u}^*$ state then splits into two minima due to the combination of dynamic Jahn-Teller effect and spin-orbit coupling. The configuration coordinates of both the RES minima are far from the coordinate of the ground state minimum. Therefore, direct excitation from the ground state to the RES minima is not observed, following Frank-Condon principle. Instead, excitation happens at lower wavelengths (higher energies) ~365 nm. The excited state population then non-radiatively transfers to the minimum A_L, emitting light with peak around 600-620 nm. At slightly lower excitation wavelengths ~345 nm, the feasibility of transferring the excited state population to A_H minimum increases, sufficiently populating of both A_L and A_H minima. Consequently, two emission peaks around 490 and 600 nm are observed at 7 K. At different excitation wavelengths, the fraction of population is divided differently between A_L and A_H, as shown in Figure 4A.12a, b and c. Therefore, we observe a small difference in the PLE spectra for 490 and 600 nm emission (Figure 4A.7). As the temperature increases, the excited state population starts transferring from A_H to A_L minimum, overcoming the barrier Δ. Consequently, the ratio I_{490}/I_{600} of emission intensity at 490 nm (I_{490}) and 600 nm (I_{600}) decreases (see Figure 4A.8a and Figure 4A.12d) with increasing temperature. Figure 4A.12e shows a bi-exponential PL decay for longer

Origin of Luminescence in Sb³⁺- and Bi³⁺-Doped Cs₂SnCl₆ 0D Perovskites: Excited State Relaxation and Spin-Orbit Coupling

wavelength (600-620 nm) emission with lifetimes 374 ns (94.5% contribution) and 5.84 µs (5.5% contribution). Jing et al. reported similar lifetime for 615 nm emission and 115 ns lifetime for 490 nm emission.[10] So both the emissions show long lifetimes ranging from hundreds of ns to microsecond, indicating the spin-forbidden nature of the transitions, which became partially allowed after the spin-orbit coupling. The difference in lifetime for both emissions is possibly due to difference in local structures at the RES minima A_H and A_L.[25, 37-38]
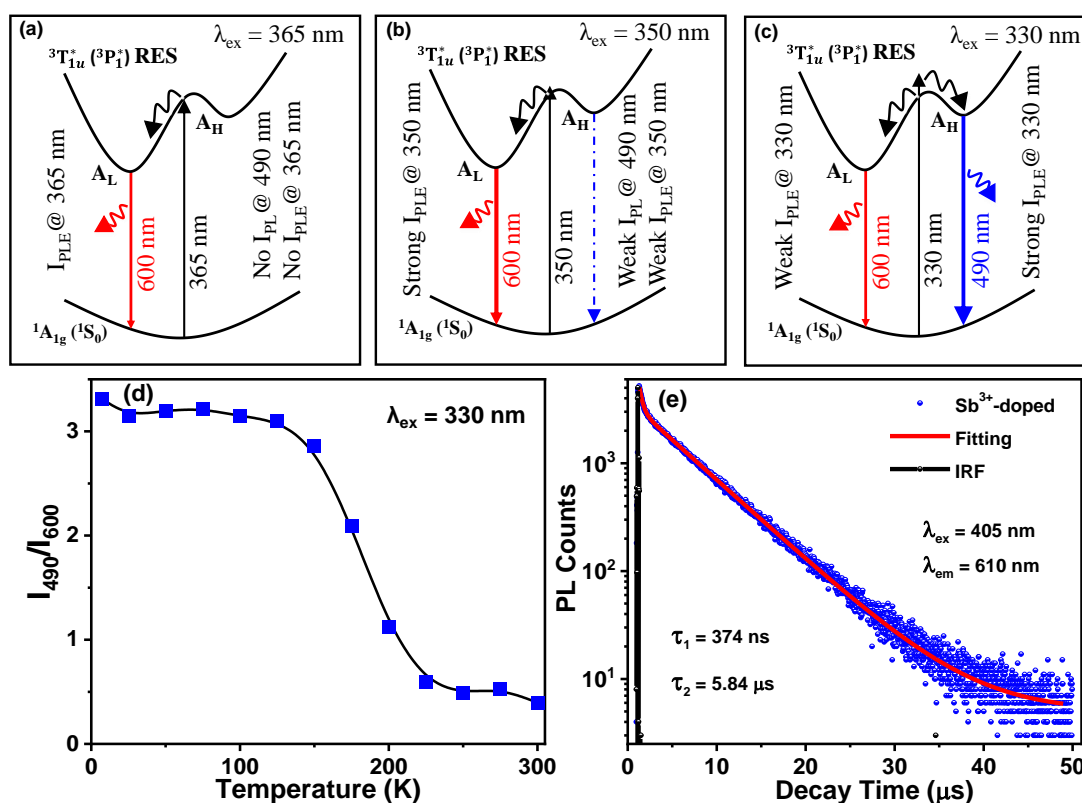
Figure 4A.12: Schematic presentations showing division of excited population between A_L and A_H minima, at three different representative excitation wavelengths (a) 365 nm (b) 350 nm (c) 330 nm, for Sb³⁺-doped Cs₂SnCl₆. I_{PLE} and I_{PL} represent the PLE and PL intensity, respectively. The fraction of population distribution between A_L and A_H changes with excitation wavelengths, that explains the small difference in the observed (Figure 4A.7) PLE spectra for 490 nm and 600 nm emission. (d) Temperature dependence of I_{490}/I_{600} emission intensity ratio. I_{490} and I_{600} are emission intensity at 490 nm and 600 nm. The blue squares are representing the experimental data and the black line is a guide to eye. (e) PL decay of 610 nm emission of Sb³⁺-doped Cs₂SnCl₆ at room temperature. 405 nm pulsed diode laser (pulse width 60 ps) is used for excitation. The decay curve is fitted with bi-exponential decay function.

4A.3.4 Optical Properties of Bi³⁺ -doped Cs₂SnCl₆

Now to investigate the role of spin-orbit coupling, Bi³⁺ ion is doped instead of Sb³⁺ ion. Figure 4A.13a shows that Bi³⁺ doping introduces a sharp absorption feature at 375 nm. Similar

Origin of Luminescence in Sb³⁺- and Bi³⁺-Doped Cs₂SnCl₆ 0D Perovskites: Excited State Relaxation and Spin-Orbit Coupling

absorption feature with Bi^{3+} doping is quite common with different metal halide perovskite host materials with very small amounts of dopants.[39-40] Therefore, such absorption feature is not characteristic of a particular host or defect bands in that host. Instead, we assign the new absorption feature to A-band ($^1A_{1g} \rightarrow {}^3T_{1u}^*$) transition of Bi^{3+} ion. Stronger spin-orbit coupling in Bi^{3+} ions is expected to make the transition more allowed compared to that of Sb^{3+} ions. Bi^{3+}-doped Cs_2SnCl_6 emits blue light with a peak at 450 nm with FWHM of 63.7 nm (0.39 eV) as shown in Figure 4A.13b. The PLE spectrum for 450 nm emission is centered at 353 nm. The onset of PLE spectrum matches with the new absorption feature introduce due to Bi^{3+} doping (Figure 4A.13b). So, the 450 nm emission peak originates due to A-band ($^1A_{1g} \rightarrow {}^3T_{1u}^*$) excitation of Bi^{3+} dopants. Bi^{3+}-doped Cs_2ZrCl_6 also show similar PLE.[39] So both the absorption and the PLE appear to originate from Bi^{3+} states, without directly involving the conduction/valence band of the host.
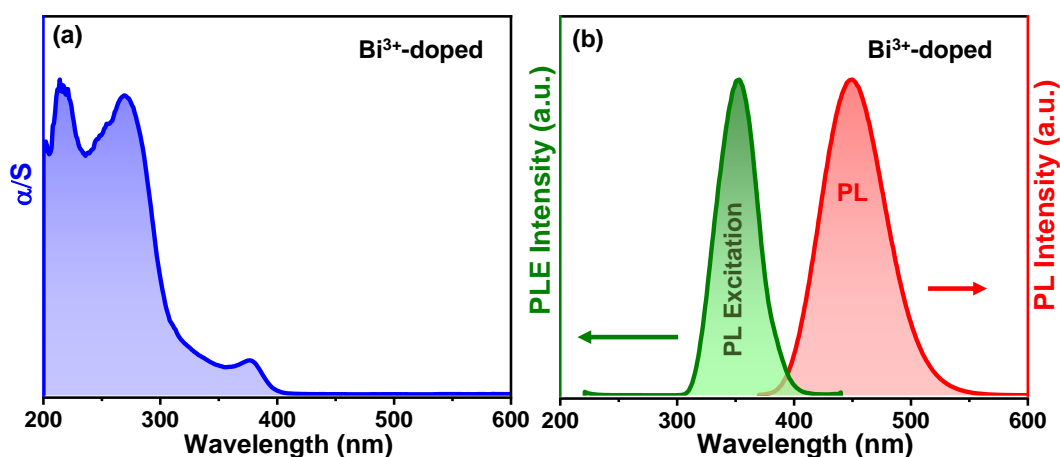
Figure 4A.13: Optical properties of Bi^{3+}-doped Cs_2SnCl_6. (a) UV-visible absorption, PL (λ_{ex} = 350 nm) and PL Excitation (λ_{em} = 450 nm) spectra at room temperature. α and S are absorption coefficient and scattering factor respectively. α/S is obtained by Kubelka-Munk transformation of diffuse reflectance spectra of powder sample. The arrows indicate towards the associated Y-axis.

Temperature dependent PL spectra in Figure 4A.14a show that the Bi^{3+}-doped Cs_2SnCl_6 exhibit a single emission peak at all temperatures in the range of 5.6 K to 300 K. Pseudo colormap in Figure 4A.14b also confirms that a single emission peak is observed at all the measured temperatures. The peak position and FWHM do not show significant changes with temperature (Figure 4A.14c), indicating such results are characteristics of localized emission. Expectedly, the PL intensity somewhat decreases with increasing temperature (Figure 4A.14d) due to non-radiative thermal quenching.

Origin of Luminescence in Sb³⁺- and Bi³⁺-Doped Cs₂SnCl₆ 0D Perovskites: Excited State Relaxation and Spin-Orbit Coupling
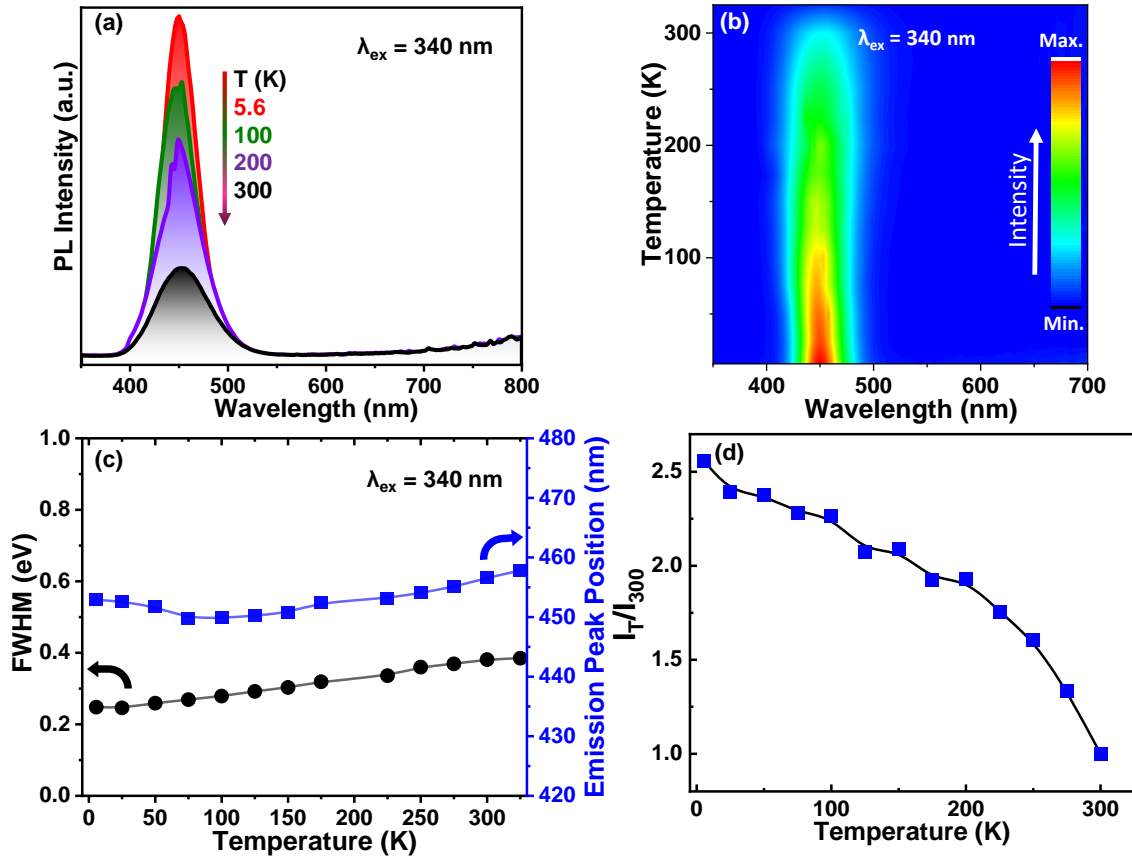
Figure 4A.14: (a) Temperature dependent PL spectra of Bi^{3+}-doped Cs$_2$SnCl$_6$ at 340 nm excitation and corresponding contour plot in (b). (c) Emission peak position (blue squares) and emission full width at half maxima (FWHM, black circles) at 340 nm excitation. The square and circle symbols are experimental data and lines are a guide to eye. (d) The relative change in emission intensity with temperature. I$_T$ and I$_{300}$ are integrated PL intensity at a variable temperature T and 300 K, respectively. Blue squares represent the experimental data and black line is just guide to eye.
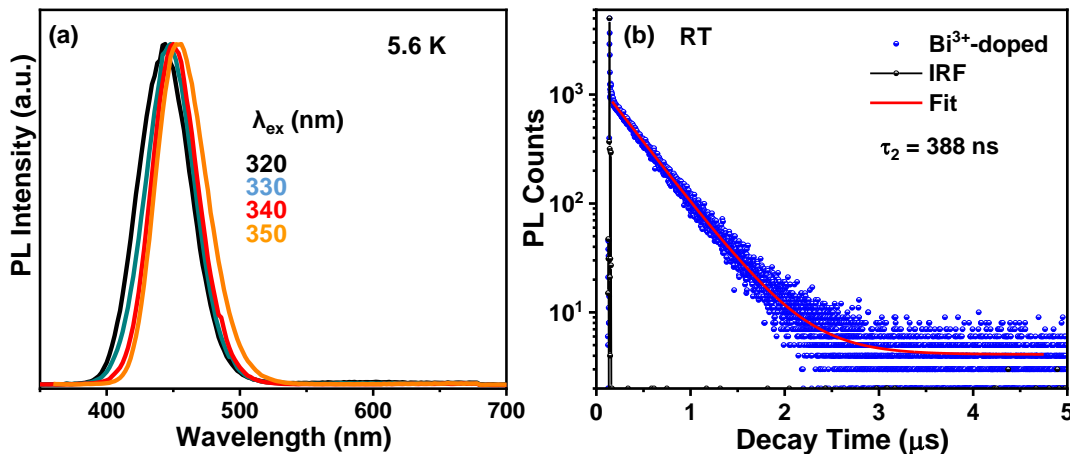
Figure 4A.15: (a) Excitation wavelength dependent PL excitation spectra of Bi^{3+}-doped Cs$_2$SnCl$_6$. (b) PL decay of 450 nm emission of Bi^{3+}-doped Cs$_2$SnCl$_6$. 340±10 nm pulsed LED (pulse width 790 ps) is used for excitation. The experimental decay curve is fitted with a mono-exponential decay function with lifetimes 388 ns are obtained.

Origin of Luminescence in Sb³⁺- and Bi³⁺-Doped Cs₂SnCl₆ 0D Perovskites: Excited State Relaxation and Spin-Orbit Coupling

Figure 4A.16: Proposed emission mechanism. Relaxed excited state (RES) emits single emission.

A variation in excitation wavelength also gives a single emission peak at 5.6 K, as shown in Figure 4A.15a. The emission peak slightly red-shifts with increasing excitation wavelengths. The 450 nm emission has a lifetime of 388 ns, as shown in Figure 4A.15b. Tan et al. also reported similar PL lifetime of 343.3 ns for the 450 nm emission.[8]

The observation of predominant single emission peak for Bi^{3+} dopant (Figure 4A.14a and 4A.15b) for all measured temperatures and excitation wavelengths is in stark difference with the observed two peaks for Sb^{3+}-doped Cs_2SnCl_6 (Figure 4A.5a and 4A.8a). It was suggested earlier that for ns^2 doped alkali halide systems, the RES can have single peak $^3T_{1u}^*$ k for high values of $\frac{12\xi(1-\beta)}{b^2}$.[25] For both Sb^{3+}- and Bi^{3+}-doped Cs_2SnCl_6, the host remains the same suggesting similar values of β and b^2 for both samples. But Bi^{3+} doping will have significantly higher value ξ (spin-orbit interaction), increasing $\frac{12\xi(1-\beta)}{b^2}$. This increase can lead to essentially a single minimum in the RES $^3T_{1u}^*$ as shown in Figure 4A.16. Therefore, a single emission peak is observed for Bi^{3+} doping. Similar single emission peak at different temperatures and A-band excitation was also observed in Bi^{3+}- and Tl^+-doped KCl, because of high value of ξ for both the dopants.[25, 38, 41]

4A.4 Conclusion

In summary, Sb^{3+}-doped Cs_2SnCl_6 show dual emission at low temperatures. The dual emission arises from the two minima on RES of $^3T_{1u}^*$, which exist due to moderate spin-orbit coupling

Chapter 4A

Origin of Luminescence in Sb³⁺- and Bi³⁺-Doped Cs₂SnCl₆ 0D Perovskites: Excited State Relaxation and Spin-Orbit Coupling
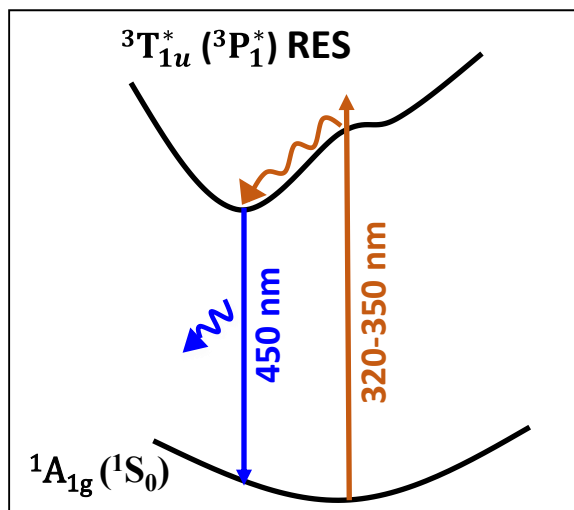
and Jahn-Teller interaction. The two minima on the RES termed as A_H (high energy) and A_L (low energy), and the 490 nm and 600 nm emissions are assigned to $A_H \rightarrow {}^1A_{1g}$ and $A_L \rightarrow {}^1A_{1g}$ transitions. Bi^{3+}-doped Cs_2SnCl_6 shows single emission with a peak at 450 nm for the entire temperature range of 5.6-300 K range. Bi^{3+} has stronger spin-orbit coupling compare to Sb^{3+}, which causes one of the minima on RES collapses to saddle point and leads to single emission. The elucidation of the origin of light absorption and emission in Sb^{3+}- and Bi^{3+}-doped Cs_2SnCl_6 will be in general helpful to understand the emission from ns^2-ion doped metal halide perovskite phosphor materials. A few aspects still require further exploration: (i) how anion vacancies alter the local structure around the aliovalent dopants Sb^{3+} and Bi^{3+}? (ii) what are the symmetries of A_H and A_L minima in the RES ${}^3T_{1u}^*$? Future experimental and theoretical works are required in this direction.

4A.5 References

1. Swarnkar, A.; Ravi, V. K.; Nag, A. Beyond Colloidal Cesium Lead Halide Perovskite Nanocrystals: Analogous Metal Halides and Doping. *ACS Energy Lett.* **2017,** *2*, 1089-1098.

2. Yuan, J. Y.; Hazarika, A.; Zhao, Q.; Ling, X. F.; Moot, T.; Ma, W. L.; Luther, J. M., Metal Halide Perovskites in Quantum Dot Solar Cells: Progress and Prospects. *Joule* **2020,** *4*, 1160-1185.

3. Ravi, V. K.; Mondal, B.; Nawale, V. V.; Nag, A. Don't Let the Lead Out: New Material Chemistry Approaches for Sustainable Lead Halide Perovskite Solar Cells. *ACS Omega* **2020,** *5*, 29631-29641.

4. Dey, A.; Ye, J.; De, A.; Debroye, E.; Ha, S. K.; Bladt, E.; Kshirsagar, A. S.; Wang, Z.; Yin, J.; Wang, Y.; Quan, L. N.; Yan, F.; Gao, M.; Li, X.; Shamsi, J.; Debnath, T.; Cao, M.; Scheel, M. A.; Kumar, S.; Steele, J. A.; Gerhard, M.; Chouhan, L.; Xu, K.; Wu, X. G.; Li, Y.; Zhang, Y.; Dutta, A.; Han, C.; Vincon, I.; Rogach, A. L.; Nag, A.; Samanta, A.; Korgel, B. A.; Shih, C. J.; Gamelin, D. R.; Son, D. H.; Zeng, H.; Zhong, H.; Sun, H.; Demir, H. V.; Scheblykin, I. G.; Mora-Sero, I.; Stolarczyk, J. K.; Zhang, J. Z.; Feldmann, J.; Hofkens, J.; Luther, J. M.; Perez-Prieto, J.; Li, L.; Manna, L.; Bodnarchuk, M. I.; Kovalenko, M. V.; Roeffaers, M. B. J.; Pradhan, N.; Mohammed, O. F.; Bakr, O. M.; Yang, P.; Muller-Buschbaum, P.; Kamat, P. V.; Bao, Q.; Zhang, Q.; Krahne, R.; Galian, R. E.; Stranks, S. D.; Bals, S.; Biju, V.; Tisdale, W. A.; Yan, Y.; Hoye, R. L. Z.; Polavarapu, L. State of the Art and Prospects for Halide Perovskite Nanocrystals. *ACS Nano* **2021,** *15*, 10775-10981.

Chapter 4A

Origin of Luminescence in Sb³⁺- and Bi³⁺-Doped Cs₂SnCl₆ 0D Perovskites: Excited State Relaxation and Spin-Orbit Coupling

5. Liu, F.; Zhang, T.; Mondal, D.; Teng, S.; Zhang, Y.; Huang, K.; Wang, D.; Yang, W.; Mahadevan, P.; Zhao, Y. S.; Xie, R.; Pradhan, N. Light-Emitting Metal-Organic Halide 1D and 2D Structures: Near-Unity Quantum Efficiency, Low-Loss Optical Waveguide and Highly Polarized Emission. *Angew. Chem. Int. Ed.* **2021,** *60*, 13548-13553.

6. Zhou, L.; Liao, J. F.; Kuang, D. B. An Overview for Zero-Dimensional Broadband Emissive Metal-Halide Single Crystals. *Adv. Opt. Mater.* **2021,**9 , 2100544.

7. Zeng, R.; Bai, K.; Wei, Q.; Chang, T.; Yan, J.; Ke, B.; Huang, J.; Wang, L.; Zhou, W.; Cao, S.; Zhao, J.; Zou, B. Boosting Triplet Self-Trapped Exciton Emission in Te(IV)-doped Cs₂SnCl₆ Perovskite Variants. *Nano Research* **2020,** *14*, 1551-1558.

8. Tan, Z. F.; Li, J. H.; Zhang, C.; Li, Z.; Hu, Q. S.; Xiao, Z. W.; Kamiya, T.; Hosono, H.; Niu, G. D.; Lifshitz, E.; Cheng, Y. B.; Tang, J. Highly Efficient Blue-Emitting Bi-Doped Cs₂SnCl₆ Perovskite Variant: Photoluminescence Induced by Impurity Doping. *Adv. Funct. Mater.* **2018,** *28*, 1801131.

9. Li, J.; Tan, Z.; Hu, M.; Chen, C.; Luo, J.; Li, S.; Gao, L.; Xiao, Z.; Niu, G.; Tang, J. Antimony Doped Cs₂SnCl₆ with Bright and Stable Emission. *Fron. Optoelectron.* **2019,** *12*, 352-364.

10. Jing, Y.; Liu, Y.; Zhao, J.; Xia, Z. Sb³⁺ Doping-Induced Triplet Self-Trapped Excitons Emission in Lead-Free Cs₂SnCl₆ Nanocrystals. *J. Phys. Chem. Lett.* **2019,** *10*, 7439-7444.

11. Dujardin, C.; Auffray, E.; Bourret-Courchesne, E.; Dorenbos, P.; Lecoq, P.; Nikl, M.; Vasil'ev, A. N.; Yoshikawa, A.; Zhu, R. Y. Needs, Trends, and Advances in Inorganic Scintillators. *IEEE Trans. Nucl. Sci.* **2018,** *65*, 1977-1997.

12. Luo, J.; Wang, X.; Li, S.; Liu, J.; Guo, Y.; Niu, G.; Yao, L.; Fu, Y.; Gao, L.; Dong, Q.; Zhao, C.; Leng, M.; Ma, F.; Liang, W.; Wang, L.; Jin, S.; Han, J.; Zhang, L.; Etheridge, J.; Wang, J.; Yan, Y.; Sargent, E. H.; Tang, J. Efficient and Stable Emission of Warm-White Light from Lead-Free Halide Double Perovskites. *Nature* **2018,** *563*, 541-545.

13. Morad, V.; Shynkarenko, Y.; Yakunin, S.; Brumberg, A.; Schaller, R. D.; Kovalenko, M. V. Disphenoidal Zero-Dimensional Lead, Tin, and Germanium Halides: Highly Emissive Singlet and Triplet Self-Trapped Excitons and X-ray Scintillation. *J. Am. Chem. Soc.* **2019,** *141*, 9764-9768.

14. Arfin, H.; Kshirsagar, A. S.; Kaur, J.; Mondal, B.; Xia, Z.; Chakraborty, S.; Nag, A., ns² Electron (Bi³⁺ and Sb³⁺) Doping in Lead-Free Metal Halide Perovskite Derivatives. *Chem. Mater.* **2020,** *32*, 10255-10267.

15. Jacobs, P. W. M., Alkali-Halide Crystals Containing Impurity Ions with the Ns² Ground-State Electronic Configuration. *J. Phys. Chem. Solids* **1991,** *52*, 35-67.

Chapter 4A

Origin of Luminescence in Sb^{3+}- and Bi^{3+}-Doped Cs$_2$SnCl$_6$ 0D Perovskites: Excited State Relaxation and Spin-Orbit Coupling

16. Li, Z.; Song, G.; Li, Y.; Wang, L.; Zhou, T.; Lin, Z.; Xie, R. J. Realizing Tunable White Light Emission in Lead-Free Indium(III) Bromine Hybrid Single Crystals through Antimony(III) Cation Doping. *J. Phys. Chem. Lett.* **2020,** *11*, 10164-10172.

17. Zeng, R.; Zhang, L.; Xue, Y.; Ke, B.; Zhao, Z.; Huang, D.; Wei, Q.; Zhou, W.; Zou, B. Highly Efficient Blue Emission from Self-Trapped Excitons in Stable Sb^{3+}-Doped Cs$_2$NaInCl$_6$ Double Perovskites. *J. Phys. Chem. Lett.* **2020,** *11*, 2053-2061.

18. Noculak, A.; Morad, V.; McCall, K. M.; Yakunin, S.; Shynkarenko, Y.; Worle, M.; Kovalenko, M. V. Bright Blue and Green Luminescence of Sb(III) in Double Perovskite Cs$_2$MInCl$_6$ (M = Na, K) Matrices. *Chem. Mater.* **2020,** *32*, 5118-5124.

19. Wu, Y.; Shi, C. M.; Xu, L. J.; Yang, M.; Chen, Z. N., Reversible Luminescent Vapochromism of a Zero-Dimensional Sb^{3+}-Doped Organic-Inorganic Hybrid. *J. Phys. Chem. Lett.* **2021,** *12*, 3288-3294.

20. Chang, T.; Wei, Q.; Zeng, R.; Cao, S.; Zhao, J.; Zou, B. Efficient Energy Transfer in Te^{4+}-Doped Cs$_2$ZrCl$_6$ Vacancy-Ordered Perovskites and Ultrahigh Moisture Stability via A-Site Rb-Alloying Strategy. *J. Phys. Chem. Lett.* **2021,** *12*, 1829-1837.

21. Sun, H. T.; Zhou, J. J.; Qiu, J. R. Recent Advances in Bismuth Activated Photonic Materials. *Prog. Mater. Sci.* **2014,** *64*, 1-72.

22. Boutinaud, P. Luminescence of Sb^{3+} in Closed Shell Transition Metal Oxides. *J. Lumin.* **2019,** *208*, 394-401.

23. Swart, H. C.; Kroon, R. E., (INVITED) Ultraviolet and Visible Luminescence from Bismuth Doped Materials. *Opt. Mater.: X* **2019,** *2*, 100025.

24. Krasnikov, A.; Mihokova, E.; Nikl, M.; Zazubovich, S.; Zhydachevskyy, Y., Luminescence Spectroscopy and Origin of Luminescence Centers in Bi-Doped Materials. *Crystals* **2020,** *10,* 208.

25. Fukuda, A. Jahn-Teller Effect on the Structure of the Emission Produced by Excitation in the A Band of KI: Tl-Type Phosphors. Two Kinds of Minima on the Γ_4^- (^{3}T$_{1u}$) Adiabatic Potential-Energy Surface. *Phys. Rev. B* **1970,** *1*, 4161-4178.

26. Wolfert, A.; Blasse, G. Luminescence of Bi^{3+}-Doped Crystals of Cs$_2$NaYBr$_6$ and Cs$_2$NaLaCl$_6$. *J. Solid State Chem.* **1985,** *59*, 133-142.

27. Choi, K. O.; Lee, S. W.; Bae, H. K.; Jung, S. H.; Chang, C. K.; Kang, J. G. Spectroscopic Studies of Sb^{3+} Color-Centers in Alkali-Halide Single-Crystals. *J. Chem. Phys.* **1991,** *94*, 6420-6428.

Chapter 4A

Origin of Luminescence in Sb³⁺- and Bi³⁺-Doped Cs₂SnCl₆ 0D Perovskites: Excited State Relaxation and Spin-Orbit Coupling

28. Kim, Y.-D.; Kang, J.-G. Luminescence of KCl:Bi³⁺ Excited at the X Absorption Band. *J. Phys. Condens. Matter* **1994,** *6*, 8949-8958.

29. Tan, Z.; Li, J.; Zhang, C.; Li, Z.; Hu, Q.; Xiao, Z.; Kamiya, T.; Hosono, H.; Niu, G.; Lifshitz, E.; Cheng, Y.; Tang, J. Highly Efficient Blue-Emitting Bi-Doped Cs₂SnCl₆ Perovskite Variant: Photoluminescence Induced by Impurity Doping. *Adv. Funct. Mater.* **2018,** *28*, 1801131.

30. Jing, Y.; Liu, Y.; Zhao, J.; Xia, Z. Sb³⁺ Doping-Induced Triplet Self-Trapped Excitons Emission in Lead-Free Cs₂SnCl₆ Nanocrystals. *J. Phys. Chem. lett.* **2019,** *10*, 7439-7444.

31. Eickhoff, T.; Grosse, P.; Theiss, W. Diffuse Reflectance Spectroscopy of Powders. *Vib. Spectrosc.* **1990,** *1*, 229-233.

32. Ahrens, L. H. The Use of Ionization Potentials Part 1. Ionic Radii of the Elements. *Geochim. Cosmochim. Acta* **1952,** *2*, 155-169.

33. Shannon, R. D. Revised Effective Ionic-Radii and Systematic Studies of Interatomic Distances in Halides and Chalcogenides. *Acta Crystallogr.* **1976,** *32*, 751-767.

34. Kaltzoglou, A.; Antoniadou, M.; Kontos, A. G.; Stoumpos, C. C.; Perganti, D.; Siranidi, E.; Raptis, V.; Trohidou, K.; Psycharis, V.; Kanatzidis, M. G.; Falaras, P. Optical-Vibrational Properties of the Cs₂SnX₆ (X = Cl, Br, I) Defect Perovskites and Hole-Transport Efficiency in Dye-Sensitized Solar Cells. *J. Phys. Chem. C* **2016,** *120*, 11777-11785.

35. Tsuboi, T.; Ahmet, P.; Kang, J. G. Optical Absorption Bands Due to the s² to sp Transition in KCl:Sb³⁺ Crystals. *J. Phys. Condens. Matter* **1992,** *4*, 531-534.

36. Vlaskin, V. A.; Janssen, N.; van Rijssel, J.; Beaulac, R.; Gamelin, D. R., Tunable Dual Emission in Doped Semiconductor Nanocrystals. *Nano Lett.* **2010,** *10*, 3670-4.

37. Ranfagni, A.; Mugnai, D.; Bacci, M.; Viliani, G.; Fontana, M. P. The Optical-Properties of Thallium-Like Impurities in Alkali-Halide Crystals. *Adv. Phys.* **1983,** *32*, 823-905.

38. Kang, J. G.; Yoon, H. M.; Chun, G. M.; Kim, Y. D.; Tsuboi, T. Spectroscopic Studies of Bi³⁺ Color-Centers in KCl Single-Crystals. *J. Phys. Condens. Matter* **1994,** *6*, 2101-2116.

39. Xiong, G. T.; Yuan, L. F.; Jin, Y. H.; Wu, H. Y.; Li, Z. Z.; Qu, B. Y.; Ju, G. F.; Chen, L.; Yang, S. H.; Hu, Y. H. Aliovalent Doping and Surface Grafting Enable Efficient and Stable Lead-Free Blue-Emitting Perovskite Derivative. *Adv. Opt. Mater.* **2020,** *8*, 2000779.

40. Arfin, H.; Kaur, J.; Sheikh, T.; Chakraborty, S.; Nag, A. Bi³⁺ -Er³⁺ and Bi³⁺ -Yb³⁺ Codoped Cs₂ AgInCl₆ Double Perovskite Near-Infrared Emitters. *Angew. Chem. Int. Ed.* **2020,** *59*, 11307-11311.

Chapter 4A

Origin of Luminescence in Sb³⁺- and Bi³⁺-Doped Cs₂SnCl₆ 0D Perovskites: Excited State Relaxation and Spin-Orbit Coupling

41. Donahue, J. M.; Teegarde, K. Luminescence from Perturbed Exciton States. *J. Phys. Chem. Solids* **1968,** *29*, 2141-2151.

Chapter 4B

Optical Properties of Bi^{3+}-Sb^{3+} Codoped Cs$_2$SnCl$_6$ 0D Perovskite

Abstract

Bi^{3+}-doped and Sb^{3+}-doped Cs$_2$SnCl$_6$ zero-dimensional perovskites exhibit strong blue and orange emissions respectively, making them promising phosphor material for light emitting diodes. The optical absorption and emission properties arise from ns^2 to ns^{1}np^1 excitation and ns^{1}np^1 to ns^2 deexcitation of isolated Bi^{3+} and Sb^{3+} ions. An intriguing query arises on how the optical properties of Bi^{3+} and Sb^{3+} will vary, if we codope both in Cs$_2$SnCl$_6$. Our investigation reveals that the optical properties of each ion remain unperturbed upon codoping. This observation is attributed to the non-overlapping nature of emission of one ion to the absorption of another, thereby not facilitating the energy transfer. Also, confirming that the both the emission originates from isolated [SbCl$_6$]$^{3-}$ or [BiCl$_6$]$^{3-}$ octahedrons that are electrotonically separated from each other. Notably, the excitation spectra of both ions exhibit significant overlap, facilitating their simultaneous excitation through a single excitation source and giving rise to broad visible emission. This study sheds light on the codoping effects on the optical properties of isolated Bi^{3+} and Sb^{3+}, which will be helpful in developing phosphor materials containing these luminescent centers.

Graphical Abstract
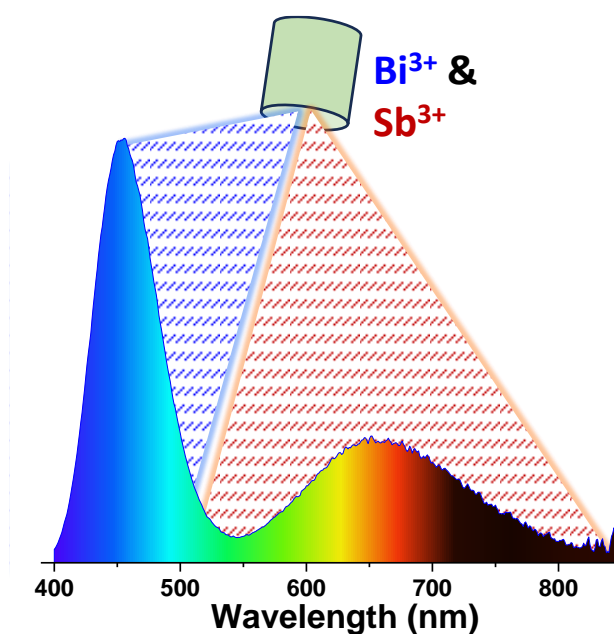
4B.1 Introduction

Cs_2SnCl_6 have high band gap $(4.89\ eV)$[1] and inherent non-luminescent nature, presents a promising host material for investigating the optical characteristics of luminescent centers. Incorporation of luminescent ions into Cs_2SnCl_6 has been achieved, resulting in intriguing optical functionalities.[2-5] Notably, Sb^{3+}-doping in Cs_2SnCl_6 induces orange emission with a photoluminescence quantum yield (PLQY) of 37%,[3] while Bi^{3+} doping yields blue emission with 79% high PLQY[2]. Moreover, Te^{4+}-doped Cs_2SnCl_6 exhibits green-yellow emission with a PLQY of 42.4%.[4] These Sb^{3+}, Bi^{3+} and Te^{4+} ion doped halide perovskites, hold potential for applications in phosphor-converted light emitting diodes (LEDs) and X-ray scintillators.[6-9] The observed optical absorption and emission properties of Bi^{3+}, Sb^{3+} and Te^{4+} doped Cs_2SnCl_6 arise from the ns^2 to ns^1np^1 and ns^1np^1 to ns^2 transitions, intrinsic to the respective ions.[10]

The ions Bi^{3+}, Sb^{3+} and Te^{4+} hold two electrons in the valence ns^2 orbital (n is the principal quantum number). These ions exhibit nearly allowed ns^2 to ns^1np^1 transitions because of strong spin-orbit coupling leading to reasonably strong absorption. Also, de-excitation leads to emission properties. Figure 4B.1 illustrates the transitions within a ns^2-ion.
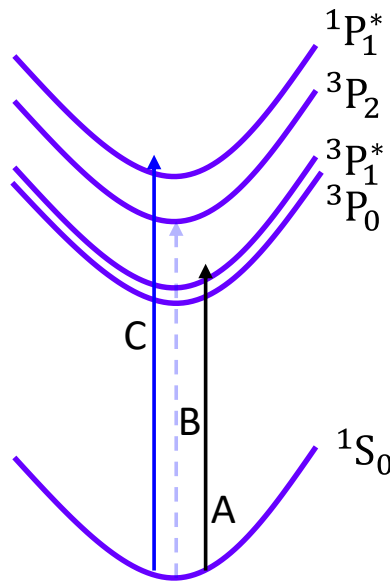
Figure 4B.1: Schematic presentation of energy states of ns^2-ion in ground state and ns^1np^1 excited states. The states are represented by the term-symbols. The "*" represent the mixing of two states ($^1P_1$ and $^3P_1$) due to spin-orbit coupling. The A, B and C indicate the electronic transition from ground state to excited states.

In their ground state, ns^2 ions are in a singlet configuration denoted by the term symbol $^1S_0$. Upon transition to the ns^1np^1 excited state, singlet and triplet states are possible, which are represented by the term symbols $^3P_{(0,1,2)}$ and $^1P_1$. Among these, the $^1S_0 \rightarrow {}^1P_1^*$ transition is

allowed. Here, the "*" represent the mixing of $^1P_1$ and $^3P_1$ states due to spin-orbit coupling. This mixing makes the spin forbidden $^1S_0 \rightarrow {}^3P_1^*$ transition nearly allowed. The $^1S_0 \rightarrow {}^3P_2$ transition is spin forbidden but becomes partially allowed through coupling with lattice vibrations. On the other hand, the $^1S_0 \rightarrow {}^3P_0$ transition is both spin-forbidden and J (0 to 0) forbidden, leading to its absence in the absorption spectrum. $^1S_0$ to $^3P_1^*$, $^3P_2$ and $^1P_1^*$ transitions are also known as A-band, B-band and C-band transitions respectively. While in crystal field environments these states are typically represent using Mulliken symbols, we will use term symbols here for simplicity. These ions, owing to their ability to fine-tune optical absorption and emission properties, have been doped in alkali halides,[10-15] metal oxides[16-18] and zeolites[19]

These ions have also demonstrated proficiency in sensitizing lanthanide ions by codoping such as Bi^{3+}-Er^{3+} codoped $Cs_2AgInCl_6$.[20-21] However, the exploration of codoping involving two ns^2 ions like Bi^{3+}, Sb^{3+} or Te^{4+} ions have remained limited.[22-23] Investigations into the potential codoping effects on the optical absorption and emission properties of these ions are scarce. Recently, the codoping of Bi^{3+} and Sb^{3+} in $Cs_2NaInCl_6$ has revealed an increased A-band splitting of Sb^{3+}.[24-26] In this study, we delve into the photoluminescence properties of Bi^{3+} and Sb^{3+} codoped Cs_2SnCl_6. The focus is on how codoping influences the optical properties of individual ions. By elucidating the interplay between these dopants, we aim to contribute to understanding of optical properties in codoped perovskite matrices.

4B.2 Experimental Section

4B.2.1 Chemicals

Cesium chloride (CsCl, 99.9 %), tin (II) chloride (SnCl₂, anhydrous powder, ≥99.99 %), bismuth chloride (BiCl₃, anhydrous powder, 99.998 %), antimony chloride (SbCl₃, 99.95%) and hydrochloric acid (HCl, 37 wt %, 99.99%) are purchased from Sigma Aldrich Chemicals. All the chemicals are used without any further purification.

4B.2.2 Synthesis of Doped and Undoped Cs₂SnCl₆

Cs₂SnCl₆ microcrystals are synthesized by following the method reported by Tan et al.[2] 189.6 mg (1 mmol) SnCl₂, 336.72 mg (2 mmol) CsCl and 4 mL HCl are taken in a polytetrafluoroethylene (PTFE) hydrothermal autoclave. The hydrothermal autoclave is kept at 180 °C for 10 h, then cooled down to room temperature over a period of 20 h. White color crystals are formed. The crystals are filtered out, washed with ethanol, and kept in vacuum for drying. The obtained sample powder is used for characterization and measurements.

For synthesis of Sb^{3+} or Bi^{3+}-doped Cs$_2$SnCl$_6$, required dopant precursors are added while maintaining the other precursors and procedure exactly same as the undoped sample. For Sb^{3+}-doped Cs$_2$SnCl$_6$, 22.6 mg SbCl$_3$ (~ 0.1 mmol) is added. For Bi^{3+}-doped Cs$_2$SnCl$_6$, 31.18 mg (~ 0.1 mmol) BiCl$_3$ precursor is used. The used dopant percentage are close to optimized value reported in prior literature.[2, 27]

For Bi^{3+}-Sb^{3+} codoped Cs$_2$SnCl$_6$, required precursors are added while maintaining the other precursors same as undoped sample. SbCl$_3$ (~ 0.05 mmol) and BiCl$_3$ (~ 0.01 mmol) is added with other precursors as mentioned for undoped sample. The hydrothermal autoclave kept at 180 °C for 10 h then cool down to room temperature naturally. The crystals are filtered out, washed with ethanol and kept in vacuum for drying. The obtained crystals are used for characterization and measurements. See Table 4A.2 for the details of dopant precursor concentrations and dopant percentages in the product.

4B.2.3 Characterization

Powder X-ray diffraction (XRD) patterns are recorded using a Bruker D8 Advance X-ray diffraction machine equipped with Cu Kα (1.54 Å) radiation. A Zeiss Ultra Plus instrument is used for field emission scanning electron microscopy (FESEM) imaging and energy dispersive X-ray spectroscopy (EDS). Diffused reflectance spectra of microcrystalline powders in the UV−visible region are recorded using a Shimadzu UV-3600 plus UV−vis−NIR spectrophotometer. Then KubelkaMunk transformation[28] is used for the analysis of diffuse reflectance spectra. It relates the reflectance data with absorption coefficient as in equation (1):

$$F(R) = \alpha/S = (1-R)^2 /2R \quad (1)$$

where F(R) is the Kubelka-Munk function, R is reflectance, α is absorption coefficient and S is the scattering factor. Steady-state photoluminescence (PL), PL Excitation (PLE), and PL decay dynamics (time-correlated single photon counting) are measured using Edinburgh FLS980 Instrument. Xenon lamp is used for steady state PL and PLE measurements. 340 nm pulsed LED (pulse width is 790 ps) and 405 nm pulsed diode laser (pulse width is 60 ps) excitation sources are used for PL decay measurement. For temperature dependent PL measurements, the sample is kept between two quartz substrate and mounted on a gold-plated sample holder. The sample holder is placed in a closed cycle He cryostat (Advanced Research Systems) attached with a temperature controller (Lake Shore Cryotronics) to achieve the desired lower temperatures.

4B.3 Results and Discussion

4B.3.1 Synthesis and Characterization of Undoped, Doped and Codoped Cs₂SnCl₆
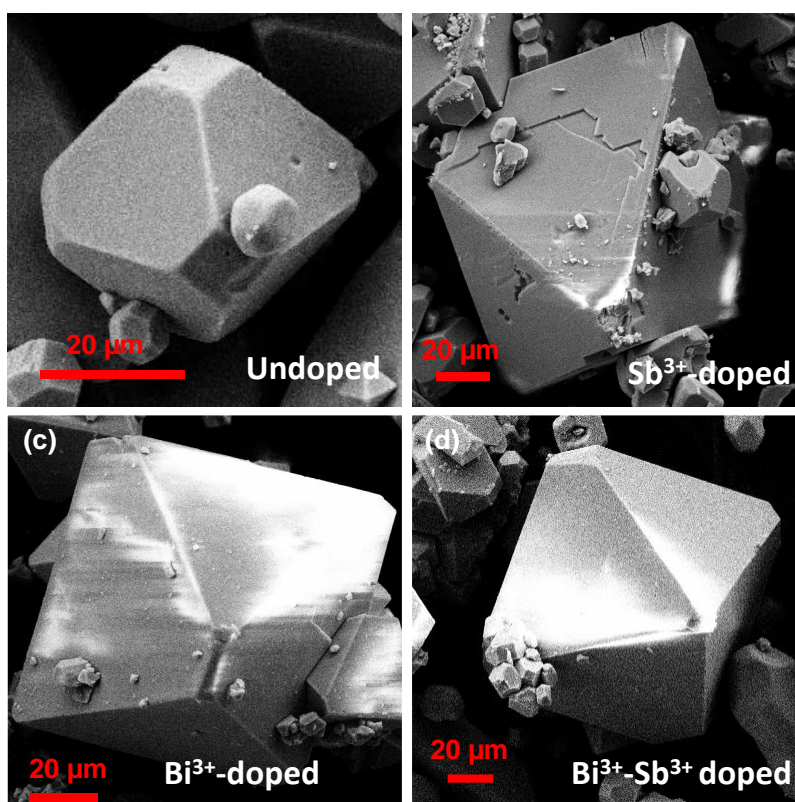
Figure 4B.2: FESEM images of (a) undoped, (b) Sb^{3+}-doped, (c) Bi^{3+}-doped and (d) Bi^{3+}-Sb^{3+} codoped Cs₂SnCl₆.

We have synthesized undoped, Sb^{3+}-doped, Bi^{3+}-doped and Bi^{3+}-Sb^{3+} codoped Cs₂SnCl₆ by following a prior report.[29] -Field emission scanning electron microscopy (FESEM) show micrometer size crystals for all the samples (Figure 4B.2). Energy dispersive X-ray spectroscopy (EDS) of all the samples show atomic ratio of Cs:Sn:Cl is close to 2:1:6 (see Table 4B.1), confirming the formation of Cs₂SnCl₆. The dopant concentrations determined by energy dispersive spectroscopy (EDS) are shown in Table 4B.2. But we note that EDS is less sensitive for quantitative estimation of small dopant concentration. Figure 4B.3 show the EDS elemental mapping of doped samples. Homogeneous distribution of host elements Cs, Sn, Cl and the dopants are found throughout the crystal. Figure 4B.3a and 4.3b show the homogeneous distribution of Sb and Bi throughout the Sb^{3+}-doped and Bi^{3+}- doped Cs₂SnCl₆, respectively. Homogeneous distribution of Bi and Sb in the codoped sample is also confirmed by the EDS elemental mapping, as shown in Figure 4B.3c. The homogenous distribution indicate that the elements are present in the crystal and not forming any separate phase.
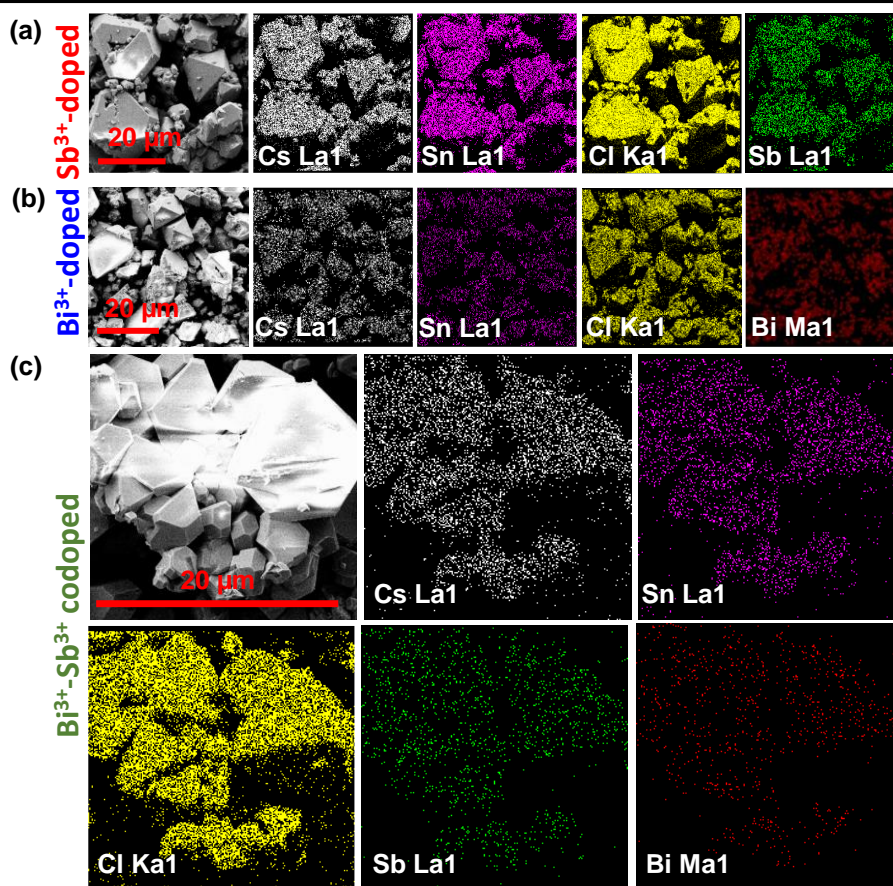
Figure 4B.3: EDS elemental mapping of (a) Sb^{3+}-doped, (c) Bi^{3+}-doped, and (d) Bi^{3+}-Sb^{3+} codoped Cs$_2$SnCl$_6$.

Table 4B.1: Elemental analysis obtained from EDS data of undoped, Sb^{3+}-doped and Bi^{3+}-doped Cs$_2$SnCl$_6$. EDS data shows that presence of Sb and Bi in the corresponding doped samples.

Sample	Cs	Sn	Cl
Undoped	2.0	1.0	6.2
Sb^{3+}-doped	2.0	1.0	6.3
Bi^{3+}-doped	2.0	1.0	6.1
Bi^{3+}-Sb^{3+} codoped	2.0	1.0	6.3

Table 4B.2: Dopant precursor feeding concentration and the determined dopant concentration by EDS in the product. Dopant % = 100×[dopant]/ ([dopant] +[Sn]).

Sample	Dopant % used in precursor	Dopant % in product (from EDS)
Sb^{3+}-doped	9.0% Sb^{3+}	1.1% Sb^{3+}
Bi^{3+}-doped	9.0% Bi^{3+}	5.4% Bi^{3+}
Bi^{3+}-Sb^{3+} codoped	5.0% Sb^{3+}-1% Bi^{3+}	1.9% Sb^{3+}-1.5% Bi^{3+}

Optical Properties of Bi³⁺-Sb³⁺ Codoped Cs₂SnCl₆ 0D Perovskites
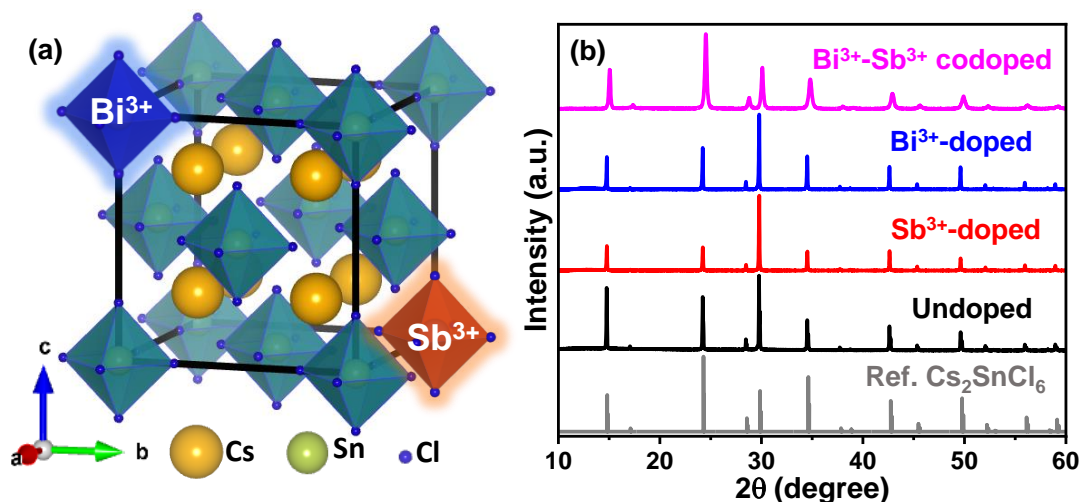
Figure 4B.4: (a) Schematics presentation of Bi^{3+} and Sb^{3+} codoping in crystal structure of Cs_2SnCl_6. The sizes of blue spheres are reduced than their actual size for clarity in presentation. (b) Powder XRD patterns of undoped, Sb^{3+}-doped, Bi^{3+}-doped, Bi^{3+}-Sb^{3+} codoped Cs_2SnCl_6. The reference pattern of cubic phase Cs_2SnCl_6 (ICSD#9023) is also shown.

Cs_2SnCl_6 adopts a cubic vacancy-ordered 0D perovskite structure, where $[SnCl_6]^{2-}$ octahedra are electronically isolated from each other.[29] The dopants Bi^{3+} and Sb^{3+} are expected to occupy these octahedral positions as illustrated in Figure 4B.4a. Figure 4B.4b show the powder X-ray diffraction (XRD) patterns of undoped, Bi^{3+}-doped, Sb^{3+}-doped, Bi^{3+}-Sb^{3+} codoped Cs_2SnCl_6, which match well with the reference data (ICSD# 9023) of Cs_2SnCl_6 with cubic space group Fm3m. The ionic radii of Sn^{4+}, Bi^{3+} and Sb^{3+} in octahedral environment are 0.69 Å, 1.03 Å and 0.76 Å, respectively.[30-31] As the metal center radii of Sn^{4+} and dopants are different so, one would expect shift in powder XRD peak positions after Bi^{3+} or Sb^{3+} doping. But the powder XRD pattern in Figure 4B.4b do not exhibit significant peak shift after doping, probably because of limited extent of doping. Also, because Bi^{3+} and Sb^{3+} are aliovalent to Sn^{4+}. So, doping of Bi^{3+} or Sb^{3+} is expected to introduce halide vacancy for maintaining charge neutrality.

4B.3.2 Optical Properties of Doped Cs₂SnCl₆

The UV-visible absorption spectra of undoped and doped Cs_2SnCl_6 samples are presented in Figure 4B.5. In the case of undoped Cs_2SnCl_6, a distinct absorption edge is observed around 300 nm, in accordance with prior reports.[28,32-33] Upon introducing Bi^{3+} dopants, a novel absorption feature emerges at 370 nm. This new absorption peak is attributed to $^1S_0 \rightarrow$ $^3P_1^*$ transition (A-band) of Bi^{3+}. Similarly, Sb^{3+} doping leads to the appearance of additional absorption features at lower energy than the intrinsic absorption edge of the host Cs_2SnCl_6, as depicted in Figure 4B.5. These absorption features are ascribed to the $^1S_0 \rightarrow {}^3P_1^*$ transition (A-

band) associated with Sb^{3+}.[34] Bi^{3+} doping introduce sharp absorption feature compare to Sb^{3+} doping. This could be related to stronger spin-orbit coupling in Bi^{3+}, which make $^1S_0 \rightarrow$ $^3P_1^*$ transition more allowed. The Bi^{3+}-Sb^{3+} codoped Cs_2SnCl_6 show absorption feature which have combined features of Bi^{3+} as well as Sb^{3+}, supporting that the codoping is achieved in the Cs_2SnCl_6 system.
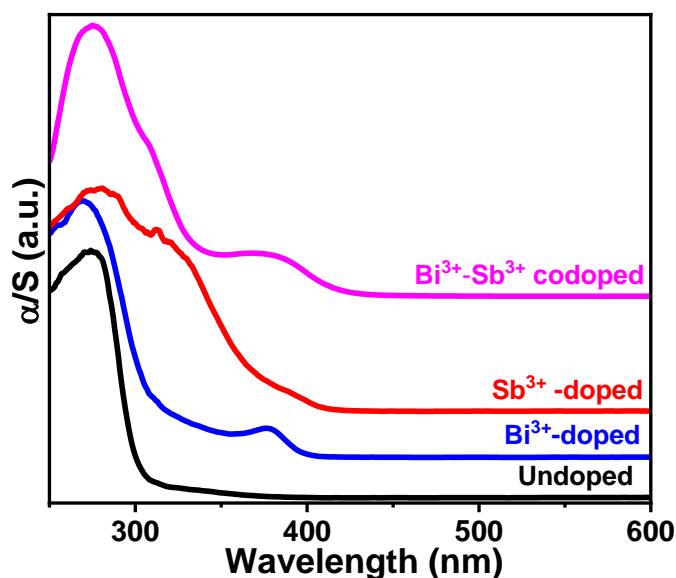
Figure 4B.5: (a) Optical absorption spectra of undoped, Bi^{3+}-doped, Sb^{3+}-doped and Bi^{3+}-Sb^{3+} codoped Cs_2SnCl_6. Absorption spectra are obtained from Kubelka-Munk transformation of diffuse reflectance spectrum α is absorption coefficient and S is a scattering factor.

The undoped Cs_2SnCl_6 is non-luminescent. However, Bi^{3+} doping in Cs_2SnCl_6 leads to the emergence of a distinct narrow blue emission peak centered at 450 nm, as shown in Figure 4B.6a. Similarly, Sb^{3+} doping results in orange color emission peaking at 650 nm. Similar results are reported in the prior literature.[33] The origin of these emissions are debated[2, 23, 33] but most accepted view that these photoluminescence are stem from the $^3P_1^* \rightarrow {}^1S_0$ (A-band) transitions, inherent to the respective ions.[33] Upon Bi^{3+} and Sb^{3+} codoping in Cs_2SnCl_6, intriguing emission spectrum is obtained as shown in Figure 4B.6a. The codoped sample exhibits two emission peaks at 450 nm and 650 nm. Remarkably, the 450 nm emission coincides with the blue emission observed in Bi^{3+}-doped Cs_2SnCl_6, while the broad 650 nm emission matches with the orange emission characteristic of Sb^{3+}-doped Cs_2SnCl_6. The matching emission features of the codoped sample with individually doped Bi^{3+} and Sb^{3+} samples underscores that the dual emission features of codoped sample originates from the Bi^{3+} or Sb^{3+} isolated octahedral sites.

PL excitation spectra in Figure 4B.6b further supports these conclusions. The PL excitation spectrum of the codoped sample closely match with that of individually Bi^{3+}-doped or Sb^{3+}-doped Cs_2SnCl_6. These properties imply a limited interaction between the codoped Bi^{3+} and Sb^{3+} centers. Nonetheless, a slight broadening in the PL excitation spectrum for the 650 nm emission in the codoped sample is observed. This broadening on the higher energy side is likely contributed by the excitation of Bi^{3+} center, as imply by the overlapping of PL excitation spectrum of spectrum of 450 nm emission (Bi^{3+}-doped) and 650 nm emission (Bi^{3+}-Sb^{3+} codoped) in Figure 4B.6b.
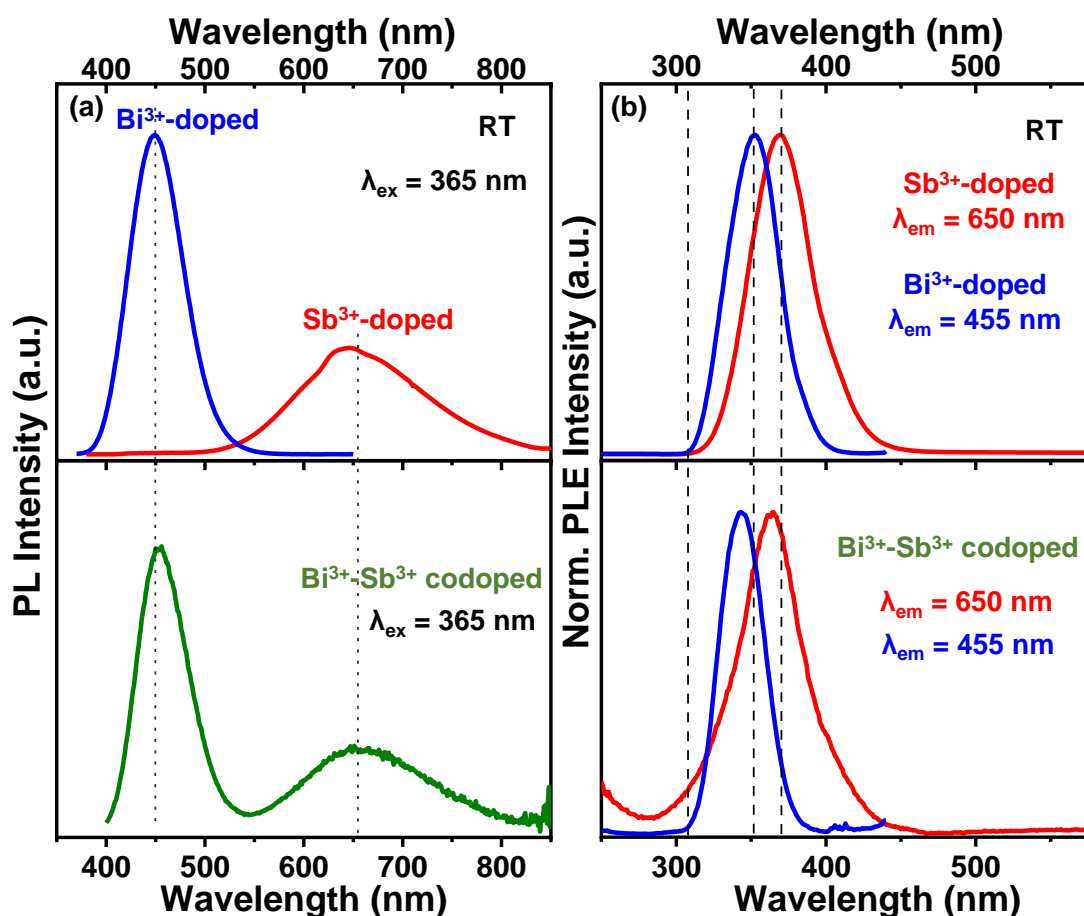
Figure 4B.6: (a) Photoluminescence (PL), and (b) PL excitation (PLE) spectra of Bi^{3+}-doped, Sb^{3+}-doped and Bi^{3+}-Sb^{3+} codoped Cs_2SnCl_6.

The PL excitation spectrum of codoped sample in Figure 4B.6b demonstrates a substantial overlap between the excitation spectra of 650 nm and 455 nm emission, intersecting at 352 nm. The substantial overlap points that both the luminescent centers (Bi^{3+} and Sb^{3+}) can be effectively excited by a single excitation source. At the same time, the PL excitation spectrum for the two emissions (455 nm and 650 nm) have non-overlapping part also (Figure 4B.6b). Which allow us to obtain excitation dependent emission spectra as shown in Figure 4B.7a. The

corresponding luminescence image under different excitation wavelength are shown in Figure 4B.7b. Such excitation dependent emitting sample might be useful in anti-counterfeiting application.[25]
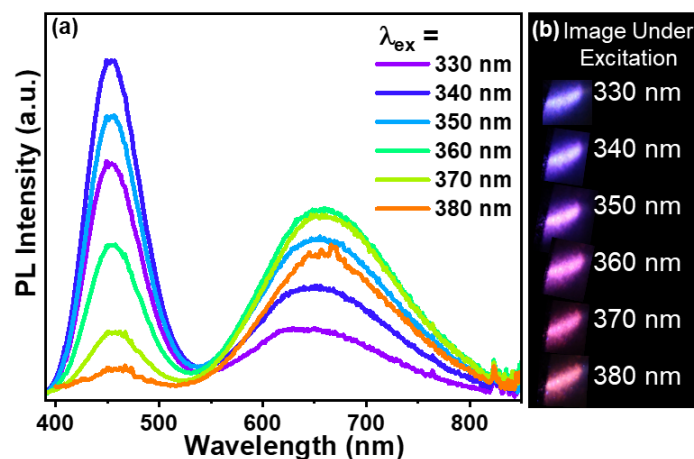
Figure 4B.7: (a) Excitation dependent PL spectrum of Bi^{3+}-Sb^{3+} codoped Cs_2SnCl_6. (b) Corresponding sample images under different excitation wavelengths.

4B.3.3 Temperature Dependent Optical Properties of Doped Cs_2SnCl_6
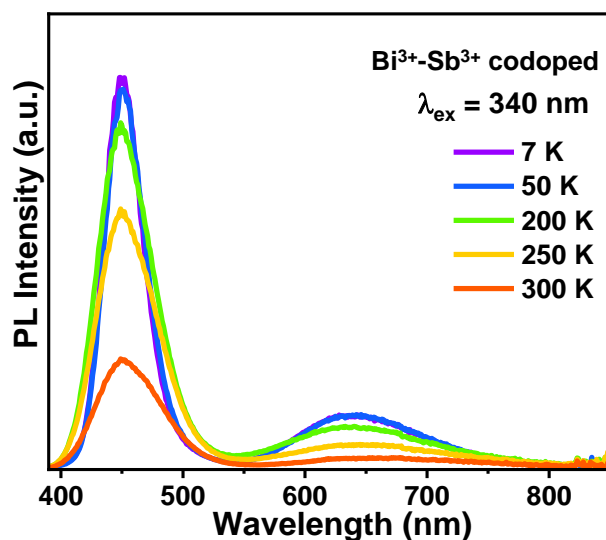
Figure 4B.8: (a) Temperature dependent emission spectra of Bi^{3+}-Sb^{3+} codoped Cs_2SnCl_6 at 340 nm wavelength excitation.

Temperature dependent photoluminescence studies are carried out to better understand the optical properties of Bi^{3+}-doped, Sb^{3+}-doped and Bi^{3+}-Sb^{3+} codoped Cs_2SnCl_6. Temperature dependent photoluminescence spectra of Bi^{3+}-Sb^{3+} codoped Cs_2SnCl_6 are shown in Figure 4B.8. Interestingly, it shows dual emission feature and the emission intensity of both the emission increases on decreasing the temperature due to suppression of non-radiative processes.

The 650 nm emission attributed to Sb^{3+}, exhibits a greater intensity increase (2.5 times) compared to the 450 nm emission (2.1 times) associated with Bi^{3+}, between 7 K and 300 K. The greater intensity increase in 650 nm emission is also contributed by the shifting of PL excitation spectra at low temperatures as shown in Figure 4B.9a. Similar PL excitation peak shift is also observed in only Sb^{3+}-doped Cs_2SnCl_6 (Figure 4B.9b).
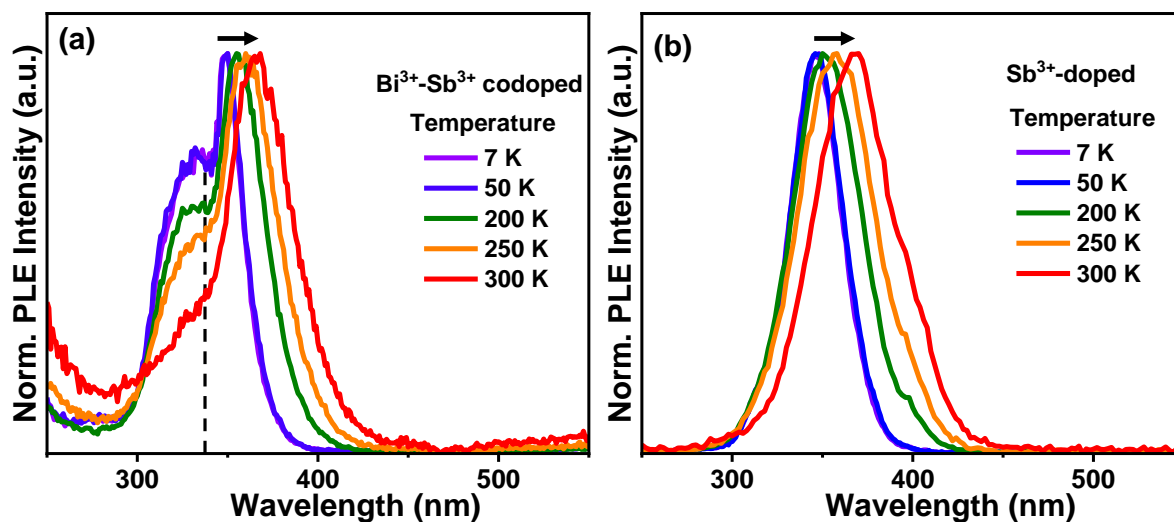
Figure 4B.9: Temperature dependent PL excitation (PLE) spectra of (a) Bi^{3+}-Sb^{3+} codoped Cs_2SnCl_6 with emission at 600 nm and (b) for Sb^{3+}-doped Cs_2SnCl_6 with emission at 620 nm. The arrow indicates the shift in peak position with increasing temperature.

To find out any changes by codoping, we have compared the low temperature photoluminescence spectra of Bi^{3+}-doped, Sb^{3+}-doped and Bi^{3+}-Sb^{3+} codoped Cs_2SnCl_6 as shown in Figure 4B.10. At 7 K temperature, the Bi^{3+}-Sb^{3+} codoped sample continues to exhibit the dual emission feature similar to that observed at room temperature (as shown in Figure 4B.6a). Notably, the 450 nm emission peak aligns perfectly with the emission profile of Bi^{3+}-doped Cs_2SnCl_6. This indicates the absence of any changes in the emission states of Bi^{3+}, reaffirming the isolated nature of Bi^{3+} center within the Cs_2SnCl_6. Intriguingly, the broad visible emission peak at 650 nm in Bi^{3+}-Sb^{3+} codoped Cs_2SnCl_6 closely matches the 620 nm emission of Sb^{3+}-doped Cs_2SnCl_6 (Figure 4B.10a). However, the feature corresponding to the 490 nm emission from Sb^{3+}-doped sample is not visible in the codoped sample. This is likely due to the relatively low intensity of the Sb^{3+}-related emission within the Bi^{3+}-Sb^{3+} codoped system.
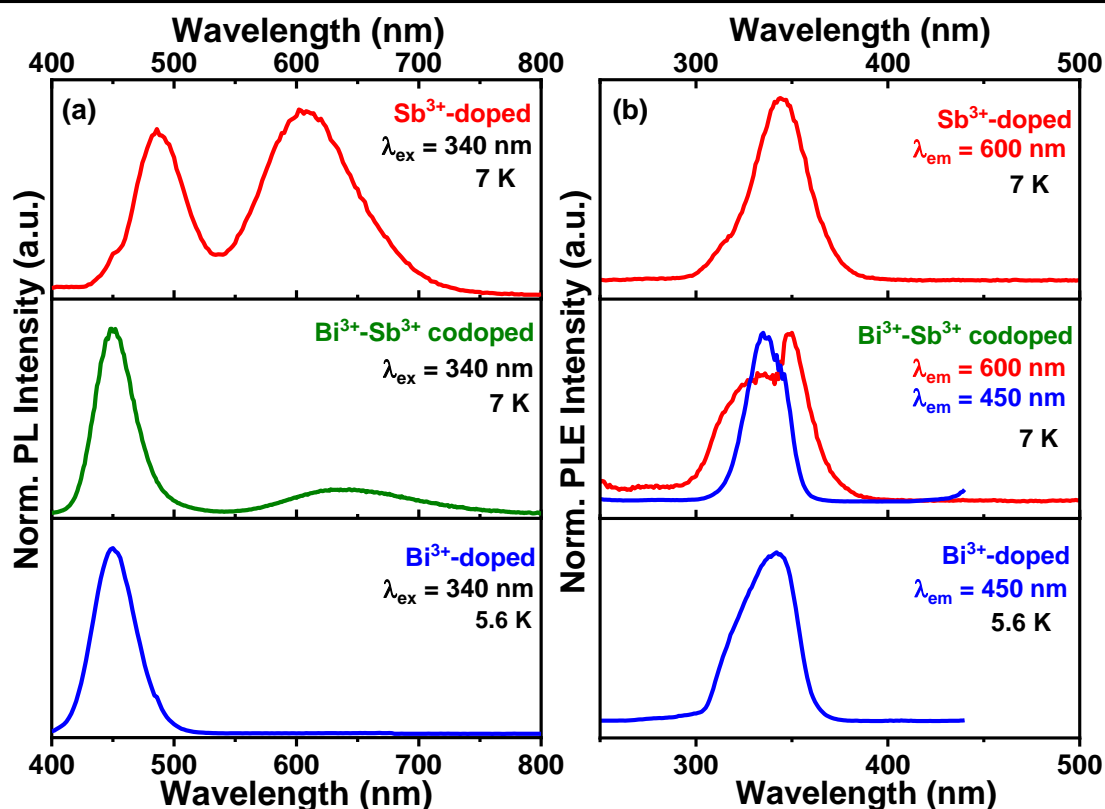
Figure 4B.10: (a) PL spectrum (b) PL excitation spectrum of Bi^{3+}-doped, Sb^{3+}-doped and Bi^{3+}-Sb^{3+} codoped Cs_2SnCl_6 at cryogenic temperature.

To elucidate the excited states contributing to emissions, PL excitation spectra are recorded at cryogenic temperatures as shown in Figure 4B.10b. Remarkably, the PLE spectra for the two emission peaks (450 nm and 650 nm) in the Bi^{3+}-Sb^{3+} codoped Cs_2SnCl_6 closely resemble those of solely Bi^{3+}-doped or Sb^{3+}-doped Cs_2SnCl_6. Additionally, the PLE spectrum at 600 nm of codoped sample demonstrates a slight broadening when compared to the PLE spectrum of Sb^{3+}-doped Cs_2SnCl_6 (Figure 4B.10b).

4B.4 Conclusion

In summary, comparative temperature dependent PL and PL excitation study of Bi^{3+}-doped, Sb^{3+}-doped and Bi^{3+}-Sb^{3+} codoped Cs_2SnCl_6 indicate almost no perturbation to the optical properties of Bi^{3+} or Sb^{3+} dopants by codoping. Bi^{3+}-Sb^{3+} codoped Cs_2SnCl_6 show dual emission. The 450 nm emission of Bi^{3+}-Sb^{3+} codoped Cs_2SnCl_6 matches with the emission of Bi^{3+}-doped Cs_2SnCl_6. The emission is attributed to $^3P_1^* \rightarrow {}^1S_0$ (A-band) transition of Bi^{3+}. The 650 nm emission of Bi^{3+}-Sb^{3+} codoped Cs_2SnCl_6 matches well with the emission of Sb^{3+}-doped Cs_2SnCl_6 and assigned to are assigned to $^3P_1^* \rightarrow {}^1S_0$ (A-band) transition of Sb^{3+}. The PL excitation spectra of both (450 nm and 650 nm) emissions of codoped sample also remain similar to that of Bi^{3+}- or Sb^{3+} -doped Cs_2SnCl_6. This unperturbed optical property of Bi^{3+} and

Sb^{3+} dopants in the codoped Cs$_2$SnCl$_6$, provides easy photoluminescence tunability by just varying the relative doping percentage of Bi^{3+} and Sb^{3+}.

4B.5 References

1. Karim, M. M. S.; Ganose, A. M.; Pieters, L.; Winnie Leung, W. W.; Wade, J.; Zhang, L.; Scanlon, D. O.; Palgrave, R. G. Anion Distribution, Structural Distortion, and Symmetry-Driven Optical Band Gap Bowing in Mixed Halide Cs$_2$SnX$_6$ Vacancy Ordered Double Perovskites. *Chem. Mater.* **2019,** *31*, 9430-9444.

2. Tan, Z.; Li, J.; Zhang, C.; Li, Z.; Hu, Q.; Xiao, Z.; Kamiya, T.; Hosono, H.; Niu, G.; Lifshitz, E.; Cheng, Y.; Tang, J. Highly Efficient Blue-Emitting Bi-Doped Cs$_2$SnCl$_6$ Perovskite Variant: Photoluminescence Induced by Impurity Doping. *Adv. Funct. Mater.* **2018,** *28*, 1801131.

3. Li, J.; Tan, Z.; Hu, M.; Chen, C.; Luo, J.; Li, S.; Gao, L.; Xiao, Z.; Niu, G.; Tang, J. Antimony Doped Cs$_2$SnCl$_6$ with Bright and Stable Emission. *Fron. Optoelectron.* **2019,** *12*, 352-364.

4. Zeng, R.; Bai, K.; Wei, Q.; Chang, T.; Yan, J.; Ke, B.; Huang, J.; Wang, L.; Zhou, W.; Cao, S.; Zhao, J.; Zou, B. Boosting Triplet Self-Trapped Exciton Emission in Te(IV)-Doped Cs$_2$SnCl$_6$ Perovskite Variants. *Nano Res.* **2020,** *14*, 1551-1558.

5. Qing, X.; Wu, C.; Han, X. Efficient Near-Infrared Luminescence Based on Double Perovskite Cs$_2$SnCl$_6$ *Molecules* **2023**, *28*, 3593.

6. Dujardin, C.; Auffray, E.; Bourret-Courchesne, E.; Dorenbos, P.; Lecoq, P.; Nikl, M.; Vasil'ev, A. N.; Yoshikawa, A.; Zhu, R. Y. Needs, Trends, and Advances in Inorganic Scintillators. *IEEE Trans. Nucl. Sci.* **2018,** *65*, 1977-1997.

7. Luo, J.; Wang, X.; Li, S.; Liu, J.; Guo, Y.; Niu, G.; Yao, L.; Fu, Y.; Gao, L.; Dong, Q.; Zhao, C.; Leng, M.; Ma, F.; Liang, W.; Wang, L.; Jin, S.; Han, J.; Zhang, L.; Etheridge, J.; Wang, J.; Yan, Y.; Sargent, E. H.; Tang, J. Efficient and Stable Emission of Warm-White Light from Lead-Free Halide Double Perovskites. *Nature* **2018,** *563*, 541-545.

8. Morad, V.; Shynkarenko, Y.; Yakunin, S.; Brumberg, A.; Schaller, R. D.; Kovalenko, M. V. Disphenoidal Zero-Dimensional Lead, Tin, and Germanium Halides: Highly Emissive Singlet and Triplet Self-Trapped Excitons and X-ray Scintillation. *J. Am. Chem. Soc.* **2019,** *141*, 9764-9768.

9. Arfin, H.; Kshirsagar, A. S.; Kaur, J.; Mondal, B.; Xia, Z.; Chakraborty, S.; Nag, A. ns^2 Electron (Bi^{3+} and Sb^{3+}) Doping in Lead-Free Metal Halide Perovskite Derivatives. *Chem. Mater.* **2020,** *32*, 10255-10267.

10. Jacobs, P. W. M., Alkali-Halide Crystals Containing Impurity Ions with the Ns^2 Ground-State Electronic Configuration. *J. Phys. Chem. Solids* **1991,** *52*, 35-67.

11. Li, Z.; Song, G.; Li, Y.; Wang, L.; Zhou, T.; Lin, Z.; Xie, R. J., Realizing Tunable White Light Emission in Lead-Free Indium(III) Bromine Hybrid Single Crystals through Antimony(III) Cation Doping. *J. Phys. Chem. Lett.* **2020,** *11*, 10164-10172.

12. Zeng, R.; Zhang, L.; Xue, Y.; Ke, B.; Zhao, Z.; Huang, D.; Wei, Q.; Zhou, W.; Zou, B. Highly Efficient Blue Emission from Self-Trapped Excitons in Stable Sb³⁺-Doped Cs₂NaInCl₆ Double Perovskites. *J. Phys. Chem. Lett.* **2020,** *11*, 2053-2061.

13. Noculak, A.; Morad, V.; McCall, K. M.; Yakunin, S.; Shynkarenko, Y.; Worle, M.; Kovalenko, M. V. Bright Blue and Green Luminescence of Sb(III) in Double Perovskite Cs₂MInCl₆ (M = Na, K) Matrices. *Chem. Mater.* **2020,** *32*, 5118-5124.

14. Wu, Y.; Shi, C. M.; Xu, L. J.; Yang, M.; Chen, Z. N. Reversible Luminescent Vapochromism of a Zero-Dimensional Sb³⁺-Doped Organic-Inorganic Hybrid. *J. Phys. Chem. Lett.* **2021,** *12*, 3288-3294.

15. Chang, T.; Wei, Q.; Zeng, R.; Cao, S.; Zhao, J.; Zou, B. Efficient Energy Transfer in Te⁴⁺-Doped Cs₂ZrCl₆ Vacancy-Ordered Perovskites and Ultrahigh Moisture Stability via A-Site Rb-Alloying Strategy. *J. Phys. Chem. Lett.* **2021,** *12*, 1829-1837.

16. Sun, H. T.; Zhou, J. J.; Qiu, J. R. Recent Advances in Bismuth Activated Photonic Materials. *Prog. Mater. Sci.* **2014,** *64*, 1-72.

17. Boutinaud, P., Luminescence of Sb³⁺ in Closed Shell Transition Metal Oxides. *J. Lumin.* **2019,** *208*, 394-401.

18. Swart, H. C.; Kroon, R. E. (INVITED) Ultraviolet and visible luminescence from bismuth doped materials. *Opt. Mater.: X* **2019,** *2*, 100025.

19. Krasnikov, A.; Mihokova, E.; Nikl, M.; Zazubovich, S.; Zhydachevskyy, Y. Luminescence Spectroscopy and Origin of Luminescence Centers in Bi-Doped Materials. *Crystals* **2020,** *10*, 208.

20. Liu, Y.; Rong, X.; Li, M.; Molokeev, M. S.; Zhao, J.; Xia, Z. Incorporating Rare-Earth Terbium(III) Ions into Cs₂AgInCl₆:Bi Nanocrystals Toward Tunable Photoluminescence. *Angew. Chem. Int. Ed.* **2020,** *59*, 11634-11640.

21. Arfin, H.; Kaur, J.; Sheikh, T.; Chakraborty, S.; Nag, A. Bi³⁺-Er³⁺ and Bi³⁺-Yb³⁺ Codoped Cs₂AgInCl₆ Double Perovskite Near-Infrared Emitters. *Angew. Chem. Int. Ed.* **2020,** *59*, 11307-11311.

22. Gong, S.; Wu, R.; Yang, S.; Wu, L.; Zhang, M.; Han, Q.; Wu, W. Tuning the Luminous Properties and Optical Thermometry of Cs₂SnCl₆ Phosphor Microcrystals via Bi and Sb Codoping. *Photonics Res.* **2021,** *9*, 2182-2189.

23. Zhang, W.; Zheng, W.; Li, L.; Huang, P.; Gong, Z.; Zhou, Z.; Sun, J.; Yu, Y.; Chen, X. Dual-Band-Tunable White-Light Emission from Bi^{3+}/Te^{4+} Emitters in Perovskite-Derivative Cs_2SnCl_6 Microcrystals. *Angew. Chem. Int. Ed.* **2022,** *61*, e202116085.

24. Zhou, B.; Liu, Z. X.; Fang, S. F.; Zhong, H. Z.; Tian, B. B.; Wang, Y.; Li, H. N.; Hu, H. L.; Shi, Y. M. Efficient White Photoluminescence from Self-Trapped Excitons in Sb^{3+}/Bi^{3+}-Codoped $Cs_2NaInCl_6$ Double Perovskites with Tunable Dual-Emission. *ACS Energy Lett.* **2021,** *6*, 3343-3351.

25. Li, X.; Xu, S.; Liu, F.; Qu, J.; Shao, H.; Wang, Z.; Cui, Y.; Ban, D.; Wang, C. Bi and Sb Codoped $Cs_2Ag_{0.1}Na_{0.9}InCl_6$ Double Perovskite with Excitation-Wavelength-Dependent Dual-Emission for Anti-Counterfeiting Application. *ACS Appl. Mater. Interfaces* **2021,** *13*, 31031-31037.

26. Liu, Z.; Zhou, B.; Fang, S.; Nie, J.; Zhong, H.; Hu, H.; Li, H.; Shi, Y. Modulation of the Excitation States in All-Inorganic Halide Perovskites via Sb^{3+} and Bi^{3+} Codoping. *J. Phys. Chem. Lett.* **2023,** *14*, 1022-1028.

27. Jing, Y.; Liu, Y.; Zhao, J.; Xia, Z. Sb^{3+} Doping-Induced Triplet Self-Trapped Excitons Emission in Lead-Free Cs_2SnCl_6 Nanocrystals. *J. Phys. Chem. lett.* **2019,** *10*, 7439-7444.

28. Eickhoff, T.; Grosse, P.; Theiss, W. Diffuse Reflectance Spectroscopy of Powders. *Vib. Spectrosc.* **1990,** *1*, 229-233.

29. Tan, Z. F.; Li, J. H.; Zhang, C.; Li, Z.; Hu, Q. S.; Xiao, Z. W.; Kamiya, T.; Hosono, H.; Niu, G. D.; Lifshitz, E.; Cheng, Y. B.; Tang, J. Highly Efficient Blue-Emitting Bi-Doped Cs_2SnCl_6 Perovskite Variant: Photoluminescence Induced by Impurity Doping. *Adv. Funct. Mater.* **2018,** *28*, 1801131.

30. Ahrens, L. H. The Use of Ionization Potentials Part 1. Ionic Radii of the Elements. *Geochim. Cosmochim. Acta* **1952,** *2*, 155-169.

31. Shannon, R. D., Revised Effective Ionic-Radii and Systematic Studies of Interatomic Distances in Halides and Chalcogenides. *Acta Crystallogr.* **1976,** *32*, 751-767.

32. Kaltzoglou, A.; Antoniadou, M.; Kontos, A. G.; Stoumpos, C. C.; Perganti, D.; Siranidi, E.; Raptis, V.; Trohidou, K.; Psycharis, V.; Kanatzidis, M. G.; Falaras, P. Optical-Vibrational Properties of the Cs_2SnX_6 (X = Cl, Br, I) Defect Perovskites and Hole-Transport Efficiency in Dye-Sensitized Solar Cells. *J. Phys. Chem. C* **2016,** *120*, 11777-11785.

33. Arfin, H.; Nag, A. Origin of Luminescence in Sb^{3+}- and Bi^{3+}-Doped Cs_2SnCl_6 Perovskites: Excited State Relaxation and Spin-Orbit Coupling. *J. Phys. Chem. Lett.* **2021,** *12*, 10002-10008.

34. Jing, Y.; Liu, Y.; Zhao, J.; Xia, Z. Sb³⁺ Doping-Induced Triplet Self-Trapped Excitons Emission in Lead-Free Cs₂SnCl₆ Nanocrystals. *J. Phys. Chem. Lett.* **2019,** *10*, 7439-7444.

Chapter 5

Thesis Summary and Future Outlook

5.1 Thesis Summary

Lead free halide perovskites are being explored as environmentally benign alternative of lead halide perovskites, for optical and optoelectronic applications. Lead free halide perovskites have octahedral sites, which are preferred by large number of luminescent centers, making halide perovskites a potential class of host materials for doping luminescent centers. This thesis explores such halide perovskites to host luminescent centers with visible and short-wave infrared emission, and develop the synthesis and understanding of photophysical processes.

Halide double perovskites like $Cs_2AgInCl_6$ consist of alternative monovalent and trivalent metal octahedral sites. In this thesis, we utilized the compositional flexibility of halide double perovskites and made them luminescent in nature by incorporation of luminescent centers. $Cs_2AgInCl_6$ double perovskite with In^{3+} metal center ionic radii ($r_{In^{3+}} = 0.80$) similar to that of the lanthanide ($r_{Er^{3+}} = 0.89$, $r_{Yb^{3+}} = 0.87$) is chosen as the host material for lanthanide doping. Er^{3+}- and Yb^{3+}-doped $Cs_2AgInCl_6$ emit short-wave infrared radiation with peaks at 1540 nm and 990 nm, respectively, which have technological importance. But these lanthanide doped systems need higher excitation energy (> 3.54 eV, 350 nm). This large energy difference between excitation and emission causes a serious energy loss. To address this issue, we proposed the codoping of Bi^{3+} ion and lanthanide ion in $Cs_2AgInCl_6$. Bi^{3+} show nearly allowed $^1S_0 \rightarrow {}^3P_1^*$ transition and absorbs at the sub-band gap level, reducing the excitation energy to 3.35 eV (Figure 5.1). Now, the Bi^{3+}-Er^{3+} and Bi^{3+}-Yb^{3+} codoped $Cs_2AgInCl_6$ can be excited by 370 nm, reducing the energy gap between the excitation and lanthanide emission. This strategy has opened a plethora of possibilities of codoping luminescent centers in halide double perovskites to obtain desired optical excitation and emission properties.

The host $Cs_2AgInCl_6$ has photostability issue due to presence of photosensitive Ag^+. So, Ag^+ is replaced with Na^+ and photostable $Cs_2NaInCl_6$ is obtained. Bi^{3+}, Sb^{3+} and Te^{4+} are separately doped in $Cs_2NaInCl_6$ to obtained suitable dopant for lower energy excitation, and found that the Te^{4+}-doped one absorbs at lowest energy of 3.1 eV (400 nm). Te^{4+} and Ln^{3+} (Ln = Er, Yb) are codoped in $Cs_2NaInCl_6$ to obtain the short-wave infrared emission of lanthanide via Te^{4+} excitation. The excited Te^{4+} ions non-radiatively transfer its energy to Ln^{3+} (Ln = Er, Yb) and the excited lanthanide ions emit characteristic emission (Figure 5.1).

In another related work (chapter 4), we have prepared Sb^{3+}-doped, Bi^{3+}-doped, and Sb^{3+}-Bi^{3+} codoped Cs_2SnCl_6 0D perovskites. On the basis of temperature dependent photoluminescence data, we find that the emitting $^3P_1^*$ state in Sb^{3+} has two minima which give rise to two

emissions at cryogenic temperatures. Whereas the stronger spin-orbit coupling in Bi^{3+} leads to single minima in $^{3}P_{1}^{*}$ state and give single emission feature at all temperatures (Figure 5.1). The absorption and emission originate from isolated Bi^{3+} and Sb^{3+} centers, which remain almost unperturbed by codoping. This allows us to obtain broad visible emission by codoping (Bi^{3+} and Sb^{3+}) and obtain tunable emission by varying the relative doping percentage. An overall graphical summary is presented in Figure 5.1.
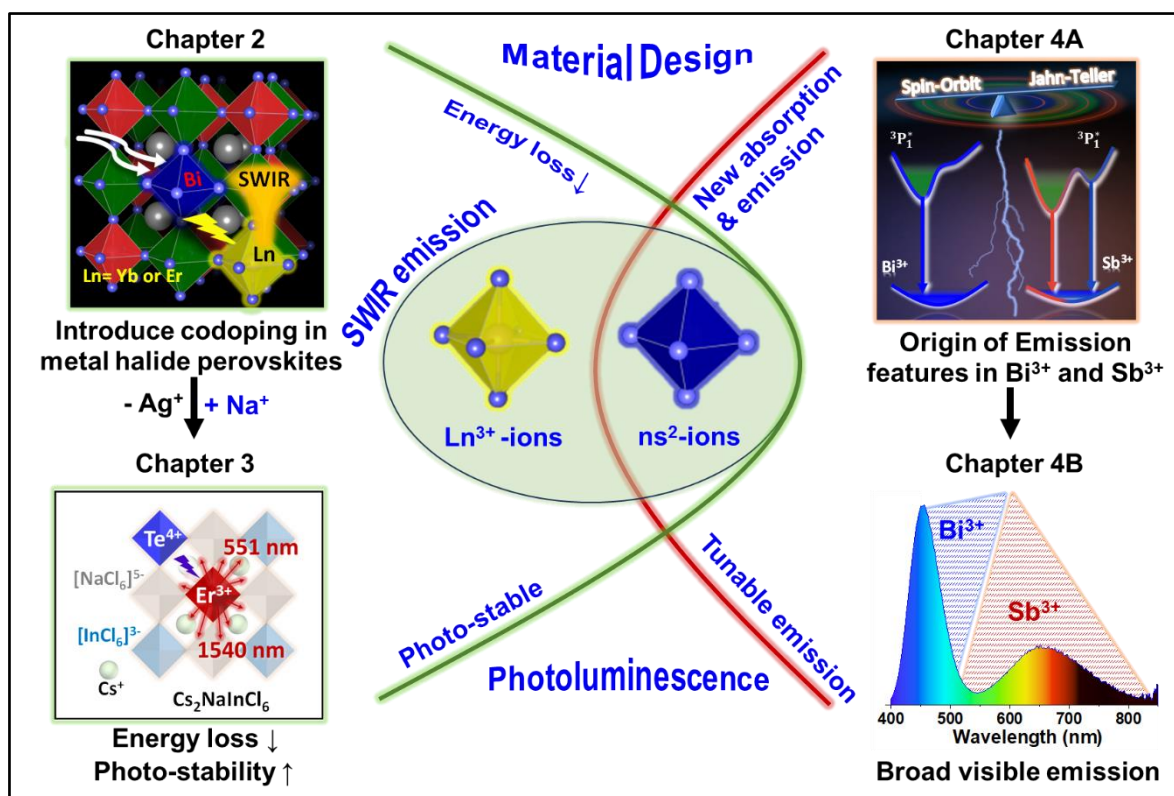
Figure 5.1: Graphical summary of this thesis. Lanthanide ion (Ln^{3+}) and ns^2-ion doping are utilized to impart optical functionality in lead free halide perovskites. In chapter 2, Bi^{3+}-Ln^{3+} codoping is introduced to decrease the excitation energy and energy loss. Addressing photo-stability concerns, Chapter 3 presents the substitution of Ag^+ with Na^+, alongside the exploration of Te^{4+} as a suitable sensitizer. Chapter 4A uncovers an intriguing correlation between the emissions of Sb^{3+} and Bi^{3+}. In chapter 4b, Bi^{3+}-Sb^{3+} codoping is utilized to get broad visible emission.

5.2 Future Outlook

Lanthanide ions (e.g., Er^{3+}, Yb^{3+}) emit technologically important short-wave infrared radiation.[1-3] Lanthanide ion doping is one of the ways to harness these emissions.[4-5] Lanthanide ion doping is mostly achieved in oxides and fluorides-based materials, whereas in halide (Cl, Br, I) based materials it is rare.[6-8] We could dope lanthanide ion in chloride-based halide double perovskites and achieved photoluminescence of lanthanides.[9-10] By coating material on

commercial UV LED chips, a phosphor converted LED is assembled which give visible as well as SWIR emission (Figure 5.2).

However, realizing electroluminescence from lanthanide-doped halide double perovskites poses significant challenges.[11] The obstacles are two-fold in achieving electroluminescence light-emitting diodes (LEDs) based on chloride-based halide double perovskites. Firstly, the formation of thin films in chloride-based systems is difficult. Secondly, the limited charge carrier mobility within these systems presents a substantial limitation.[11] The challenge of thin film fabrication can be overcome by employing colloidal nanocrystal synthesis techniques.[12-14] To address the charge mobility issue, a strategic approach involves substituting chlorine with its larger counterparts, bromine or iodine.[15] The bromine and iodine have $4p^5$ and $6p^5$ valence shell orbitals which are comparatively larger in size than $3p^5$ orbital of chlorine. Consequently, a more favorable overlap between the metal center and halide orbitals is anticipated, which is expected to enhance charge carrier mobility within the system. The material could be explored to fabricate electroluminescence LEDs as schematically presented in Figure 5.2.
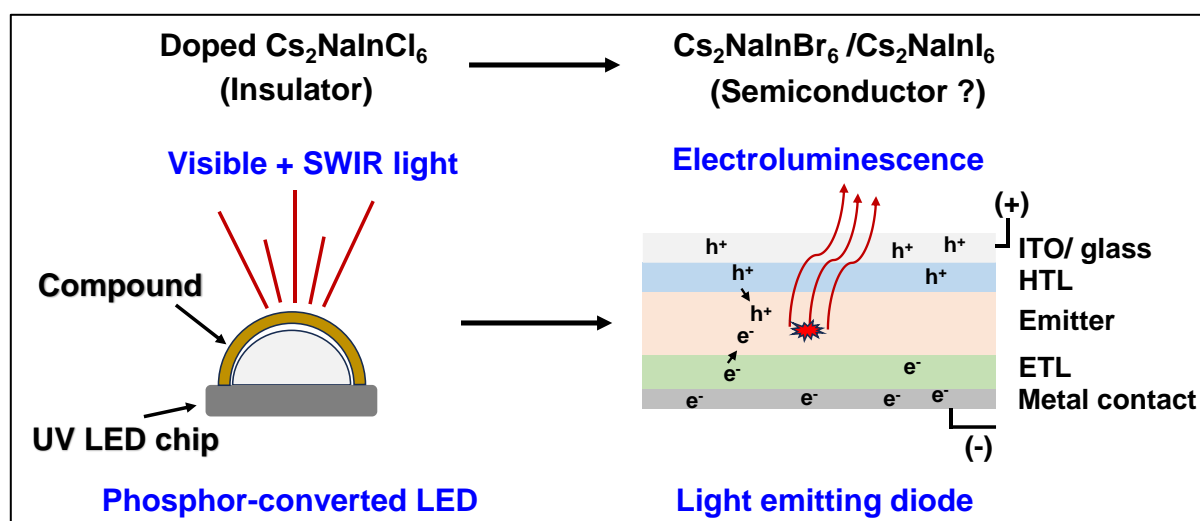
Figure 5.2: Schematic presentation of a phosphor-converted LED (left side) and electroluminescence LED (right side). In phosphor converted LED, doped phosphor material coated on the UV LED gets photo-excited by the UV lights emitted by the LED chip. The excited doped phosphor emits visible and SWIR light. A multilayer device consisting of appropriate emitter, hole transport layer (HTL), electron transport layer (HTL) and metal contacts need to be fabricated to obtain electroluminescence. When the potential applied to this device, electron and hole flow via contact layers and get combine in emitting layer and release photon.

5.3 References

1. Marin, R.; Jaque, D. Doping Lanthanide Ions in Colloidal Semiconductor Nanocrystals for Brighter Photoluminescence. *Chem. Rev.* **2021,** *121*, 1425-1462.

2. Park, W.; Lu, D.; Ahn, S. Plasmon Enhancement of Luminescence Upconversion. *Chem. Soc. Rev.* **2015,** *44*, 2940-2962.

3. Tessitore, G.; Mandl, G. A.; Maurizio, S. L.; Kaur, M.; Capobianco, J. A. The Role of Lanthanide Luminescence in Advancing Technology. *RSC Adv.* **2023,** *13*, 17787-17811.

4. Marciniak, L.; Bednarkiewicz, A.; Drabik, J.; Trejgis, K.; Strek, W. Optimization of Highly Sensitive YAG:Cr^{3+},Nd^{3+} Nanocrystal-Based Luminescent Thermometer Operating in an Optical Window of Biological Tissues. *Phys. Chem. Chem. Phys.* **2017,** *19*, 7343-7351.

5. Pan, G.; Bai, X.; Yang, D.; Chen, X.; Jing, P.; Qu, S.; Zhang, L.; Zhou, D.; Zhu, J.; Xu, W.; Dong, B.; Song, H. Doping Lanthanide into Perovskite Nanocrystals: Highly Improved and Expanded Optical Properties. *Nano Lett.* **2017,** *17*, 8005-8011.

6. Mir, W. J.; Sheikh, T.; Arfin, H.; Xia, Z. G.; Nag, A. Lanthanide Doping in Metal Halide Perovskite Nanocrystals: Spectral Shifting, Quantum Cutting and Optoelectronic Applications. *Npg Asia Mater.* **2020,** *12*, 9.

7. Wang, X.; Valiev, R. R.; Ohulchanskyy, T. Y.; Ågren, H.; Yang, C.; Chen, G. Dye-Sensitized Lanthanide-Doped Upconversion Nanoparticles. *Chem. Soc. Rev.* **2017,** *46*, 4150-4167.

8. Zheng, W.; Zhou, S.; Chen, Z.; Hu, P.; Liu, Y.; Tu, D.; Zhu, H.; Li, R.; Huang, M.; Chen, X. Sub-10 nm Lanthanide-Doped CaF_2 Nanoprobes for Time-Resolved Luminescent Biodetection. *Angew. Chem. Int. Ed.* **2013,** *52*, 6671-6676.

9. Arfin, H.; Kaur, J.; Sheikh, T.; Chakraborty, S.; Nag, A. Bi^{3+}-Er^{3+} and Bi^{3+}-Yb^{3+} Codoped $Cs_2AgInCl_6$ Double Perovskite Near-Infrared Emitters. *Angew. Chem. Int. Ed.* **2020,** *59*, 11307-11311.

10. Arfin, H.; Rathod, R.; Shingote, A. S.; Priolkar, K. R.; Santra, P. K.; Nag, A. Short-Wave Infrared Emissions from Te^{4+}–Ln^{3+} (Ln: Er, Yb)-Codoped $Cs_2NaInCl_6$ Double Perovskites. *Chem. Mater.* **2023,** Article ASAP. DOI: 10.1021/acs.chemmater.3c01413.

11. Luo, J.; Wang, X.; Li, S.; Liu, J.; Guo, Y.; Niu, G.; Yao, L.; Fu, Y.; Gao, L.; Dong, Q.; Zhao, C.; Leng, M.; Ma, F.; Liang, W.; Wang, L.; Jin, S.; Han, J.; Zhang, L.; Etheridge, J.; Wang, J.; Yan, Y.; Sargent, E. H.; Tang, J. Efficient and Stable Emission of Warm-White Light from Lead-Free Halide Double Perovskites. *Nature* **2018,** *563*, 541-545.

12. Locardi, F.; Cirignano, M.; Baranov, D.; Dang, Z.; Prato, M.; Drago, F.; Ferretti, M.; Pinchetti, V.; Fanciulli, M.; Brovelli, S.; De Trizio, L.; Manna, L. Colloidal Synthesis of

Double Perovskite $Cs_2AgInCl_6$ and Mn-Doped $Cs_2AgInCl_6$ Nanocrystals. *J. Am. Chem. Soc.* **2018,** *140*, 12989-12995.

13. Locardi, F.; Sartori, E.; Buha, J.; Zito, J.; Prato, M.; Pinchetti, V.; Zaffalon, M. L.; Ferretti, M.; Brovelli, S.; Infante, I.; De Trizio, L.; Manna, L. Emissive Bi-Doped Double Perovskite $Cs_2Ag_{1-x}Na_xInCl_6$ Nanocrystals. *ACS Energy Lett.* **2019,** *4*, 1976-1982.

14. Liu, Y.; Rong, X.; Li, M.; Molokeev, M. S.; Zhao, J.; Xia, Z. Incorporating Rare-Earth Terbium(III) Ions into $Cs_2AgInCl_6$:Bi Nanocrystals Toward Tunable Photoluminescence. *Angew. Chem. Int. Ed.* **2020,** *59*, 11634-11640.

15. Herz, L. M. Charge-Carrier Mobilities in Metal Halide Perovskites: Fundamental Mechanisms and Limits. *ACS Energy Lett.* **2017,** *2*, 1539-1548.

List of Publications

Included in the Thesis:

➤ **Arfin, H.**; Kaur, J.; Sheikh, T.; Chakraborty, S.; Nag, A., Bi^{3+} -Er^{3+} and Bi^{3+} -Yb^{3+} Codoped $Cs_2AgInCl_6$ Double Perovskite Near-Infrared Emitters. *Angew. Chem. Int. Ed.* **2020,** *59*, 11307-11311.

➤ **Arfin, H.**; Nag, A., Origin of Luminescence in Sb^{3+}- and Bi^{3+}-Doped Cs_2SnCl_6 Perovskites: Excited State Relaxation and Spin–Orbit Coupling. *J. Phys. Chem. Lett.* **2021**, *12*, 10002–10008.

➤ **Arfin, H.**; Rathod, R.; Sundarnath, S.A.; Santra P. K.; Nag A. Short Wave Infrared Emissions from Te^{4+}-Ln^{3+} (Ln: Er, Yb) Codoped $Cs_2NaInCl_6$ Double Perovskites. *Chem. Mater.* **2023**, DOI: 10.1021/acs.chemmater.3c01413.

➤ **Arfin, H.**; Kshirsagar, A. S.; Kaur, J.; Mondal, B.; Xia, Z.; Chakraborty, S.; Nag, A. ns^2 Electron (Bi^{3+} and Sb^{3+}) Doping in Lead-Free Metal Halide Perovskite Derivatives. *Chem. Mater.* **2020,** *32*, 10255-10267 (perspective).

➤ **Arfin, H.**; Nag, A., Optical Properties of Bi^{3+}-Sb^{3+} Codoped Cs_2SnCl_6 0D Perovskite (manuscript under preparation).

Not Included in the Thesis:

➤ Mir, W. J.; Sheikh, T.; **Arfin, H.**; Xia, Z. G.; Nag, A., Lanthanide Doping in Metal Halide Perovskite Nanocrystals: Spectral Shifting, Quantum Cutting and Optoelectronic Applications. *NPG Asia Mater.* **2020,** *12*, 9. (review article)

➤ Saikia, S.; Joshi, A.; **Arfin, H.**; Badola, S.; Saha, S.; Nag, A., Sb^{3+} -Er^{3+} Codoped $Cs_2NaInCl_6$ for Emitting Blue and Short-Wave Infrared Radiation. *Angew. Chem. Int. Ed.* **2022,** *61*, e202201628.

➤ Kshirsagar, A.S.; **Arfin, H**.; Banerjee, S.; Mondal, B.; Nag, A. Colloidal Sb^{3+}-Doped $Cs_2InCl_5 \cdot H_2O$ Perovskite Nanocrystals with Temperature-Dependent Luminescence. *J. Phys. Chem. C* **2021**, *125*, 27671−27677.

Copyrights and Permissions

Reuse of figure in thesis_non profit

ACS Publications <acs@service-now.com>   Mon, Aug 28, 2023 at 11:13 PM
Reply-To: support@services.acs.org
To: arfin.habibul@students.iiserpune.ac.in

Hello Dr. Arfin,

I hope this message reaches you well, and thank you for contacting ACS Publications Support.

Your permission requested is granted and there is no fee for this reuse.

In your planned reuse, you must cite the ACS article as the source, add this direct link: https://pubs.acs.org/doi/10.1021/nl5048779 and include a notice to readers that further permission related to the material excerpted should be directed to the ACS.

Please do not hesitate to contact me if you need any further assistance.

Drew Jenkins
ACS Publications Support
Customer Services & Information
Website: https://acs.service-now.com/acs
Email: support@services.acs.org
Phone: 800-227-9919 | 202-872-(HELP) 4357

Case Info:

Case Number : CSCSI0158507

Created On: 08-28-2023 01:28:49 PM EDT

Short Description: Reuse of figure in thesis_non profit

Description: Dear ACS team,
I would like to reuse one of the figures from the given below paper in my introduction part of the thesis. I pledge to give proper citations and credits.
Details:
Link of the paper: https://pubs.acs.org/doi/10.1021/nl5048779
Title of the paper: Nanocrystals of Cesium Lead Halide Perovskites (CsPbX3, X = Cl, Br, and I): Novel Optoelectronic Materials Showing Bright Emission with Wide Color Gamut
Figure: 2
Details of where the content will be used
Thesis author: Habibul Arfin
Title of the thesis: ns2-Ion and Lanthanide Ion Doping in Metal Halide Perovskites: Visible to Short Wave Infrared Emission.
Presentation date: September 2023
Institute: IISER Pune

Please grant me permission to do so. I would be very grateful for this.

Regards,
Habibul Arfin
Dr. Angshuman Nag Lab
IISER PUNE
Mob. No. 8527848616

Case CSCSI0158508 comments added

1 message

ACS Publications <acs@service-now.com>   Mon, Aug 28, 2023 at 11:16 PM
Reply-To: ACS Publications <acs@service-now.com>
To: arfin.habibul@students.iiserpune.ac.in

Short Description: Reuse of figure in thesis_non profit

Priority: 3 - Moderate

Click here to view the case: LINK

Comments:

08-28-2023 01:45:51 PM EDT - Drew Jenkins   Additional comments
Hello Dr. Arfin,

I hope this message reaches you well, and thank you for contacting ACS Publications Support.

Your permission requested is granted and there is no fee for this reuse.

In your planned reuse, you must cite the ACS article as the source, add this direct link:
https://pubs.acs.org/doi/10.1021/acsenergylett.6b00499 and include a notice to readers that
further permission related to the material excerpted should be directed to the ACS.

Please do not hesitate to contact me if you need any further assistance.

Drew Jenkins
ACS Publications Support
Customer Services & Information
Website: https://acs.service-now.com/acs
Email: support@services.acs.org
Phone: 800-227-9919 | 202-872-(HELP) 4357

Ref:MSG1227434_jXRUbU2j1myMdAlRgBPV

Design of Lead-Free Inorganic Halide Perovskites for Solar Cells via Cation-Transmutation

ACS Publications
Most Trusted. Most Cited. Most Read.

Author: Xin-Gang Zhao, Ji-Hui Yang, Yuhao Fu, et al

Publication: Journal of the American Chemical Society

Publisher: American Chemical Society

Date: Feb 1, 2017

Copyright © 2017, American Chemical Society

PERMISSION/LICENSE IS GRANTED FOR YOUR ORDER AT NO CHARGE

This type of permission/license, instead of the standard Terms and Conditions, is sent to you because no fee is being charged for your order. Please note the following:

- Permission is granted for your request in both print and electronic formats, and translations.
- If figures and/or tables were requested, they may be adapted or used in part.
- Please print this page for your records and send a copy of it to your publisher/graduate school.
- Appropriate credit for the requested material should be given as follows: "Reprinted (adapted) with permission from {COMPLETE REFERENCE CITATION}. Copyright {YEAR} American Chemical Society." Insert appropriate information in place of the capitalized words.
- One-time permission is granted only for the use specified in your RightsLink request. No additional uses are granted (such as derivative works or other editions). For any uses, please submit a new request.

If credit is given to another source for the material you requested from RightsLink, permission must be obtained from that source.

BACK   CLOSE WINDOW

CCC
RightsLink

Absolute energy level positions in tin- and lead-based halide perovskites

SPRINGER NATURE

Author: Shuxia Tao et al

Publication: Nature Communications

Publisher: Springer Nature

Date: Jun 12, 2019

Copyright © 2019, The Author(s)

Creative Commons

Parity-Forbidden Transitions and Their Impact on the Optical Absorption Properties of Lead-Free Metal Halide Perovskites and Double Perovskites

ACS Publications
Most Trusted. Most Cited. Most Read.

Author: Weiwei Meng, Xiaoming Wang, Zewen Xiao, et al

Publication: Journal of Physical Chemistry Letters

Publisher: American Chemical Society

Date: Jul 1, 2017

Copyright © 2017, American Chemical Society

PERMISSION/LICENSE IS GRANTED FOR YOUR ORDER AT NO CHARGE

This type of permission/license, instead of the standard Terms and Conditions, is sent to you because no fee is being charged for your order. Please note the following:

- Permission is granted for your request in both print and electronic formats, and translations.
- If figures and/or tables were requested, they may be adapted or used in part.
- Please print this page for your records and send a copy of it to your publisher/graduate school.
- Appropriate credit for the requested material should be given as follows: "Reprinted (adapted) with permission from {COMPLETE REFERENCE CITATION}. Copyright {YEAR} American Chemical Society." Insert appropriate information in place of the capitalized words.
- One-time permission is granted only for the use specified in your RightsLink request. No additional uses are granted (such as derivative works or other editions). For any uses, please submit a new request.

If credit is given to another source for the material you requested from RightsLink, permission must be obtained from that source.

BACK   CLOSE WINDOW

Doping Lanthanide into Perovskite Nanocrystals: Highly Improved and Expanded Optical Properties

ACS Publications
Most Trusted. Most Cited. Most Read.

Author: Gencai Pan, Xue Bai, Dongwen Yang, et al

Publication: Nano Letters

Publisher: American Chemical Society

Date: Dec 1, 2017

Copyright © 2017, American Chemical Society

PERMISSION/LICENSE IS GRANTED FOR YOUR ORDER AT NO CHARGE

This type of permission/license, instead of the standard Terms and Conditions, is sent to you because no fee is being charged for your order. Please note the following:

- Permission is granted for your request in both print and electronic formats, and translations.
- If figures and/or tables were requested, they may be adapted or used in part.
- Please print this page for your records and send a copy of it to your publisher/graduate school.
- Appropriate credit for the requested material should be given as follows: "Reprinted (adapted) with permission from {COMPLETE REFERENCE CITATION}. Copyright {YEAR} American Chemical Society." Insert appropriate information in place of the capitalized words.
- One-time permission is granted only for the use specified in your RightsLink request. No additional uses are granted (such as derivative works or other editions). For any uses, please submit a new request.

If credit is given to another source for the material you requested from RightsLink, permission must be obtained from that source.

BACK   CLOSE WINDOW

Compact ultrabroadband light-emitting diodes based on lanthanide-doped lead-free double perovskites

SPRINGER NATURE

Author: Shilin Jin et al

Publication: Light: Science & Applications

Publisher: Springer Nature

Date: Mar 8, 2022

Copyright © 2022, The Author(s)

Creative Commons

Upconversion Luminescence of Monodisperse CaF2:Yb3 /Er3 Nanocrystals

ACS Publications
Most Trusted. Most Cited. Most Read.

Author: Guofeng Wang, Qing Peng, Yadong Li

Publication: Journal of the American Chemical Society

Publisher: American Chemical Society

Date: Oct 1, 2009

Copyright © 2009, American Chemical Society

PERMISSION/LICENSE IS GRANTED FOR YOUR ORDER AT NO CHARGE

This type of permission/license, instead of the standard Terms and Conditions, is sent to you because no fee is being charged for your order. Please note the following:

- Permission is granted for your request in both print and electronic formats, and translations.
- If figures and/or tables were requested, they may be adapted or used in part.
- Please print this page for your records and send a copy of it to your publisher/graduate school.
- Appropriate credit for the requested material should be given as follows: "Reprinted (adapted) with permission from {COMPLETE REFERENCE CITATION}. Copyright {YEAR} American Chemical Society." Insert appropriate information in place of the capitalized words.
- One-time permission is granted only for the use specified in your RightsLink request. No additional uses are granted (such as derivative works or other editions). For any uses, please submit a new request.

If credit is given to another source for the material you requested from RightsLink, permission must be obtained from that source.

BACK   CLOSE WINDOW

The Fermi energy as common parameter to describe charge compensation mechanisms: A path to Fermi level engineering of oxide electroceramics

SPRINGER NATURE

Author: Andreas Klein et al

Publication: Journal of Electroceramics

Publisher: Springer Nature

Date: Aug 9, 2023

Copyright © 2023, The Author(s)

Creative Commons

Aug 29, 2023

This Agreement between Mr. HABIBUL ARFIN ("You") and John Wiley and Sons ("John Wiley and Sons") consists of your license details and the terms and conditions provided by John Wiley and Sons and Copyright Clearance Center.

License Number	5618300895190
License date	Aug 29, 2023
Licensed Content Publisher	John Wiley and Sons
Licensed Content Publication	Angewandte Chemie International Edition
Licensed Content Title	Bi3 -Er3 and Bi3 -Yb3 Codoped Cs2AgInCl6 Double Perovskite Near-Infrared Emitters
Licensed Content Author	Angshuman Nag, Sudip Chakraborty, Tariq Sheikh, et al
Licensed Content Date	Mar 31, 2020
Licensed Content Volume	59
Licensed Content Issue	28
Licensed Content Pages	5
Type of use	Dissertation/Thesis

Requestor type	Author of this Wiley article
Format	Print and electronic
Portion	Full article
Will you be translating?	No
Title	Doping ns2 -Ions and Lanthanide Ions in MetalHalide Perovskites: Visible to Short-Wave Infrared Emission
Institution name	IISER Pune
Expected presentation date	Oct 2023
Requestor Location	Mr. HABIBUL ARFIN Room No. 309, Hostel -2 IISER PUNE PUNE pune, 411008 India Attn: IISER PUNE
Publisher Tax ID	EU826007151
Customer VAT ID	INBUQPA2537R
Total	0.00 USD

Terms and Conditions

you opened your RightsLink account (these are available at any time at
http://myaccount.copyright.com).

Terms and Conditions

- The materials you have requested permission to reproduce or reuse (the "Wiley Materials") are protected by copyright.

- You are hereby granted a personal, non-exclusive, non-sub licensable (on a stand-alone basis), non-transferable, worldwide, limited license to reproduce the Wiley Materials for the purpose specified in the licensing process. This license, **and any CONTENT (PDF or image file) purchased as part of your order,** is for a one-time use only and limited to any maximum distribution number specified in the license. The first instance of republication or reuse granted by this license must be completed within two years of the date of the grant of this license (although copies prepared before the end date may be distributed thereafter). The Wiley Materials shall not be used in any other manner or for any other purpose, beyond what is granted in the license. Permission is granted subject to an appropriate acknowledgement given to the author, title of the material/book/journal and the publisher. You shall also duplicate the copyright notice that appears in the Wiley publication in your use of the Wiley Material. Permission is also granted on the understanding that nowhere in the text is a previously published source acknowledged for all or part of this Wiley Material. Any third party content is expressly excluded from this permission.

- With respect to the Wiley Materials, all rights are reserved. Except as expressly granted by the terms of the license, no part of the Wiley Materials may be copied, modified, adapted (except for minor reformatting required by the new Publication), translated, reproduced, transferred or distributed, in any form or by any means, and no derivative works may be made based on the Wiley Materials without the prior permission of the respective copyright owner.**For STM Signatory Publishers clearing permission under the terms of the STM Permissions Guidelines only, the terms of the license are extended to include subsequent editions and for editions in other languages, provided such editions are for the work as a whole in situ and does not involve the separate exploitation of the permitted figures or extracts,** You may not alter, remove or suppress in any manner any copyright, trademark or other notices displayed by the Wiley Materials. You may not license, rent, sell, loan, lease, pledge, offer as security, transfer or assign the Wiley Materials on a stand-alone basis, or any of the rights granted to you hereunder to any other person.

- The Wiley Materials and all of the intellectual property rights therein shall at all times remain the exclusive property of John Wiley & Sons Inc, the Wiley Companies, or their respective licensors, and your interest therein is only that of having possession of and the right to reproduce the Wiley Materials pursuant to Section 2 herein during the continuance of this Agreement. You agree that you own no right, title or interest in or to the Wiley Materials or any of the intellectual property rights therein. You shall have no rights hereunder other than the license as provided for above in Section 2. No right, license or interest to any trademark, trade name, service mark or other branding ("Marks") of WILEY or its licensors is granted hereunder, and you agree that you shall not assert any such right, license or interest with respect thereto

- NEITHER WILEY NOR ITS LICENSORS MAKES ANY WARRANTY OR REPRESENTATION OF ANY KIND TO YOU OR ANY THIRD PARTY, EXPRESS, IMPLIED OR STATUTORY, WITH RESPECT TO THE MATERIALS OR THE

ACCURACY OF ANY INFORMATION CONTAINED IN THE MATERIALS, INCLUDING, WITHOUT LIMITATION, ANY IMPLIED WARRANTY OF MERCHANTABILITY, ACCURACY, SATISFACTORY QUALITY, FITNESS FOR A PARTICULAR PURPOSE, USABILITY, INTEGRATION OR NON-INFRINGEMENT AND ALL SUCH WARRANTIES ARE HEREBY EXCLUDED BY WILEY AND ITS LICENSORS AND WAIVED BY YOU.

- WILEY shall have the right to terminate this Agreement immediately upon breach of this Agreement by you.

- You shall indemnify, defend and hold harmless WILEY, its Licensors and their respective directors, officers, agents and employees, from and against any actual or threatened claims, demands, causes of action or proceedings arising from any breach of this Agreement by you.

- IN NO EVENT SHALL WILEY OR ITS LICENSORS BE LIABLE TO YOU OR ANY OTHER PARTY OR ANY OTHER PERSON OR ENTITY FOR ANY SPECIAL, CONSEQUENTIAL, INCIDENTAL, INDIRECT, EXEMPLARY OR PUNITIVE DAMAGES, HOWEVER CAUSED, ARISING OUT OF OR IN CONNECTION WITH THE DOWNLOADING, PROVISIONING, VIEWING OR USE OF THE MATERIALS REGARDLESS OF THE FORM OF ACTION, WHETHER FOR BREACH OF CONTRACT, BREACH OF WARRANTY, TORT, NEGLIGENCE, INFRINGEMENT OR OTHERWISE (INCLUDING, WITHOUT LIMITATION, DAMAGES BASED ON LOSS OF PROFITS, DATA, FILES, USE, BUSINESS OPPORTUNITY OR CLAIMS OF THIRD PARTIES), AND WHETHER OR NOT THE PARTY HAS BEEN ADVISED OF THE POSSIBILITY OF SUCH DAMAGES. THIS LIMITATION SHALL APPLY NOTWITHSTANDING ANY FAILURE OF ESSENTIAL PURPOSE OF ANY LIMITED REMEDY PROVIDED HEREIN.

- Should any provision of this Agreement be held by a court of competent jurisdiction to be illegal, invalid, or unenforceable, that provision shall be deemed amended to achieve as nearly as possible the same economic effect as the original provision, and the legality, validity and enforceability of the remaining provisions of this Agreement shall not be affected or impaired thereby.

- The failure of either party to enforce any term or condition of this Agreement shall not constitute a waiver of either party's right to enforce each and every term and condition of this Agreement. No breach under this agreement shall be deemed waived or excused by either party unless such waiver or consent is in writing signed by the party granting such waiver or consent. The waiver by or consent of a party to a breach of any provision of this Agreement shall not operate or be construed as a waiver of or consent to any other or subsequent breach by such other party.

- This Agreement may not be assigned (including by operation of law or otherwise) by you without WILEY's prior written consent.

- Any fee required for this permission shall be non-refundable after thirty (30) days from receipt by the CCC.

- These terms and conditions together with CCC's Billing and Payment terms and conditions (which are incorporated herein) form the entire agreement between you and WILEY concerning this licensing transaction and (in the absence of fraud) supersedes all prior agreements and representations of the parties, oral or written. This Agreement

- may not be amended except in writing signed by both parties. This Agreement shall be binding upon and inure to the benefit of the parties' successors, legal representatives, and authorized assigns.

- In the event of any conflict between your obligations established by these terms and conditions and those established by CCC's Billing and Payment terms and conditions, these terms and conditions shall prevail.

- WILEY expressly reserves all rights not specifically granted in the combination of (i) the license details provided by you and accepted in the course of this licensing transaction, (ii) these terms and conditions and (iii) CCC's Billing and Payment terms and conditions.

- This Agreement will be void if the Type of Use, Format, Circulation, or Requestor Type was misrepresented during the licensing process.

- This Agreement shall be governed by and construed in accordance with the laws of the State of New York, USA, without regards to such state's conflict of law rules. Any legal action, suit or proceeding arising out of or relating to these Terms and Conditions or the breach thereof shall be instituted in a court of competent jurisdiction in New York County in the State of New York in the United States of America and each party hereby consents and submits to the personal jurisdiction of such court, waives any objection to venue in such court and consents to service of process by registered or certified mail, return receipt requested, at the last known address of such party.

WILEY OPEN ACCESS TERMS AND CONDITIONS

Wiley Publishes Open Access Articles in fully Open Access Journals and in Subscription journals offering Online Open. Although most of the fully Open Access journals publish open access articles under the terms of the Creative Commons Attribution (CC BY) License only, the subscription journals and a few of the Open Access Journals offer a choice of Creative Commons Licenses. The license type is clearly identified on the article.

The Creative Commons Attribution License

The [Creative Commons Attribution License (CC-BY)](#) allows users to copy, distribute and transmit an article, adapt the article and make commercial use of the article. The CC-BY license permits commercial and non-

Creative Commons Attribution Non-Commercial License

The [Creative Commons Attribution Non-Commercial (CC-BY-NC)License](#) permits use, distribution and reproduction in any medium, provided the original work is properly cited and is not used for commercial purposes.(see below)

Creative Commons Attribution-Non-Commercial-NoDerivs License

The [Creative Commons Attribution Non-Commercial-NoDerivs License](#) (CC-BY-NC-ND) permits use, distribution and reproduction in any medium, provided the original work is properly cited, is not used for commercial purposes and no modifications or adaptations are made. (see below)

Use by commercial "for-profit" organizations

Use of Wiley Open Access articles for commercial, promotional, or marketing purposes requires further explicit permission from Wiley and will be subject to a fee.

Further details can be found on Wiley Online Library
http://olabout.wiley.com/WileyCDA/Section/id-410895.html

Other Terms and Conditions:

v1.10 Last updated September 2015

Questions? customercare@copyright.com.

Origin of Luminescence in Sb3 - and Bi3 -Doped Cs2SnCl6 Perovskites: Excited State Relaxation and Spin–Orbit Coupling

ACS Publications
Most Trusted. Most Cited. Most Read.

Author: Habibul Arfin, Angshuman Nag

Publication: Journal of Physical Chemistry Letters

Publisher: American Chemical Society

Date: Oct 1, 2021

Copyright © 2021, American Chemical Society

PERMISSION/LICENSE IS GRANTED FOR YOUR ORDER AT NO CHARGE

This type of permission/license, instead of the standard Terms and Conditions, is sent to you because no fee is being charged for your order. Please note the following:

- Permission is granted for your request in both print and electronic formats, and translations.
- If figures and/or tables were requested, they may be adapted or used in part.
- Please print this page for your records and send a copy of it to your publisher/graduate school.
- Appropriate credit for the requested material should be given as follows: "Reprinted (adapted) with permission from {COMPLETE REFERENCE CITATION}. Copyright {YEAR} American Chemical Society." Insert appropriate information in place of the capitalized words.
- One-time permission is granted only for the use specified in your RightsLink request. No additional uses are granted (such as derivative works or other editions). For any uses, please submit a new request.

If credit is given to another source for the material you requested from RightsLink, permission must be obtained from that source.

BACK   CLOSE WINDOW

Short-Wave Infrared Emissions from Te4 –Ln3 (Ln: Er, Yb)-Codoped Cs2NaInCl6 Double Perovskites

ACS Publications
Most Trusted. Most Cited. Most Read.

Author: Habibul Arfin, Radha Rathod, Ajinkya Sundarnath Shingote, et al

Publication: Chemistry of Materials

Publisher: American Chemical Society

Date: Aug 1, 2023

Copyright © 2023, American Chemical Society

PERMISSION/LICENSE IS GRANTED FOR YOUR ORDER AT NO CHARGE

This type of permission/license, instead of the standard Terms and Conditions, is sent to you because no fee is being charged for your order. Please note the following:

- Permission is granted for your request in both print and electronic formats, and translations.
- If figures and/or tables were requested, they may be adapted or used in part.
- Please print this page for your records and send a copy of it to your publisher/graduate school.
- Appropriate credit for the requested material should be given as follows: "Reprinted (adapted) with permission from {COMPLETE REFERENCE CITATION}. Copyright {YEAR} American Chemical Society." Insert appropriate information in place of the capitalized words.
- One-time permission is granted only for the use specified in your RightsLink request. No additional uses are granted (such as derivative works or other editions). For any uses, please submit a new request.

If credit is given to another source for the material you requested from RightsLink, permission must be obtained from that source.

BACK   CLOSE WINDOW